Theoretical Analysis and Experimental Optimization of Solar Updraft Power Generator

Hadyan Hafizh

2015

KYOTO UNIVERSITY
KYOTO 學 JAPAN
FOUNDED 1897

Theoretical Analysis and Experimental Optimization of Solar Updraft Power Generator

Hadyan Hafizh

2015

KYOTO UNIVERSITY
KYOTO 學 JAPAN
FOUNDED 1897

Abstract

Solar radiation is the largest source of energy available on earth and the solar updraft power generator (SUPG) is a renewable energy facility capable of harnessing its abundant power. The solar updraft power generator offers compelling concepts in producing electrical power. It utilizes solar radiation to increase the airflow temperature, making it less dense than the ambient air which induces a buoyancy force in the form of an updraft flow. Although solar radiation is intermittent and available only during daytime, the heat from solar heating process during the daytime can be stored. However, the solar updraft power generator has an inherent low total efficiency due to the conversion of thermal energy into pressure energy. Acknowledging the low efficiency and considering its potential as a renewable energy facility, the current work aims to increase the total efficiency of the solar updraft power generator. A systematic study has been proposed where the main objective was translated into three specific research questions: How to obtain the mathematical model of SUPG? How to solve the developed mathematical model? Does SUPG have an optimum design and configuration? To answer these three questions, three research methodologies were applied which included theoretical analysis, numerical simulation, and experimental investigation.

A set of mathematical models of the solar updraft power generator have been developed where a thermal network model of a single collector was proposed to derive the heat balance equations. Furthermore, the simplified governing equations of fluid dynamics were used to obtain the collector airflow equation, the tower airflow equation, and the turbine airflow equation. All of these equations were combined to form an integrated model. The result was a set of nonlinear equations describing the transformation of solar radiation into heat-flux of collector airflow. An iterative method was applied through a computer program which was written in the MATLAB environment to solve the developed equation. The performance of Manzanares SUPG and a lab-scale SUPG were assessed numerically. Simulated results were validated by comparing them with those from experiments. A good agreement has been attained between experiment and simulation results.

To find an optimum design and configuration, a series of experiments on a lab-scale SUPG were conducted. Experiments was carried out for two types of collectors, namely collector type A and collector type B. For each type of collector, tower diameter, tower height, and collector height were varied to form a total of 72 experimental cases. From this experimental optimization study, an optimum design and configuration has been observed. However, the updraft velocity from the optimum configuration shows high fluctuations over time which is unfavorable for power production. To overcome this issue, series of straight guide walls was installed inside the collector to enhance the inertia and buoyancy forces so that the entrainment effect towards the center of the collector is higher than it is at the edge of that collector. The results showed that the addition of straight guide walls was able to produce a smoother profile of updraft velocity.

In pursuance of increasing the magnitude of the updraft velocity, another experiment was conducted where series of curved guide walls were installed. A small fan was placed at the bottom of the tower and its rotations were tracked by a high-speed camera so that the time taken to finish one rotation can be recorded and then converted into revolutions per minute (RPM). Experimental results showed that the case with 8 curved guide walls exhibited a higher RPM compared to the case without guide walls. It demonstrates that the curved guide walls configuration has the potential to increase the total efficiency of SUPG.

An assessment concerning power potential of SUPG was also discussed. It was found that the yearly mean energy production in Japan would not be significantly different from those in Manzanares despite the different pattern of monthly mean energy. The selected cities in Indonesia exhibited a higher monthly mean energy production compared to those in Manzanares. In particular a site like Kupang, would generate two times the energy of the Manzanares SUPG. The power production is sufficient for the needs of this isolated area in Indonesia and has the potential to solve the energy issue.

Acknowledgements

I would like to express my sincere appreciation to my supervisor Prof. Hiromichi Shirato, whose encouragement, help, and guidance were indispensable to the completion of this work. For his patience and understanding I am most sincerely grateful.

Special thanks must go to my committee members Prof. Hiromichi Shirato, Prof. Hideo Yoshida, and Prof. Tomomi Yagi for useful remarks and suggestions. Dr. Hiroshi Hattori is thankfully acknowledged for his help and support during my first year in Kyoto University. Also, thanks to Prof. Toyoaki Miyagawa and Prof. Chul-Woo Kim for keeping track of my research.

I sincerely also have to thank all the colleagues in the Bridge Engineering Laboratory, Dept. of Civil and Earth Resources Engineering, Kyoto University, for the help I have often received during these three years and for their friendly companionship. I would also like to thank Mr. Yasuhiro Miyasaka for providing the sensors and equipment throughout the preliminary experiment. Additional recognition is deserved by Ms. Tomoko Souda for her support in academic procedures.

I gratefully acknowledge financial support from the Ministry of Education, Culture, Sports, Science and Technology (MEXT) of Japan for the Japanese government (Monbusho) scholarship.

I would like to thank my family for having supported me for all these years. Finally, the deepest appreciation goes to my fiancé who have silently borne the burden imposed by my graduate studies. To her, this dissertation is dedicated.

Contents

List of Symbols

A_{col}	Area of solar collector	[m^2]
A_{rot}	Area of rotor	[m^2]
a	Inflow coefficient or the ratio of velocity deficit with the oncoming velocity for free flow case	[-]
a_0	Inflow coefficient or the ratio of velocity deficit with the oncoming velocity for constrained flow case	[-]
c_p	Specific heat capacity	[J/kg K]
$C_{\mathcal{T}}$	Coefficient of thrust	[-]
C_P	Coefficient of power	[-]
dz	Differential height	[m]
dr	Differential radius	[m]
D_g	Ground diameter	[m]
D_h	Hydraulic diameter	[m]
e	Specific internal energy	[J/kg]
$\vec{f}_{body}$	The proper form of body force per unit mass	[N/kg]
$\vec{f}_{viscous}$	The proper form of viscous force per unit mass	[N/kg]
g	Gravity constant	[m/s^2]
h_{col}	Height of solar collector	[m]
h_{tow}	Height of solar tower	[m]

h_{c-a}^{conv}	Convection heat transfer coefficient between cover and airflow	[W/m² K]
h_{g-a}^{conv}	Convection heat transfer coefficient between ground and airflow	[W/m² K]
$h_{c-a_\infty}^{conv}$	Convection heat transfer coefficient between cover and ambient air	[W/m² K]
h_{c-s}^{rad}	Radiation heat transfer coefficient between cover and sky	[W/m² K]
h_{g-c}^{rad}	Radiation heat transfer coefficient between ground and cover	[W/m² K]
$h_{g-g_\infty}^{cond}$	Conduction heat transfer coefficient between ground at the surface and ambient ground	[W/m² K]
h_{p-c}^{rad}	Radiation heat transfer coefficient between the aluminum plate and cover	[W/m² K]
h_{p-a}^{conv}	Convection heat transfer coefficient between the aluminum plate and airflow	[W/m² K]
I	Irradiance	[W/m²]
k_a	Airflow thermal conductivity	[W/m K]
$\dot{m}$	Mass flow rate	[kg/s]
Nu	Nusselt number	[-]
p	Pressure	[Pa]
${p_{rot}}^+$	Pressure at the upstream part of the rotor	[Pa]
${p_{rot}}^-$	Pressure at the downstream part of the rotor	[Pa]
p_r	Airflow pressure at the solar collector	[Pa]
p_z	Airflow pressure at the solar tower	[Pa]
P	Mechanical power	[W]
Pr	Prandtl number	[-]
$\dot{q}$	Rate of heat flux transferred to the airflow	[W/m²]
$\dot{q}_{addition}$	Volumetric heating due to conduction and radiation	[W/m³]
$\dot{q}_{viscous}$	Volumetric heating due to viscous effects	[W/m³]
$\dot{q}_{gain}$	Heat gain by the airflow inside the collector of a lab-scale SUPG	[W/m²]

$\dot{q}_{loss}$	Heat loss by the airflow inside the collector of a lab-scale SUPG	[W/m²]
R	Ideal gas constant	[J/kg K]
r	Radial coordinate	[m]
r_{tow}	Radius of the solar tower	[m]
r_{blade}	Radius of wind turbine blade	[m]
Ra	Rayleigh number	[-]
Re	Reynolds number	[-]
S	Conduction shape factor	[-]
t	Time	[s]
T	Temperature	[K]
T_c	Temperature of cover	[K]
T_a	Temperature of airflow	[K]
T_g	Temperature of ground	[K]
T_{a_∞}	Temperature of ambient air	[K]
T_s	Sky temperature	[K]
T_{g_∞}	Ambient ground temperature	[K]
T_p	Temperature of aluminum plate	[K]
$\mathcal{T}$	Thrust	[N]
u_r	Radial airflow velocity	[m/s]
u_z	Axial airflow velocity	[m/s]
u	Velocity deficit due to kinetic energy extraction by the wind turbine for free flow case	[m/s]
u_{rot}	Airflow velocity at the rotor region	[m/s]
$\tilde{u}$	Velocity deficit due to kinetic energy extraction by the wind turbine for constrained flow case	[m/s]
$\vec{V}$	Velocity in vector form	[m/s]
$\dot{w}_{viscous}$	The proper form of rate of work done due to viscous effects	[W/m³]
$\dot{w}_{external}$	The proper form of rate of work done due to external effects	[W/m³]
z	Axial coordinate	[m]

α_c	Absorptivity coefficient of cover	[-]
α_g	Absorptivity coefficient of ground	[-]
∇	Del operator	[-]
Δ	Difference operator	[-]
ε_c	Emissivity coefficient of cover	[-]
ε_g	Emissivity coefficient of ground	[-]
η	Efficiency	[-]
ρ	Air density	[kg/m^3]
τ_c	Transmissivity coefficient of cover	[-]
σ	Stefan-Boltzmann constant	[W/m^2 K^4]

List of Figures

CHAPTER 1

CHAPTER 2

CHAPTER 3

CHAPTER 4

CHAPTER 5

CHAPTER 6

CHAPTER 7

CHAPTER 8

List of Tables

CHAPTER 2

CHAPTER 3

CHAPTER 4

CHAPTER 5

CHAPTER 6

CHAPTER 7

Introduction

Chapter 1

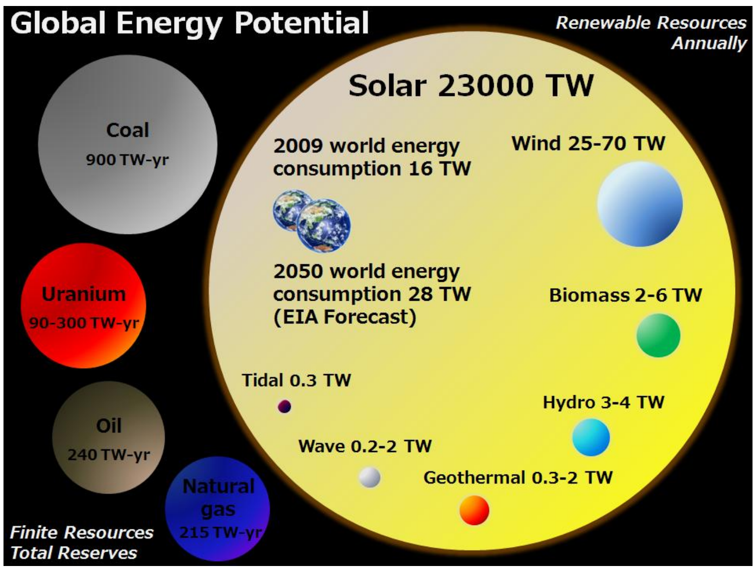

Chapter 1 serves as introductory chapter and it consists of research background, problem statements, research objectives, research methodology, and outline of dissertation. The research work is mainly driven by the effort to increase the total efficiency of a SUPG besides the global motivation to harness the solar radiation as the biggest energy resources on the planet. The research question is how to increase the total efficiency of a SUPG, and to answer that question, series of research works are conducted. It is started with the development of mathematical model in Chapters 2 and 3. The developed models are then used to simulate the performance characteristics of a SUPG in Chapter 4. Useful information from the previous chapters provides a guidance to design an experiment in Chapter 5. Each experiment cases are analyzed in Chapter 6 to seek an optimum design and configuration which gives an improvement in term of its mechanical power. Assessment concerning the power potential of a SUPG is also discussed in Chapter 7, and the last chapter gives a series of conclusions and suggestion for future works.

1.1 Research Background

The global energy is primarily supplied from fossil fuels and the fact that fossil fuels are not a sustainable resource along with demand for this finite resource is only increasing add another issue of global energy. Even if the global fossil fuels are not running out soon, it might be the case that one country has run out of fossil fuels and this country might have to depend on another country's resources in the future. So the energy security supply is also one of the reasons why it is necessary to look into a variety of renewable resources and shift the global energy supply from finite to a sustainable resource.

Solar updraft power generator or SUPG is one of the sustainable power production facilities – consists of solar collector, solar tower, and wind turbine – which utilize solar radiation to increase the temperature of working fluid under the solar collector so that it is less dense than the ambient air at the top of solar tower, inducing a buoyancy force in form of updraft flow that simultaneously entrains the working fluid. The desired kinetic energy from the updraft flow is then harvested into electrical energy by installing one wind turbine at the bottom of the solar tower or series of wind turbine in circumferential manner at the center of collector.

Unlike the conventional wind turbines that harness natural wind in the atmosphere and often encounter with the intermittent issue or even complete cut-off from airflow, the SUPG creates artificial wind as a result of solar-induced convective flows. With this mechanism, a consistent supply of airflow can be managed since the heat from solar radiation can be stored and controlled to be used as a source of continuous energy.

The SUPG also has distinctive characteristic from that of solar photovoltaic where it convert solar radiation directly into electrical energy. The power production in SUPG comes from the conversion process of thermal energy into kinetic energy. These two-steps energy conversion process has the advantages in term of resource intermittency because the thermal energy can be stored either naturally by the soil under the collector or artificially through commercial heat storage medium. Although the excess power from solar photovoltaic can also be stored via batteries, it cannot be operated when no solar radiation is present. Therefore, the concept of SUPG offers a compelling solution to the intermittent issue occur in conventional wind turbines and solar photovoltaic.

In order to verify the concept of SUPG, a research project commissioned by the Minister of Research and Technology of the Federal Republic of Germany was conducted in the 1980's in Manzanares, Spain [1]. The prominent results from this project is that the SUPG inherently has low total efficiency and the reason was reported due to the conversion of thermal energy into pressure energy; in other words the high temperature contains in the working fluid is only used to establish the necessary pressure difference or respectively the density difference of the working fluid inside and outside of the SUPG. Nevertheless, the low total efficiency is tolerated by virtue of simplicity in construction and operation including low cost involved in this power generator [2].

Despite the SUPG has an inherent low total efficiency, its innovative concept has been successfully attract many researcher around the world to investigate the performance of SUPG and develop series of variety power plant owing to the SUPG design and principle. Moreover, a scale-up of power generator based on the principle and results of the Manzanares SUPG has been proposed in two notorious projects as a result of cooperation between Schlaich-Bergermann Solar GmbH, Germany [3] with the Hyperion Energy, Australia [4], and EnviroMission, Australia [5] respectively. These two ongoing projects have planned a large commercial SUPG to be built in Australia and it will be able to produce 200 MW of power. However, in exchange of that power the height of solar tower need to be built up to 1000 m with the radius of solar collector around 3500 m.

The design of the propose plan can be seen in Fig. 1.1 (a) to (c) where the solar collector cover a vast area with very high solar tower erected at the center of solar collector and series of circumferentially arranged turbine. This tremendous size of solar collector and solar tower has become a major challenge for the first construction of commercial and professional SUPG. Moreover, it is generally accepted that increasing of height of solar tower and radius of solar collector of SUPG are the most effective way to boost the amount of power and it has consequence that there is no optimum – in term of power production – geometrical design and configuration of SUPG.

To deal with this issue, the effort to increase the total efficiency of SUPG has not limited to the conventional design as in the Manzanares, Spain. Alteration to the design and concept of SUPG has resulted in a number of innovative power generator such as the atmospheric vortex engine developed in Canada [6] which share the same principle with the SUPG but the solid wall of solar tower has been replaced by a strong updraft vortex so the issue of solar tower in the SUPG could be resolved in this concept. The prototype of atmospheric vortex engine has been built and tested and currently it is an ongoing project where its result is much anticipated since its concept offer an interesting solution to the issue exists in SUPG. Another power generator which also has similar principle with the SUPG is currently being developed at the Fluid Mechanics Research Laboratory, Georgia Institute of Technology, USA [7]. This project attempts to sustain a columnar vortex for power production instead of updraft flow as in the Manzanares SUPG. An outstanding claim from this project that a 5 m vortex diameter coupled to a 10 m turbine diameter with tangential and axial velocity around 8 m/s and 11 m/s respectively, capable to produce the same amount of power generated by the Manzanares SUPG while at the same time successful to eliminate the necessity to have large size of solar collector and solar tower.

All of these efforts to increase the total efficiency and decrease the size of SUPG are clearly demonstrate that the SUPG has excellent potential to be developed as one of the future power generator. However, there is a missing link in these processes for example the previous statement mentioned about the direct way to increase the amount of power of SUPG is to increase both the size of solar collector and solar tower. On the other hand, there are a number of active researches conducted based on the concept of the Manzanares SUPG but the produced power from the solar-induced or heat-induced convective flow does not necessarily have an enormous size of solar tower and solar collector to be able to generate a significant amount of power.

The author notices that this contradiction is due to the gap during the process and effort to increase the total efficiency of SUPG. Therefore, the author proposes a systematic study on the efficiency of a solar updraft power generator in attempt to clarify that whether there is an optimum design and configuration of SUPG exist or not. This question is essential since the optimum design and configuration is directly associated with a highly efficient process and it also become part of the main purpose of this dissertation i.e. to increase the total efficiency of a SUPG. The systematic studies begin with theoretical analysis of a SUPG to provide a set of simple but accurate mathematical model to be solved via numerical scheme. The results from simulation are used as a guideline for the experimental works in finding optimum design and configuration and eventually increasing the total efficiency.

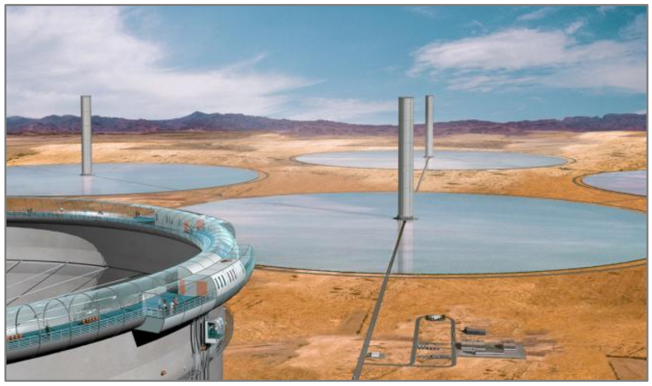

(a) Layout of the proposed scale-up SUPG by the Hyperion Energy

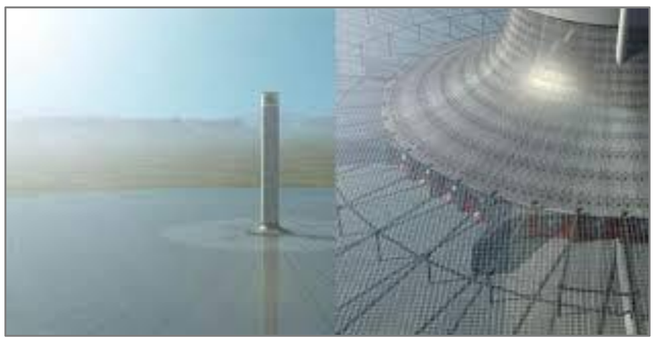

(b) Close-up view of the solar collector showing the arrangement of turbines

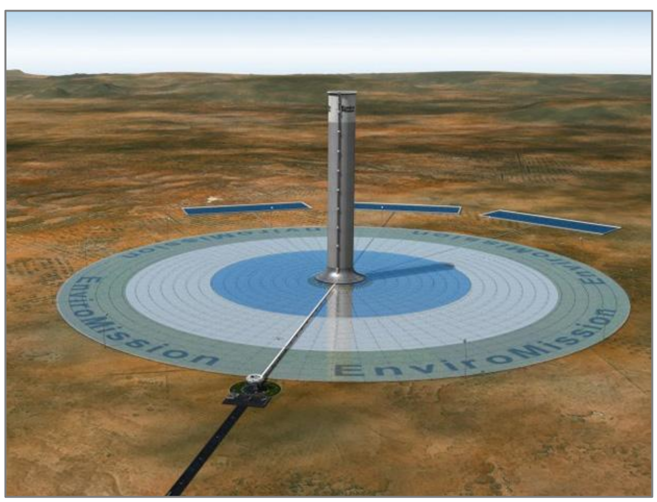

(c) Design of the proposed scale-up SUPG by the EnviroMission

Fig. 1.1 Illustration of the proposed scale-up SUPG capable to deliver 200 MW of power. Picture from: *http://solar-updraft-tower.com* and *http://spectrum.ieee.org.*

1.1.1 Global Motivation

The SUPG has the job to harness the solar energy and indirectly convert it to electrical energy thus this section will provides a complementary assessment on the current situation of the solar energy among other global available resources. Fig. 1.2 shows the recent situation of the global energy potential illustrated in spheres which represents the amount of global energy resources. Useful data for this figure were obtained from [8] and [9]. The finite resources are written in term of total reserves while the renewable resources are in yearly potential. There are four biggest energy resources from the finite group where three of them are comes from fossil fuels. Coal is the biggest reserves in this group with 900 TW-year of total reserves followed by uranium: 90-300 TW-year, oil: 240 TW-year, and natural gas: 215 TW-year respectively.

In the group of renewable resources, solar is the leading with 23000 TW in term of annual reserves, followed by wind: 25-70 TW, Biomass: 2-6 TW, Hydro: 3-4 TW, Geothermal: 0.3-2 TW, Wave: 0.2-2 TW, and Tidal: 0.3 TW respectively. It can be seen that the renewable resources despite its wide variety of choose, they are in diffuse characteristics, in other words they have small power per unit area. For example, in order to replace the fossil fuels as world's energy supply, the size of renewable power generator facilities have to be country-sized because they are so diffuse. This situation has been carefully studied in [10] and it comes with a suggestion that the best option for utilization of renewable energy is to consider all the possible renewable resource instead of focus into one resource. Although the study comes with recommendation to develop all the renewable resources, but the assessment for the global energy potential as shown in Fig. 1.1 has given a clear direction where the effort should be put towards future sustainable energy.

There will of course be challenges in managing solar resource which is locally variable; however, it is globally stable and predictable. These properties of solar resource make the prediction of the SUPG performance can be realized and estimation of power potential in selected locations in the world can also be accomplished. Such works are included in this dissertation as part of results and application of the SUPG. Two countries are chosen for the analysis of power potential of SUPG i.e. Japan and Indonesia, and their solar resources are presented and discussed in the next section.

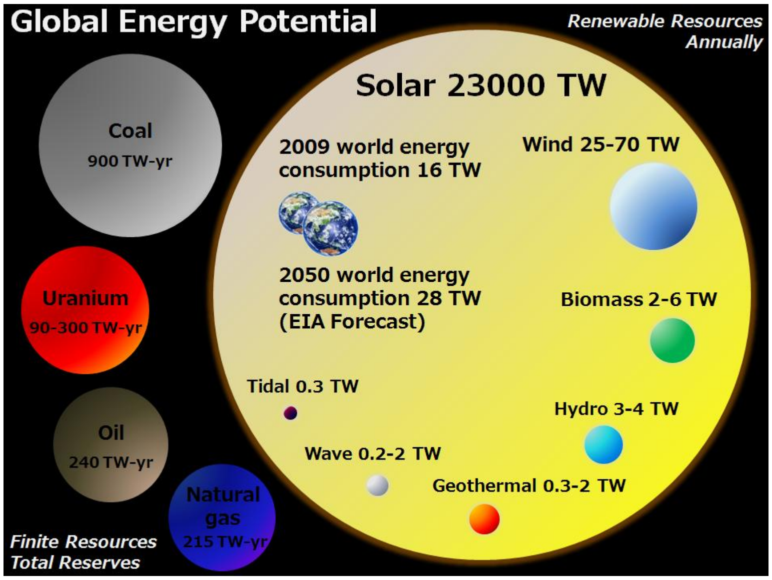

Fig. 1.2 The global energy potential showing the total reserves of finite resources and the yearly reserves of renewable resources.

1.1.2 Regional Opportunity

The solar energy can be viewed as regional opportunity for developing renewable power facilities considering its abundant resource on earth. Despite its amount vary with location as shown in Fig. 1.3, and some regions have high intensity such as in Africa, Middle-east region, Australia, and southwest of USA, other locations in the world are still receive the solar radiation, but how much it can be categorized to be significant for SUPG application. This question will be answered in Chapter 7 of this dissertation; however in this section the solar resources in selected locations e.g. Japan and Indonesia are compared to emphasize that tropical countries like Indonesia have the opportunity for development of SUPG. This comparison can be seen in Fig. 1.4 which shows the monthly mean solar radiation for selected 30 cities in Indonesia and a yearly mean solar radiation in Kyoto, Japan. It can be seen that Indonesia has more solar radiation than Kyoto and it also will have better opportunity for application of SUPG. It is also expected that the application of SUPG in Indonesia could contribute as one of the compelling solution of the current energy issue.

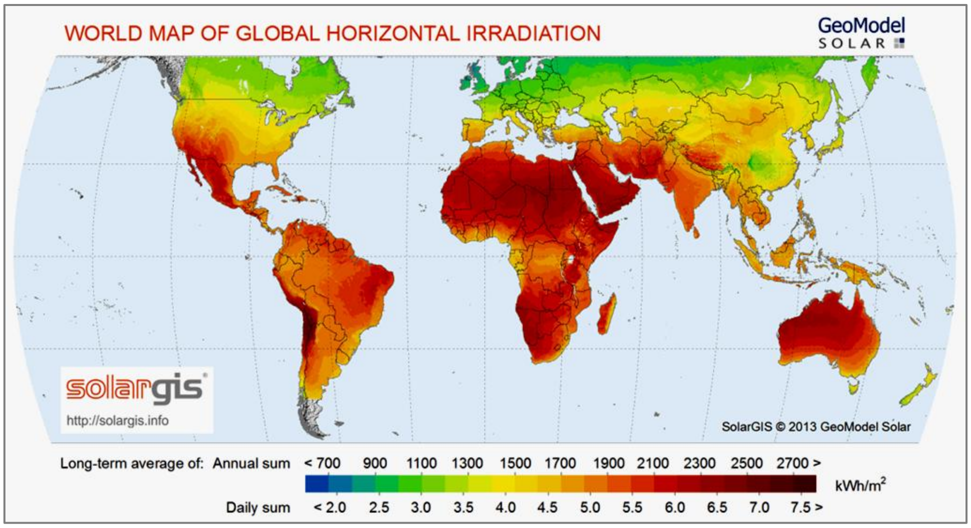

Fig. 1.3 The world map of global horizontal solar radiation. The source of solar radiation data represented on the maps is from SolarGIS database which is provided by SolarGIS © 2013 GeoModel Solar and can be accessed in *http://solargis.info.*

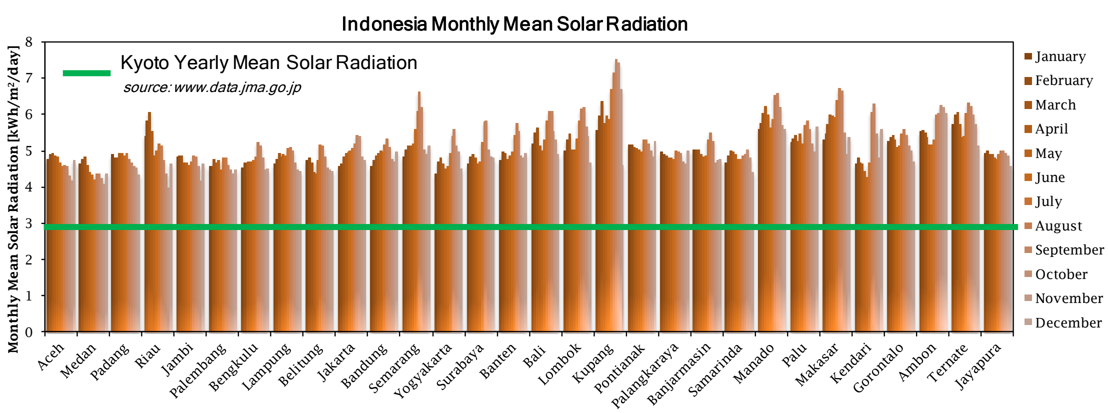

Fig. 1.4 Comparison of Indonesia monthly mean solar radiation with Kyoto yearly mean solar radiation. Data for Indonesia solar radiation are retrieved from [11] and for Kyoto solar radiation is obtained from *http://data.jma.go.jp.*

1.2 Problem Statements

According to the research background, the main issue in developing of a SUPG is due to its inherent low total efficiency. Thus, the following problem can be formulated:

How to increase the total efficiency of a solar updraft power generator?

Solution to the above problem will involve a systematic methodology that has several steps before able to give a straightforward answer. Each step will have their own challenge to be faced within the limited time and capacity. Therefore, the research works will be confined to finding an optimum design and configuration of a SUPG through series of experiment on a lab-scale of SUPG. The preeminent reasons for this are: 1) the lab-scale model of SUPG has the flexibility to be investigated compares to the real scale-down model, since the collector type, collector height, tower diameter, and tower height can be conveniently changed to suits the purpose of the experiment, 2) The ambient environment such as ambient air temperature and solar radiation can be controlled and predicted since the experiment is carried out inside a room which gives low fluctuation of ambient temperature during the measurement, and the solar radiation as source of heat has been replaced with a heating element installed beneath a one square aluminum plate where its temperature is recorded to access and control the amount of heat given to the SUPG system.

It should be noted that the systematic methodology under development in this dissertation should not posses in any form restraint for useful involvement of other design and concept related to SUPG. This circumstance will allow the incorporation of the innovative concept to be potentially implemented in the conventional design of SUPG. Furthermore, to provide the answer to the confined problem statement, a series of sub-problem is proposed as listed below:

- How to obtain the mathematical model of a SUPG which has the following requirements: traceable, simple but accurate, and reliable for parametric studies?
- How to solve the mathematical model of a SUPG through numerical techniques where rapid computational time being a desirable factor?
- Does the SUPG have optimum configuration and which design would work best to meet the main objective i.e. increasing the total efficiency?

1.3 Research Objectives

In accordance with the main formulated problem, the central objective of this research works is appointed **to increase the total efficiency of a solar updraft power generator**. However, the complete process and development to achieve such aim would demand an incremental and iterative approach. Thus, a series of systematic study is proposed to provide a solid guideline and pave the way to contribute to the improvement of total efficiency. These studies include theoretical analysis, numerical simulation, and also experimental investigations of a SUPG with their purposes are listed as follows:

- To formulate a set of traceable, simple but accurate, and reliable mathematical model of a SUPG.
- To develop a set of speedy computer program tailored for SUPG performance analysis and numerical parametric studies.
- To find the optimum design and configuration of a lab-scale SUPG.

These objectives are to be realized in a systematic approach offers in this dissertation and they are best describes in the research methodology section.

1.4 Research Methodology

The methodologies to perform the research works are designated to include the theoretical, numerical, and experimental approach. These methodologies are implemented in order to construct a systematic study on how to increase the total efficiency of a SUPG. From theoretical analysis, it will provide a description on basic mechanism of SUPG. The numerical analysis will solve the formulated equations from the theoretical analysis so that the numerical parametric study can be conducted. The results will be used as a guideline in designing the experimental works for finding an optimum design and configuration.

In summary, the content of introductory chapter in this dissertation can be illustrated as shown in Fig. 1.5. The research background which is combination of the global motivation and regional opportunity provides motivation to propose the research questions and followed by research objectives. Then, the research methodology can be adopted thereafter.

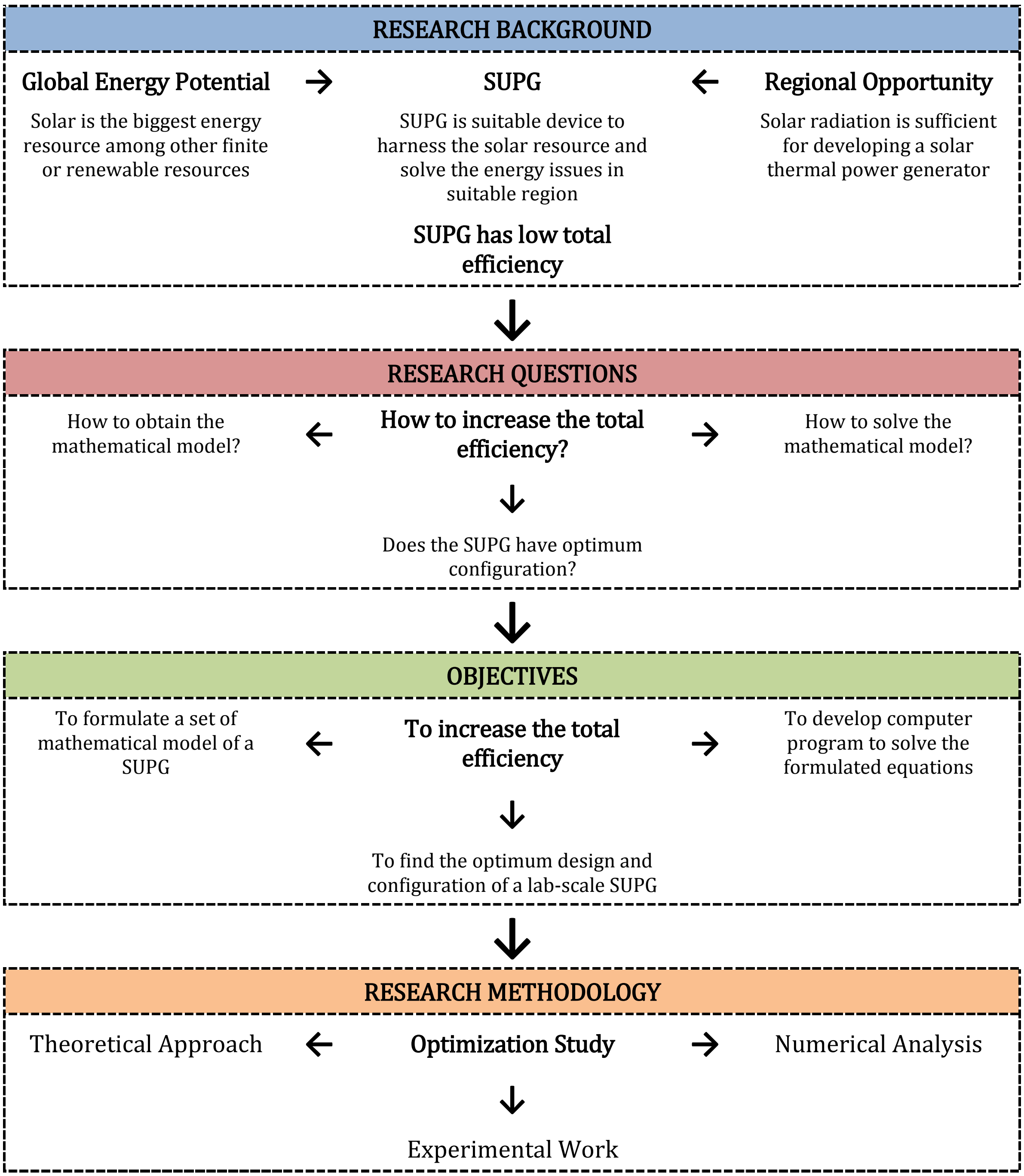

Fig. 1.5 A flow diagram of research works showing the research background as a basis for developing the research questions and objectives to be solved by the proposed methodologies.

1.5 Outline of Dissertation

The content of this dissertation is divided into eight chapters with two chapters as research motivation and background, three chapters describing the methods and the results, and another two chapters for analysis and discussions. The complete structure of dissertation can be seen in Fig. 1.6 and elaboration of each chapter is written as follows:

Chapter 1

In this chapter, the research background is presented which highlighting the proposed plan of several big companies to build a commercial and professional SUPG. On the contrary there are number of active research which stated that the scale of SUPG could be reduced by offering an innovative concept in harnessing solar radiation without losing a significant amount of output power. The reason of enormous scale of SUPG is mainly due to its inherent low total efficiency. Thus the research question is then proposed: how to increase the total efficiency of a SUPG? A straightforward answer to this question should undergo systematic approaches so that the aforementioned contradiction can also be explained and hopefully reveal the mechanism to increase the total efficiency. These systematic approaches are listed in the research objectives, and research methodology section. Finally, this chapter is closed by the outline of dissertation.

Chapter 2

Chapter 2 begins with explanation concerning the basic mechanism of a SUPG. After that, literature reviews of the previous research on SUPG are presented. The pioneer project where the first large prototype was built in 1980’s in Manzanares, Spain is also reviewed and the experimental data from this project is collected for comparison purposes with the results from numerical simulation. The review works is continued for the recent development of SUPG concentrating on the development of its mathematical and physical model. Previous works related to the development of mathematical model is selected and will be used as guidance in developing a set of traceable, simple but accurate, and reliable mathematical model, and the result from the review works in development of physical model of SUPG, will be used to navigate the proposed design in the experiment works as part of effort to find an optimum design and configuration.

Chapter 3

The governing equation of fluid dynamics will be presented in the first section of Chapter 3 since these set of fundamentals equation will used as fundamental reference in deriving the equations for solar collector, solar tower, and wind turbine. The derivation begins with the model of solar collector to obtain the equations for velocity, pressure, and temperature of the airflow inside the solar collector. After that, the model of solar tower will be derived to acquire the equation for velocity of the updraft flow inside the tower. The equation for wind turbine is derived thereafter to obtain the model of mechanical power extracted by the turbine from the updraft flow inside the tower. To establish an integrated model of SUPG, all the previous derived equations are combined and the result is a set of nonlinear equation in matrix form. These set of nonlinear equation are derived for two case studies i.e. the Manzanares SUPG and the lab-scale SUPG.

Chapter 4

Chapter 4 is devoted for developing a computer program to solve the nonlinear equation from Chapter 3. The proposed algorithm and the simulation procedure are explained in detail. The simulation procedures are consist of setting-up the initial and boundary conditions, calculation of thermal properties, and solution to the matrix equation. Simulations are also carried out for two case studies as in Chapter 3. Simulation results for the Manzanares SUPG are validated with the measurement data and they are also compared with the results from other researcher to ensure the reliability of the proposed model. The validated model are then used to study the performance of the Manzanares SUPG which includes the effects of solar radiation, effects of inflow coefficient, effects of collector radius and tower height, along with the effects of ambient temperature. Similar procedures are also applied to the lab-scale SUPG. Validation is conducted by comparing the simulation results of updraft velocity and temperature with those from the experimental works. The applicability of heat transfer correlation is then accessed along with the computational performance of the developed program.

Chapter 5

This chapter mainly presents the experimental works on a lab-scale SUPG. It begins with the elaboration of the design of heating system, collector, tower, and guide walls to form a lab-scale SUPG system. Furthermore, the experimental setup is described following by the measurement procedures. Measurement results are presented for two types of collector design (type A and type B). The updraft velocity and temperature are then presented for various configurations of collector height, tower diameter, and tower height. The optimum configuration is then used to study about the addition of straight and curved guide walls. In addition, it is also used to study about the flow inside the collector and the tower. The procedure to count the fan rotation for guide walls configuration is also presented.

Chapter 6

Analysis and discussion concerning the results from the previous chapter are presented in this section. Discussions are focused on the effects of geometry of a SUPG – collector height, tower diameter, tower height, and guide walls – to the updraft flow and temperature. The purpose is to find an optimum design and configuration which will gives the highest updraft velocity, mass flow rate and mechanical power at the bottom of solar tower. The judgment for optimum design and configuration is based on the mechanical power. Since the amount of input – in this case heat flux – is approximately similar for all cases, thus the performance of a lab-scale SUPG will be judged for particular configuration which produce a higher kinetic energy (as indicated by the updraft flow), by using the least amount of thermal energy (as indicated by the updraft temperature).

Chapter 7

This chapter provides the information about the application of a SUPG for selected locations in Japan and Indonesia. The power potential is accessed by using real meteorological data such as daily and monthly solar radiation and ambient temperature for selected regions in Japan and Indonesia. The purpose of this calculation is to gather the information about the applicability of this power generator at two different regions i.e. Japan and Indonesia where these two countries are selected as the target for development of SUPG for a small scale prototype in the future.

Chapter 8

This final chapter gives a summary of the research works written in this dissertation. The conclusions are presented for each chapter and some of the ideas for future works are also listed as a part of realizing a high efficient SUPG.

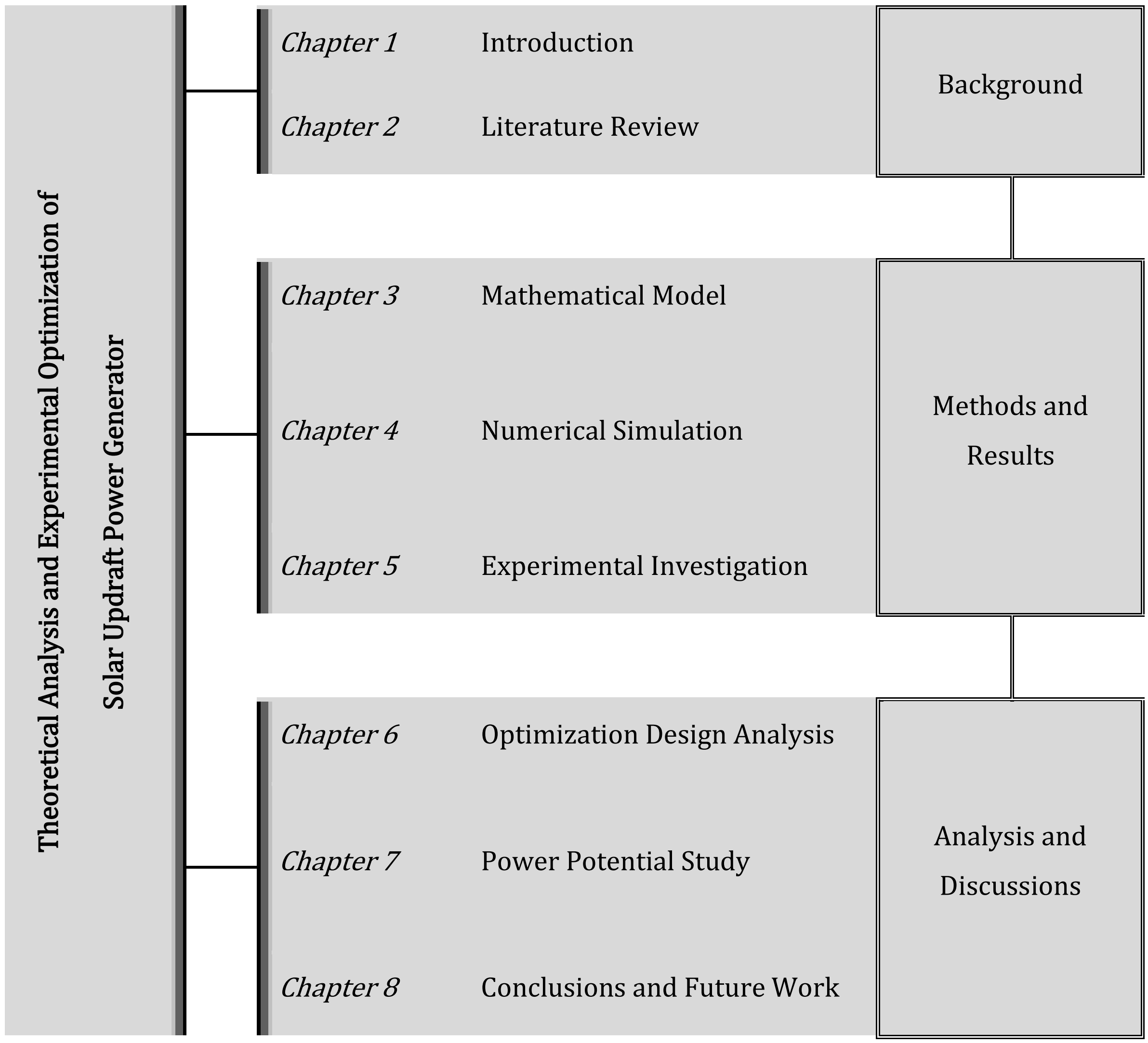

Fig. 1.6 The structure of dissertation.

Literature Review

Chapter 2

Chapter 2 is assigned as review chapter. The review work is start with the explanation regarding the basic mechanism of a SUPG. The role of each component of SUPG – solar collector, solar tower, and wind turbine – is explained in detail along with the energy conversion process in a SUPG. After that, literature review of the pioneer project namely the Manzanares project is discussed. This is the first large prototype which was built in 1980's in Manzanares, Spain. Based on this experiment, list of the advantageous and disadvantageous of a SUPG is also discussed in order to reveal the potential of this power generator. Furthermore, review works concerning the recent development of SUPG is examined focusing on the development of its mathematical and physical model. Selected earlier works in development of mathematical model are reviewed in seeking a combination of traceable, simple but accurate, and reliable model. The review work is continued for the recent development of physical model of SUPG. The discussion is divided into two types of updraft flow i.e. radial updraft flow and vortex updraft flow, in order to make a systematic discussion and simultaneously classifying the variant of SUPG.

2.1 Basic Mechanism of SUPG

A solar updraft power generator in short is a renewable power production facility which utilizes solar radiation to increase the temperature of working fluid under the solar collector allowing the updraft flow entrained the working fluid and thus converting the thermal energy into kinetic energy. The energy conversion process is described as in Fig. 2.1 which shows a diagram explaining the utilization of solar radiation to generate the updraft flow. In this figure, the input for a solar updraft power generator system is solar radiation. When the solar radiation arrived at the surface of the solar collector, part of it is absorbed and most of the solar radiation is transmitted to the down layer. The amount of solar radiation absorbed and transmitted by the cover of solar collector is depending on the optical properties of the cover material i.e. absorptivity coefficient and transmissivity coefficient. The desired condition is low absoprtivity coefficient and high transmissivity coefficient. Such material can be found in low iron glass or high quality PVC film and these materials are grouped into translucent materials.

The transmitted solar radiation is absorbed by the ground under the solar collector. Since the ground surface is act as grey body which has the property to emit radiation, thus part of solar radiation arrived at the ground surface is emitted to its nearest grey body – depends on the angle of incoming ray – which in this case is the cover of solar collector. The cover itself is also act as grey body which emits the incoming solar radiation. This absorption and emission process makes the modeling of heat transfer process becomes complex. Even so, most of the modeling works use some assumptions which capture the most essential processes and still able to produce an accurate model.

Furthermore, the absorbed solar radiation by the ground surface is then transferred in form of heat flux. The transfer process is occurring simultaneously in two modes which are convection to the airflow above the ground surface and conduction to the down layer of the ground. Heat transfer via convection mode to the airflow creates the differences in term of its density, pressure, and temperature. The pressure difference at the solar collector conceives the inertia force and the density difference due to temperature difference organizes the buoyancy force. These two forces must be balance at the center of collector allowing an aerodynamic entrainment to occur inside the SUPG.

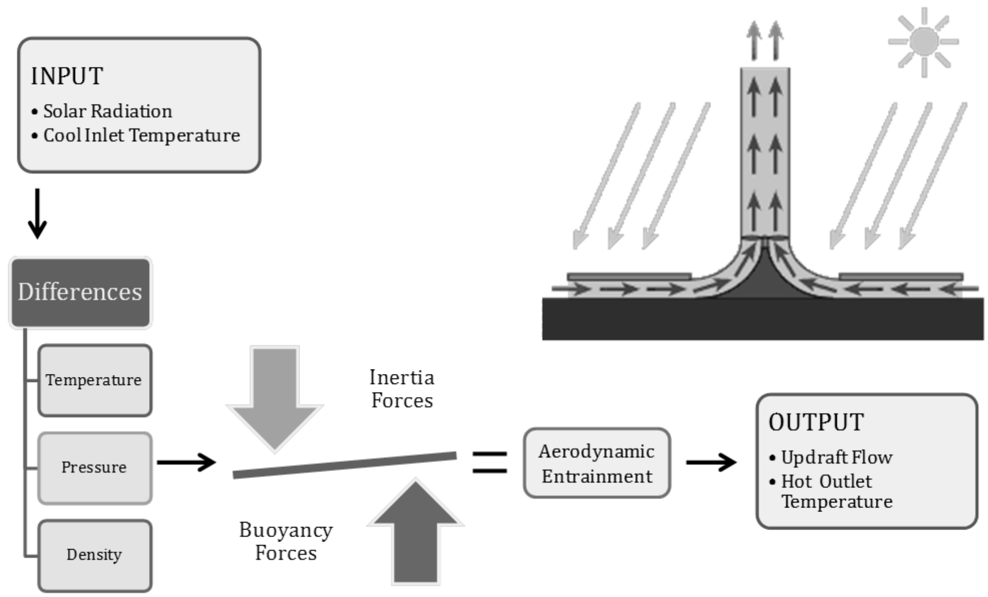

Fig. 2.1 A diagram displaying how a solar updraft power generator works and highlighting the transformation of solar radiation as input to the updraft flow as output. Picture from: *http://mtholyoke.edu*

This aerodynamic entrainment can be sustained as long as there is temperature difference or density difference between the airflow and ambient air. Thus, it can be summarized that the input for this process is solar radiation which is absorbed as thermal energy and through convection process it is converted to kinetic energy and finally by installing wind turbine it is transformed into electrical energy.

Considering the complex energy transformation process in the solar updraft power generator, it is helpful for elaborating the role of each component of a solar updraft power generator as shown in the Fig. 2.2. The main parts of a solar updraft power generator are the solar collector, solar tower and wind turbine. The solar collector comprise of translucent cover which has the function to allow the penetration of the electromagnetic wave from the sun (solar radiation) and simultaneously block the thermal radiation (infrared wavelength). These mechanisms increase the internal energy of the airflow and making the airflow temperature larger than the ambient air.

The materials of the cover could be glass, PVC film or any translucent materials which has the high transmissivity coefficient and low absorptivity coefficient because it is desirable to have more transmitted solar radiation than absorbed solar radiation by the cover. Furthermore, to support these cover structures, an arrays of poles acting as the supporting structures are installed between cover and ground. The supporting structures should not disrupt the airflow or decrease the pressure difference inside the collector, thus the pole structure not only needs careful design but also needs careful arrangement.

In between cover and ground is the space for the airflow which receives the heat flux through convection mode from the ground surface and the cover surface. The hot air is less dense than the ambient air inducing buoyancy force and the updraft flow is quickly organized and simultaneously entrains the airflow inside the solar collector. Since the airflow receives heat flux through convection from the ground surface, thus the ground itself plays an important role in the system of a solar updraft power generator. Usually, the solar updraft power generator is built at the dessert area since this location has abundant solar radiation and has lot of unoccupied land. Although the dessert is the best location for building the solar updraft power generator, the other locations such as uninhabited soil can also be used for the construction of this power generator. The quality of heat absorbed by the ground is depends on the type of soil. The desirable properties of soil are usually related to how much the heat can be absorbed by the soil surface and stored in its down layer so that it can be released at the night time for sustaining the temperature difference and thus allowing 24 hours utilization of power generator. Therefore, the ground itself performs as natural thermal storage which is one of the advantageous in developing this type of power generator. In order to enhance the thermal storage capacity, addition of the water-filled bags under the cover is also one of the choices among the other method for storing the thermal energy.

The wind turbine has the job to harness the kinetic energy from the updraft flow. Arrangement of this turbine can be in the form of single configuration located at the bottom of solar tower or series of them in circumferential manner at the end of solar collector. The turbine system consists of rotor blades and the electric generator. The number of blades can be adjusted to meet the maximum extraction of kinetic energy and the design of the turbine blade can also be optimized to increase the efficiency of wind turbine.

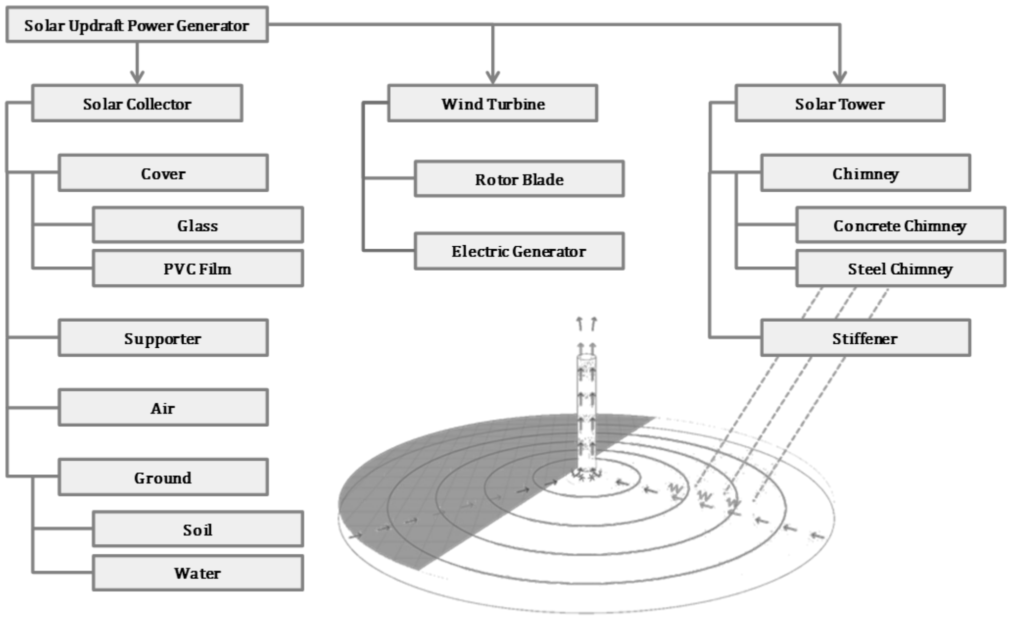

Fig. 2.2 Breakdown of each component of a solar updraft power generator showing that it consist of three main parts: solar collector, solar tower, and wind turbine. Picture from: *http://solar-updraft-tower.com*

As for the solar tower, it is built in form of a chimney where the materials could be concrete or steel. Steel material might be suitable for the short tower instead of concrete since it is relatively easy to manufacture and also widely available in a chimney shape with various diameter. The use of concrete materials should be applied for the case of long and big tower since the thickness of the chimney can be economically regulate to suit the structural stability and safety requirement for this type of structure. Moreover, in the proposed plan of a 200 MW power facilities as discussed in the Chapter 1, concrete material will be used in their construction combines with a series of stiffeners.

These three main parts are then combined in an innovative way to assemble a solar updraft power generator. Although there has been number of works in SUPG with some modification from the conventional configuration, the concept for generating the power is generally similar with the works done in Manzanares, Spain, in 1980's. Thus, it necessary to review about this works and it is discussed in the upcoming section.

2.2 The Manzanares Project

A prototype of the solar updraft power generator was constructed and operated since June 7th, 1982 on a site in Manzanares provided by the Spanish utility Union Electrica Fenosa. This project serves as verification tools, through field measurements, the performance projected from theory, and to observe the individual components on the plant's output as well as its efficiency under realistic engineering and meteorological conditions. Therefore the Manzanares prototype has purposes to determine the feasibility and costs, and verifying the physical principle of the solar updraft power generator.

The prototype has 194.6 m of tower height with diameter of 10.16 m, and the collector has 244 m mean diameter covered by different types of film-PVC with thickness of 0.1 mm. The collector canopy was installed 2 m from the ground level. To extract the kinetic energy from the updraft flow, 4-blade vertical-axis wind turbine was placed at a height of 9 m from the ground level and has 5 m of blade radius. With this configuration, the prototype was able to produce 50 kilowatt of peak power [1].

Basic idea of the SUPG is not entirely new since it is a combination of three old technologies which are solar air collector, chimney/tower, and wind turbine. The original idea in order to harness the solar energy is by making use of the greenhouse effect produced by the solar collector. Moreover, the tower and the wind turbine were combined in an uncomplicated system. The solar collector is composed by translucent covers which allow the penetration of the electromagnetic wave from the sun and simultaneously blocks the thermal radiation (infrared wavelength). These mechanisms increase the internal energy of the airflow and make the temperature larger than the ambient. The hot air rises towards the tower due to buoyancy effects and creates the updraft flow. A wind turbine is placed at the base of the tower to convert kinetic energy from the updraft flow into electrical energy. The whole process can be sustained as long as there is a temperature differences between the airflow inside the SUPG and the ambient air. The efficiency is low due to conversion of thermal energy into pressure energy. In other words, the high heat content (associated with high energy) within the air is only used to create the necessary drive for the updraft flow. According to Haaf [2] the low efficiency is tolerated since it involves extremely low costs and simplicity in the construction and operation.

Fig. 2.3 A picture of the Manzanares solar updraft power generator during a sunny day in the 1980's in Spain.

Fig. 2.3 shows the prototype of the Manzanares solar updraft power generator. The dimensions of the Manzanares SUPG were selected – as shown in the Table 2.1 – to allow the representative experiment results for other possible locations which have different climatic and ground characteristics. In particular for the size of solar tower and solar collector, they were selected to assure the temperature difference between the airflow at center of collector and the ambient air yields around 20 ^{0}C. Moreover, it was reported that the high temperature difference would have beneficial for accuracy in measurement and confirming the principle. However, the high temperature difference would also yields to low collector efficiency due to the excessive heat losses to the ambient environment.

Fig. 2.4 presents the main parts of the Manzanares SUPG. They are the solar tower (a), the solar collector (b), and the wind turbine (c). The solar tower was built 1.2 mm thick trapezoid sheets with reinforcing rings and it was guyed in three directions with four pairs of cables (Fig. 2.4a). The locations of this solar tower must be installed at center of solar collector in return to a strong updraft flow at the bottom of solar tower.

(a) Tower part

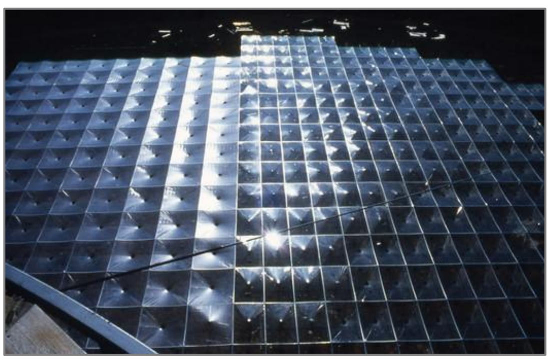

(b) Collector part

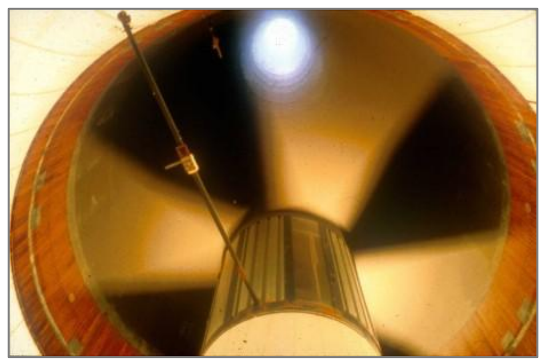

(c) Turbine part

Fig. 2.4 Series of pictures showing the main parts of the Manzanares SUPG. Top picture is the tower part and bottom pictures are the collector and turbine part.

The cover was fabricated from different types of PVC film which has 0.1 mm thickness and it was seated in series of steel-framed panels measuring 6×4 and 6×6 m^2. Each panel was anchored to the ground with help of plastic discs installed at its centre (Fig. 2.4b). The vertical-axis wind turbine was installed at the centre of solar collector or at the bottom of solar tower because at this region the airflow reaches its highest velocity.

Table 2.1 presents the general properties of the Manzanares SUPG which includes the information about dimension of each main part, design thermal properties, design efficiency, and design output of the Manzanares SUPG. The collector of the Manzanares SUPG was built mainly of PVC film covering 87 % of the total collector area and the remaining area was covered by the glass material. As for the wind turbine, it was designed to be operated in grid connection or stand-alone condition. It was consists of 4 blades arranged in vertical-axis to harness the updraft flow from the solar collector.

The solar radiation and the ambient air temperature were designed for 1000 W/m^2 and 302 K respectively. These design thermal properties were able to produce up to 20 K of temperature difference between the airflow at the center of solar collector and the ambient air. The efficiency of solar collector produced from this configuration was around 32 %, however despite its primitiveness, the solar collector efficiency of the Manzanares SUPG was reported reached over 50 %. These conditions include the heat temporarily stored in the ground. For the wind turbine, the efficiency was noted beyond the Betz limit; the maximum power that can be extracted from the wind, due to the diffuser effect from the wall of the solar tower. This wall encapsulated the turbine so that it acts like diffuser and makes the efficiency calculation from the conventional open flow configuration – where the maximum power is usually govern by the Betz limit – cannot be implemented directly. Nevertheless, the efficiency of solar collector was reported 83 % in the Manzanares SUPG. Output from the thermal design was the updraft flow where its velocity reached 15 m/s on release condition and 9 m/s on load condition. A 50 kW of electrical power can be generated when the temperature difference and updraft flow reaches 20 K and 15 m/s.

As for the efficiency of the solar tower, it depends on the pressure losses due to the friction. The pressure difference was measured from the canopy entrance to the top of the tower with high resolution equipment. The measured losses were higher than predicted and it was recognized due to obstructions by the inlet throttle gates and disturbance in the inlet gates. The searching for the right angle of turbine blade was also a major issue in the Manzanares experiment since it directly affects the power produced by the turbine. Besides that, other issues which also affect the produced power are the condensation on the film panels, the continuous life of the power plant for low temperature difference, and the effect of changing atmospheric stratification.

Table 2.1 General properties of the Manzanares SUPG*

Collector		
	Mean collector radius	122.0 [m]
	Mean roof height	1.85 [m]
	Roof covered with polymer sheets	40000 [m^2]
	Roof covered with glass	6000 [m^2]
Tower		
	Tower height	194.6 [m]
	Tower radius	5.08 [m]
Turbine		
	Rotor blade radius	5 [m]
	Number of turbine blades	4
	Blade profile	FX W-151-A
	Tip-to-wind speed ratio	1:10
	Operation modes	Stand-alone or grid connection
Design Thermal Properties		
	Irradiation	1000 [W/m^2]
	Fresh-air temperature	302 [K]
	Temperature increase (mean)	20 [K]
Design Efficiency		
	Collector (mean)	0.32
	Turbine	0.83
	Friction loss factor	0.9
Design Output		
	Updraft velocity under load conditions	9 [m/s]
	Updraft velocity on release	15 [m/s]
	Power (peak)	50 [kW]

**Data has been collected from reference [1] and [3].*

During construction of the prototype and data collecting, several challenges were faced by the Manzanares team. It was found that the dust deposits have a significant influence on the transmission of electromagnetic wave from the sun to the various type of film they used as cover in the solar collector. Their solution was to find the materials which have the self-cleaning property. Polyester and PVC film were chosen to be used over large areas since the dust adhesion was extremely slight, they reported.

Furthermore, in order to evaluate the efficiency and performance of the SUPG system, the following 5 parameters were measured individually: velocity, pressure, temperature, humidity, and irradiance. Measurements were conducted at 5 radially arranged measuring points between the edge of the film canopy and the inlet to the tower and their role is written in Table 2.2.

Table 2.2 Measured parameters in the Manzanares SUPG

Parameters	Remarks
Velocity	The radial wind velocity was measured in order to obtain the radial wind field under the cover
Pressure	Pressure was measured in order to determine the losses caused by friction
Temperature	The airflow temperature was measured to obtain the vertical temperature profiles
Humidity	The relative humidity was measured to obtain an accurate determination of the density as well as its losses due to water evaporation
Irradiance	The radiation balances were evaluated from the electromagnetic wave spectrum and focused on two particular spectra which are ultraviolet spectra and infrared spectra

Upon reviewing the Manzanres SUPG, it is beneficial to list the advantageous and disadvantageous of a solar updraft power generator. The complete summary can be seen in the Table 2.3. The first advantageous of a SUPG is it utilizes both direct and diffuse solar radiation. The direct solar radiation is the solar radiation received from the sun without having been scattered by the atmosphere while the diffuse solar radiation is the solar radiation received from the sun after its direction has been scattered by the atmosphere [12]. Thus, a SUPG has the characteristics to use the sum of the direct and the diffuse solar radiation on a surface which is also referred as the global solar radiation. This characteristic is also makes SUPG different from solar photovoltaic which mostly utilize the direct solar radiation. Moreover, the heat from solar radiation can be stored naturally in a SUPG system by the ground beneath the solar collector. This mechanism allows the SUPG to operate 24 hours on pure solar energy since the heat absorbed during the day will be released at night into the airflow inside the solar collector.

A solar updraft power generator is also reliable and needs little maintenance compare to the other power generator such as steam turbine where more complicated parts contains in one turbine beside the boiler equipments that also needs careful maintenance. Additionally, since the working fluid of a SUPG is the hot air and it uses the wind turbine thus the cooling water and the combustible fuels does not involves as in the conventional steam turbine. Therefore, with these series of valuable features, the SUPG can be built immediately without worrying about its building materials since the glass or PVC film, the concrete or steel materials are widely available in sufficient amount even in the less developed country.

However, in order to generate a significant amount of electrical power to compete with the existing fossil fuel power generator, the SUPG needs a tremendous size of solar collector and solar tower. To emphasize this condition, a study conducted by Schlaich et al. in [19] and [23] reported that for 200 MW of electrical power the size of the solar tower needs to be 1000 m long and 120 m in diameter along with 7000 m of collector diameter. This size is required to compensate its inherent low total efficiency. This situation motivates a number of researchers to increase its total efficiency by intensively studying the principle of a SUPG and even develop a new design of power generator where its share the same mechanism with the Manzanares SUPG. This development will be reviewed in the upcoming section.

Table 2.3 Advantageous and disadvantageous of a SUPG*

Advantageous	
	The collector can use all solar radiation, both direct and diffuse.
	The soil under the collector working as a natural heat storage system, SUPG will operate 24 hours on pure solar energy.
	SUPG are particularly reliable. Turbines and generators – subject to a steady flow air – are the plant's only moving parts.
	The simple and robust structure guarantees operation that needs little maintenance.
	SUPG do not need cooling water and of course no combustible fuel.
	The building materials are available everywhere in sufficient quantities.
	SUPG can be built now, even in less industrially developed countries.
Disadvantageous	
	The total efficiency of SUPG is low compare to the other solar thermal power generator.
	In order to produce a 200 MW of electrical power, the solar tower must be built up to 1000 meter. It challenges the current engineering technology.
	The solar collectors require significant area of land.

**Data has been collected from reference [1], [2], and [3].*

2.3 Recent Development of SUPG

The solar updraft power generator has been gaining attention from researchers after the experimental works in 1980's in Manzanares, Spain, because it has the potential to be one of the clean and safe future power plants. However, its total efficiency remains low, thus many researchers focus their efforts on how to increase its total efficiency. Outcomes from their studies are range from fundamental examination on the mechanism of energy conversion in the SUPG which is lead to the development of mathematical model, to the investigation of design and configuration which pave the way to an innovative concept of utilizing the solar energy. Correspondingly, the discussion regarding recent development of SUPG can be divided into two sections i.e. development of the mathematical model and development of the physical model. These review works will be used as a guideline in developing mathematical model in Chapter 3 and experimental model in Chapter 5.

2.3.1 Development of Mathematical Model

Discussion for the development of mathematical model of a SUPG can be divided into 2 groups. The first group presents the review works on the progress of theoretical models and the second group contains the selected works on the progress of numerical simulation which consist of the development of computer program specified for solving the theoretical model and implementation of commercial CFD software into the SUPG problem. The summary of these review in form of selected works are presented in Table 2.4 and Table 2.5 for the first and second group respectively.

Table 2.4 provides the information concerning progress of theoretical model of a solar updraft power generator where they are arranged with respect to the year of publications. Furthermore, the parameters to be highlighted in this table – which are showing in the features column – are related to the assumptions employed in the derivation of theoretical models and the strategies to solve the developed equations. The results from these review works will be used to develop the mathematical model in Chapter 3 in which the following requirements should be satisfied: traceable, simple but accurate, and reliable for prediction and parametric studies, and also its solution strategies in Chapter 4.

Table 2.4 Selected works on the development of mathematical model of SUPG focusing on the progress of theoretical models

Year	Researcher	Feature
1998	Pasumarthi et al. [13], [14]	Mathematical model was obtained based on the energy balance at the solar collector with the following assumptions: steady state condition, axisymmetric flow, average value for optical properties, inviscid flow, and ambient ground temperature equal to the ambient air temperature. Boussinesq approximation was employed and turbine model was derived upon the Betz limit. Solution was obtained through the iterative techniques.
1999	Padki et al. [15]	A simple analytical model has been developed based on differential equation. The solution was obtained by integrating the equations with employing few assumptions (steady, constant density, and Boussinesq flow) to obtain a closed form algebraic formula for power and efficiency.
2000	Gannon et al. [16]	An ideal air standard cycle was used to calculate the performance of a SUPG with the following assumptions: steady state, dry air, ideal gas, constant specific heat, and constant vertical temperature profile at the solar collector. Friction in the solar tower and exit kinetic energy loss were included in the analysis.
2000	Hedderwick et al. [17]	The developed energy equation was discretized with the following assumptions: constant vertical temperature

		profile at the solar collector, constant specific heat, and dry air. Finite difference scheme and a simple backward time central space numerical scheme were used to solve the equations.
2000	Von Backstrom et al. [18]	One-dimensional compressible flow approach was used and solved by numerical integration for adiabatic tower condition.
2003	J. Schlaich et al. [19]	Explicit formula of the maximum velocity at the solar tower along with the total efficiency has been proposed.
2003	Bernardes et al. [20]	Thermal network model was implemented for energy balance analysis at the solar collector with inclusion of friction. Various heat transfer correlations were employed in the theoretical model for steady axisymmetric flow. The developed model was solved via iteration scheme and validated with the result from the Manzanares SUPG.
2004	Pretorius et al. [21]	The theoretical model and the numerical scheme were based on the previous study in [17]. The use of a quasi-steady state solution procedure. The implementation of more accurate second and higher order discretization scheme for the ground energy equations. The inclusion of wind effects and tower shadows. The development of a user-friendly computer simulation.
2004	Pastohr et al. [22]	Simple analytical models were proposed for steady state

		condition, one-dimensional, axisymmetric, and incompressible flow. The developed simple analytical model doesn't need turbine and solar tower model. Radiation model, solar tower model, and the outflow model does not included in the theoretical model. The solution was computed by using Mathematica software.
2005	Schlaich et al. [23]	The developed model was based on the study in [19] and was used to estimate the power for scale-up model of SUPG
2006	Ming et al. [24]	The effects of various parameters on the relative static pressure, driving force, power output and efficiency have been further investigated for a constant density fluid.
2006	Von Backstorm et al. [25]	Formulation of the optimal ratio of turbine pressure drop has been proposed owing to the power law model.
2007	Koonsrisuk et al. [26]	Dimensionless variables was proposed to guide the experimental study of flow in a small-scale SUPG, however the validity and completeness of the proposed equations remain to be proven.
2007	Zhou et al. [27], [28]	A steady-inviscid model for ideal gas fluid with inclusion of the buoyancy force has been developed in this study.
2008	Fluri et al. [29]	The performance of various layouts for the turbine was compared by using analytical models and optimization techniques. It was found that the single rotor layout without inlet

		guide vanes perform very poorly.
2008	Fluri et al. [30]	Three configurations of turbine have been compared and analyzed i.e. the single vertical axis, the multiple vertical axis, and the multiple horizontal axis. It was found that the single vertical axis configuration has slight advantage in term of efficiency, however its output torque is tremendous and making its feasibility questionable.
2009	Koonsrisuk et al. [31]	In this study, dimensional analysis was used together with engineering intuition to combine eight primitive variables (density, area, velocity, heat flux, specific heat capacity, buoyancy force, tower height, gravity) into only one dimensionless variable that establishes a dynamic similarity between a prototype and its scaled models.
2009	Koonsrisuk et al. [32]	Several theoretical models which was developed in [23], [24], and [36] have been compared. According to this study, the recommended model was the models in [23] and the current proposed model [32].
2009	Koonsrisuk et al. [33]	This study improved the previous study in [26] on the achievement of complete dynamic similarity.
2009	Maia et al. [34]	The conservation and transport equations for axisymmetric, ideal gas were solved numerically using the finite volumes technique in generalized coordinates.
2009	Bernardes et al. [35]	Comparisons for the previous developed models in [20] and [21] were made in terms of various heat transfer coefficients, temperature, and generated power.

		The effect of friction was included in the theoretical model with assumption of 1D axisymmetric flow and ideal gas. In conclusion, both methods applied different heat transfer coefficients thus resulting in different power curve but have similar profile.
2009	Zhou et al. [36]	The theoretical model was developed with the following assumptions: ideal gas fluid, buoyancy force is only considered in the solar tower, linear physical properties of airflow. The developed model was solved with help of MATLAB.
2010	Koonsrisuk et al. [37]	The maximum mass flow rate and power in a SUPG has been analyzed by introducing the concept of Svelteness number; the ratio between external length scale and internal length scale of the system. It was found that the maximum flow power is a function of the length scale of the plant.
2010	Nizetic et al. [38]	Simplified analytical approach for evaluating the factor of turbine pressure drop in SUPG has been investigated. It was concluded that for SUPG, turbine pressure drop factors are in the range of 0.8–0.9.
2012	Koonsrisuk et al. [39]	The mathematical for sloped-SUPG has been proposed and solved through iterative calculation. The turbine was treated as the Rankine-Froude actuator disc where the following assumptions were employed: steady homogenous wind, uniform flow velocity at disc, static pressure decrease

		discontinuously across the disc, and no rotation of flow produced by disc.
2013	Koonsrisuk et al. [40]	The solar collector, solar tower, and wind turbine were modeled together theoretically. Iteration techniques were used to solve the resulting mathematical models. The turbine was treated as the Rankine-Froude actuator disc. The optimal pressure ratio was assumed to be 2/3.
2013	Gholamalizadeh et al. [41]	Main assumptions for the developed model are: perfect gas, gravity independent of altitude, and constant temperature lapse rate. Another assumption for derivation the theoretical models are: One-dimensional flow field, steady state condition. The strongly coupled equations were solved by using finite difference approximation and calculate the output simultaneously via computer simulation program.
2013	Hamdan et al. [42]	In this study, a mathematical thermal model for steady state airflow inside a SUPG using modified Bernoulli equation with buoyancy effect and ideal gas equation has been developed. The result showed that using a constant density assumption through the solar tower, simplify the analytical model. However it over predicts the power generation.

		The developed model was solved using Engineering Equation Solver (EES) software.
2013	Ming et al. [43]	The proposed models were based on the following assumptions: axisymmetric flow of the air in solar collector, incompressible flow, constant air volume and constant air velocity before reaches the solar tower, average value for optical properties. Solution was obtained through iterative calculation.
2014	Zhou et al. [44]	Steady compressible fluid model was employed. Friction was neglected in the developed model. The developed equations were solved by using Runge-Kutta numerical method in MATLAB environment.

In the Table 2.4, Pastohr et al. [22] proposed an uncomplicated model based on the simplified governing equations which served the purpose for comparison and parameter studies. They also make use of CFD software (FLUENT) as basis of their numerical work. The authors realized that the description of the operation mode and efficiency has to be improved. Therefore they have carried out an analysis to improve this issue. A pressure jump model was selected in order to model the turbine. An iterative process was followed thereafter. However, such scheme was reported to be very time consuming. Therefore, they decided to use the Betz power limit as pressure jump model at the turbine section. The simulation does not include radiation model in their computation. Hence, the temperature of cover surface and ground surface was assumed and treated as constant value over the collector. In order to improve this numerical model, Sangi et al. [49] computes the temperature of cover, airflow, and ground surface as function of collector radius. Thus, these temperatures would serve as boundary condition in their CFD simulation. Their numerical work was also based on CFD software (FLUENT). The authors not only conducted a numerical simulation, but also utilized simple model as proposed by Pastohr. Moreover, they also included the pressure model which was solved via iterative scheme. Results from theoretical model with inclusion of friction and numerical simulation were reported to be consistent with the experimental data of the Manzanares SUPG.

A more sophisticated theoretical model was introduced by Bernardes et al. [20] and Pretorius et al. [21]. Works by these two researchers were mainly focused on the development of theoretical model and numerical simulation of a solar updraft power generator. Significant differences between the developed theoretical models are comes from the applied heat transfer coefficients. Bernardes works employ various heat transfer coefficients which most of them are available in the heat transfer textbooks. As for Pretorius works, the heat transfer coefficients were based on their recent measurement. Moreover, these two authors collaborate in order to compare their numerical simulation. Results of this comparison have been reported in Bernardes et al. [35] and it was found that both of theoretical models use different heat transfer coefficients and had practically similar governing equations. In terms of mechanical power and mass flow rate, these two schemes agreed well. In conclusion, different theoretical model and numerical scheme could produce similar results and hence allowing a comparative study to be conducted.

The following summary can be listed from the result of review works presented in Table 2.4. The majority of theoretical works are based on several assumptions such steady state condition, one-dimensional axisymmetric flow, incompressible flow, inviscid flow, ideal gas, and Boussinesq fluid. These are the main assumptions used in the previous theoretical works. Some of the previous works were also employed additional assumptions, for example assigning the Betz limit for the turbine model or used a turbine pressure drop factor in the range of 0.8 – 0.9, used of average value for optical properties, constant specific heat, and constant vertical temperature profiles in the solar collector. Nevertheless, these assumptions are essential in developing the theoretical model since the mechanism of fluid flow receiving heat from solar radiation and forming the updraft flow are a complex process. By applying the suitable and appropriate assumptions to the governing equations of fluid dynamics, the solution to the equations along with their analysis can be conducted conveniently without losing its accuracy.

Solution to the theoretical model can be obtained by solving all the governing equation simultaneously in order to obtain the physical parameters. Basically, there are four physical parameters needs to be solved. They are density, velocity, pressure, and temperature. All the physical parameter can be solved simultaneously if the number of equations matches with the number of unknowns. From the results in Table 2.4, the majority works use the fluid dynamic governing equation which comes from the conservation of mass, momentum and energy. These equations are usually in form of differential equation where its analytical solution can be obtained only for certain and limited cases. Although there was some previous works provide an analytical solution to the developed theoretical model, but most of the earlier works was used the numerical scheme. This is because the developed theoretical model mostly results in a strongly coupled with nonlinearity embodied in the equations which makes the analytical solution are difficult to obtain. This type of equation is convenient to be solved numerically by discretizing the equations or implementing the iterative scheme.

In particular for discretization of the governing equations, it is conveniently done by the commercial software in the framework of computational fluid dynamics or CFD. Therefore, it is also necessary to review the earlier work on the development or implementation of CFD in solving the governing equations of a solar updraft power generator.

Table 2.5 Selected works on the development of mathematical model of SUPG focusing on the progress of numerical simulations

Year	Researcher	Feature
1999	Bernardes et al. [45]	The mathematical model (Navier-Stokes and energy equations) was analyzed by the finite volumes method in generalized coordinates. Temperatures were prescribed and used as boundary condition. The solution was obtained in a fixed computational domain independent of the geometrical shape of the physical system.
2008	Ming et al. [46]	Numerical simulations were explored based on the numerical CFD program FLUENT. Temperatures and pressure were prescribed and used as boundary conditions. Using the Spanish prototype as a practical example, numerical simulation results for the prototype with a 3-blade turbine show that the maximum power output of the system is a little higher than 50 kW.
2009	Zhou et al. [47]	A plume in an atmospheric cross flow from a SUPG was investigated using a three-dimensional numerical simulation model. Temperatures, velocity, relative humidity, and pressure were prescribed and used as boundary conditions. The numerical code uses the finite volume method. The solutions of equations are based on the algorithm Semi-Implicit Method for Pressure-Linked Equations (SIMPLE).
2010	Chergui et al.	In this study, the heat transfer process and the fluid flow in the

	[48]	solar collector and the solar tower under some imposed operational conditions were simulated. Temperatures were prescribed and used as boundary condition. Results were related to the temperature distribution and the velocity field in the solar tower and in the solar collector. They were determined by solving the energy equation, and the Navier-Stokes equations, using finite volume method.
2011	Sangi et al. [49]	Numerical simulation was performed using the CFD software FLUENT to simulate a two-dimensional axisymmetric model of a SUPG with the standard k-epsilon turbulence model. Temperatures and pressure were prescribed and used as boundary conditions. The results from numerical simulation were consistent with the experimental data of the Manzanares SUPG.
2011	Ming et al. [50]	The numerical simulation was processed by software FLUENT, adopting the finite volume method for the solution of the differential equations, the standard k-epsilon equation model as the turbulent flow model, standard wall function method in wall treatment SIMPLEC algorithm in pressure and velocity decoupling. Convection heat transfer coefficient, temperatures, and pressure were prescribed and used as boundary conditions.
2012	Ming et al. [51]	The computations were performed by using the general purpose CFD program FLUENT. The turbine was regarded as a reversed fan with pressure drop across it being pre-set. The numerical simulation results reveal that ambient crosswind

		has influence on the performance of the SUPPS in two ways. On one hand, when the ambient crosswind is comparably weak, it will deteriorate the flow field and reduce the output power of the SUPG. On the other hand, it may even increase the mass flow rate and output power if the crosswind is strong enough.
2013	Cao et al. [52]	In this study, a program based on TRNSYS was built to simulate the performance of SUPG. Model of heat transfer coefficients were provided in TRNSYS program. Nightly power production is not included in the analysis since no model for transient heat transfer in ground was used in this study.
2013	Fasel et al. [53]	Numerical investigation of SUPG was conducted using ANSYS FLUENT and an in-house developed CFD code. The ambient boundary was modeled by an isothermal wall with prescribed ambient temperature and at the inflow boundary the static pressure was extrapolated and the velocity and temperature were prescribed. The results confirm that the power output follows the cubic scaling predicted by theory for all but the very small-scale plants where the flow is laminar.
2013	Guo et al. [54]	The optimal ratio of the turbine pressure drop to the available total pressure difference in a SUPG system was investigated using theoretical analysis and 3D numerical simulations. Temperatures and pressure were prescribed and used as boundary conditions. The simulations were all conducted for steady flow using the

		commercially available CFD package (ANSYS FLUENT).
2013	Ming et al. [55]	The computations were performed by using the general purpose CFD program FLUENT. The QUICK scheme was used to discretize the convective terms and a second order accurate treatment was used for the diffusion terms. Radiation heat transfer among the walls of SUPG in the model is negligible.
2013	Kratzig et al. [56], [57]	A computer program which was able to simulate the physical process in the SUPG was proposed which have the capability to describe the transformation of the solar irradiation into heat-flux of the collector airflow. The computation of power in a SUPG was attained a sufficient exactness with fast computing speed and it is most suitable to be applied for a highly nonlinear equations.
2014	Gholamalizadeh et al. [58]	In this study, to solve the radiative transfer equation the discrete ordinates (DO) radiation model was implemented, using a two-band radiation model. To simulate radiation effects from the sun's rays, the solar ray tracing algorithm was coupled to the calculation via a source term in the energy equation. Commercial CFD software FLUENT provides a solar load model that can be used to calculate radiation effects from the sun's rays that enter a computational domain.
2014	Xu et al. [59]	The commercial CFD code FLUENT was used for the numerical simulation. The SIMPLE-C algorithm was used for pressure velocity coupling calculations. The second order upwind scheme was used to discretized the energy and momentum equation.

2014	Guo et al. [60]	In this study, a three-dimensional numerical approach incorporating the radiation, solar load, and turbine models were proposed. A solar ray-tracing model provided by FLUENT was used to calculate the radiation effects of the sun's rays entering the computational domain.
2014	Patel at al. [61]	Optimizing the geometry of the major components of a SUPG using a computational fluid dynamics (CFD) software ANSYS-CFX was aimed in this study. Temperatures and pressure were prescribed and used as boundary conditions. The results showed that increasing the collector inlet opening significantly influences the overall performance of a SUPG.

Table 2.5 present a summary of the previous works related to the progress of numerical simulation. The solution techniques reviewed in Table 2.5 can be categorized into two groups. The first group is related to the development of computer program specified for solving the governing equations of a SUPG and the second group is for implementation of commercial CFD software. In the first group, works conducted by Sangi et al. [49] and Kratzig et al. [56], [57] provides an excellent example of the theoretical model along with its numerical scheme to solve the developed equations. In particular for the developed equations by Kratzig, it has the desirable property; able to describe the transformation of thermal energy from solar radiation to the kinetic energy in form of updraft flow. Moreover, the iterative techniques developed in this study offer a compelling method in solving the governing equations rather than directly use the commercial CFD software to solve them.

In the second group, most of the earlier works use the FLUENT software to solve the governing equation in a SUPG system. The widely use boundary conditions can be listed as follows: prescribed temperature of walls, prescribed heat flux, and prescribed pressure of the airflow. By implementing these types of boundary conditions, the transformation of solar radiation into thermal energy in form of collector airflow heat-flux cannot be described since the results of thermal heating process by solar radiation had been replaced by the prescribed wall temperatures.

Because the purpose of the present work is to develop a set of traceable, simple but accurate, and reliable model as stated in Chapter 1, thus the CFD solver does not seem meet these criteria due to limitation in the modeling of transformation of thermal energy into the collector airflow heat-flux. However, some of the previous works – as shown by Gholamalizadeh et al. [58] and Guo et al. [60] – had implemented the solar radiation model by using a solar ray-tracing model provided by FLUENT. The results from this numerical simulation were reported to be consistent with the experimental data in Manzanares SUPG. However, it does not attain a sufficient exactness combines with a fast computing speed. This is due to the modeling of turbine in the FLUENT environment was done by assuming the value of turbine efficiency which gives an inaccurate prediction of the generated power. On the other hand, the traceable model combines with a fast iterative calculation offers by Bernardes [20] and Kratzig [56], [57] does seem meet the criteria of theoretical model and numerical scheme required in the Chapter 1.

2.3.2 Development of Physical Model

After reviewing the previous works related to the development of theoretical model and its numerical scheme to solve those models, in this chapter the review works is continued with the discussion on the development of physical model of a solar updraft power generator. As in the development of mathematical model, the examination for the development of physical model can also be divided into two groups. The classification is made with regards to the types of the updraft flow namely updraft radial flow and updraft vortex flow. The physical model of a solar updraft power generator has the job to realize these two types of flow depend on its design and configuration. Therefore, it is necessary to track the progress of physical model of SUPG since it demonstrates the effort of researchers to increase the total efficiency where it is not only limited to the optimization of the conventional model of SUPG like in the Manzanares, but also has been expanded to study and investigate a new design and configuration, for example producing the updraft vortex flow instead of updraft axial flow.

Fig. 2.5 shows the recent project of solar updraft power generator prototype. The top picture displays the pilot power generator operated in Wuhai city of Inner Mongolia Autonomous Region on North China. The prototype has 53 m of tower height and this value much lower compare to the Manzanares SUPG. This is due to the restriction of the requirements of airport clearance protection since this prototype was built near the Wuhai airport. The design of its collector is in ellipse shape covering 6170 m^2 desert land where glass was selected as the cover material. Configuration of the turbine is in horizontal-axis single-rotor type which can be operated in stand-alone or connected (to the grid) mode. The power is also expected much lower than the Manzanares SUPG: 3 kW for average ambient air velocity lower than 2 m/s [62].

The bottom picture in Fig. 2.5 shows the scale model of Manzanares SUPG. A 1:30 scale model of the Manzanares SUPG was constructed and tested for validation purposes. The analysis for this scale model was conducted in collaboration between the New Mexico State University and University of Arizona. Since there is a plan to build a larger scale of solar updraft power generator in Arizona – for example the proposed project by the Enviromission team [5] – thus, the result from this experiment is highly anticipated.

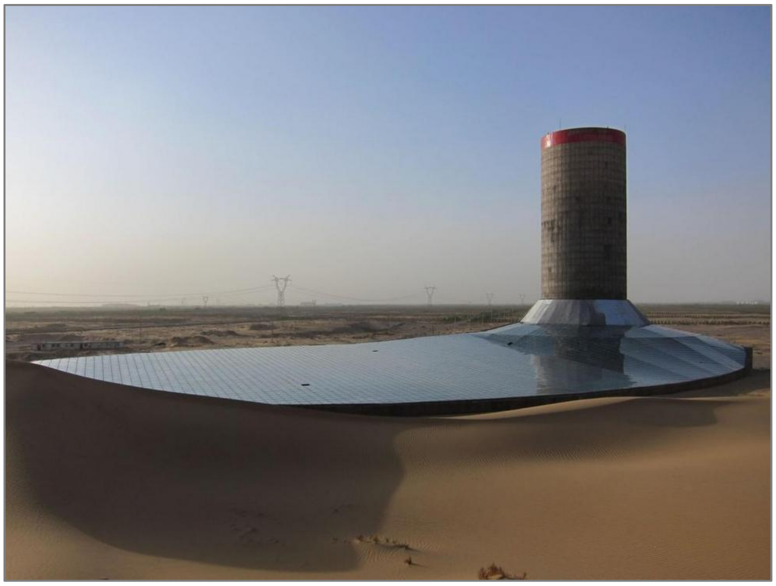

Picture from: http://scmp.com/news/china/article/1487659/solar-chimneys-may-help-solve-chinas-energy-woes

Picture from: http://dept-wp.nmsu.edu/activites/sample-page/page7-2

Fig. 2.5 Pictures showing the two recent projects of SUPG prototype. Top picture is the prototype built in Wuhai, China and the bottom picture is the scale model of the Manzanares SUPG constructed in Arizona, USA.

(a) A picture of SUPG protype in Botswana [63]

(b) A picture of SUPG prototype in China [63]

Fig. 2.6 Pictures of two recent prototypes of SUPG showing that both the solar collector has the upward-slope configuration.

Fig. 2.6 (a) presents the prototype of a solar updraft power generator built in Botswana. This experimental model has 2 m and 22 m of solar tower diameter and height respectively. The solar tower was made of glass reinforced polyester material. The height of the outer solar collector from the ground is around 10 cm and covered around 160 m^2 of land area. The cover was made of clear glass materials where the thickness approximately 5 mm and it was supported from the ground by series of steel framework. The ground itself was covered by two layers of compacted soil and a layer of crushed stones where it was spread uniformly on the surface of the compacted soil layer. The purpose was to increase the absorption of solar radiation. The nozzle or the bottom of the solar tower was situated 2.8 m from the ground and subsequently a 6-blade turbine was installed at the exit end of the nozzle [64].

Fig. 2.6 (b) displays the experimental model of a solar updraft power generator constructed in Huazhong University of Science and Technology, China. In this project, the configuration of the cover was selected in form of conical shape having upward-slope. The angle was chosen as 8^0 and the inner height of solar collector was parked 0.8 m from the ground and the outer height was 0.05 m from the ground. The solar tower was made from PVC drain-pipes having 0.3 m diameter and 8 m height. The diameter was selected not to big enough so that the tower should not be too high to avoid too much frictional loss during airflow in the tower and too large heat loss to the ambient environment. The size of solar collector was 10 m in diameter and supported by iron framework. The material for the cover was made from a single sheet of transparent glass fiber reinforced plastic and it was also used mixed asphalt and black gravel as the absorber (for solar radiation). The designed power in this project was 5 W generated by a single multiple-blade turbine which was installed at the base of solar tower [28].

Both of the prototypes in Fig. 2.6 have the upward-slope solar collector configuration. The study conducted in [28] reported that the reason for this configuration was to maximize the absorption of solar radiation. In this study it was also noted that the optimum slope must be equal to the local altitude. However, the realized slope in their experimental model much lower than the required due to consideration of construction costs. As for the study in [64] it was not discussed the consideration of choosing an upward-slope configuration for the solar collector.

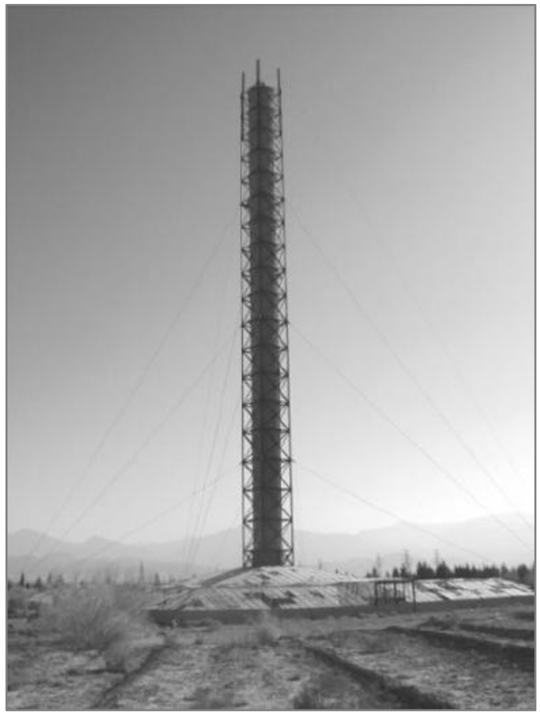

(a) A picture of SUPG prototype in Kerman, Iran [65]

(b) A picture of SUPG prototype in Belo Horizonte, Brazil [38]

(c) A picture of SUPG prototype in Florida, USA [13], [14]

Fig. 2.7 Pictures of several experimental model of SUPG showing that all the models have the upward-slope configuration.

Fig. 2.7 (a) presents the SUPG prototype which was built in Kerman, Iran. The solar tower was constructed with 3 m of diameter and 60 m of height while its solar collector has the radius around 20 m covered around 1600 m^2 of land area. From this configuration it was reported that 400 W of electrical power could be generated in solar radiation of 800 W/m^2 [65]. The strategies to increase its total efficiency were investigated for example: installation of conical shape in the entrance of the solar tower. This particular strategy leads to an upward-slope configuration of the solar collector which was widely used in most of experimental models. Another strategy which was explored in this project is related to the usage of asphalt or rubber in the bottom of solar collector. It was reported that combination of the aforementioned strategies could enhanced the power up to 7 kW.

Fig. 2.7 (b) shows the experimental model of a SUPG constructed in Belo Horizonte, Brazil. This small-scale SUPG was not studied for power generation only but also for food drying processes as well. Similar design, in particular for the conical configuration at the inlet and outlet of solar collector is observed. In this project, the solar tower of 12. 3 m in height was constructed with sheets of wood and covered by fiberglass with a diameter of 1 m. The cover for solar collector was made of a plastic thermodiffusor film and it has a diameter of 25 m. The solar collector was fixed 0.5 m from the ground surface by using a series of metallic structure. In order to increase the solar radiation absorption, the ground was built in concrete and black-painted. In particular for the inner part of solar collector or the entrance region for the airflow, the height was reduced to 0.05 m with purpose to minimize the effects of the external wind speed under the coverage and the consequent cooling of the absorber ground [66].

One of the pioneer projects on a small-scale SUPG is presented in Fig. 2.7 (c). This experimental model was constructed in Florida, USA with purpose to study the temperature and velocity profiles within the SUPG system. The solar tower has 7.92 m of height and the solar collector has 9.15 m of diameter. The cover of solar collector was composed by a polycarbonate sheet with an aluminum plate installed as absorber. This situation makes the thermal energy not dissipated to the ground and it was expected that the collector efficiency can be increased significantly. The design of collector area was selected to be increased radially, and it was reported that this mechanism would increase the airflow temperature before it enters the solar tower section [13], [14].

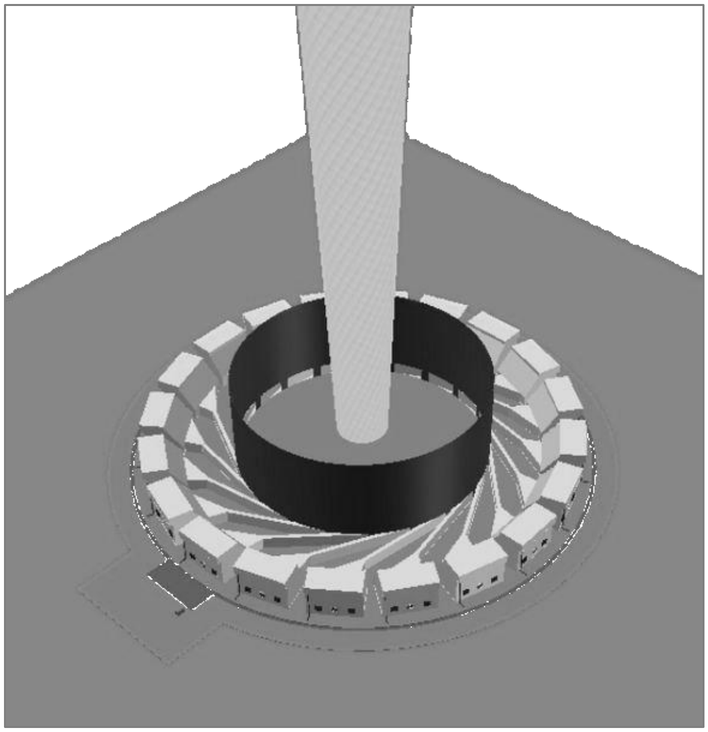

(a) Illutration of an atmosperic vortex engine [6]

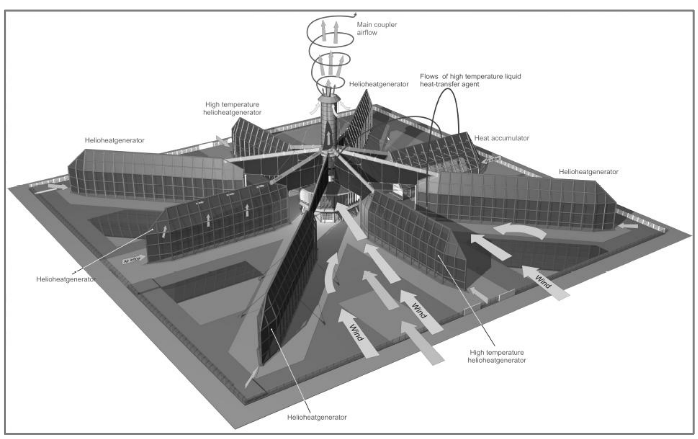

(b) Design of an artifical tornado power generator [67]

Fig. 2.8 Pictures showing the design and concept of the atmospheric vortex engine and the artificial tornado power generator.

Despite the active development on the conventional design and configuration of a solar updraft power generator, there is also a number of active research groups who concentrates on finding an innovative method in utilizing the solar-induced wind energy concept and designing a new configuration of solar updraft power generator. For example: the concept of generating the atmospheric vortex which has been realized into a vortex engine by Michaud et al. [6]. The design of this engine can be seen in Fig. 2.8 (a) which shows the formation of an updraft vortex as a result of channeling the airflow by series of guide walls. The source of heat in this engine can be from fuel burning, solar heating, or waste-heat from the fossil fuel power facilities. The research work is actively conducted and recently the vortex engine team have been tested a prototype and the positive results from this experiment is much anticipated since the requirement of having a tall solar tower could be eliminated. Similar concept with the vortex engine but different realization in the physical model was also introduced by a research team in Italy [67] and the design can be seen in Fig. 2.8 (b). The concept for this type power generator is similar with the conventional SUPG and instead of producing the updraft radial flow, this power generator generate an updraft vortex. The working fluid used in this concept is also the hot air and the heat source comes from the side walls which absorbed heats from solar radiation to be transferred to the airflow. A prototype of this power generator has also been constructed.

Another power generator which aims to produce an updraft vortex has also been investigated by a research group in Georgia Institute of Technology, USA [7]. The design from this group can be seen in Fig. 2.9 (a). The electrical power is generated from "anchored" columnar vortices that can be controllably formed in areas with high surface heating rates. These vortices entrain the ground-heated air layer where the solar heating process from solar radiation is occurred and subsequently converting the (gravitational) potential energy into kinetic energy [68]. The main difference between this project and the previous vortex engine is: this power generator deliberately triggered and anchored columnar vortices in order to sustain an updraft vortex. The vortex engine must rely on the existence of the entrainment effect from the updraft vortex since the turbine was placed in circumferential manner and does not anchored to the vortex itself. Thus, it may seems that this power generator have an advantageous from the vortex engine in term of sustaining the updraft vortex.

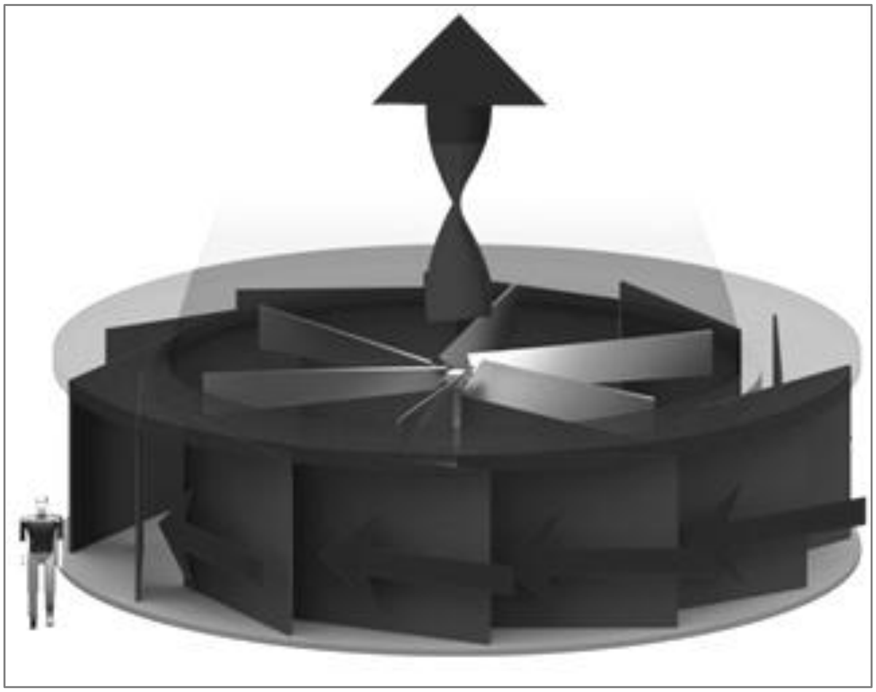

(a) Illustration of a solar vortex power generator [7]

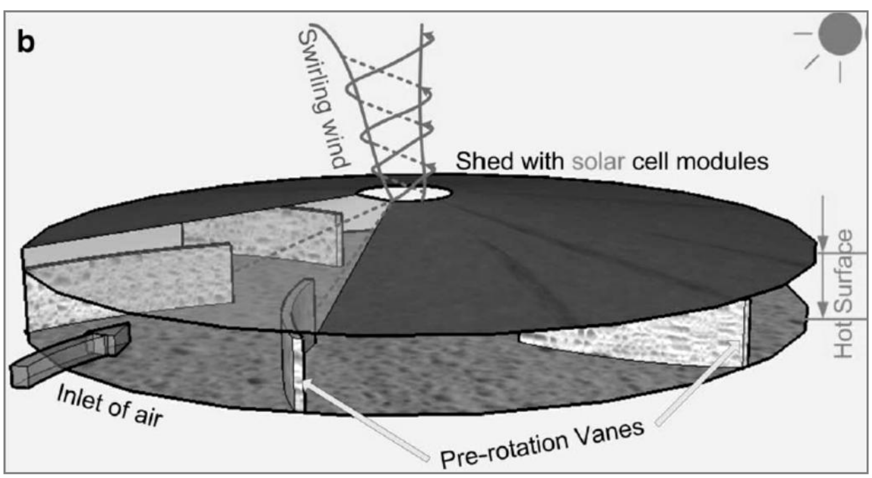

(b) Schematic drawing of a model of solar-induce updraft vortex flows [69]

Fig. 2.9 Pictures showing the experimental models of the recent development in solar-induced wind energy devices.

A recent article published in Nature Scientific Reports [69] shows that the formation of an updraft vortex can be realized by introducing series of guide walls in between the cover of solar collector and the ground surface. In this study, an experimental model was built to study the mechanism of the updraft vortex and evaluate the potential of this type of power generator. The source of heat was obtained from the plate heating system which can be controlled and measured. The temperature was measured by using thermocouple sensor and the wind velocity was recorded with digital air velocity meter for two components of wind velocity i.e. axial and tangential velocity. The results from this study was illustrated a promising potential of the circular shed for generating swirling wind energy via the collection of low-temperature solar energy.

2.4 Remarks

The literature review began with a historical review of the first large prototype of a solar updraft power generator which was conducted in Manzanares, Spain. Then, a literature study concerning the development of a solar updraft power generator, after the first large prototype in the Manzares Spain, has been presented. The progress of research works related to the solar updraft power generator is discussed in two separate groups. The first group consists of the progress in the development of mathematical model and the second group consists of the progress in the development of physical model. The result of review works from the first group reveals that most of the mathematical model employs the following assumptions: steady state condition, one-dimensional axisymmetric flow, inviscid flow, and ideal gas. The purpose is to simplify the analysis without losing the accuracy of the model itself. The result from the second group showed that most of the experimental models for conventional SUPG use an upward-slope configuration for solar collector. Furthermore, the recent proposed design for creating a sustainable updraft vortex offers a great promising as one of the solution to increase the total efficiency of a conventional solar updraft power generator. The useful result from the first group will be used in Chapter 3 as a guideline in developing the mathematical model which has the properties of: traceable, simple but accurate, and reliable for prediction tools. The result from the second group will be used in Chapter 5 in finding a new design and innovative concept.

Mathematical Model

Chapter 3

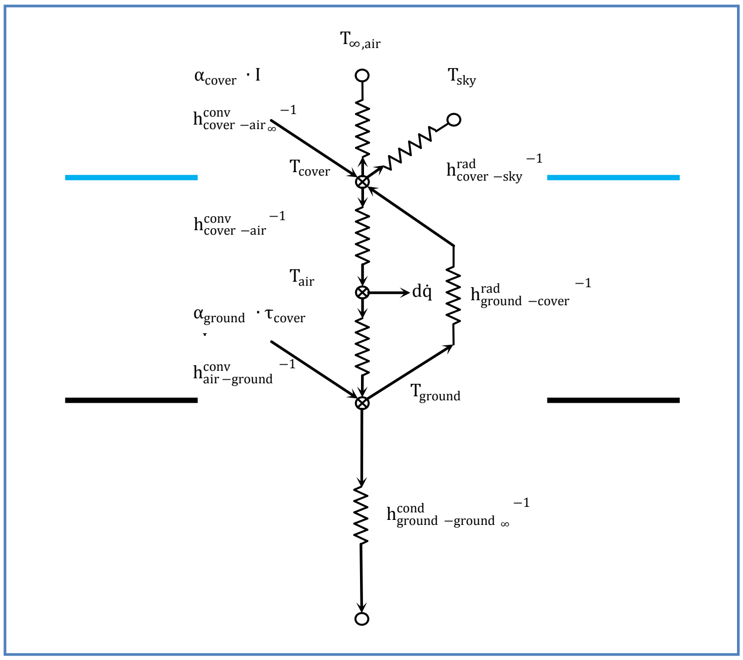

Chapter 3 consists of study on the derivation of mathematical model of a solar updraft power generator. The governing equation of fluid dynamics is used to obtain the model of airflow inside the solar updraft power generator where several suitable assumptions are applied. The equations are derived for three regions i.e. solar collector, solar tower, and wind turbine. At the solar collector, the equations for airflow velocity, pressure, and temperature are formulated from the principle of mass, momentum, and energy conservation. At the solar tower, the equation for updraft velocity is derived with regards of free convection process. As for the wind turbine, the generalized actuator disk theory is implemented to obtain the equation for power generation. Finally, all of these equations are combined to form an integrated model of a solar updraft power generator.

3.1 Introduction

In pursuance of increasing the total efficiency of a solar updraft power generator, an accurate and reliable mathematical model holds an important factor. Accurate mathematical model makes the estimation and prediction of the performance of a solar updraft power generator reliable. The parametric study can also be studied by exploiting this model in finding a method to increase the total efficiency. This parametric study includes the effects of geometry and ambient conditions to the efficiency of each part in a solar updraft power generator system.

However, having an accurate and reliable model is not sufficient enough in understanding the mechanism of energy conversion in a SUPG system. Perhaps, a traceable and simple model are also becomes the desirable properties since the main parameters can be captured without getting distracted with every little detail of modeling process. These main parameters are translated as the variables that plays important and significant role in the power production of a solar updraft power generator.

Tractability and simplicity of a model is defined as the ability of the developed model to capture the main variables involves in power production while also successfully to described the conversion of solar radiation to the collector airflow heat-flux. This heat flux is to be transformed into kinetic energy of the updraft flow and to be harvested into electrical energy by the turbine. This complex process of energy conversion must be included in the developed model so that each process can be optimized to achieve a highly efficient energy conversion process.

Furthermore, an accurate and reliable model is defined as the ability of the developed model to simulate the complex process of energy conversion inside a solar updraft power generator where the results of simulation are consistent and in good agreement with the real physical process in the SUPG, for example with the experimental model in Manzanares, Spain. Accurate model is expected to produce a consistent performance estimation and prediction, or any desirable results with the result from the other methods – for example results from other researchers – for any changes in the parameters of the developed model. Therefore, these 4 models properties will be realized during derivation of the mathematical model. It is begin with the evaluation of governing equation of fluid dynamics.

3.2 Governing Equations

The mathematical model is based on the fundamental governing equations of fluid dynamics – the continuity, momentum, and energy equations. They are the mathematical statements of three fundamental physical principles upon which all of fluid dynamics is based: 1) Mass is conserved, 2) Newton's second law, 3) Energy is conserved [70]. These three fundamental principles are written in form of partial differential equation as shown in Table 3.1 [71], where the continuity, momentum, energy, and one state equation are presented. This addition of state equation is required to solve the equations since the number of unknown variables from the continuity, momentum and energy equations (density, pressure, velocities, and internal energy) is more than the number of equations. So this equation will relate the pressure, temperature, and specific volume of a substance [72], in this case is the hot air. Despite there are several equations of state has been established, but in this study the ideal gas equation of state is selected. This set of governing equation will be used as fundamental reference in deriving the equation of airflow at the solar collector, solar tower, and turbine region where several suitable assumptions will also be implemented. The complete derivation is presented in the Appendix A.

Table 3.1 The governing equations of fluid dynamics

Continuity equation	$\frac{\partial}{\partial t}\rho + \left(\nabla \cdot \rho\vec{V}\right) = 0$	(3.1)
Momentum equation	$\frac{\partial}{\partial t}\rho\vec{V} + \rho\vec{V} \cdot \left(\nabla\vec{V}\right) = -\nabla p + \rho\vec{f}_{body} + \vec{f}_{viscous}$	(3.2)
Energy equation	$\frac{\partial}{\partial t}\left[\rho\left(e + \frac{\vec{V}^2}{2}\right)\right] + \nabla \cdot \left[\rho\left(e + \frac{\vec{V}^2}{2}\right)\vec{V}\right] = \rho\dot{q}_{addition} + \dot{q}_{viscous} -$ $\nabla \cdot \left(p\vec{V}\right) + \rho\left(\vec{f}_{body} \cdot \vec{V}\right) + \dot{w}_{viscous} + \dot{w}_{external}$	(3.3)
State equation	$p = \rho RT$	(3.4)

3.3 Mathematical Model of Solar Collector

A schematic drawing of solar updraft power generator can be seen in Fig. 3.1 where the solar collector receives heats from solar radiation and the airflow travel from the outer part to the inner part of collector before harvested by a wind turbine at the bottom of solar tower. The airflow inside the solar collector is flowing in radial direction (r) of cylindrical coordinate – the circumferential direction is not included due to the axisymmetric flow assumption – and in the axial direction (z) for the airflow inside the solar tower.

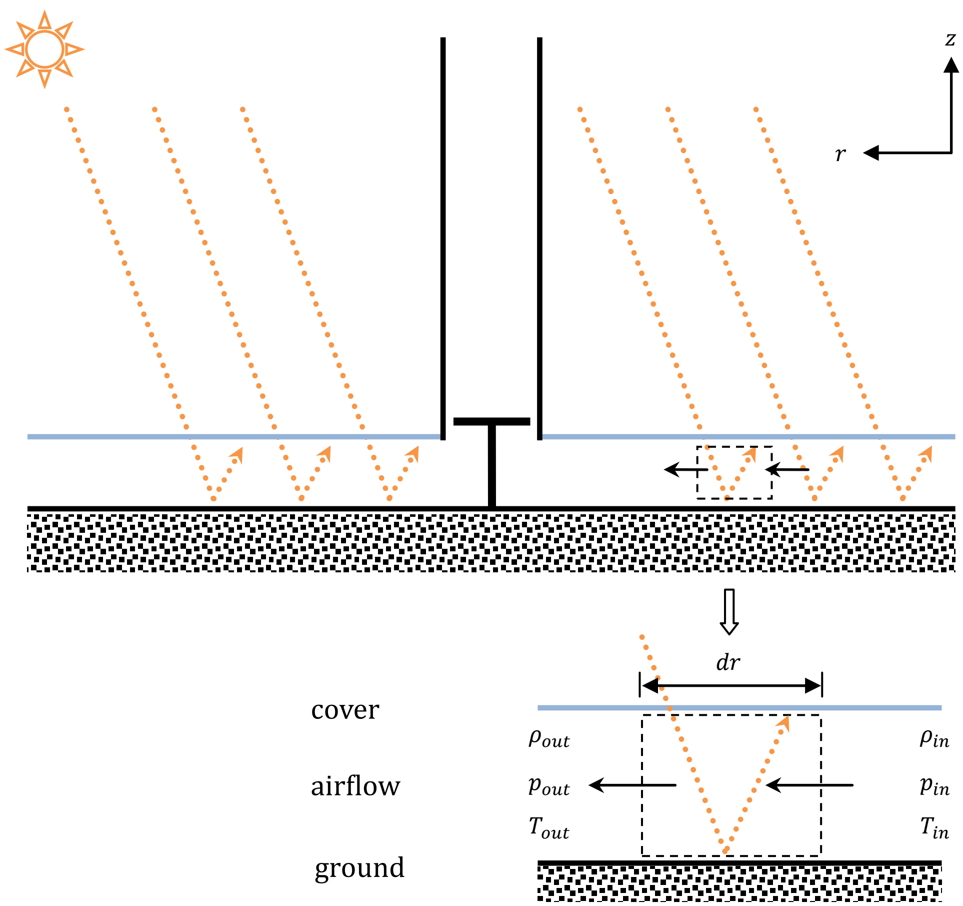

Fig. 3.1 Schematic drawing of a solar updraft power generator focusing on the solar collector where solar radiation heats the air inside.

The solar collector is amount to the cover, the ground, and the hot air or working fluid flowing in between. The solar heating process causes the differences in term of density, pressure, and temperature simultaneously in two separate points at distance dr inside the solar collector. For instance, the density, pressure and temperature of the airflow at the first point can be labeled as $\rho_{in}, p_{in}, T_{in}$ respectively and $\rho_{out}, p_{out}, T_{out}$ at the other point. These three physical quantities must be represented by mathematical equations which describe their behavior under certain conditions.

Table 3.2 Assumptions and simplified equations used in the analysis of solar collector

	Assumptions	Simplified Equations	
Continuity equation	○ Axisymmetric flow ○ Steady-state condition ○ Fluids are treated as ideal gases	$\frac{1}{r}\frac{\partial}{\partial r} r\rho u_r = 0$	(3.5)
Momentum equation	○ Axisymmetric flow ○ Steady-state condition ○ Fluids are treated as ideal gases ○ Body forces are neglected ○ Viscous forces are neglected	$\rho u_r \frac{\partial u_r}{\partial r} + \frac{\partial p}{\partial r} = 0$	(3.6)
Energy equation	○ Axisymmetric flow ○ Steady-state condition ○ Fluids are treated as ideal gases ○ Work done due to body and external forces are neglected ○ Viscous heating is neglected	$\rho u_r c_p \frac{\partial T}{\partial r} + \frac{\partial \dot{q}}{\partial r} = 0$	(3.7)

The equations Eq. (3.1) – Eq. (3.4) to represent the aforementioned physical quantities are derived from the governing equation of fluid dynamics by applying several selected assumptions. Judgment criteria for these assumptions are based on the review study regarding the mathematical model in Chapter 2. The applied assumptions and the result of simplified equations are presented in Table 3.2.

Three equations are obtained from implementing the selected assumptions to the governing equation of fluid dynamics. The state equation is used to relate the internal energy e in Eq. (3.3) with the temperature T and specific heat capacity c_p of the airflow. The resulting equations are summarized in Table 3.2 and they are regarded as the model of the airflow at the solar collector. The solutions for these equations are to be obtained for velocity, pressure, and temperature and it is discussed in the upcoming section.

3.3.1 Velocity Equation

Recall the continuity equation as shown in Eq. (3.5). This equation relates the flow field variables at a point in the airflow inside the solar collector where u_r is the radial air velocity flowing in radial direction r with density ρ. The product of air velocity and air density is denoted as mass flux and if it passes in normal direction per unit time through a collector area A_{col} thus its value must be constant. Therefore, the continuity equation in differential form can be expressed in form of mass flow rate $\dot{m}$ as

$$\dot{m} = \rho u_r A_{col} \tag{3.8}$$

The mass flux must be normal to the surface area. As in Fig. 3.2 this surface is represented by a differential height dz times $2\pi r$ for inclusion of the axisymmetric condition. Integration from the ground surface $z = 0$ to the cover surface $z = h$ gives the expression of collector area as follow

$$A_{col} = 2\pi r h_{col} \tag{3.9}$$

where r is the radial coordinate, subscript col denoted as collector and hence A_{col} and h_{col} are defined as the area and height of the collector.

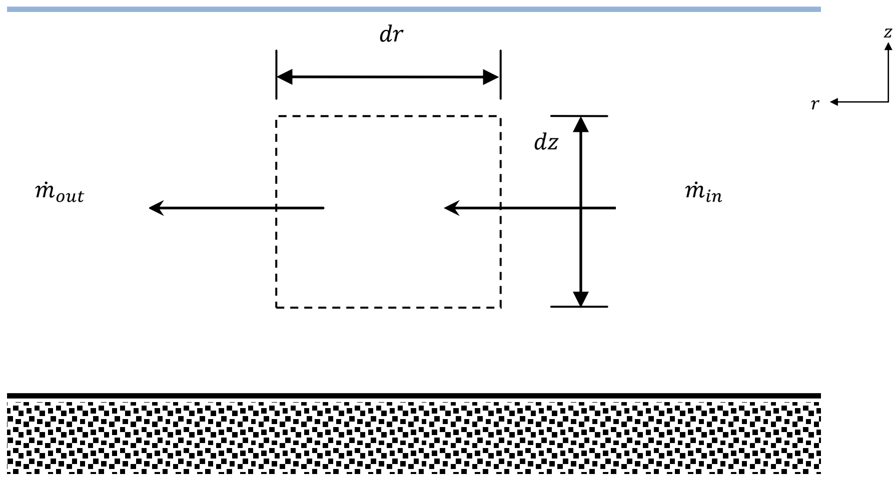

Fig. 3.2 Sketch for discussion of mass flow rate going in $\dot{m}_{in}$ and out $\dot{m}_{out}$ through area A_{col} which is the product of differential height dz and $2\pi r$ to incorporate the axisymmetric condition.

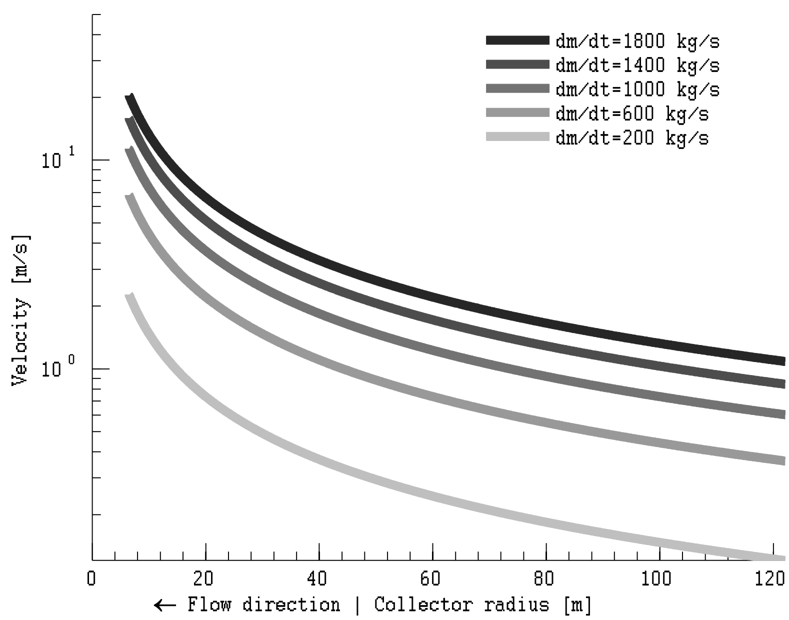

Fig. 3.3 Velocity profile of the airflow inside the solar collector for prescribed mass flow rate. The result is computed for collector radius = 122 m and collector height = 1.85 m with constant density.

In order to obtain a solution for velocity profile of the airflow in the radial direction, Eq. (3.8) is rearranged as

$$u_r = \frac{\dot{m}}{\rho A_{col}} \tag{3.10}$$

Providing the value of $\dot{m}$ and ρ, the radial velocity u_r for a chosen geometry can be computed as shown in Fig. 3.3. From this figure it can observed that the velocity is increasing from the outer collector into the inner collector. It has dramatic increase of velocity when they about to reach the center of collector.

3.3.2 Pressure Equation

Derivation for pressure equation is based on Fig. 3.4 which shows the net momentum flux – loosely mass flux ρu_r times velocity u_r – and the net pressure force in the radial direction. The mass flux must be constant for a given area while the velocity u_r and the pressure p are varied in the radial direction. This figure is sketched after implementing several assumptions such as steady axisymmetric flow, and exclusion of body and viscous forces. Only two forces are included in this analysis which is the inertia force and the pressure force. The balance of these two forces can be written in form of mathematical equation according to Fig. 3.4 as follow

$$\rho u_r u_r + \rho u_r \frac{\partial u_r}{\partial r} dr - \rho u_r u_r = p - \left(p + \frac{\partial p}{\partial r} dr\right) \tag{3.11}$$

Adding and cancelling term, resulting in the same expression as in Eq. (3.6), that is

$$\rho u_r \frac{\partial u_r}{\partial r} + \frac{\partial p}{\partial r} = 0 \tag{3.12}$$

Eq. (3.12) represents the simplified momentum equation at the solar collector where three physical parameters involves in this equation which are density ρ, velocity u_r, and pressure p. To solve for the pressure, this equation is converted from partial derivative into exact derivative form and subsequently integrating it for specified boundary condition.

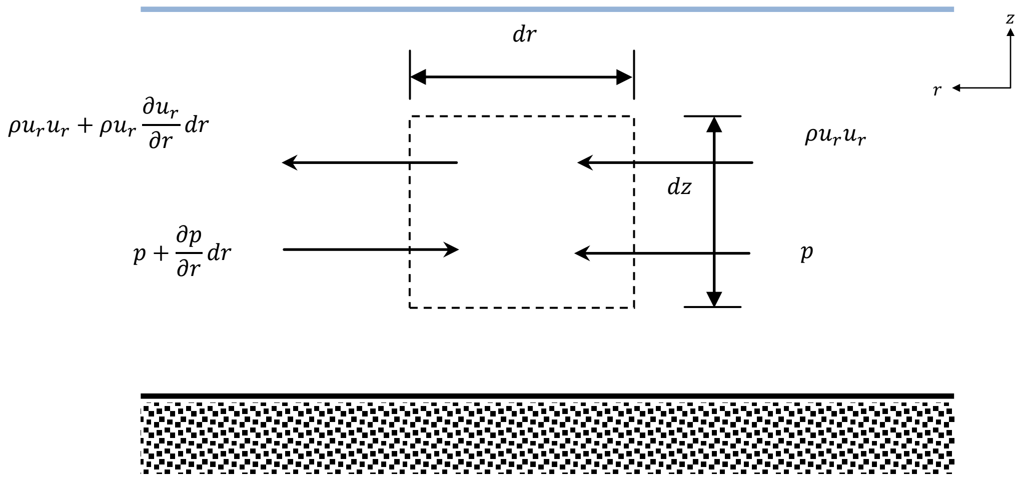

Fig. 3.4 Sketch for discussion of momentum flux through a normal surface $2\pi r dz$ and the change of velocity and pressure in differential radius dr. The net balance of pressure force is also showed in this figure.

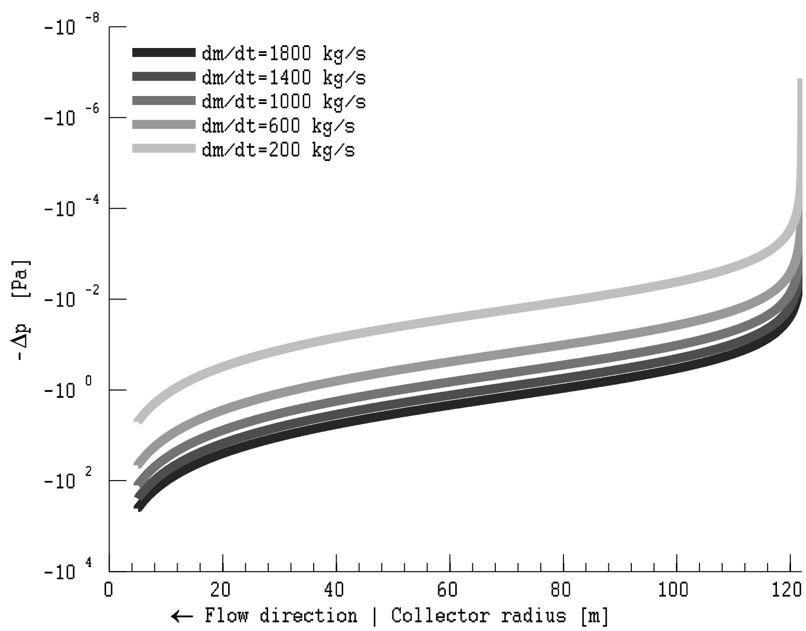

Fig. 3.5 Pressure profile of the airflow fluid inside the solar collector for prescribed mass flow rate. The result is computed for collector radius = 122 m and collector height = 1.85 m with constant density.

The integration process is elaborated in detail and presented in Appendix A. During the integration process, the mass flux has been written in form of mass flow rate $\dot{m}$ owing to the relation in Eq. (3.10). The result of integration is given as follow

$$-\Delta p = \frac{\dot{m}^2}{8\rho\pi^2 h_{col}^2}\left[\frac{1}{{r_{col}}^2} - \frac{1}{r^2}\right] \tag{3.13}$$

Eq. (3.13) is the pressure equation at the solar collector. The h_{col} refer to the height of solar collector from the ground surface to the cover surface, r_{col} is the fixed radius of solar collector measuring from the outer collector to the inner collector, and r is the variable radius of solar collector where its values are in the range of outer and inner collector. The pressure or the pressure difference Δp to be exact has been computed for selected value of mass flow rate as shown in Fig. 3.5. From this figure it can be shown that the pressure difference is decreasing along the collector and drops when it reached the center of the solar collector. Decreasing of static pressure indicates that the dynamic pressure is increasing towards the center of collector. It also implies that the velocity is increasing toward the center and gives consistent result from the previous analysis.

3.3.3 Temperature Equation

The temperature equation can be obtained by evaluating the net energy balance in Fig. 3.6. This figure actually describes the heat flux $\left(\rho u_r c_p T\right)$ of the differential airflow varied in the radial direction where the heat comes from solar radiation and it is modeled by the radiation heat flux $\dot{q}$. This power balance can be written as follow

$$\rho u_r(2\pi r dz)c_p T - \rho u_r(2\pi r dz)c_p T - \rho u_r(2\pi r dz)c_p \frac{\partial T}{\partial r} dr = d\dot{q}(2\pi r dr) \tag{3.14}$$

The airflow heat flux must be normal to the surface represented by a differential height dz times $2\pi r$ for inclusion of the axisymmetric condition. Similar with the previous process, integration is applied from the ground surface $z = 0$ to the cover surface $z = h$. The normal surface for the radiation heat flux is $2\pi r dr$, because heats from solar radiation is absorbed by the ground surface, thus it must be upwardly convected in differential distance dr.

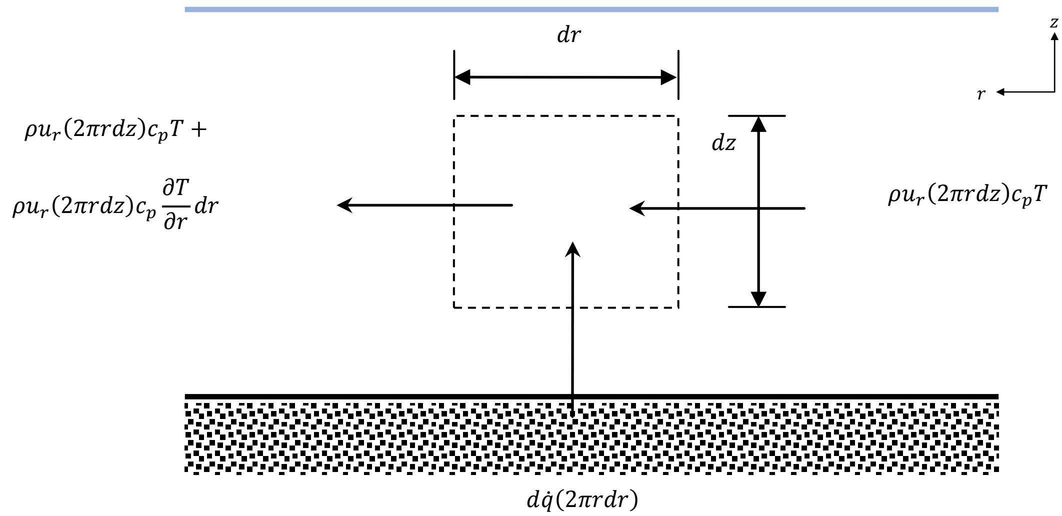

Fig. 3.6 Sketch for discussion of heat flux through normal surface $2\pi rdz$ for the airflow heat flux and $2\pi rdr$ for the radiation heat flux.

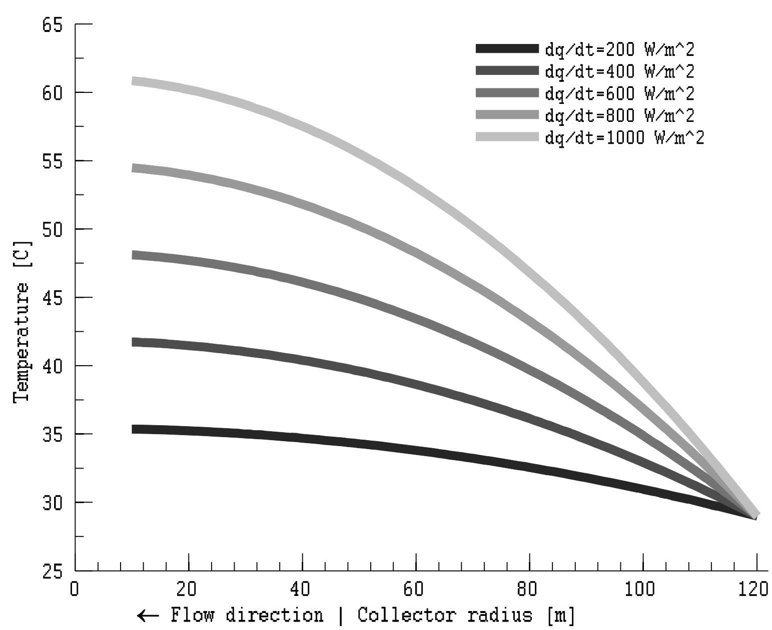

Fig. 3.7 Temperature profile of the airflow from Eq. (3.16). The results have been computed for selected value of radiation heat flux and prescribed mass flow rate.

Furthermore, Eq. (3.14) can be simplified after some addition and cancellation terms process where the resulting equation is in similar form with Eq. (3.7).

$$\rho u_r c_p \frac{\partial T}{\partial r} + \frac{\partial \dot{q}}{\partial r} = 0 \tag{3.15}$$

Eq. (3.15) represents the simplified energy equation of airflow at the solar collector. There are 5 physical parameters involve which are: airflow density ρ, airflow velocity u_r, airflow specific heat capacity c_p, airflow temperature T, and solar radiation heat flux $\dot{q}$. The mass flux ρu_r must be constant and the specific heat capacity is assigned as function of the airflow temperature. The remaining two parameters which are the temperature and the solar radiation heat flux are changed in the radial direction. The solution of this equation can be obtained by integrating the airflow temperature and the solar radiation heat flux with respect to the collector radius. The integration process is presented in detail in Appendix A and the result is given as follow

$$T_a(r) = T_{a_\infty} + \frac{d\dot{q}}{\dot{m}c_p}\pi({r_{col}}^2 - r^2) \tag{3.16}$$

Eq. (3.16) is the temperature equation which describe the profile of the airflow temperature along the radius of solar collector as function of ambient air temperature T_{a_∞}, radiation heat flux $\dot{q}$, mass flow rate $\dot{m}$, specific heat capacity, c_p, and radius of solar collector: r_{col} for fixed radius measuring from the outer collector to the inner collector, r for the variable radius of solar collector where its values are in the range of outer and inner collector. Graphical solution to this simple temperature equation is presented in Fig. 3.7. The result presented in Fig. (3.7) has been computed for prescribed mass flow rate, several selected value of the solar radiation heat flux, and prescribed geometry: height of collector is 1.85 m and radius of collector is 122 m. This particular solar collector geometry is taken from the Manzanares SUPG geometry. From this figure, it can be observed that there is an increasing in temperature along the solar collector. Moreover, increases in airflow temperature are proportional to increases in solar radiation heat flux. Thus, from this simple model an initial prediction of the temperature profile along the solar collector can be obtained which is useful in the conceptual design process.

From the temperature equation Eq. (3.16), the right hand side of this equation representing the ambient temperature plus the ratio of rate of heat transferred to the airflow and rate of heat stored by the airflow for each section of the collector. The result of this ratio is increases for the airflow temperature since the fluid releasing its energy in form of heat along the solar collector. It is desirable to know how these heats could be transferred to the airflow from the solar radiation. Moreover, one of the purposes in developing the mathematical model is to derive a set of traceable model, which means the process of heat transfer from the ground surface to the airflow must be included and appropriately modeled in the developed equation.

From the physical process inside the solar collector, it is recognized that the solar radiation is absorbed by the ground surface and then it is upwardly convected to the airflow. Thus, the heat transfer mode is convection and it involves the convection not only from the ground to the airflow but also from the cover to the airflow since part of the heats from solar radiation is also absorbed by the cover of solar collector. This convection process can be modeled as follow

$$\dot{q} = h_{c-a}^{conv}(T_c - T_a) + h_{g-a}^{conv}\left(T_g - T_a\right) \tag{3.17}$$

Convection heat transfer between the cover and the airflow is denoted as h_{c-a}^{conv} and convection between the ground and the airflow is labeled as h_{g-a}^{conv}. The temperature of cover, airflow, and ground are written as T_c, T_a, and T_g respectively. Eq. (3.17) states that for a given energy in form of heat to the airflow, it must be balanced every time by heat losses via convection to the surrounding which are cover and ground surfaces. A more refined solution to the temperature profile along the solar collector can be obtained by substituting Eq. (3.17) into Eq. (3.16). However, the temperature of cover and ground are also varied in the radial direction of the solar collector. Nevertheless, to allow a closed form solution, the cover and the ground temperature can be assumed to be constant along the collector radius. Moreover, the convection heat transfer coefficients are also assumed to be constant along the radius. The thermal properties of the airflow such as density and the specific heat capacity are assigned as function of the airflow temperature. This condition is consistent with the assumption that the airflow is treated as ideal gas; consequently the airflow density and specific heat capacity are function of the airflow temperature.

With these assumptions, the solution can be obtained as presented in Eq. (3.18). A detail derivation of this solution is elaborated in Appendix A.

$$T_a = \left[T_{a_\infty} + \frac{h^{conv}\left(T_c + T_g\right)}{\dot{m}c_p}\left(\pi {r_{col}}^2 - \pi r^2\right)\right]\mathcal{C} \tag{3.18}$$

where $\mathcal{C} = \left[1 + \frac{2h^{conv}}{\dot{m}c_p}\left(\pi {r_{col}}^2 - \pi r^2\right)\right]^{-1}$

Note the similarity of Eq. (3.18) and Eq. (3.16). The amount of heat flux which comes from solar radiation in Eq. (3.16) now has been transformed to the airflow temperature via convection process from the cover and the ground surfaces. Despite its simplicity, this model has been able to provide useful information that gives the knowledge about temperature profile along the solar collector.

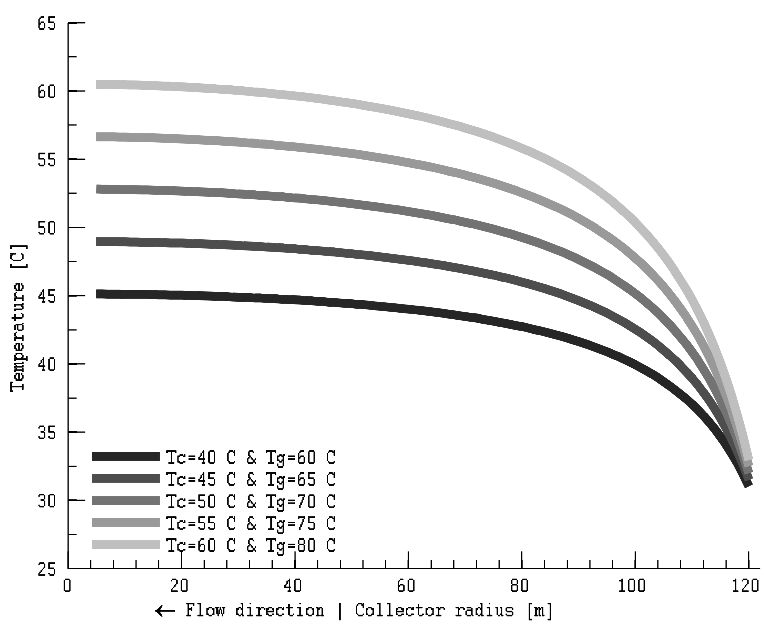

Fig. 3.8 Temperature profile of the airflow from Eq. (3.18). Values of T_c and T_g can be arbitrarily selected as long as $T_g > T_c$. In this work they have been selected with constant difference for the sake of simulation.

3.4 Mathematical Model of Solar Tower

In this section, the mathematical model of airflow inside the solar tower is derived, in particular for the airflow at the base of the solar tower or at the inner part of the solar collector as illustrated in Fig. 3.9. This figure present a schematic drawing of solar tower where the height and the radius are denoted as h_{tow} and r_{tow} respectively. The tower inlet can also be regarded as the collector outlet where the maximum velocity of the airflow is recognized at this region. The airflow temperature T_a is also maximum at this region and it will decrease along the solar tower before eventually in the same condition with the ambient air temperature T_{a_∞}.

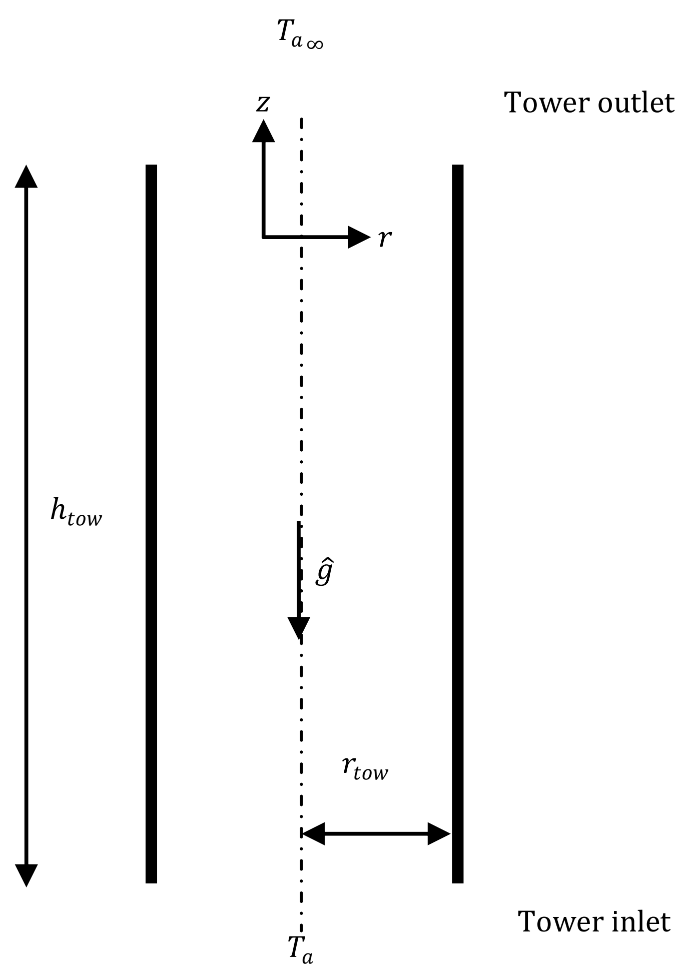

Figure 3.9 Schematic drawing of solar tower.

The updraft flow from the solar collector is in high temperature condition and when it reaches the solar tower, the hot air immediately encapsulated the tower wall. The flow carrying heat from the collector is rises towards the tower due to its buoyancy forces. This airflow (inside the tower) is less dense than the ambient air at the outside of tower, thus when these two fluid mixed at the outlet of the tower, the equilibrium condition will be achieved and the pressure of this fluid will be the same with the atmospheric pressure.

The updraft flow moving in the positive axial direction and the gravity acts in the negative axial direction. The gravity needs to be considered in this analysis because the body force – in particular gravity force – in Eq. (3.2) cannot be neglected. The inclusion of gravity force in the analysis of solar tower can be seen in Fig. 3.10. In this figure, the viscous force is omitted and only the buoyancy, pressure, and inertia forces are included. Thus, the net momentum flux inside the solar tower can be written as

$$\rho u_z u_z + \rho u_z \frac{\partial u_z}{\partial z} dz - \rho u_z u_z = p - \left(p + \frac{\partial p_z}{\partial z} dz\right) - \rho g dz \tag{3.19}$$

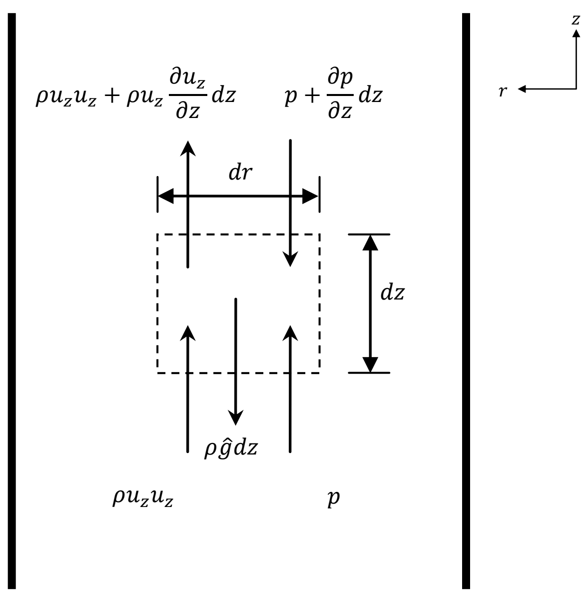

Fig. 3.10 Sketch for discussion of momentum flux for a differential volume of airflow inside the solar tower. The buoyancy force is also showed in this figure.

Addition and canceling terms in Eq. (3.19) gives

$$\rho u_z \frac{\partial u_z}{\partial z} = -\frac{\partial p}{\partial z} - \rho g \tag{3.20}$$

The hot air encapsulated the tower wall will rises along the solar tower which lead to the natural convection process. This phenomenon is best described by the boundary layer equation, in particular for vertical plate free convection problem. The fluid velocity outside the boundary layer region is zero and eventually becomes equal to the velocity of hot air rises from the collector. Therefore, the following relation can be established [73]

$$\frac{\partial p}{\partial z} = -\rho_{T=T_a} g \tag{3.21}$$

The pressure gradient away from the encapsulated hot air will be in form of Eq. (3.21). Solution of Eq. (3.20) can be obtained for updraft velocity u_z by substituting Eq. (3.21) to Eq. (3.20) and integrate along the solar tower with implementation of the Boussinesq approximation which relate the change of density with the change of temperature. The complete process can be found in Appendix A. The result is given as

$$u_z = \sqrt{2g \frac{T_a - T_{a\infty}}{T_{a\infty}} h_{tow}} \tag{3.22}$$

Eq. (3.22) represents the updraft velocity located at the base of solar tower where at this region, the velocity is reaches its maximum value and for that reason a wind turbine is installed in this area. The updraft velocity has been obtained as function of the gravity g, the airflow temperature T_a, the ambient air temperature $T_{a\infty}$, and the height of solar tower h_{tow}. Since the amount of kinetic energy is depends on the updraft velocity u_z, thus the strategies to increase this velocity can be listed as follows: 1) Increasing the temperature difference between the airflow and the ambient air. 2) Increasing the solar tower height. The strategy number 1 can be achieved by supplying a great amount of heat; for example concentrating the solar radiation and managing the distribution of heat transfer inside the solar collector. As for the strategy number 2 it is limited by the feasibility to build an ultra-high tower and it becomes a great challenge in the development of a SUPG.

3.4.1 Mass Flow Rate Equation

Updraft velocity equation as in Eq. (3.22) can also be expressed in term of mass flow rate. The relation in Eq. (3.8) can be used to transform the updraft velocity into the mass flow rate equation by changing the collector area into the tower area as $A_{tow} = \pi {r_{tow}}^2$. Substitute Eq. (3.8) into Eq. (3.22) by changing the collector area into tower area yields

$$\dot{m} = \rho \pi {r_{tow}}^2 \sqrt{2g \frac{T_a - T_{a\infty}}{T_{a\infty}} h_{tow}} \tag{3.23}$$

The tower radius is denoted as r_{tow} and the airflow density is depends on the airflow temperature. Graphical solution to Eq. (3.23) is presented in Fig. 3.11. The simulation result in this figure is computed for free tower case, in other words the kinetic energy of upward flow is not extracted by the turbine. Thus, the next evaluation is about the turbine model.

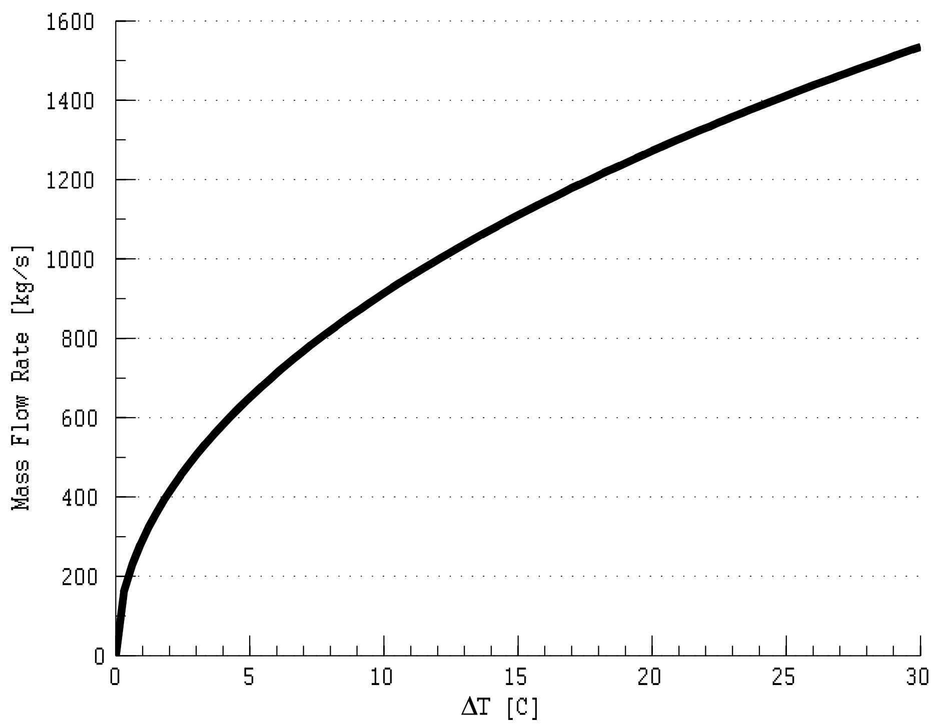

Fig. 3.11 Mass flow rate profile for prescribed airflow density, temperature difference $\Delta T = (T_a - T_{a\infty})$, and geometry of solar tower.

3.5 Mathematical Model of Wind Turbine

Basic principle of a turbine harvesting energy is by extracting some of wind kinetic energy when it passing through the blades and as the consequences the wind velocity is slowing down. Physical model of upstream wind passing through the rotor blades inside the solar updraft tower can be illustrated in Fig. (3.12).

In this figure, a stream-tube created by wind passing through the rotor blades is illustrated. The stream-tube model creates a boundary representing the affected and the non-affected area with respect to the mass of air. The affected area means the wind velocity is slowing down due to the rotating blades while the non-affected area means the wind velocity is undisturbed and remains the same with the upstream velocity. A single wind turbine has been selected to be placed at the center of collector although a solar updraft power generator often has more than one turbine.

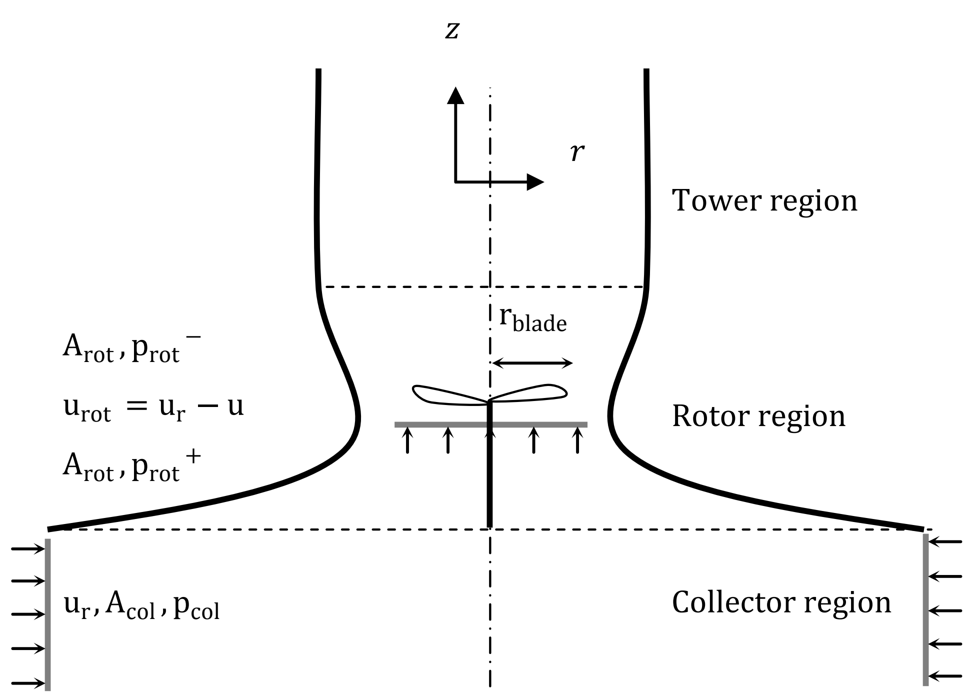

Fig. 3.12 Sketch for discussion of wind turbine model which shows the stream-tube model for energy extraction.

3.5.1 Generalized Actuator Disk Theory

The airflow inside the solar tower can be regarded as concentrated flow since the solar tower wall act as diffuser and resulting in a ducted rotor system. Consequently, the analysis for the maximum power could be extracted by the turbine (the Betz limit) is no longer valid since the limit could be exceeded in this case. The power coefficient is related to the area of energy extraction device and the maximum power extracted by the turbine could be exceeded from the Betz limit if additional mass flow is induced through the area of the device, say by a duct or diffuser [74]. Therefore, the actuator disk theory [75] which includes the effects of the augmented or concentrated flow is implemented in this analysis and makes the conventional actuator disk theory as a special case which is for open flow. However, the actuator disk theory has several limitations i.e. inviscid flow model and ideal diffuser condition. Nevertheless, this theory is regard as a starting point to analyze the complex flow field inside the solar updraft power generator.

Three laws of physics must be satisfied in modeling of flow around a turbine with diffuser. They are conservation of mass, momentum, and energy. Conservation of mass stated that the mass flow rate must be constant everywhere. For example; wind velocity at the tower region is slowing down due to extraction of its kinetic energy. Therefore to accommodate the slower wind velocity, the cross-sectional area of the stream tube must expand.

As for the momentum conservation, the rate of change of momentum must be balance every time. For example; the presence of turbine causes the upstream flow slows down such that when the air arrives at the turbine blades, its velocity already lowers than the collector velocity. Since no external work yet has been done on or by the air, the static pressure will increase in order to accommodate the decrease of velocity. As the air passes through the turbine blades, the static pressure will decrease due to special design of blades shape. Therefore the air then proceeds downstream with reduced static pressure and wind velocity. The area where the air is in reduced static pressure condition is usually called wake region, and in this case it is located at the tower region. Eventually, the static pressure will increase in order to achieve the equilibrium with the atmospheric level with an additional consequence that the wind velocity must be slowing down. This condition is achieved at the far downstream or in this case at the tower outlet. Therefore, there is no difference of the static pressure between far upstream (collector inlet) and far downstream (tower outlet) area but there is a reduction in its wind velocity.

In order to discuss the airflow passing through a wind turbine, consider the Bernoulli's equation applied for upstream and downstream of the turbine region. The total pressure equation along a streamline at the collector, turbine, and tower region can be written in a single equation as follows

$$\left(\frac{1}{2}\rho {u_r}^2 + p_r = \frac{1}{2}\rho {u_{rot}}^2 + {p_{rot}}^+ \middle| \frac{1}{2}\rho {u_{rot}}^2 + {p_{rot}}^- = \frac{1}{2}\rho {u_z}^2 + p_z\right) \tag{3.24}$$

Substitute the expression of velocity at the turbine region as function of velocity deficit u and velocity at the tower region as function of velocity deficit $\tilde{u}$. The inflow coefficient at the turbine and tower region can be defined as follows

$$u_{rot} = u_r - u = u_r\left(1 - \frac{u}{u_r}\right) = u_r(1-a) \tag{3.25}$$

$$u_{tow} = u_r - \tilde{u} = u_r\left(1 - \frac{\tilde{u}}{u_r}\right) = u_r\big(1 - f(a)\big) \tag{3.26}$$

The velocity at the turbine and tower region as function of inflow coefficient a can be expressed as in Eq. (3.25) and Eq. (3.26). Substitute these velocities for each region and performing momentum balance analysis for upstream region and downstream region of the energy extraction plane yields in

$$\frac{1}{2}\rho {u_r}^2 + p_r = \frac{1}{2}\rho(1-a)^2 + {p_{rot}}^+ \qquad \textit{upstream} \tag{3.27}$$

$$\frac{1}{2}\rho(1-a)^2 + {p_{rot}}^- = \frac{1}{2}\rho\big[u_r\big(1 - f(a)\big)\big]^2 + p_z \qquad \textit{downstream} \tag{3.28}$$

The pressure drop or pressure difference across the turbine blade during extraction of kinetic energy of upward flow can be obtained by subtracting the upstream and the downstream momentum equation. Hence

$$\left(\frac{1}{2}\rho {u_r}^2 + p_r = \frac{1}{2}\rho(1-a)^2 + {p_{rot}}^+\right) - \qquad \textit{upstream} \qquad (3.29)$$

$$\left(\frac{1}{2}\rho(1-a)^2 + {p_{rot}}^- = \frac{1}{2}\rho\left[u_r\big(1-f(a)\big)\right]^2 + p_z\right)$$

$$\left(\frac{1}{2}\rho {u_r}^2 + p_r\right) - \left(\frac{1}{2}\rho\left[u_r\big(1-f(a)\big)\right]^2 + p_z\right) = \qquad \textit{downstream} \qquad (3.30)$$

$$\left(\tfrac{1}{2}\rho(1-a)^2 + {p_{rot}}^+\right) - \left(\tfrac{1}{2}\rho(1-a)^2 + {p_{rot}}^-\right) \quad -$$

$$\frac{1}{2}\rho {u_r}^2\left[1 - \big(1-f(a)\big)^2\right] + (p_r - p_z) = {p_{rot}}^+ - {p_{rot}}^- \qquad (3.31)$$

If the difference of local pressure at the collector and the tower region can be assumed small enough relative to the difference of its dynamic pressure, thus the term $p_r - p_z$ can be omitted from Eq. (3.31). Therefore, the momentum equation reduces to

$$\left[1 - \big(1-f(a)\big)^2\right] = \frac{2({p_{rot}}^+ - {p_{rot}}^-)}{\rho {u_r}^2} \qquad (3.32)$$

During extraction of kinetic energy by the turbine, the flow at the upstream of the turbine experienced a “suction” force. This force is best described as thrust $\mathcal{T}$ (not to be confused with the temperature) and it is discussed in the upcoming section.

3.5.2 Thrust and Power Coefficients

Thrust can be defined in two ways. First, it can be defined as function of dynamic pressure, rotor swept area A_{rot}, and coefficient of thrust $C_{\mathcal{T}}$ and second, it can be expressed as force acting on turbine blades as a result of pressure difference. Therefore, at any plane of area A_{rot} within the control volume where there is pressure difference associated with energy extraction, the Thrust is given as

$$\mathcal{T} = \frac{1}{2}\rho {u_r}^2 A_{rot} C_{\mathcal{T}} = ({p_{rot}}^+ - {p_{rot}}^-)A_{rot} \qquad (3.33)$$

It is convenient to relate the pressure difference with the thrust coefficient, because the amount of mechanical power that could be extracted by the turbine is defined as thrust times reference velocity (in this case collector velocity u_r). Solve for $C_{\mathcal{T}}$ yields

$$C_{\mathcal{T}} = 2f(a) - f(a)^2 \tag{3.34}$$

Now the question is: what is the mathematical expression of the inflow coefficient at the tower region $f(a)$. To answer this, let a_0 be the axial inflow coefficient at the energy extraction plane with the absence of energy extraction. This condition yields to $f(a) = 0$ since no energy extraction occur thus the velocity deficit $\tilde{u}$ doesn't exist. Hence $f(a_0) = 0$, and therefore $(a - a_0)$ is one the factor of $f(a)$. If other factor exist in the mathematical expression of $f(a)$, thus it can be defined as

$$f(a) = k(a - a_0) \tag{3.35}$$

In order to determine the value of k, consider the condition when $a = 1$. This condition represents total blockage condition of flow through the system. In reality, it would experience a large thrust due to drag, but since the flow is inviscid, thus the drag force is zero and it gives $C_{\mathcal{T}} = 0$. Substitute these conditions into the thrust coefficient equation yields

$$k = \frac{2}{(1 - a_0)} \tag{3.36}$$

Hence the mathematical expression for $f(a)$ is obtained through substitution the value of k as follow

$$f(a) = \frac{2(a - a_0)}{(1 - a_0)} \tag{3.37}$$

Substitute the inflow coefficient into coefficient of thrust equation gives

$$C_{\mathcal{T}} = \frac{4(a - a_0)(1 - a)}{(1 - a_0)^2} \tag{3.38}$$

In order to check the consistency of the inflow coefficient derivation, the value of $C_{\mathcal{T}}$ can be compared with those for open flow analysis. In open flow analysis: $C_{\mathcal{T}} = 4a(1-a)$. Thus, in the generalized actuator theory substitute $a_0 = 0$ and the equation of $C_{\mathcal{T}}$ correspond as they must to the established equation for open flow.

The amount of mechanical power P could be extracted from the updraft flow by the turbine can be regard as function of dynamic pressure, rotor swept area A_{rot}, and coefficient of power C_P, in other words it also can be viewed as a product of force and velocity as applied at the rotor plane. They are respectively

$$P = Tu_r = \frac{1}{2}\rho {u_r}^3 A_{rot} C_P \tag{3.39}$$

Therefore, the coefficient of power is obtain as

$$C_P = \frac{P}{\frac{1}{2}\rho {u_r}^3 A_r} \tag{3.40}$$

Recalling the expression of $C_{\mathcal{T}}$, the ratio of C_P and $C_{\mathcal{T}}$ can be derived by substituting the relation for u_r. Thus

$$C_P = C_{\mathcal{T}}(1-a) \tag{3.41}$$

The coefficient of power C_P can also be expressed as function of inflow coefficient by substituting the value of $C_{\mathcal{T}}$ and it gives

$$C_P = \frac{4(a-a_0)(1-a)^2}{(1-a_0)^2} \tag{3.42}$$

Therefore, the maximum mechanical power that could be extracted by the turbine can be derived. The maximum and minimum value of C_P is obtain by differentiating with respect to inflow coefficient a. Furthermore

$$\frac{d}{da} C_P = \frac{d}{da}\left[\frac{4(a-a_0)(1-a)^2}{(1-a_0)^2}\right] = (3\mathrm{a} - 2\mathrm{a}_0 - 1)(\mathrm{a} - 1) \tag{3.43}$$

The maximum solution among these two solutions according to Jamieson [74] is the one in the first bracket. Thus following Jamieson, the maximum inflow coefficient a_m can be written as

$$a_m = \frac{1 + 2a_0}{3} \tag{3.44}$$

Substituting into the power and thrust coefficient equation, results in the theoretical maximum power and thrust could be produced by the turbine. They are respectively

$$C_{P_m} = \frac{16}{27}(1 - a_0) \tag{3.45}$$

As for maximum thrust

$$C_{\mathcal{T}_m} = \frac{8}{9} \tag{3.46}$$

Recalling the definition of thrust and writes for optimum energy extraction

$$({p_{rot}}^{+} - {p_{rot}}^{-}) = \frac{4}{9}\rho {u_r}^2 \tag{3.47}$$

This result means that the pressure drop across the rotor plane for optimum energy extraction is always $4/9\,(\rho {u_r}^2)$. Therefore, regardless of whether the flow is open or constrained (in this case by a diffuser), 8/9 of source upstream kinetic energy is the maximum fraction extractable from an extraction energy device (in this case by a turbine) located anywhere in its associated stream-tube [74].

The result of the previous derivation is the mathematical expression of pressure drop across the rotor; Eq. (3.33) which is function of coefficient of thrust. This equation can be written in form of mass flow rate as

$$\Delta p_{rot} = \frac{\dot{m}^2 C_{\mathcal{T}}}{2\rho\pi^2 {r_{blade}}^4} \tag{3.48}$$

Eq. (3.48) represents the pressure drop across the rotor blade where its radius is denoted as r_{blade}.

Graphical solution of Eq. (3.48) is presented in Fig. 3.13. From this result, the value of pressure drop across the rotor blade as function of mass flow rate and coefficient of thrust can be simulated. A contour plot of pressure drop simulation with the geometry of the Manzanares SUPG as benchmark for computation is presented in Fig. 3.13. From this figure it can be observed that low mass flow rate and small thrust coefficient would not give an appreciable pressure drop across the rotor blade. The black line at $C_{\mathcal{T}} = 8/9$ in the figure represents the boundary of maximum thrust coefficient. Since the pressure drop is directly related to the mechanical power, thus it is expected that the extracted power should follow the similar behavior.

Noted that, the calculation of Fig, 3.13 is conducted for $a_0 = 0$. The reason is because the value of this inflow coefficient must be obtained from the experiment. It means the effect of augmented flow is summed up in the inflow coefficient a instead of a_0.

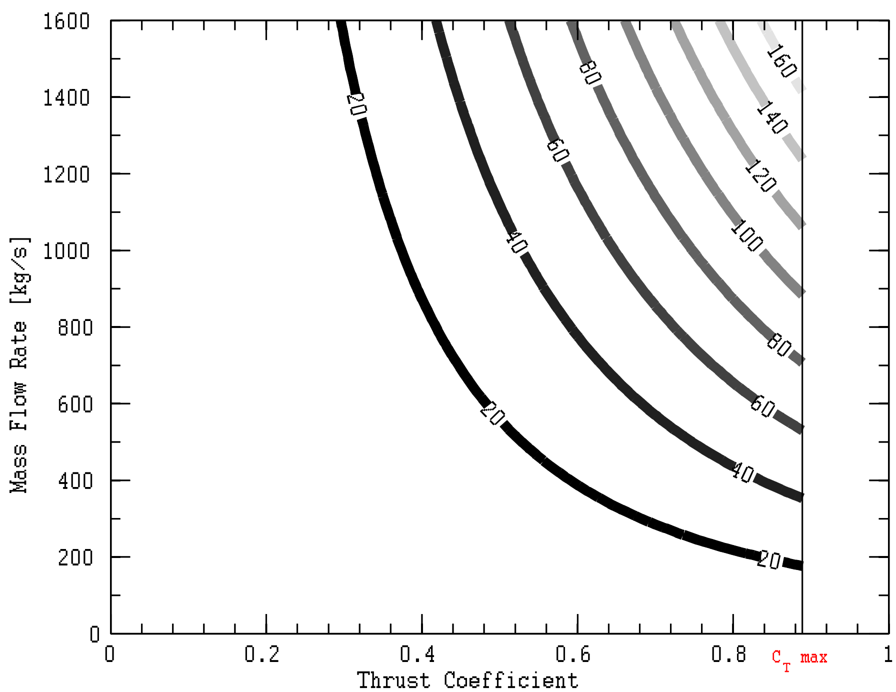

Fig. 3.13 Graphical solution of Eq. (3.48) which shows the effect of coefficient of thrust and mass flow rate to the pressure drop across the rotor blade.

Pressure drops implicitly affects the mechanical power through the thrust force. Since the thrust force is depends on the thrust coefficient (beside the dynamic pressure), thus it is expected that a large thrust coefficient will result in a large mechanical power. Following the previous analysis, Eq. (3.39) can be expressed in terms of mass flow rate. The relation between power coefficient C_P and thrust coefficient can be used for this purpose. Upon substituting this relation, it results in Eq. (3.49). Fig. 3.14 demonstrates the effect of thrust and inflow coefficient to the mechanical power extracted by wind turbine.

$$P = \frac{\dot{m}^3 C_P}{2\rho^2 \pi^2 {r_{blade}}^4} \tag{3.49}$$

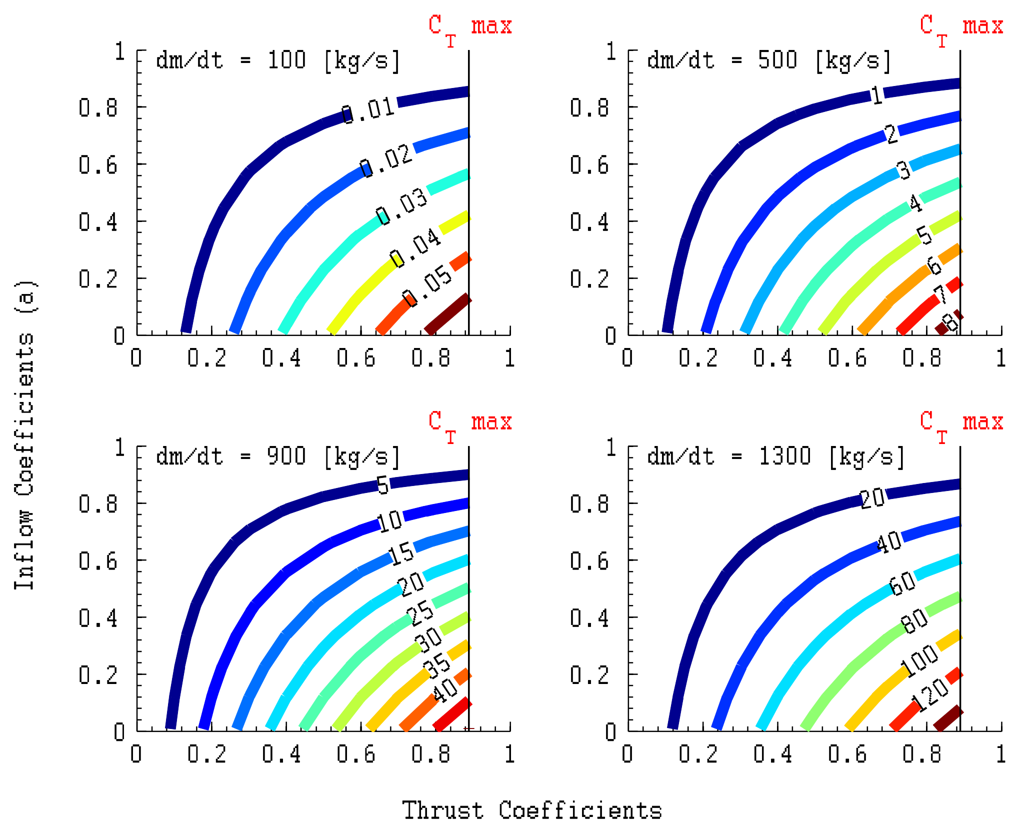

Fig. 3.14 Graphical solution of Eq. (3.49) which shows the effects of inflow coefficients and thrust coefficients to the power production by a wind turbine.

3.6 Integrated Model of SUPG

Mathematical model for each main parts of a solar updraft power generator has been derived in the previous section. Evaluation for the model of solar collector results in the velocity, pressure, and temperature equation. These three equations describe the behavior of airflow inside the solar collector and all of them depend on the mass flow rate where its value is prescribed to obtain a graphical solution. Analysis of the airflow at the solar tower leads to the mass flow rate equation which has been found to be associated with the airflow temperature. Similar case has been obtained in the model of wind turbine where the mechanical power is closely governed by the mass flow rate. Therefore, the mass flow rate should be properly computed rather than prescribed as in the previous analysis. Moreover, the heat transfer process in the previous analysis is assumed to be constant where it should be properly relate by a heat transfer correlation formula for each heat transfer mode. The strategy to accommodate all of these requirements is to establish an integrated model of a solar updraft power generator.

In this section, two integrated models are developed: 1) Integrated model of Manzanares SUPG and 2) Integrated model of lab-scale SUPG. These two integrated models will be used in simulating the performance of both Manzanares SUPG and lab-scale SUPG in Chapter 4.

3.6.1 Integrated Model of Manzanares SUPG

Consider the thermal network model for a single cover in the SUPG system as shown in Fig. 3.15. This figure describes the complex heat transfer process at the solar collector which can be described as follows: When solar radiation arrived at the surface of the cover with initial quantity I, part of it is absorbed by the product of $\alpha_{cover} \cdot I$ and the remaining (usually larger than the absorbed part) is transmitted and absorbed by the ground where the initial solar radiation now becomes $\alpha_{ground} \cdot \tau_{cover} \cdot I$: where α_{ground} is the absoprtivity coefficient of the ground and τ_{cover} is the transmissivity coefficient of the cover. Part of the absorbed solar radiation is conducted to the down layer of the ground with thermal resistance labeled as $1/h_{g-g_\infty}^{cond}$. The absorbed solar radiation by the ground is also emitted and exchange radiation with the cover of solar collector where its thermal resistance is defined as $1/h_{g-c}^{rad}$. Part of the absorbed solar radiation is also convected to the airflow above the ground surface and its thermal resistance is denoted as $1/h_{a-g}^{conv}$. The airflow not only receives the heats from the ground but also from the cover of solar collector and its thermal resistance is defined as $1/h_{c-a}^{conv}$. The heat flux $\dot{q}$ (gained by the airflow) will be distributed along the solar collector. The cover itself is also experienced heat losses to the ambient. The losses are divided into two modes which are convection and radiation. The convection losses to the ambient air has the thermal resistance $1/h_{c-a\infty}^{conv}$ and the radiation heat transfer between the cover and the sky has the thermal resistance $1/h_{c-s}^{rad}$.

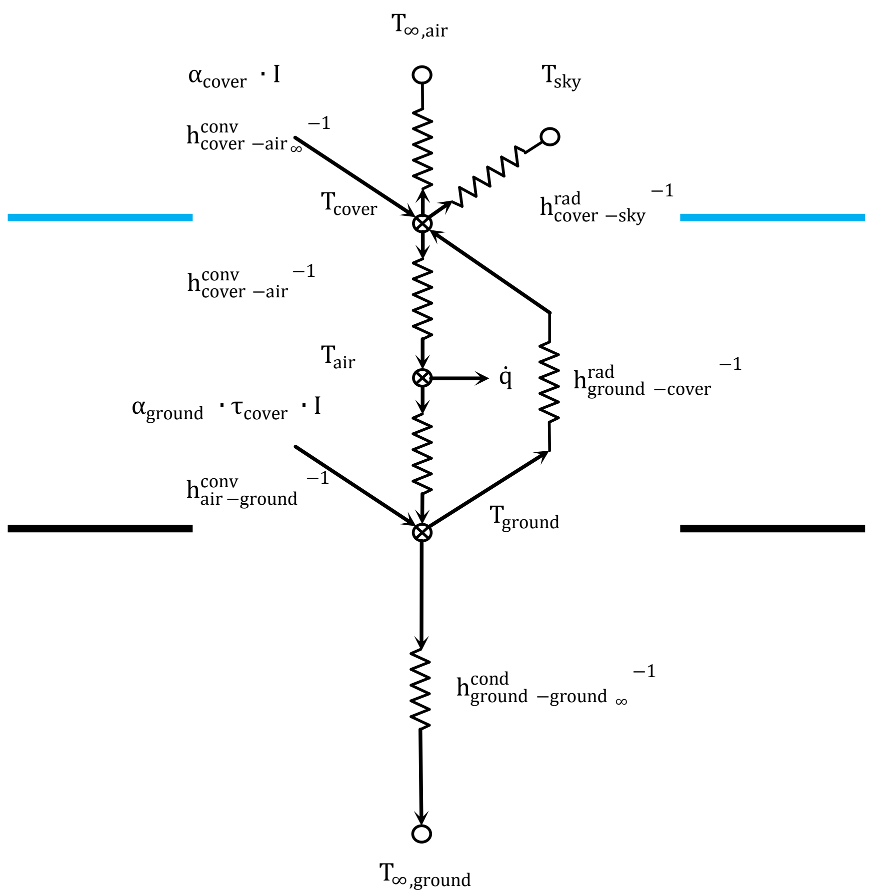

Fig. 3.15 A schematic drawing of thermal network model of Manzanares SUPG which shows the complex heat transfer process at the solar collector.

From Fig. 3.15, the heat balance equation can be established as in Table 3.3. These equations are obtained at each evaluation points i.e. cover surface, airflow, and ground surface and describe the balance of heat flux at the solar collector. At the cover surface, the heat transfer mode involves are: 1) convection between the cover surface at temperature T_c with the ambient air at temperature T_{a_∞}, 2) convection between the cover surface at temperature T_c with the airflow at temperature T_a, 3) radiation between the cover surface at temperature T_c with the sky at temperature T_s, and 4) radiation between the cover surface at temperature T_c with the ground surface at temperature T_g. At the airflow, the heat transfer mode involves are: 1) convection between the airflow at temperature T_a with the cover surface at temperature T_c, and 2) convection between the airflow at temperature T_a with the ground surface at temperature T_g. At the ground surface, the heat transfer mode involves are: 1) convection between the ground surface at temperature T_g with the airflow at temperature T_a, 2) radiation between the ground surface at temperature T_g with the cover surface at temperature T_c, and conduction between the ground surface at temperature T_g with the ambient ground at temperature T_{g_∞}.

Table 3.3 Heat balance equation at each evaluation points for the Manzanares SUPG

Cover	$\alpha_c I - h_{c-a_\infty}^{conv}\left(T_c - T_{a_\infty}\right) - h_{c-a}^{conv}(T_c - T_a) - h_{c-s}^{rad}(T_c - T_s) + h_{g-c}^{rad}\left(T_g - T_c\right) = 0$	(3.50)
Airflow	$h_{c-a}^{conv}(T_c - T_a) - h_{a-g}^{conv}\left(T_a - T_g\right) - \dot{q} = 0$	(3.51)
Ground	$h_{a-g}^{conv}\left(T_a - T_g\right) - h_{g-c}^{rad}\left(T_g - T_c\right) - h_{g-g_\infty}^{cond}\left(T_g - T_{g_\infty}\right) + \alpha_g \tau_c I = 0$	(3.52)

An explicit expression of the heat transfer coefficient for each heat transfer modes can be obtained from the available literature such as reviewed in Chapter 2. Subsequently, selected heat transfer coefficients formulas are discussed in the upcoming section.

Convection between cover and ambient air

Convection process between the cover surface and the ambient air can be regarded as heat losses to the environment since the cover surface temperature is always bigger than the ambient air temperature $\left(T_c > T_{a_\infty}\right)$ in a normal operating condition. Thus, the direction of heats flowing should be from the cover surface to the ambient air and it can be formulated as follow

$$q_{c-a_\infty}^{conv} = h_{c-a_\infty}^{conv}\left(T_c - T_{a_\infty}\right) \tag{3.53}$$

The term $q_{c-a_\infty}^{conv}$ is defined as the convection heat flux between the cover surfaces with the ambient air, $h_{c-a_\infty}^{conv}$ is the convection heat transfer coefficient, T_c and T_{a_∞} are the cover surface and the ambient air temperature respectively. The convection heat transfer coefficient can be written as

$$h_{c-a_\infty}^{conv} = \frac{k_a}{D_h} Nu\left(T_a, T_{a_\infty}\right) \tag{3.54}$$

where k_a is defined as the thermal conductivity of the airflow, D_h is the hydraulic diameter of the solar collector where its value is given in [12] as

$$D_h = \frac{4 \cdot Area}{Perimeter} \tag{3.55}$$

The Nusselt number is correlated by the Rayleigh number due to implementation of the free convection process in this analysis. The heat transfer correlation for a flat plate under a free convection process can be used in this analysis as shown in [20]. The correlation equations can be written as follow

$$Nu = 0.54 Ra\left(T_a, T_{a_\infty}\right)^{1/4} \qquad for\ 10^4 \le Ra \le 10^7, Pr \ge 0.7 \tag{3.56}$$

$$Nu = 0.14 Ra\left(T_a, T_{a_\infty}\right)^{1/3} \qquad for\ 10^7 \le Ra \le 10^{11}, all\ Pr \tag{3.57}$$

These correlated equations will be used in Chapter 4 to calculate the amount of heat transfer from the cover surface to the ambient air.

Convection between cover and airflow

Convection process between cover surface and the airflow inside the solar tower is recognized as a forced convection process instead of free convection as in convection process between the cover surface and the ambient air. The direction of heat flowing in this process is depends on the airflow temperature and the cover surface temperature. Nevertheless, as an initial condition, the cover temperature is assumed to have a bigger value than the airflow temperature. Thus, its heat flux can be written as

$$q_{c-a}^{conv} = h_{c-a}^{conv}(T_c - T_a) \tag{3.58}$$

The term q_{c-a}^{conv} is defined as the convection heat flux between the cover surfaces with the airflow. The convection heat transfer coefficient is given as

$$h_{c-a}^{conv} = \frac{k_a}{D_h} Nu(T_c, T_a) \tag{3.59}$$

The hydraulic diameter is already presented in Eq. (3.55) and the Nusselt number is depends on the temperature of the cover surface and the temperature of the airflow. Correlated equation for this process is characterized by the Reynolds number where its value depends on the flow regimes: laminar or turbulent flow.

$$Nu = \frac{2\sqrt{Re}\sqrt{Pr}}{\sqrt{\pi}(1 + 1.7Pr^{1/4} + 21.36Pr)^{1/6}} \qquad \begin{array}{l} \textit{Laminar flow} \\ \textit{for}\, Re < 5 \times 10^5, \textit{all Pr} \end{array} \tag{3.60}$$

$$Nu = \frac{0.037Re^{0.8}Pr(T_a)}{1 + 2.443Re^{-0.1}[Pr(T_a)^{2/3} - 1]} \qquad \begin{array}{l} \textit{Turbulent flow} \\ \textit{for}\ 5 \times 10^5 < Re < 10^7, \\ \quad 6 \times 10^{-1} < Pr < 2 \times 10^3 \end{array} \tag{3.61}$$

The heat transfer correlation in Eq. (3.60) and Eq. (3.61) are adopted from [20]. These equations are initially developed for a flat plate under forced convection process case and it has been utilized in this analysis to obtain the correlation function by changing the hydraulic diameter of a flat plate to the solar collector duct.

Convection between airflow and ground

Convection between the airflow and the ground surface is treated similar with the convection between the cover surface and the airflow in a sense of the correlated equation as in Eq. (3.60) and Eq. (3.61) are also applied to this case. However, the expression of its heat flux is different since it is depends on the airflow temperature and the ground surface temperature as stated in the following equation.

$$q_{g-a}^{conv} = h_{g-a}^{conv}\left(T_g - T_a\right) \tag{3.62}$$

The term q_{a-g}^{conv} is defined as the convection heat flux between the airflow with the ground surface and the flow of heat is recognized to be from the ground surface to the airflow. The reason is because the ground surface absorbed heats from solar radiation in a great amount before it is convected to the airflow.

Radiation between cover and sky

Radiation between the cover surfaces with the sky is regarded as heat losses to the environment since the sky temperature is usually lower than the cover surface temperature. The heat flux of this process is given as

$$q_{c-s}^{rad} = h_{c-s}^{rad}(T_c - T_s) \tag{3.63}$$

The term q_{c-s}^{rad} is defined as the convection heat flux between the cover surfaces with the sky. As for the sky temperature, a correlated model developed in [76] is implemented in this analysis, such that

$$T_s = 5.52 \times 10^{-2}\left(T_{a_\infty}\right)^{1.5} \tag{3.64}$$

The radiation heat transfer coefficient h_{c-s}^{rad} is adopted from [12] as

$$h_{c-s}^{rad} = \sigma\varepsilon_c(T_c + T_s)\left({T_c}^2 + {T_s}^2\right) \tag{3.65}$$

The term σ is the Stefan-Boltzmann constant and ε_c is the emissivity coefficient of cover.

Radiation between ground and cover

Radiation between the ground surface and the cover surface is recognized as heat losses from the ground surface to the cover surface. This is because the temperature of ground surface is usually larger than the temperature of cover surface. This condition can be traced from their absorptivity coefficient where the ground absorptivity coefficient holds a larger value than the cover. Therefore the heat flux equation can be written as

$$q_{g-c}^{rad} = h_{g-c}^{rad}(T_g - T_c) \tag{3.66}$$

The term q_{g-c}^{rad} is defined as the radiation heat flux between the ground surfaces with the cover surfaces. Equation for the radiation heat transfer coefficient h_{g-c}^{rad} is adopted from [12] and it is given as follow

$$h_{g-c}^{rad} = \frac{\sigma(T_g + T_c)({T_g}^2 + {T_c}^2)}{({\varepsilon_g}^{-1} + {\varepsilon_c}^{-1} - 1)} \tag{3.67}$$

The term ε_g is denoted as the emissivity coefficient of the ground. These equations will be used in Chapter 4 to calculate radiation heat transfer between the ground and the cover surfaces.

Conduction between ground and ambient ground

Conduction heat transfer process between the ground surfaces with the ambient ground which in this case is defined as the down layer of the ground surfaces is treated as heat losses to the environment. This is because the temperature of ground at the surface is larger than down layer of the ground. Therefore, the heat flux equation for this process can be written as

$$q_{g-g\infty}^{cond} = h_{g-g\infty}^{cond}(T_g - T_{g\infty}) \tag{3.68}$$

The term $q_{g-g\infty}^{cond}$ is defined as the conduction heat flux between the ground surfaces with the ambient ground.

The conduction heat transfer coefficient is adopted from [77] where the conduction process is assumed from objects held at an isothermal temperature T_g that are embedded within an infinite medium of uniform temperature T_{g_∞}. The explicit formulation for this heat transfer coefficient is given by

$$h_{g-g_\infty}^{cond} = Sk_g\left(T_g - T_{g_\infty}\right) \tag{3.69}$$

where S is defined as the conduction shape factors and can be written as

$$S = 2D_g \tag{3.70}$$

The term D_g is denoted as the ground diameter in which the solar radiation is absorbed from the transmission process at the solar collector. In other word, the ground diameter holds a same value with the diameter of the solar collector.

3.6.2 Integrated Model of Lab-Scale SUPG

In this section, an integrated model of lab-scale SUPG is developed. The model itself is slightly different with the integrated model of Manzanares SUPG. For example, in the lab-scale SUPG there is no radiation exchange between the cover and sky since the experiment was conducted inside a laboratory room. Moreover, heat conduction between the ground surfaces with the ambient ground is excluded in the model of lab-scale SUPG. This is because the source of heat (from solar radiation) in the Manzanares SUPG had been replaced by an electric heating element installed beneath a 1 m^2 aluminum plate. The electric heating element is fixed inside the isolator material, allowing the heats flow only in the axial direction, and thus there is no conduction to the down layer.

Consider a thermal network model for a laboratory scale prototype of SUPG in Fig.3.2. Prior to Fig. 3.2, the heat balance equation can be established for each evaluation points i.e. cover, air, and plate as shown in Eq. (3.71) – Eq. (3.73). Two heat transfer modes are involved in the modeling process which is convection and radiation. Convective heat transfer mode takes part in the heat losses from plate to airflow, airflow to cover, and cover to ambient air. Furthermore, radiative heat transfer mode operates between plate and cover. The various heat transfer correlations have been employed from previous literatures and they are summarized in Table 3.5. As for optical properties of materials, they are widely available and their value depends on the type of materials.

Free convection mode has been applied in the modeling of convective heat transfer between cover and ambient air. The Nusselt numbers for this process are grouped into two regions depending on the value of Rayleigh numbers. Convective heat transfer process between cover and airflow are modeled as forced convection mode, similar with previous case (Manzanares SUPG) where the Nusselt numbers for this case is correlated through Reynolds number. Furthermore, convective heat transfer process between plate and airflow are also selected as forced convection mode. In this mode, flow region can be categorized into two states which are laminar and turbulent flow, depending on the value of Reynolds numbers. Lastly, the radiative heat transfer process is modeled as two infinite parallel plates exchange infrared radiation between gray surfaces.

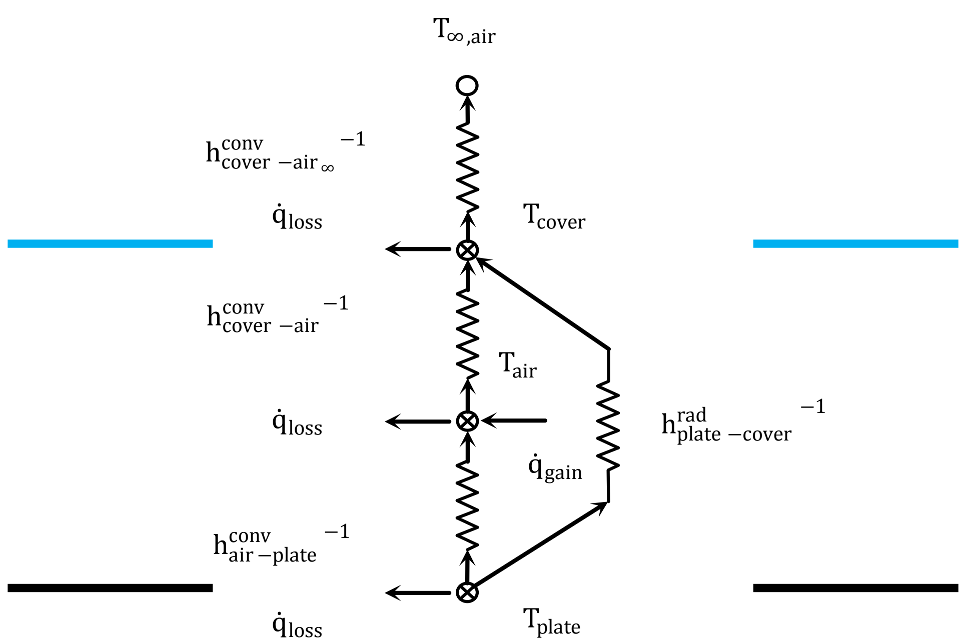

Fig. 3.16 A schematic drawing of thermal network model of lab-scale SUPG which shows the heat transfer process at the solar collector.

Table 3.4 Heat balance equation at each evaluation points for a lab-scale SUPG

Cover	$-h_{c-a_{\infty}}^{conv}\left(T_c - T_{a_{\infty}}\right) + h_{a-c}^{conv}(T_a - T_c) + h_{p-c}^{rad}\left(T_p - T_c\right) - \dot{q}_{loss} = 0$	(3.71)
Airflow	$-h_{a-c}^{conv}(T_a - T_c) + h_{p-a}^{conv}\left(T_p - T_a\right) + \dot{q}_{gain} - \dot{q}_{loss} = 0$	(3.72)
Ground	$-h_{p-a}^{conv}\left(T_p - T_a\right) - h_{p-c}^{rad}\left(T_p - T_c\right) - \dot{q}_{loss} = 0$	(3.73)

Table 3.4 summarized the heat balance equation from Fig. 3.16. The heat from electric heating element is convected through forced convection process to the airflow above the aluminum plate with thermal resistance $1/h_{air-plate}^{conv}$. The radiation exchange between the surface of aluminum plate and the cover surface has the thermal resistance as $1/h_{plate-cover}^{rad}$. At the airflow evaluation point, the heat gain from the convection process is denoted as $\dot{q}_{gain}$ and subsequently it was also recognized that there is a significant heat losses to the edge of collector and it is modeled as $\dot{q}_{loss}$. The airflow is then transferring the heats to the cover surface with thermal resistance $1/h_{cover-air}^{conv}$ before eventually loss to the ambient air with thermal resistance $1/h_{cover-air_{\infty}}^{conv}$.

Basically the correlation coefficients used to characterize the heat transfer coefficients are similar with those in the integrated model of Manzanares SUPG. For example, the heat transfer correlation for the forced convection in the lab-scale SUPG used the same equations as in Eq. (3.60) and (3.61). The heat transfer correlation for the free convection process is expressed by Eq. (3.56) and (3.57). All of these equations are summarized in Table 3.5.

Development of mathematical model of a lab-scale SUPG has the purpose to obtain a reliable and accurate model so that it can be used later for estimation and prediction through numerical simulation. Therefore, the simulated result from a lab-scale SUPG will be compared with the result from experiment. The comparison will be made in terms of updraft temperature and updraft velocity at the bottom of solar tower. The validity of the employed heat transfer correlation will also be checked to ensure that these correlations are always in the valid range during the calculation. Moreover, the developed computer program in Chapter 4 to solve these equations will be also presented.

Table 3.5 Heat transfer correlation used in the modeling of lab-scale SUPG

	Heat transfer mode	Equation used for heat transfer correlation
Cover – Ambient air	Free convection	Eqs. (3.56) and (3.57)
Cover – Airflow	Forced convection	Eqs. (3.60) and (3.61)
Airflow – Plate	Forced convection	Eqs. (3.60) and (3.61)

3.7 Remarks

The development of mathematical model of a solar updraft power generator has been presented in this chapter. Therefore several summaries can be listed as follows

- Mathematical model of solar collector, solar tower, and wind turbine has been derived where the requirement in developing theoretical models has been met; traceable and simple but accurate models.
- The tractability of the developed models has been proved since the model has the capability to describe the transformation of solar radiation into collector airflow heat-flux. In addition, the transformation of the collector airflow heat-flux to the updraft velocity and mechanical power have been also included in the model, so that the energy transformation occur at the solar collector can be explained.
- An integrated model of the Manzanares SUPG has been developed based on the concept of thermal network model where each heat transfer process can be simultaneously included in the analysis.
- As for the integrated model of a lab-scale SUPG, it has also been obtained from the thermal network concept applied to the laboratory model of SUPG.

Mathematical equation from Chapter 3, in particular for the integrated models will be solved in Chapter 4 by implementing numerical techniques via iteration scheme. Therefore the next evaluation is about the development of numerical simulation.

Numerical Simulation

Chapter 4

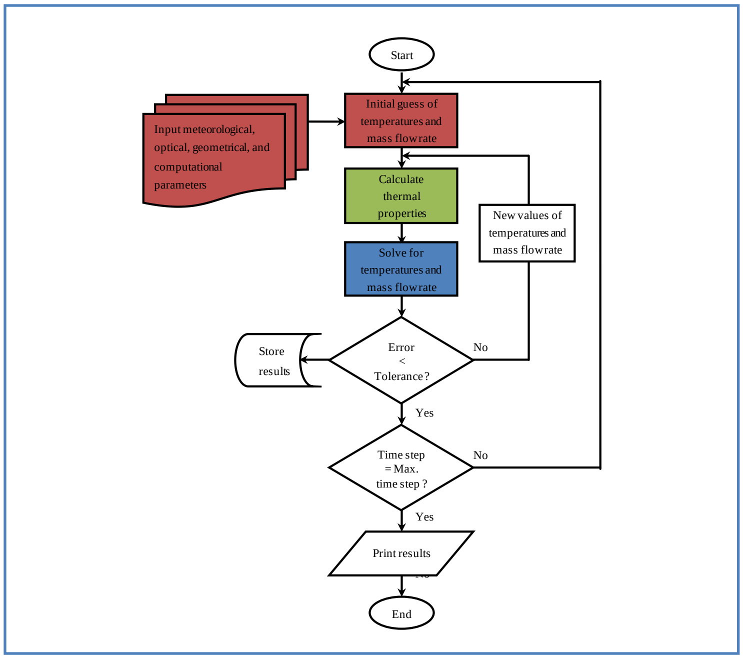

In this chapter, development of numerical techniques and computer program to solve the nonlinear mathematical model from Chapter 3 are presented. The iterative scheme is implemented to calculate the desired output such as temperatures and mass flow rate. Simulation procedures are also elaborated in this chapter where it is consists of setting-up the initial and boundary conditions, calculation of thermal properties of airflow, and computing the matrix equation numerically. Simulation is carried out for two cases: Manzanares SUPG and a lab-scale SUPG. Simulation results of the Manzanares SUPG are validated with the experimental data and also compare with other researcher results for the same geometry. Validation results show a good agreement. The applicability of heat transfer correlation and the computational performance of the developed program are also accessed.

4.1 Introduction

Mathematical model of solar updraft power generator has been successfully derived in Chapter 3. Therefore, in this chapter those models will be solved numerically and their simulation results are also discussed in detail. An iterative scheme is implemented in order to solve the integrated model where the resulting equations are in nonlinear form. This method is chosen based on the result of review works in Chapter 2.

The governing equation is often solved numerically with help of the available computational fluid dynamics (CFD) software. However, description of the nonlinear radiation problem in most CFD solvers is difficult to trace, for example transformation of solar radiation into thermal energy in form of collector airflow heat-flux. Thus, it is important to have a set of traceable model which has the capability to describe the transformation of energy from solar radiation to thermal energy of collector airflow. This model can be categorized from the simplest form which has many assumptions and often far from the real condition to a sophisticated model which employ fewer assumptions.

Despite of their limitation, these solvers are able to provide a useful insight concerning the complex heat transfer phenomena at the collector and often help engineers during conceptual and preliminary design phase. Tractability of CFD radiation model, motivate the current work to develop a solver which able to compute the amount of heat-flux contained in the airflow as a result of conversion of solar radiation to thermal energy.

The solver is written in MATLAB environment and divided into several sub routines which has been integrated into one computer program. This computer program is then used to simulate the performance characteristic of the Manzanares SUPG and also the lab-scale SUPG. Simulation procedures is elaborated in this section and it is consists of three major steps. Furthermore, the effects of solar radiation are discussed through simulation results of the Manzanares SUPG. Additionally, the effects of inflow coefficient, collector radius and tower height, as well as the ambient air temperature are also examined in detail through simulation results of the Manzanares SUPG. The Applicability of heat transfer correlations is investigated in detail for the case of lab-scale SUPG by simulating the non-dimensional number involves in the equation of heat transfer coefficients. Then the simulation result of the lab-scale SUPG is then compared with the experiment to validate the developed models.

4.2 Iterative Scheme

One of the simple iterative methods in finding a root of an equation is known as the fixed-point iteration or also called as one-point iteration. The idea of this method is to predict a new value of the unknown parameter as a function of its previous value. Formal explanation of fixed-point iteration method and discussion of its convergence rate are given in [78] and [79]. Consider solving an equation

$$x^2 - a = 0 \; for \; a > 0 \tag{4.1}$$

This equation can be transformed either by algebraic manipulation or by simply adding x to both sides of the original equation. Therefore

$$x = x^2 + x - a \; or \; x = a/x \tag{4.2}$$

These two equations are the same and differ only in their writing style. More general, fixed-point iteration works by rearranging the function $f(x) = 0$ so that x is on the left hand side of the equation.

$$x = g(x) \tag{4.3}$$

where $g(x)$ is transformed function of $f(x)$.

The idea is to provide a formula to predict a new value of x as a function of its previous value. Hence, providing an initial guess at the solution x_i, the equation can be transformed to calculate a new estimate of x_{i+1}. It can be expressed by the iterative formula as

$$x_{i+1} = g(x_i) \tag{4.4}$$

This equation is regarded as a new estimated value for the root of equation. The calculation is then repeated until the approximate error for this equation meet the error estimator. The error estimator is given by

$$\varepsilon = \left|\frac{x_{i+1} - x_i}{x_{i+1}}\right| 100\% \tag{4.5}$$

Like other iteration method, it is desirable to know how this method achieves its convergence or could it always obtain a convergence results? These questions are answered by studying the convergence properties of fixed-point iterations as follows. Suppose the true solution for the iterative equation is obtained as

$$x_{true} = g(x_{true}) \tag{4.6}$$

The difference of true solution and iterative calculation is obtained by subtracting those equations, it yields to

$$x_{true} - x_{i+1} = g(x_{true}) - g(x_i) \tag{4.7}$$

Graphical illustration of this difference equation is presented in Fig. 4.1 and this figure is made with help of the derivative mean value theorem analysis.

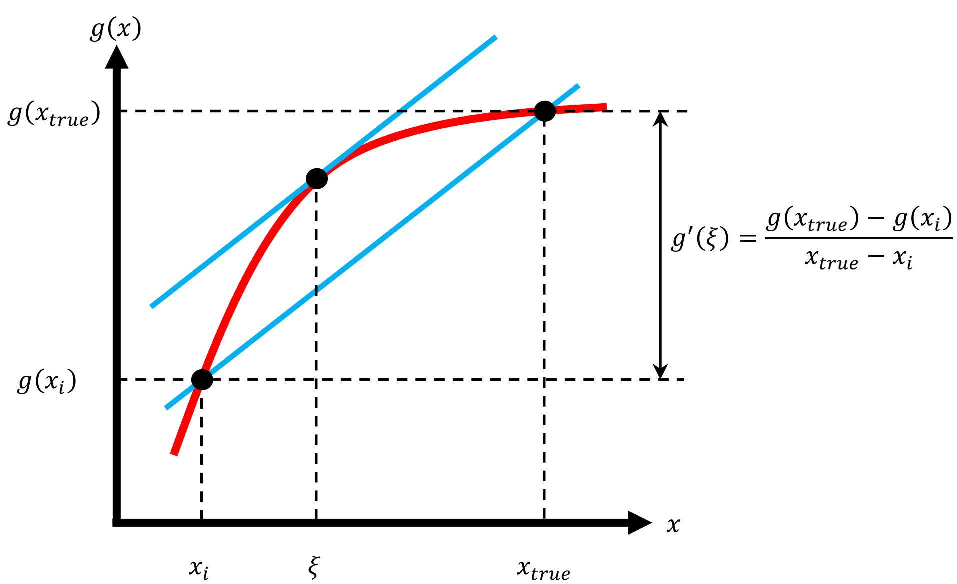

Fig. 4.1 Graphical depiction of the mean value theorem.

The derivative mean value theorem states that if a function $g(x)$ and its first derivative are continuous over an interval $a \leq x \leq b$, then there exist at least one value of $x = \xi$ within the interval [79]. Substitute $a = x_i$ and $b = x_{true}$ thus, the statement of the mean value theorem can be written as follow

$$g(x_{true}) - g(x_i) = [x_{true} - x_i]g'(\xi) \tag{4.8}$$

where ξ is somewhere between the interval x_i and x_{true}.

Substitute this result into difference equation yields

$$x_{true} - x_{i+1} = [x_{true} - x_i]g'(\xi) \tag{4.9}$$

Define the true error for iteration i as $E_{true,i} = x_{true} - x_i$, Thus the difference equation becomes

$$g'(\xi) = \frac{E_{true,i}}{E_{true,i+1}} \tag{4.10}$$

The errors will decrease and the solution will converge if condition $|g'(\xi)| < 1$ is satisfied. As for $|g'(\xi)| > 1$, the errors will grows and the solution will diverge. From the error equation Eq. (4.10), to produce a convergence result the $E_{true,i}$ must always be less than $E_{true,i+1}$. In other words, the initial guess for x_i must be carefully selected to be close enough so that $x_{true} - x_i$ will gives a small number. Therefore, the iterative calculation is expected to produce a convergence result.

Considering the simplicity of this itervative method and its robustness in providing a convergence result, the fixed-point iteration is selected to be implemented in this works. A computer algorithm in the framework of this method is presented in Fig. 4.2. In this figure, the input data for simulation is provided and the program will read these data. The input data includes: meteorological data which is consist of solar radiation and ambient air temperature data, geomerical parameters, and optical parameters. Then the initial guess of temperatures and mass flow rate is provided to calculate the thermal properties of the airflow, for example, aiflow density, thermal conductivity, kinematic viscosity, and specific heat capacity. These calculated thermal properties is then used to solve the temperatures and mass flow rate. The current results are compared with the previous result, therefore the iterative process is started until their value meet the desired tolerance.

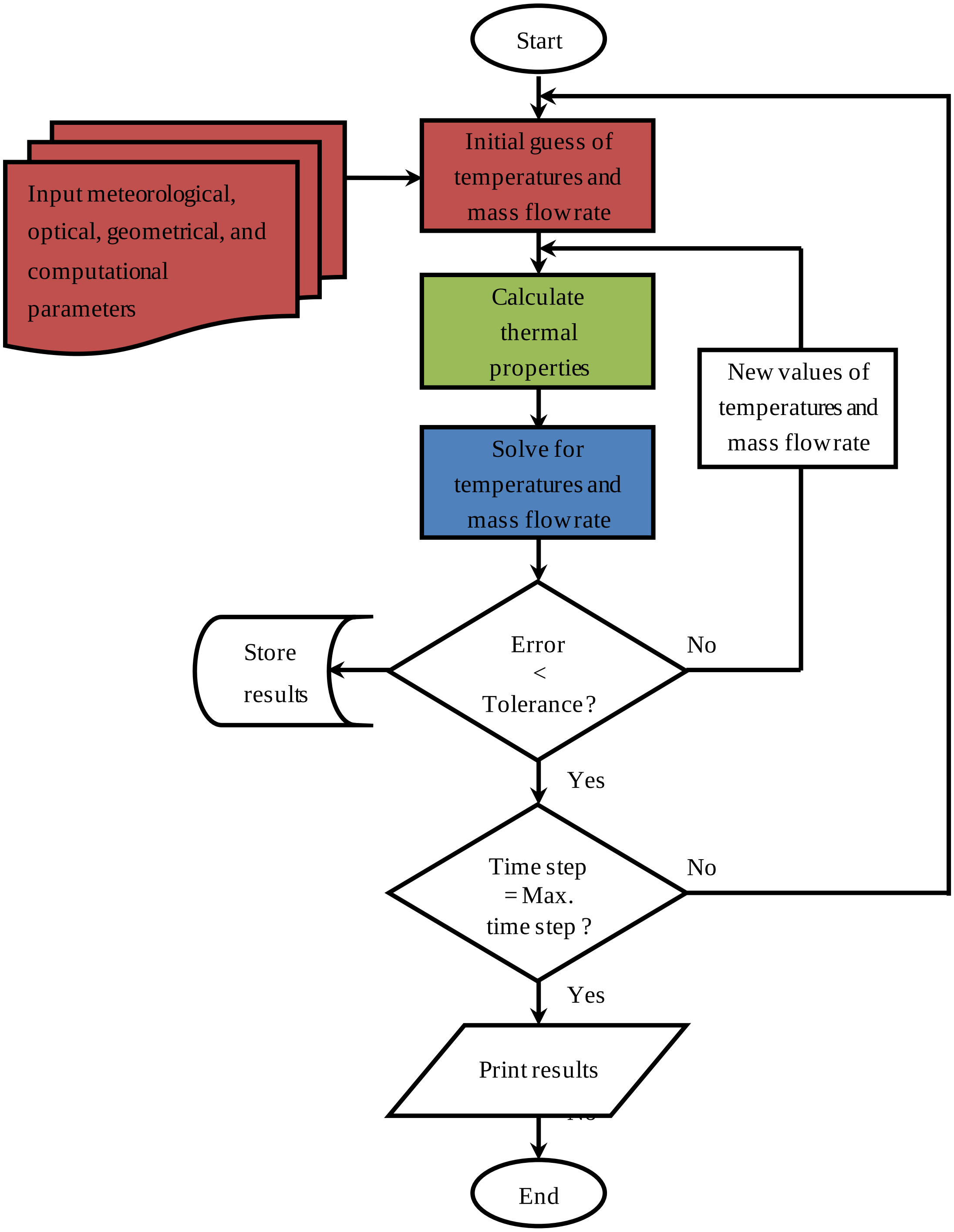

Fig. 4.2 Flow chart of the developed computer program.

4.3 Simulation Procedures

A more comprehensive explanation of simulation procedures is presented in this section. Basically, the developed computer program as can be seen in a flow chart (Fig. 4.2) is composed by three main steps. Step 1 is marked by red color in Fig. 4.2 and it is amount to data preparation. Step 2 is marked by green color in Fig. 4.2 and it is dedicated to calculate the airflow thermal properties. Step 3 is marked by blue color in Fig. 4.2 and it is devoted to solve the equations numerically. The complete process is presented as follows:

Step 1

Prepare the following data in form of arrays:

Meteorological data: solar radiation and ambient air temperature.

Geometrical data: dimension of solar collector, solar tower and wind turbine.

Optical data: Absorptivity, transmissivity, and emissivity coefficients.

Step 2

Load the data from step 1 to calculate the following thermal properties:

The cover, airflow, and ground mean temperature.

The airflow density, thermal conductivity, specific heat capacity, kinematic viscosity.

Prandtl number, Grashof number, Rayleigh number, Reynolds number, Nusselt number.

Step 3

Compute the associated heat transfer coefficients and correlation with regards to the thermal properties from step 2.

Solve the integrated model for temperatures and mass flow rate through iteration scheme and stored each results during the iterative calculation. The converged results are then used to calculate the performance of SUPG.

4.3.1 Initial and Boundary Conditions

The initial and boundary conditions used in the simulation works are presented in Table 4.1. The content of Table 4.1 is divided into 4 parts which are the computational parameter, geometrical data, optical data, and meteorological data. The computational parameter is regarded as the initial condition in the simulation procedures. Initial guess of temperatures and mass flow rate must be firstly selected to be used for iterative calculation. There are three temperatures used in the simulation which are the cover surface temperature, airflow temperature, and the ground surface temperature. These three temperatures coming from the integrated model developed in Chapter 3. The objective is to solve the integrated model for temperatures and of mass flow rate. The initial value of mass flow rate is also need to be provided in this process.

After that, the maximum number of iteration and the maximum allowable tolerance must be inputted in this process. Although the number of iteration could exceed the selected value, a 1×10^5 value is selected in all the simulation works. Suppose the iteration exceeds the selected previous value, a flag to warn this condition has been included in the developed computer program. As for the maximum tolerance, it is desirable that this value is selected as low as possible. However, this condition only gives a longer computational time because to achieve such condition, it probably took a more iteration. Nevertheless, a 1×10^{-5} value is selected in all the simulation works.

The boundary conditions in the simulation procedures is defined as the geometry of a solar updraft power generator such as the radius and height of solar collector, the radius and height of solar tower, and the radius of wind turbine. The dimension of a solar updraft power generator must be inputted in this process. In particular for the radius of solar collector, the dimension should include the outer radius and the inner radius. Same case with the solar tower it is measured from the bottom to the top of solar tower.

In addition, the optical properties – such as the cover absorptivity, transmissivity, emissivity coefficients, and the ground absorptivity, emissivity coefficients – must be also provided in advance. The most essential data is the meteorological data: solar radiation and ambient air temperature, because these two parameters are regarded as the input for the simulation works.

Table 4.1 Initial and boundary conditions used for simulation

Computational parameters	Values	Units
Maximum number of iteration	1×10^5	-
Maximum number of tolerance	1×10^{-5}	-
Initial guess of mass flow rate	1×10^0	kg/s
Initial guess of cover temperature	3×10^2	K
Initial guess of air temperature	3×10^2	K
Initial guess of ground temperature	3×10^2	K
Geometrical data		
Collector radius (outer to inner part)	r_{col}	m
Collector height	h_{col}	m
Tower radius	r_{tow}	m
Tower height (bottom to top part)	h_{tow}	m
Turbine/rotor radius	r_{rot}	m
Optical data		
Cover absorptivity	α_{col}	-
Cover transmissivity	τ_{col}	-
Cover emissivity	ε_{col}	-
Ground absorptivity	α_{ground}	-
Ground emissivity	ε_{ground}	-
Meteorological data		
Irradiance	From meteorological data	
Ambient air temperature	From meteorological data	

4.3.2 Calculation of Thermal Properties

Calculation of thermal properties is defined as the second step process in the simulation procedures. It means that to calculate the thermal properties, previous initial guess of some parameters are needed in this process. The thermal property is devoted for the airflow inside the solar collector and the ambient air. It includes the airflow density, thermal conductivity, thermal diffusivity, specific heat capacity, kinematic viscosity, and Prandtl number. A continuous function is prepared based on the data provided in [72] for ideal gas condition. The fitting function to the provided data can be found in Fig. 4.3. These functions are then translated into a computer code, and for each temperature the thermal properties of airflow can be computed and provided.

The thermal properties are used to calculate the heat transfer coefficients and correlations. In Chapter 3, an integrated model of SUPG has been developed and the expression of their heat transfer coefficient and correlations are mostly complex. It requires calculation of some non-dimensional numbers such as Grashof number, Rayleigh number, Reynolds number, and Nusselt number. These non-dimensional numbers can be calculated if the temperatures of the associated problem and the thermal properties are available. Also, these non-dimensional numbers are essential parameters for the calculation of solution in the step 3 of simulation procedure.

Calculation of the mean temperature is also included in this process. The calculation of mean temperature is important since all the thermal property is function of the temperature. For example, to provide the thermal properties for the convection process between the ground surfaces with the airflow, the mean temperature is then average of the ground surface temperature and the airflow temperature. Once this mean temperature T_m is obtained, it will be used immediately to calculate the density $\rho(T_m)$, thermal conductivity $k(T_m)$, specific heat capacity $c_p(T_m)$, kinematic viscosity $\mu(T_m)$, thermal diffusivity $\alpha(T_m)$, and Prandtl number $Pr(T_m)$. The same procedure is also applied for the other heat transfer modes.

In summary, calculation of thermal properties requires an estimation of mean temperature for the associated heat transfer modes. After the estimation of the thermal properties, the heat transfer coefficients and correlation can be computed.

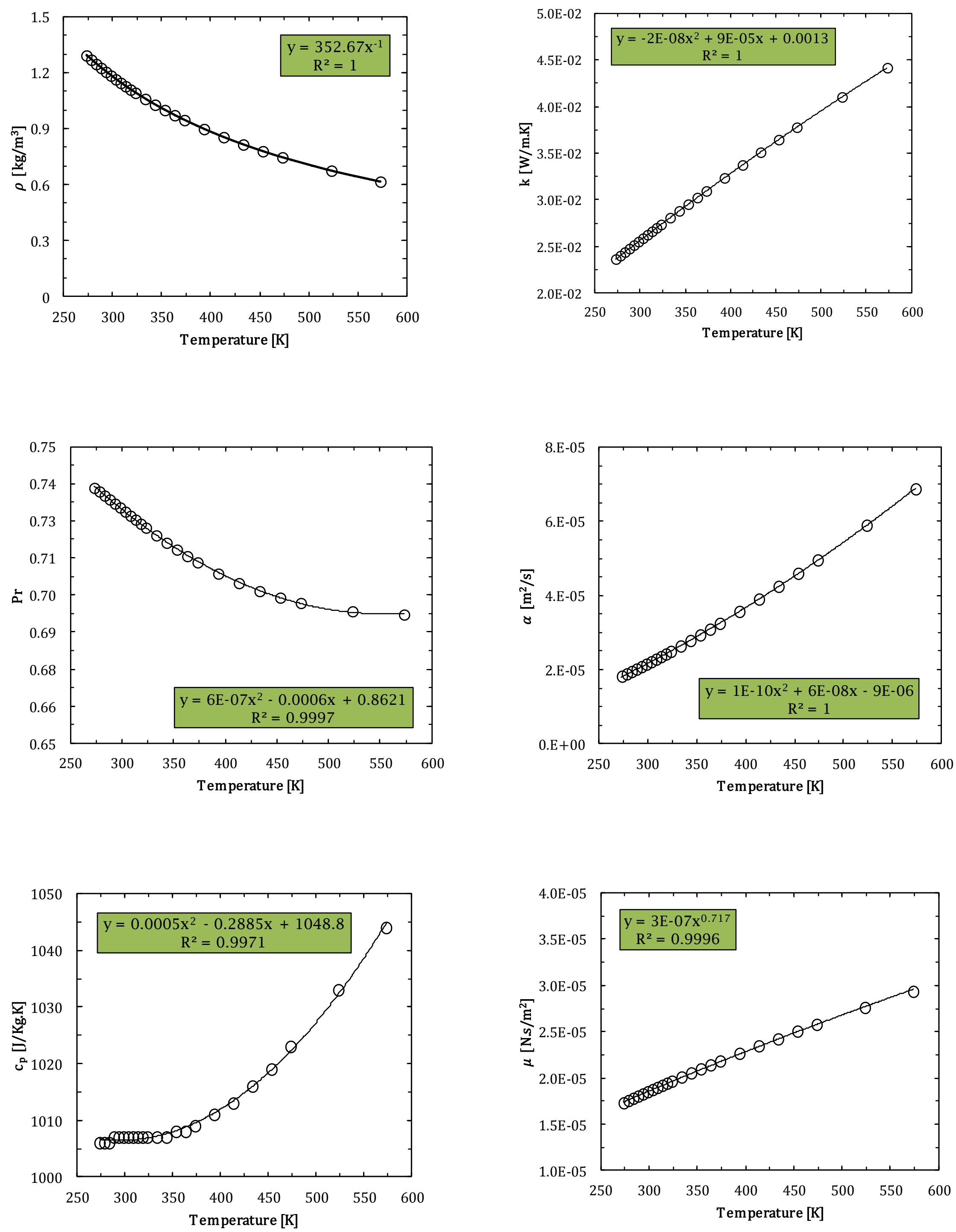

Figure 4.3 Thermal properties used for simulation.

4.3.3 Solution of Matrix Equation

Solution to the integrated model which has been developed in Chapter 3 is presented in this section. Consider the heat balance equation for the Manzanares SUPG: Eq. (3.50) to Eq. (3.52). These equations are transformed into a matrix form. Such that

$$[Q] = [H]\{T\} \tag{4.11}$$

in which,

$$T = \begin{Bmatrix} T_c \\ T_a \\ T_g \end{Bmatrix} \in \mathbb{R}^{3\times 1} \tag{4.12}$$

$$Q = \begin{bmatrix} \alpha_c I + h_{c-a_\infty}^{conv} T_{a_\infty} + h_{c-s}^{rad} T_s \\ \dfrac{\dot{m} c_p (T_a) T_{a\infty}}{(\pi {r_{col}}^2 - \pi r^2)} \\ \alpha_g \tau_c I + h_{g-g_\infty}^{cond} T_{g_\infty} \end{bmatrix} \in \mathbb{R}^{3\times 1} \tag{4.13}$$

$$H = \begin{bmatrix} h_{11} & h_{12} & h_{13} \\ h_{21} & h_{22} & h_{23} \\ h_{31} & h_{32} & h_{33} \end{bmatrix} \in \mathbb{R}^{3\times 3} \tag{4.14}$$

The matrix $[Q]$ in Eq. (4.11) is defined as the heat flux matrix since it contains the solar radiation heat flux as well as the collector airflow heat flux. It also contains the effect of ambient condition such as ambient air temperature, and solar radiation. The matrix $[H]$ in Eq. (4.11) is designated as the heat transfer coefficients since it contains all the heat transfer coefficients in the integrated model. The component of this matrix is presented in Table 4.2. In this table the convection, conduction and radiation heat transfer coefficients are arranged with respect to the temperature matrix $\{T\}$. This matrix contains the unknown parameters and subjected to be solved in the simulation procedures. The unknown parameters in the temperature matrix are the cover temperature, airflow temperature, and the ground temperature. In addition, the mass flow rate which is contained in the heat flux matrix and the heat transfer coefficient matrix is also one of the computed parameters in the simulation procedures. Noted that the size of the heat transfer matrix is depends on the number of unknown temperatures.

Table 4.2 Heat transfer coefficients

$h_{11} =$	$h_{c-a_\infty}^{conv} + h_{c-a}^{conv} + h_{c-s}^{rad} + h_{g-c}^{rad}$
$h_{12} =$	$-h_{c-a}^{conv}$
$h_{13} =$	$-h_{g-c}^{rad}$
$h_{21} =$	$-h_{c-a}^{conv}$
$h_{22} =$	$h_{c-a}^{conv} + h_{a-g}^{conv} + \dfrac{\dot{m}c_p(T_a)}{(\pi {r_{col}}^2 - \pi r^2)}$
$h_{23} =$	$-h_{a-g}^{conv}$
$h_{31} =$	$-h_{g-c}^{rad}$
$h_{32} =$	$-h_{a-g}^{conv}$
$h_{33} =$	$h_{a-g}^{conv} + h_{g-c}^{rad} + h_{g-g_\infty}^{cond}$

Solution to Eq. (4.11) can be obtained by simply calculate the inverse of the heat transfer coefficient matrix, such that

$$\{T\} = [H]^{-1}[Q] \tag{4.15}$$

However, this scheme is not complete since most of the expression of each heat transfer coefficients are function of the unknown parameters i.e. temperature of the cover, airflow, and ground. The heat transfer coefficients and heat flux matrices contain the unknown parameters as well. Directly solving the matrix equation using inversion scheme would not gives a correct result. Thus, the iterative calculation takes part in this process to obtain a correct solution. Implementation of this iterative scheme is conducted to access the performance of SUPG. Two cases are simulated which are the Manzanares SUPG and the lab-scale SUPG. The results are presented in the upcoming section.

4.4 Numerical Simulation of Manzanares SUPG

The performance of the Manzanares solar updraft power generator is simulated in this section by using real on-site meteorological data at the Manzanares, Spain as reported by Haaf et al. [2]. The meteorological data contains the solar radiation and the ambient temperature for 24 hours. These data are used as input to the developed computer program. The result is calculated for geometry of Manzanares SUPG as presented in Table 4.3 and meteorological condition as presented in Table 4.4. Comparison between simulation results with the experimental data is also presented in this section to validate the developed model. Furthermore, the effects of solar radiation, inflow coefficients, collector radius and tower height, and ambient air temperature are also discussed.

Table 4.3 Geometrical and optical data used in the simulation of Manzanares SUPG

Geometrical data		
Collector radius	122	m
Collector height	1.85	m
Tower radius	5.08	m
Tower height	194.6	m
Optical data		
Cover absorptivity	0.04	
Cover transmissivity	0.7	
Cover emissivity	0.87	
Ground absorptivity	0.9	
Ground emissivity	0.9	

Table 4.4 Meteorological data used in the simulation of Manzanares SUPG [2]

Time [Hr]	Irradiance [W/m²]	Ambient air temperature [C]	Time [Hr]	Irradiance [W/m²]	Ambient air temperature [C]
0:00	0	22.0	12:00	840	26.8
0:20	0	21.9	12:20	860	27.5
0:40	0	21.7	12:40	850	27.9
1:00	0	21.6	13:00	830	27.6
1:20	0	21.5	13:20	820	28.0
1:40	0	21.4	13:40	780	28.3
2:00	0	21.2	14:00	730	28.6
2:20	0	21.1	14:20	690	28.7
2:40	0	21.0	14:40	650	29.0
3:00	0	20.9	15:00	590	29.2
3:20	0	20.8	15:20	520	29.3
3:40	0	20.6	15:40	455	29.5
4:00	0	20.5	16:00	400	29.4
4:20	0	20.3	16:20	320	29.5
4:40	0	20.1	16:40	250	29.5
5:00	0	19.9	17:00	200	29.0
5:20	0	20.2	17:20	120	28.3
5:40	20	20.4	17:40	80	28.2
6:00	40	20.6	18:00	40	27.8
6:20	105	21.1	18:20	20	27.5
6:40	140	21.3	18:40	0	26.3
7:00	220	21.8	19:00	0	26.2
7:20	280	22.2	19:20	0	26.1
7:40	350	22.4	19:40	0	25.9
8:00	400	23.0	20:00	0	25.8
8:20	490	23.2	20:20	0	26.4
8:40	550	23.5	20:40	0	26.6
9:00	600	23.9	21:00	0	26.8
9:20	650	24.3	21:20	0	26.8
9:40	690	24.7	21:40	0	26.5
10:00	750	25.0	22:00	0	26.2
10:20	775	25.8	22:20	0	26.0
10:40	785	26.2	22:40	0	25.7
11:00	820	26.5	23:00	0	25.5
11:20	825	26.8	23:20	0	25.2
11:40	850	27.0	23:40	0	25.0

4.4.1 Validation with the Manzanares Experimental Results

In order to ensure the validity of the developed model in Chapter 3, a comparison between the simulation results and the experimental results of the Manzanares SUPG is conducted. The experimental data from Manzanares experiment is retrieved from reference [2] where the following parameters are collected: 1) updraft temperature, 2) updraft velocity, 3) mechanical power, and 4) efficiency of solar collector. These 4 parameters are also computed in the simulation works.

Fig. 4.4 shows the comparison of simulated updraft temperature and updraft velocity with the experimental updraft temperature and updraft velocity. Comparison for the updraft temperature is presented with regard to time (24 hours). In this figure, the prediction of updraft temperature from 6 am to midday has attained a remarkable agreement. Some discrepancies are observed after the midday but the simulated results quickly follow the experimental data. This is because in the real condition, part of heats from solar radiation is absorbed by the ground and thus conducted to its down layer. These heats will be released depending on the temperature gradient of the ground layer. Such complex mechanism is not included in the current model since the study focus is about performance. Nevertheless, it is successfully achieved a satisfactory results.

A more remarkable result is shown by simulation of updraft velocity as presented in Fig. 4.4 (bottom figure). In this figure, the updraft velocity from simulation and from experiment is displayed with regards to the solar radiation (Irradiance). Close observations to this figure reveal that the updraft velocity is ranging for Irradiance value start from 100 W/m^2 to 900 W/m^2. Perhaps the maximum solar radiation at that day was around 900 W/m^2 where the experimental maximum updraft velocity shows value around 9 m/s. At solar radiation below 100 W/m^2, the updraft velocity does not exist. Noted that, the experimental updraft velocity in this case was measured with turbine running at the bottom of solar tower, thus part of the kinetic energy from this updraft velocity had been used to rotate the turbine. Therefore, it can be concluded that the cut-in wind velocity for this particular turbine design and configuration is around 3 m/s. In addition, the experimental updraft velocity shows fluctuation profile while the simulation results of updraft velocity seems situated at the average of the experimental results.

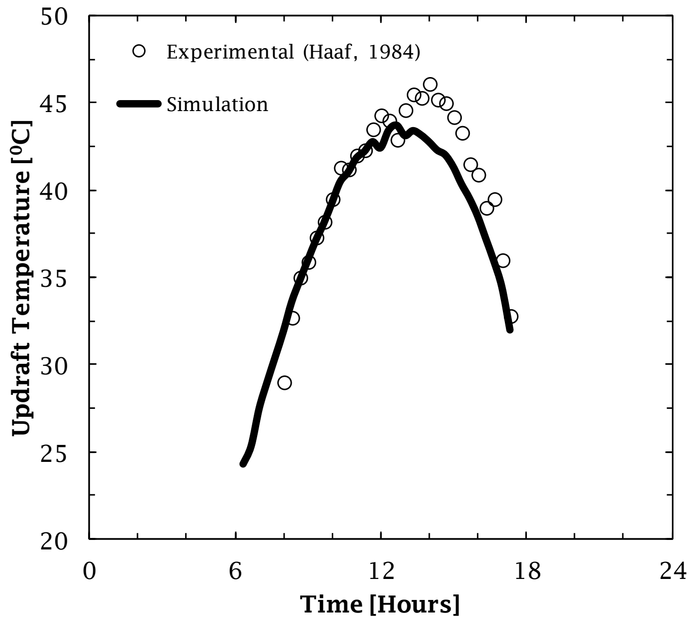

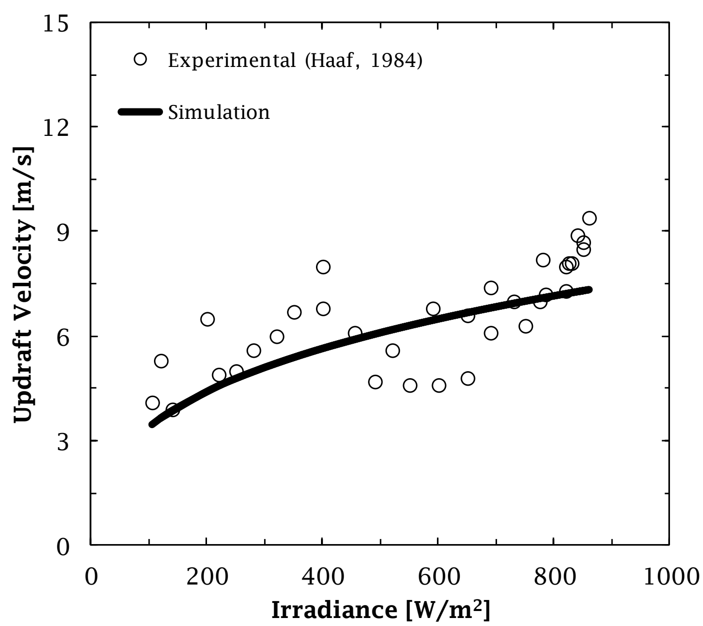

Fig. 4.4 Comparison of updraft temperature and updraft velocity between simulation results and the experimental results from the Manzanares experiment.

Validation study is also conducted by comparing the mechanical power and the efficiency of solar collector from simulation with those from experimental result. The mechanical power is the amount of energy that could be extracted by the wind turbine and become the most important parameter in the analysis of a solar updraft power generator. From Chapter 2, the design power for the Manzanares prototype is around 50 kW where the design solar radiation is around 1000 W/m^2. However, the maximum solar radiation in the current analysis is around 860 W/m^2. Thus, the mechanical power produced by the turbine is expected to be smaller than the designated power.

Fig. 4.5 shows the comparison between the simulated mechanical power and the experimental mechanical power. They are plotted with respect to time (24 hours). In this figure a rather small discrepancies are observed in the beginning of sunrise – in particular from 6 am to midday – where the prediction of mechanical power exceeding the experimental data. This is because the thermal inertia effect is not included in the developed model. Since the ground beneath the solar collector has the capability to store some heats from solar radiation, thus when the ground surface receives solar radiation in the morning, part of them is conducted to the down layer of the ground, so there is somehow a "delay" process of heating the airflow inside the collector. This "delay" will results in relative low airflow temperature and thus producing a lower mechanical power compare as appear in Fig. 4.5 (top figure).

A comparison between the efficiency of solar collector from simulation and those from experiment is presented in Fig. 4.5 (bottom figure). The experimental and simulation results of solar collector efficiency are plotted as function of Irradiance. In particular for experimental result, it was reported by Haaf et al. [2] that during night when no solar radiation, the mean collector efficiency will be somewhat higher than its momentary midday values. This is because the efficiency was calculated from the following equation

$$\eta = \dot{m} c_p \Delta T / A_{col} I \tag{4.16}$$

According to their analysis, the finite product of $\dot{m}\Delta T$ is the one who responsible for this condition. Since $\dot{m}$ and ΔT are also increase with I, thus simulation result gives almost a constant trend of collector efficiency. About 31% of daily mean collector efficiency was realized from the experimental data while 27% has been obtained from simulation.

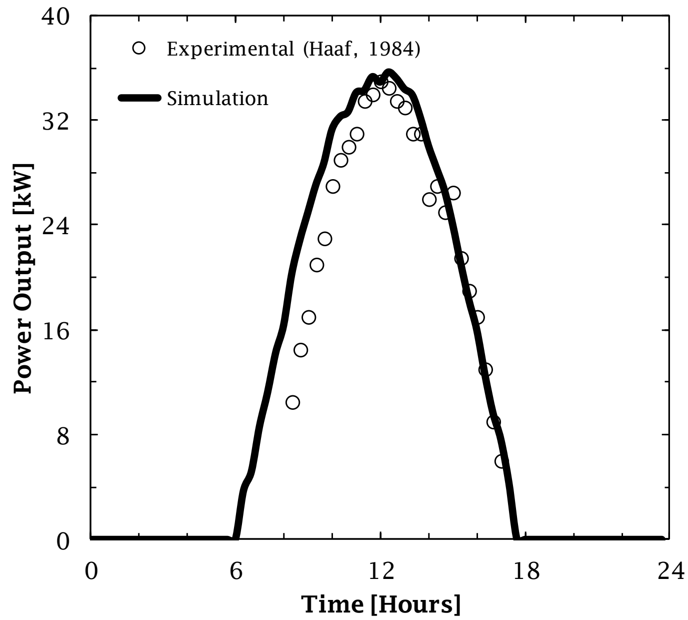

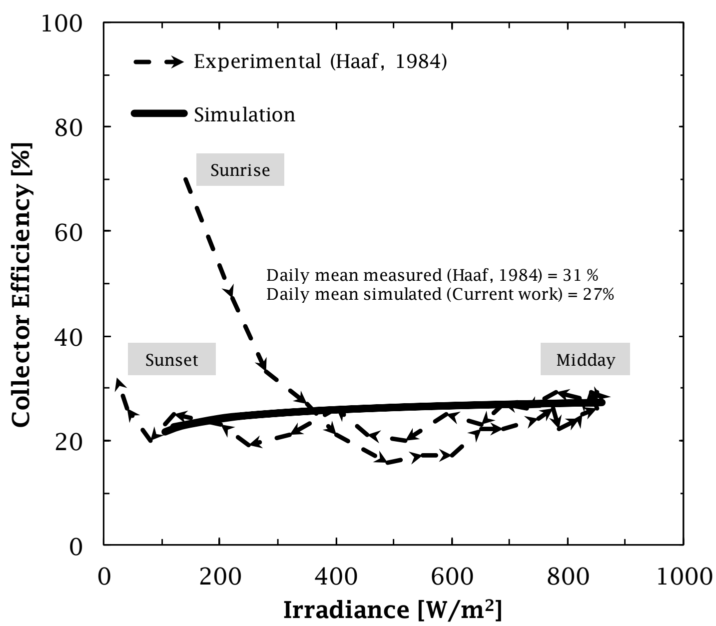

Fig. 4.5 Comparison of mechanical power and efficiency of solar collector between simulation results and the experimental results from the Manzanares experiment.

4.4.2 Effect of Solar Radiation

The effect of solar radiation to the performance of solar updraft power generator is discussed in this section. Parameters to be used in the performance analysis are the updraft temperature, updraft velocity, and mechanical power. These three parameters have been simulated for geometry of Manzanares solar updraft power generator. The radius and the height of solar collector were inputted for 122 m and 1.85 m respectively. The radius and the height of solar tower were also inputted for 5.08 m and 194.6 m. The Irradiance value for simulation was generated linearly from 10 W/m^2 to 1000 W/m^2. With this configuration and input, the updraft temperature, velocity, and mechanical power was simulated and the results are presented in Fig. 4.6.

From Fig. 4.6, the updraft velocity shows a quadratic profile although the solar radiation is given in a linear distribution. In contrast with the updraft velocity, the mechanical power shows a consistent profile with the solar radiation i.e. linear profile. Therefore it is recognized that the solar radiation has a linear relationship with the mechanical power produced by the turbine. As for the updraft temperature, it shows a slightly curved profile. The ambient air temperature used in this simulation is 302.15 K. At Irradiance value 1000 W/m^2 the solar updraft power generator system produces around 19.61 K of temperature increases. Also, at $I = 1000$ W/m^2, the simulated updraft velocity under load condition (with turbine) and mechanical power are obtained around 8.57 m/s and 48.61 kW respectively. The complete comparison is presented in Table 4.5.

Table 4.5 Comparison between simulation and experiment results at $I = 1000$ W/m^2

Results	Temperature increase	Updraft velocity	Mechanical power
Experiment (Manzanares)	$\Delta T = 20\ K$	9 m/s	50 kW
Simulation (Current Works)	$\Delta T = 19.61\ K$	8.57 m/s	48.61 kW
Difference	1.95 %	4.76 %	2.78 %

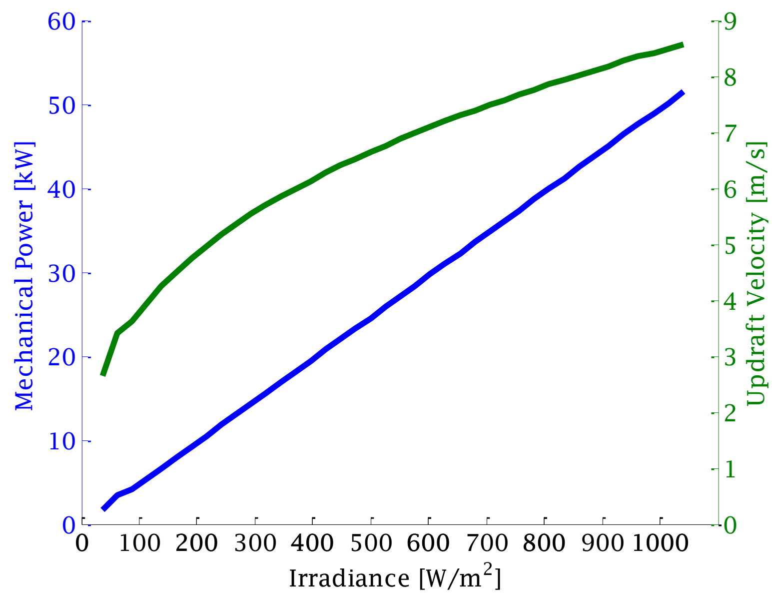

(a) Updraft velocity and mechanical power vs Irradiance

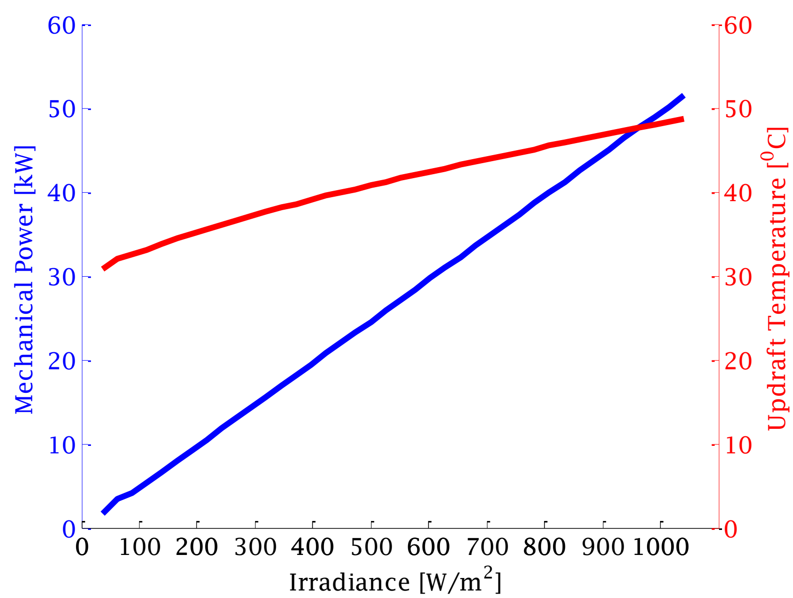

(b) Updraft temperature and mechanical power vs Irradiance

Fig. 4.6 Effects of solar radiation to the updraft velocity, updraft temperature, and mechanical power of the Manzanares SUPG.

4.4.3 Effect of Inflow Coefficients

In the model of wind turbine, the power coefficient is strongly depends on the inflow coefficients (labeled as a and a_0 in the equation). It has been shown in Eq. (3.41) and (Eq. (3.49) from Chapter 3. The inflow coefficient (a) is defined as the ratio of extracted wind velocity with the oncoming wind velocity for open flow case [80]. The inflow coefficient a_0 share the same definition but for the augmented flow case [75]. Although the solar updraft power generator has an augmented flow, as a first step towards a more complex analysis, the augmentation effects is not separated from the inflow coefficient a. In other words, the effects of flow augmentation due to the tower walls is summed up into only one coefficient rather separated into two coefficients (a and a_0). This is because the only accurate way to obtain the effects of flow augmentation is from experimental data. Rather than troublesome with the inclusion of the augmentation effects a simple approach is selected in the current analysis.

Furthermore, the value of inflow coefficient (a) should be carefully selected because it affects the amount of power directly. Thus, what is the suitable value of this inflow coefficient? To answer this question, a series of numerical parametric study are conducted. The mechanical power as in Eq. (3.49) is computed for a selected range of inflow coefficient value. Not only the mechanical power but also the mass flow rate is calculated for a selected range of inflow coefficient value. The equation for mass flow rate has been derived in Chapter 3 and the result is Eq. (3.23). However this equation is for free tower case or without wind turbine case. The equation of mass flow rate under load condition or with turbine case is obtained as follow

$$\dot{m} = \rho \pi {r_{tow}}^2 \sqrt{2 g h_{tow} \frac{T_a - T_{a\infty}}{T_{a\infty}} C_{\mathcal{T}} (1 - a)} \tag{4.17}$$

Therefore, the mass flow rate as in Eq. (4.17) and the mechanical power as in Eq. (3.49) can be simulated for a selected range of inflow coefficient value. The results of this simulation works are presented in Fig. 4.7. In order to obtain a suitable value of inflow coefficient, a direct comparison with those from the experimental (Manzanares) is conducted. The comparison gives a suitable value of inflow coefficient around $a \approx 2/3$.

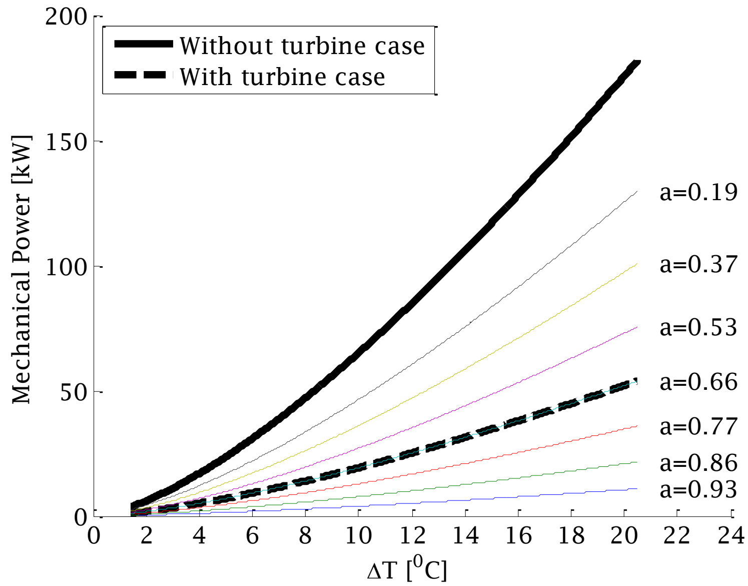

(a) Mechanical power vs temperature difference

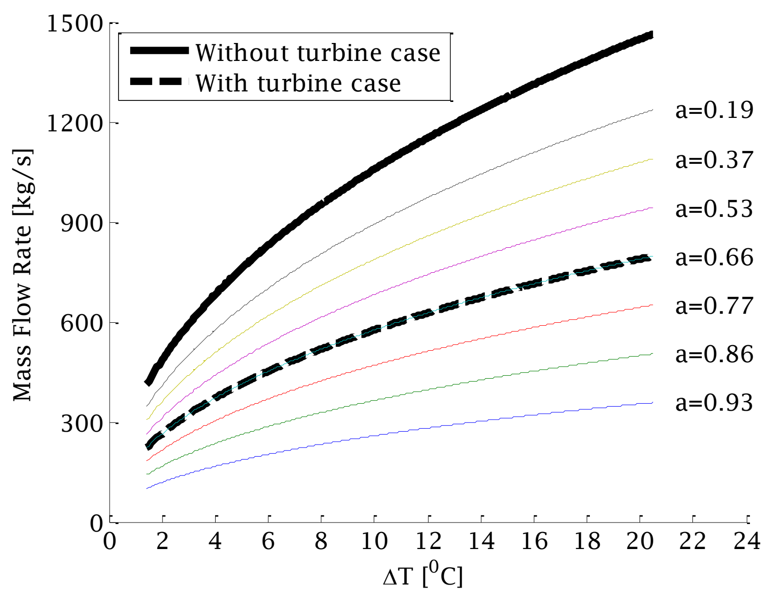

(b) Mass flow rate vs temperature difference

Fig. 4.7 Effects of inflow coefficient to the mass flow rate and mechanical power of the Manzanares SUPG.

4.4.4 Effect of Collector Radius and Tower Height

In this section, the geometrical effect to the power production and to the updraft temperature is examined. The geometry includes the radius of solar collector, and the height of solar tower. Effects of collector radius and tower height to the mechanical power and updraft temperature have been simulated and analyzed. Its graphical results are presented in Fig. 4.8 where the top figure is for simulated mechanical power and the bottom figure is for simulated updraft temperature.

Simulation had been conducted for Irradiance value equal to 1000 W/m^2, with maximum setting of thrust coefficient. The value of inflow coefficient was set for 2/3 and mechanical power had been computed for collector radius and tower height up to 250 m. It was found that the geometry plays important role in the production of power. The longer the collector radius and the higher the tower height is, the greater the power generation will be. Therefore, these results suggested that there is no optimum configuration of a solar updraft power plant. However, optimizing the design of a SUPG could be done through optimum design of wind turbine. Moreover, arrangement and installation of wind turbine is also has significant effect to the power production. If the cost is included as optimization parameters, thus the optimum design and configuration might also be affected by the initial capital cost and interest rate.

Increasing the size of a solar updraft power generator (collector radius and tower height) does not necessarily followed by rapid increment of airflow temperature as shown in Fig. 4.8 (bottom figure). The airflow heat-flux is always balance with the convection, conduction, and radiation process at the collector. Nevertheless; it is desirable to have a collector system with minimal heat-losses.

Furthermore, investigation concerning optimum design and configuration of a solar updraft power generator is continued to be discussed in Chapter 5 through series of experimentation, although the current simulation results indicates that there is no optimum configuration of a solar updraft power generator.

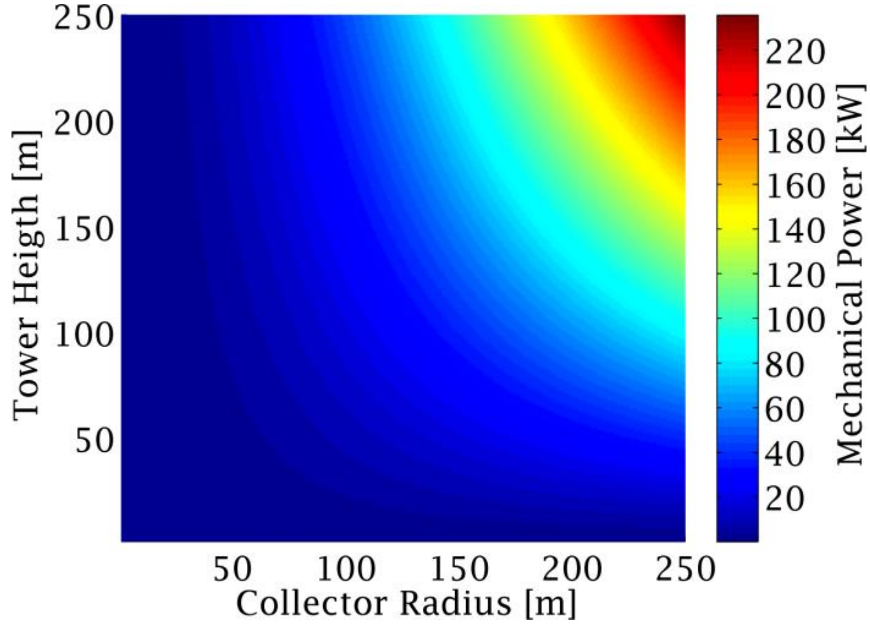

(a) Geometrical effect to the mechanical power

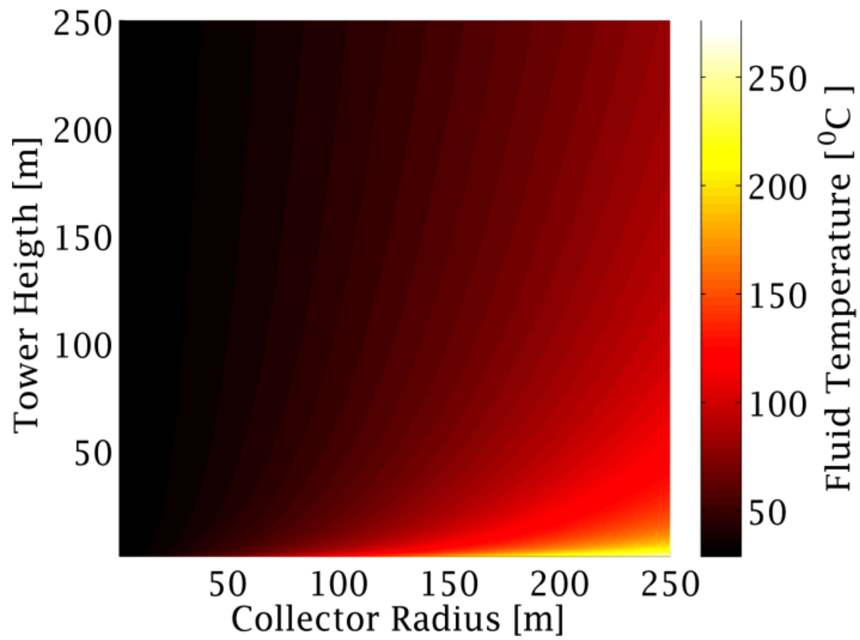

(b) Geometrical effect to the updraft temperature

Fig. 4.8 Effects of collector radius and tower height to the mechanical power and updraft temperature.

4.4.5 Effect of Ambient Temperature

The effect of ambient air temperature to the power production of a solar updraft power generator is investigated in this section. Besides the solar radiation, the ambient air temperature also affects the mechanical power and it is necessary to be studied because the solar updraft power generator can be built in different location where the solar radiation is abundant and has different ambient temperature. However, mostly this location has a relative high ambient air temperature. Therefore, simulation is conducted to compute the mechanical power for a selected range of ambient air temperature.

Fig. 4.9 shows the effects of ambient air temperature to the mechanical power. It is observed that the ambient air temperature has a small effect to the power production. In addition, increases in the ambient air temperature will also gives an increment for the mechanical power but only in moderate effect.

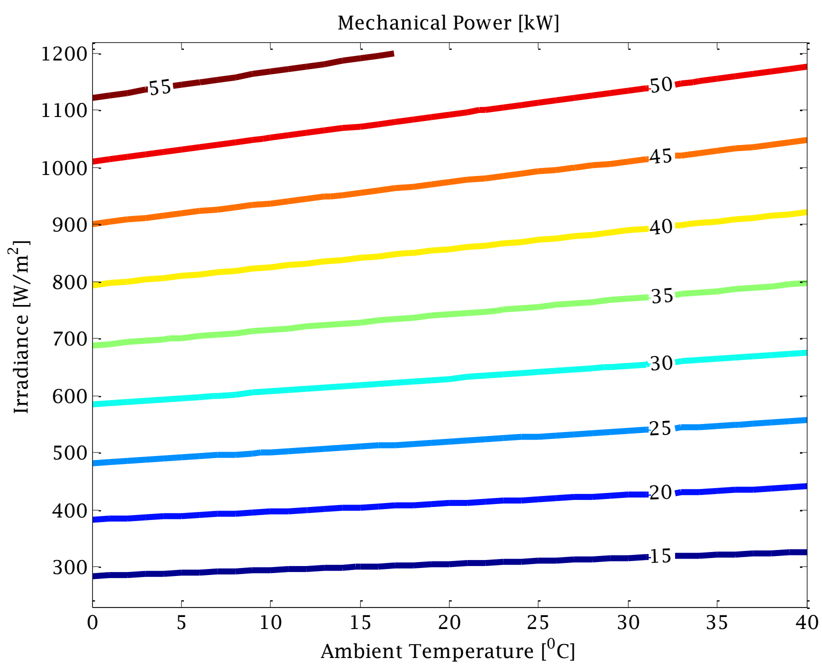

Fig. 4.9 Effect of ambient air temperature to the mechanical power of the Manzanares SUPG.

4.5 Numerical Simulation of Lab-Scale SUPG

Simulation to estimate the performance of a lab-scale solar updraft power generator is investigated in this section. Since the result of this simulation will also be used for comparison with the experimental data while the experiment itself has several cases, thus only one case is selected in this section. The geometry of the selected case of a lab-scale solar updraft power generator is elaborated as follows. Collector radius is 0.5 m, mean collector height is 0.05 m, tower radius is 0.05 m, and tower height is 1.5 m. Summary of the aforementioned geometrical data along with the optical data used in the simulation are presented in Table 4.6. Furthermore, the applicability of heat transfer correlation via Rayleigh, Reynolds, and Prandtl numbers is also accessed in order to ensure that the employed correlations are always in their valid range. Computational performance of the developed computer program is also investigated and discussed in this section.

Table 4.6 Geometrical and optical data used to simulate the performance of a lab-scale SUPG

Geometrical data		
Collector radius	0.5	m
Collector height (mean)	0.05	m
Tower radius	0.05	m
Tower height	1.5	m
Optical data		
Cover absorptivity	0.04	
Ground emissivity	0.9	

4.5.1 Applicability of Heat Transfer Correlations

The employed heat transfer correlations mostly have a range of validity since this correlation was obtained from empirical relation. Therefore, in this section the validity of the employed heat transfer correlation is accessed. Assessments are conducted through scrutinization of Rayleigh, Reynolds, and Prandtl numbers, where these three non-dimensional numbers characterize the heat transfer correlations. Simulation through iterative scheme is carried out for time steps 1 to 60 minutes and for each time step and iteration number, the Rayleigh, Reynolds and Prandtl numbers are calculated and stored.

Since the heat transfer between the cover and ambient air is modeled as free convection process (hot surface up), thus its heat transfer correlation is characterized by the Rayleigh number. Simulated Rayleigh number for each time step and iteration number is presented in Fig. 4.10. In this figure, the simulated Rayleigh number is shown in the valid range for all time steps and iteration numbers. In addition, the Nusselt number – used in the calculation of heat transfer coefficients – is correlated for two regions depending on the value of Rayleigh number. In this figure, it is observed that the Nusselt number is switched during the iteration process before eventually reach a converge value. Although the Nusselt number is switched during the iteration process, all the computed Rayleigh number successfully attain a convergence value in the valid range. For Rayleigh number at the range of $10^4 \leq Ra \leq 10^7$ the associated Nusselt number is $Nu = 0.54Ra\left(T_a, T_{a_\infty}\right)^{1/4}$ and for Rayleigh number at the range of $10^7 \leq Ra \leq 10^{11}$, the associated Nusselt number is $Nu = 0.14Ra\left(T_a, T_{a_\infty}\right)^{1/3}$.

As for heat transfer between cover and airflow, it has been selected as forced convection process. The heat transfer correlation for this case is presented in Eq. (3.60). It can be shown that the Reynolds number for this case is in the valid range for all time step and iteration number. All of the Reynolds numbers are also attains a convergence result. Similar results were also showed by Reynolds and Prandtl numbers for forced convection process between plate and airflow. Both of them are in the valid range, in particular for Reynolds number, it falls into laminar flow region. In summary, assessment of the heat transfer correlation is necessary to ensure their applicability.

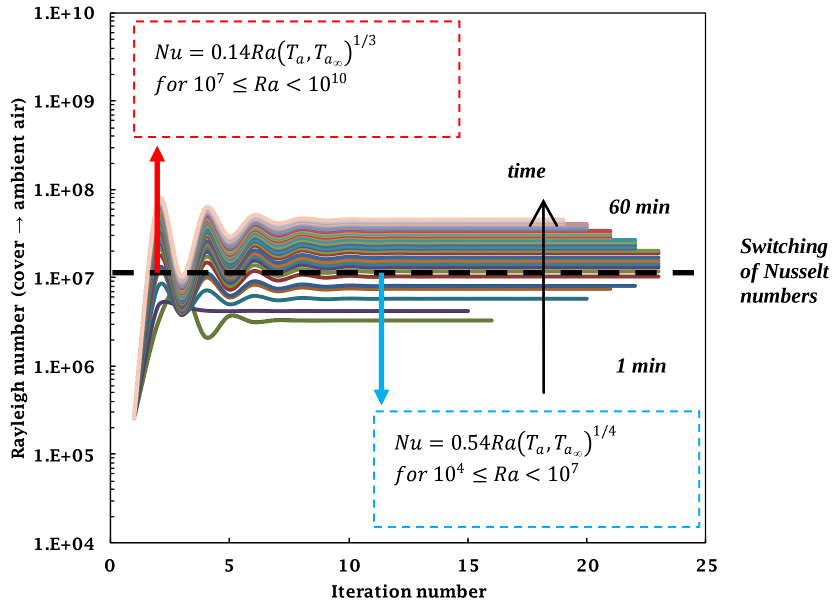

(a) Simulated Rayleigh number for heat transfer between cover and ambient air

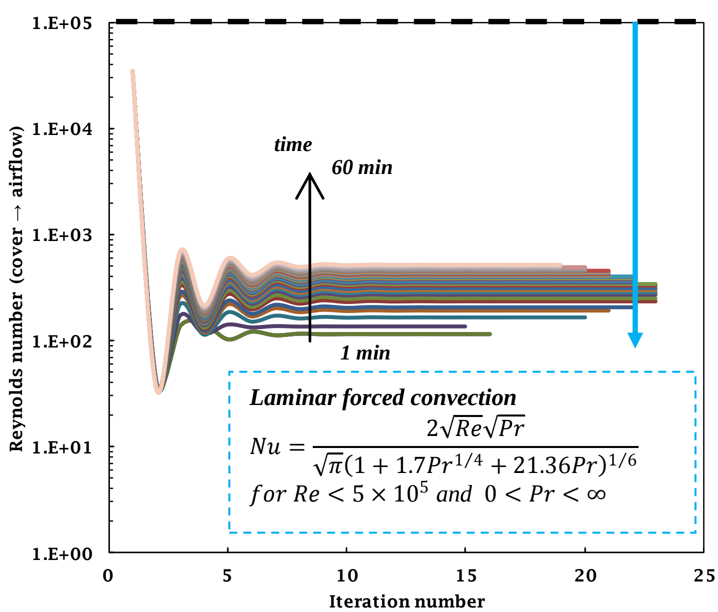

(b) Simulated Reynolds number for heat transfer between airflow and cover

Fig. 4.10 Simulation results of Rayleigh and Reynolds number for free and forced convection process showing its range of validity.

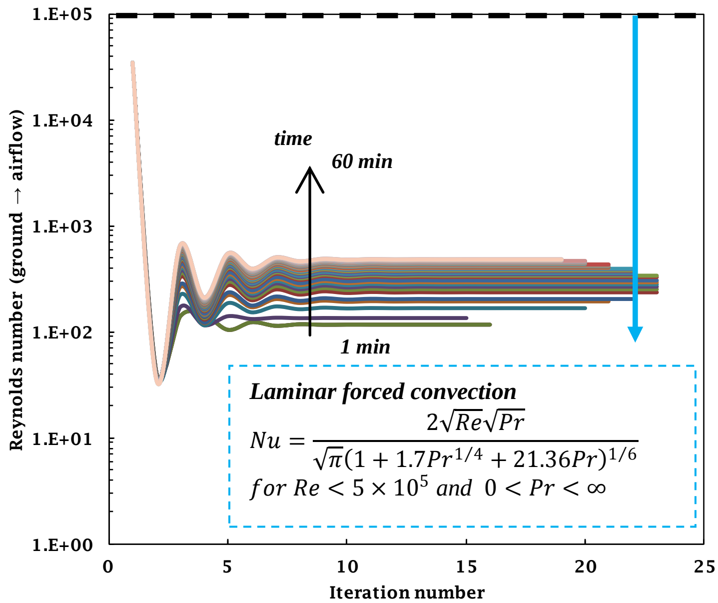

(a) Simulated Reynolds number for heat transfer between airflow and plate

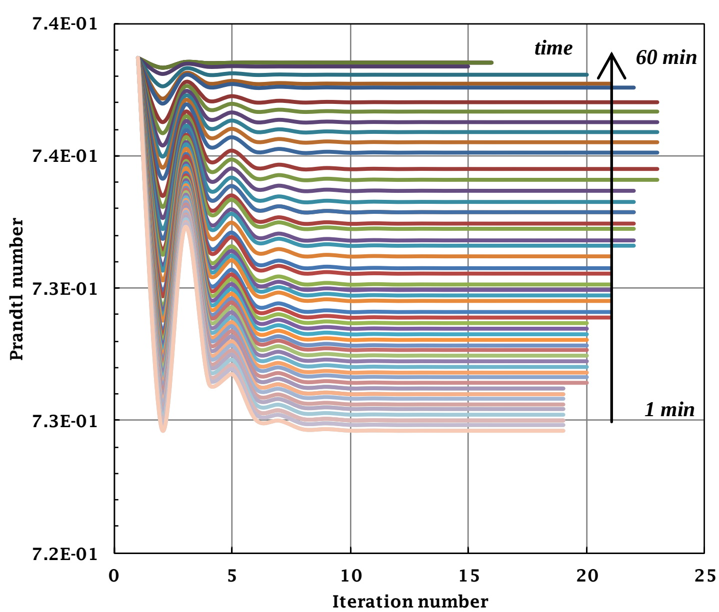

(b) Simulated Prandtl number for heat transfer between airflow and plate

Fig. 4.11 Validity of simulated Reynolds number and and Prandtl number for forced convection process.

4.5.2 Computational Performance

After the assessment on the applicability of heat transfer correlation, the next evaluation is about investigation related to the computational performance of the developed computer program. The computer program is written in MATLAB environment and used the built in function to solve the inverse equation numerically. The computation performance parameters are judged based on the rate of iteration process, in other words it is judged according to how fast the developed computer program produces or attains a convergence result.

As a case study, the updraft temperature and the mass flow rate are simulated and their results are stored for each time step and iteration number. The time step is selected from 1 to 60 minutes. The simulation result is computed and stored not only for the updraft temperature and the mass flow rate but also for their relative error norm which measure the accuracy and performance of the developed model and program. The result of simulated updraft temperature is presented in Fig. 4.12. From this figure it is observed that the results converge quickly to the correct values where the iteration number is less than 25. Similar results are also shown by the computation of relative error norm for the updraft temperature. It is observed that the relative error norm converges quickly to the correct values and thus meet the desired tolerance.

Fig. 4.13 shows the simulated mass flow rate and their relative error norm. These two simulation results are also has a superior performance in term of the convergence rate. It is also recognized that as long as the heat transfer correlations are always fall in the valid range, thus a faster iteration process can be always guaranteed. Therefore, the selection and implementation of the suitable and proper heat transfer correlation is regarded as the most important process in the numerical simulation.

It is essential to investigate the applicability of heat transfer correlations and also to examine the performance of the developed computer program. This is because the simulated results – in term of updraft temperature and mass flow rate – will be used in the next section to be compared with the result from the experiment. Having a solid confident in the applicability of the employed heat transfer correlations and also the performance of the developed computer program will result in a reliable theoretical model.

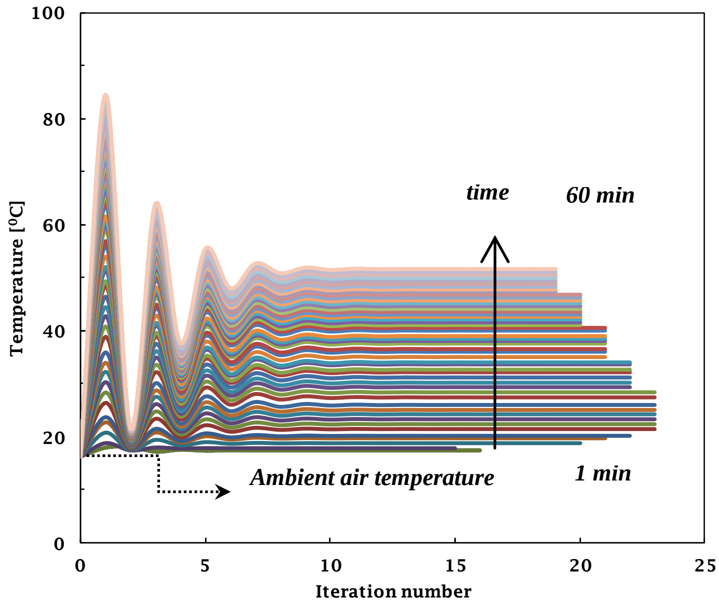

(a) Updraft temperature for each iteration number

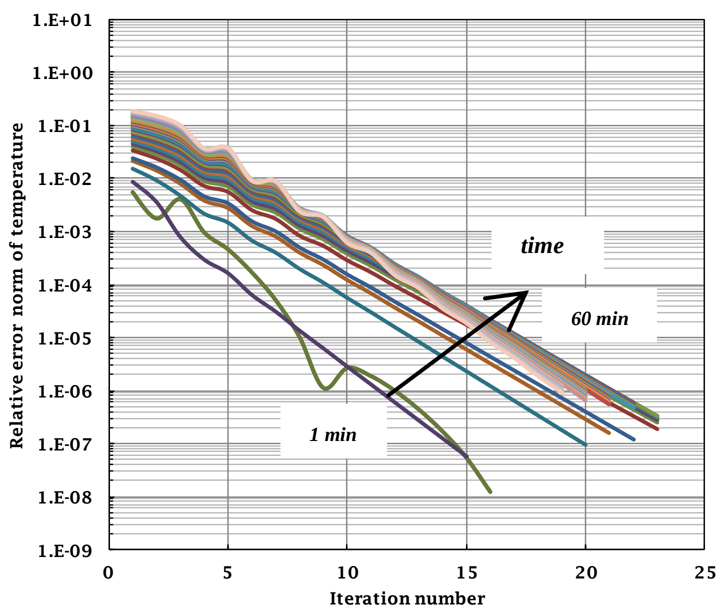

(b) Relative error norm of mechanical power for each iteration number

Fig. 4.12 Simulated updraft temperature and its relative error norm showing that a convergence results has been successfully attained.

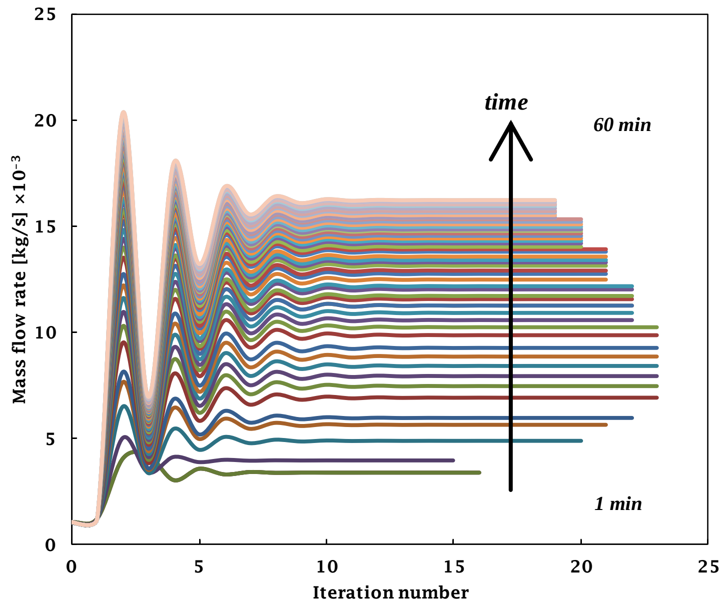

(a) Mass flow rate for each iteration number

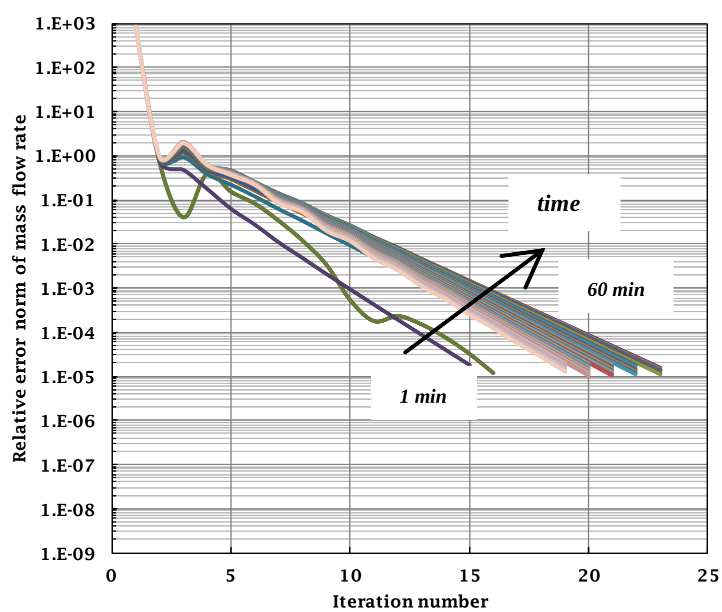

(b) Relative error norm of mass flow rate for each iteration number

Fig. 4.13 Simulated mass flow rate and its relative error norm showing that a convergence results has been successfully attained.

4.5.3 Updraft Temperature and Updraft Velocity

Discussion regarding the simulated updraft temperature and updraft velocity is presented in this section. These two parameters are selected as the updated variables during the iteration process. However, only the airflow temperature and updraft velocity are discussed in this analysis since the developed program also calculates the cover surface temperature. Simulations are carried out for time step 1 to 60 minutes and only the converged result is presented in this section. The geometry of the simulated lab-scale SUPG is presented in Table 4.6.

Fig. 4.14 shows the simulated updraft temperature and updraft velocity. Simulations are conducted for 5 cases where each case has different value of heat losses $\dot{q}_{loss}$. In the real condition, the heat losses (at the edge of collector) are changing with time. However, in this analysis the heat losses are modeled as constant value (through time). This is because the heat transfer correlation for heat losses at the edge of collector is not widely available in the literature. Therefore as initial step, the value of heat losses at the edge of collector are assumed to hold a constant value. The updraft temperature is simulated for different value of heat losses; ranging from 1 W/m^2 to 5 W/m^2. It can be observed that the suitable value of heat losses is around 3 W/m^2. In addition, for a small value of heat losses it gives an overestimate result of the updraft temperature, while for a high value of heat losses it produces an underestimate result of the updraft temperature.

Similar situation is observed in estimation of the updraft velocity. It is calculated also for 5 different values of heat losses and from the simulation result it can be observed that a suitable value of heat losses is also around 3 W/m^2. Heat losses at the edge of collector affect the amount of updraft temperature and the updraft velocity. Since the mechanical power is also depends on these two parameters, thus it is indirectly affect the amount of power for a SUPFG system. Therefore, it is desirable to have small heat losses at the edge of collector. The strategy to minimize these losses is investigated in Chapter 5 through series of experiments.

In summary, the developed model has been able to represents the airflow inside the collector and the developed computer program has also been able to solve the corresponding equations via iterative scheme.

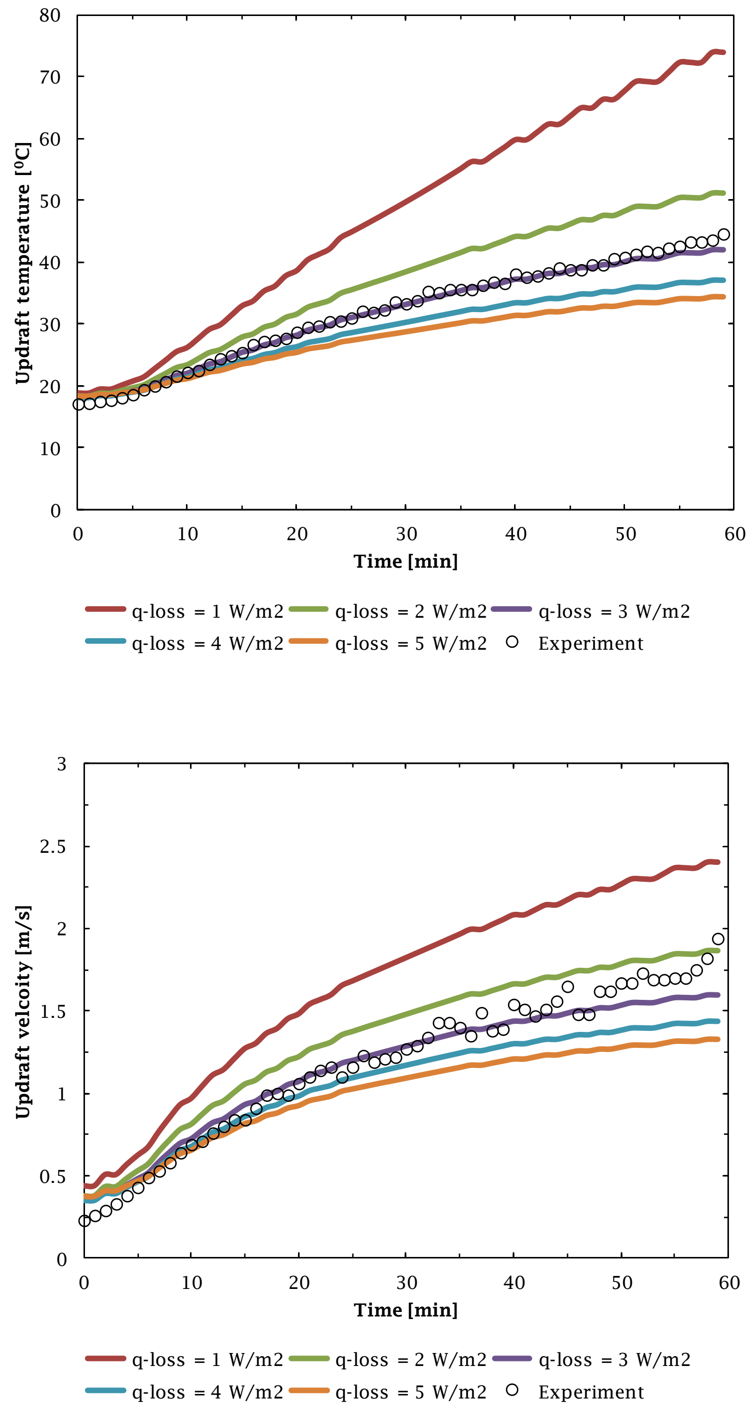

Fig. 4.14 Comparison between simulated updraft temperature and updraft velocity with the experimental results of a lab-scale SUPG.

4.6 Remarks

A set of computer program written in MATLAB environment which is based on the iterative scheme has been developed in this Chapter. Numerical parametric studies have been conducted with the developed program. Therefore, the following summaries can be listed as follows:

- A computer program to solve the mathematical model of a solar updraft power generator has been developed.
- Simulation result from the developed program has been validated with the experimental data of the Manzanares SUPG. From this validation study, a remarkable agreement has been obtained; demonstrating the accuracy of the developed models.
- The validated models are then used to simulate the performance characteristics of the Manzanares SUPG and the lab-scale SUPG.
- Effects of solar radiation, effects of inflow coefficient, effects of collector radius and tower height, as well as effects of the ambient air temperature have been investigated and discussed through simulation results of the Manzanares SUPG.
- Applicability of heat transfer correlations and the computational performance have been examined for the case of lab-scale SUPG. The discussion has been made through simulation result and it has been obtained that the employed heat transfer correlations are suitable for the simulation.

In conclusion, Chapter 4 is mainly devoted to develop a numerical tool in solving the developed mathematical model in Chapter 3.

Experimental Investigation

Chapter 5

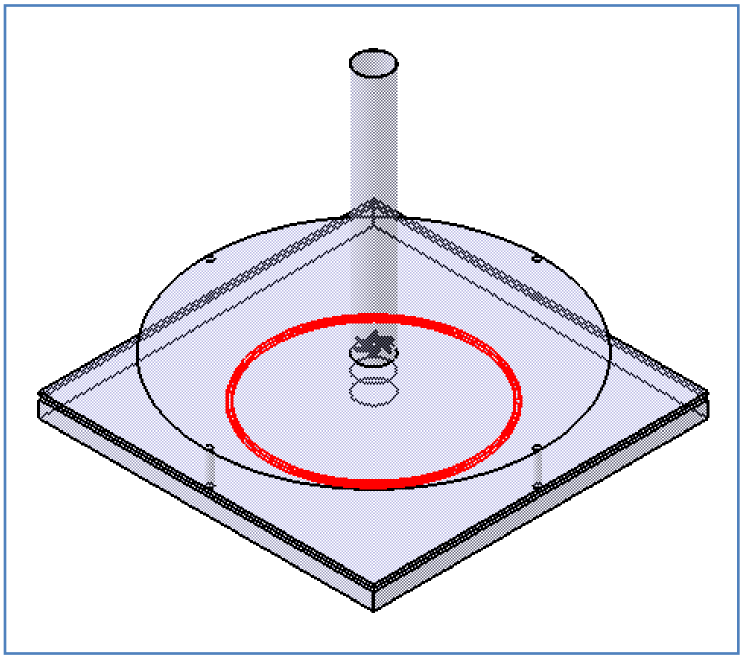

In Chapter 5, experiment on a lab-scale solar updraft power generator is discussed. The discussion begins with description of experimental design. Series of schematic drawing related to the design of collector, design of tower, design of guide walls, as well as design of heating system are provided. After that, discussions concerning experimental setup and measurement procedures are elaborated step by step, so that the experiment can be reproduced in the future. Results of experiment are presented for two cases according to the type of collector. There are two types of collector being investigated namely collector type A and collector type B. For each type of collectors, the collector height, tower diameter, and tower height are varied with purpose to find an optimum combination; indicating a highly efficient process. Experiment results with addition of guide walls are also discussed and presented in this chapter.

5.1 Introduction

Experimental investigation is one of the research methods implemented in the current work besides the theoretical and numerical work. This method holds an important role because the experiment is not only conducted to seek an optimum design and configuration of a solar updraft power generator, but also serves as source of data to be used in the development of theoretical model and its numerical simulation. Experiment can be conducted for a small prototype in the real outside condition where the experimental model receives solar radiation as source of heat. However, a laboratory scale (lab-scale) of a solar updraft power generator is used to be tested inside a laboratory room instead of an outdoor model of SUPG. The reason is due to the flexibility of experiment. If an outdoor model is built instead of a lab-scale SUPG, the effort to find an optimum design and configuration would be enormous and can be considered not practical since the experiment had been design for a large number of cases.

The experiment cases are managed by varying the configuration of a solar updraft power generator system. For example: changing the collector height, tower diameter, and tower height, until an optimum combination is obtained. The optimum combination is based on the condition where certain combination of collector height, tower diameter, and tower height produce a higher updraft velocity compare to the other configurations with the same amount of heat given to the system. At the outdoor environment, the amount of heat cannot be controlled since it is depends on the intensity of solar radiation. Thus, a direct comparison study for each experiment cases cannot be performed. With this reason, in the current study the source of heat is provided from an electric thermal element where a consistent heat source can be supplied.

Furthermore, an innovative way to increase the total efficiency of a solar updraft power generator has been proposed by installing a series of guide walls inside the collector, with purpose to concentrate the airflow and producing an updraft vortex instead of axial updraft flow as in the conventional SUPG. The hypothesis is: Addition of guide walls will produce a stronger entrainment effect compare to those without guide walls. Because the turbine at the center of collector will entrain the collector airflow in a swirl pattern, thus a higher updraft velocity is expected from this particular configuration.

5.2 Design of Experiment

Before conducting the experiment on a lab-scale solar updraft power generator, it is necessary to select the geometry to be tested. Two types of collector have been selected in this study. They are labeled as collector type A and collector type B. These two types of collector are selected based on the result of review works in Chapter 2. From the result of review works on the development of physical model of a SUPG in Chapter 2, it was found that most of the collector has the design and configuration in form of collector type A. Therefore, in this study a different approach is proposed where the collector type A is installed in reverse or backwards configuration resulting to a new type of collector which is labeled as collector type B. Physical reasoning for this mechanism is based on continuity of flow; the volume flow through the duct is constant, thus if the area decreases along the flow (convergent duct), the velocity increases, if the area increases (divergent duct) the velocity decreases [71].

However, there is of course a limit where the decrement of collector area will also reduce the velocity due the friction between the plate and the collector walls. Moreover, enlargement of collector area has a limit as well since the given heat to the airflow will easily loss to the environment and thus reducing the velocity and efficiency. With this reason, it is predicted that at least one optimum configuration must be exist where the velocity is higher than the other configuration for a same amount of input (heat given to the airflow). Experiment which is designed in this section has the purpose to find this optimum design and configuration. Since the optimum point could be obtained for at least three data points, thus the experiment by varying the geometry of lab-scale SUPG can be stopped if the optimum point is found within three experiment cases. Otherwise the experiment is continued for more than three cases.

Discussions begin with the design of heating system as the source of heat, replacing solar radiation in the outdoor system. After that the design of collector is elaborated and it is followed by discussion of design of tower. Since the experiment is also includes implementation of guide walls, thus the design of guide walls is also discussed. Discussion concerning design of SUPG parts is essential for manufacturing purposes. They provide the dimension of SUPG geometry (in mm) and also description of the materials.

5.2.1 Design of Heating System

Heating system in this experiment consists of one electric thermal element made by nichrome materials and has good performance under high temperature since the melting point of nichrome is high and does not easily expand when it heats up. It also has a reasonable resistance and produces a consistent amount of heat when it connects to electricity. The nichrome material is in shape of wire and circularly buried inside an isolator materials. In order to control the direction of heat flux, a gap of 10 mm opening is provided. The heats from this heating element are then convected and absorbed by a 1m × 1m aluminum plate with 10 mm thickness. The bottom surface of aluminum plate is exposed to a high temperature air from the heating process by the nichrome and then it is conducted to the upper surface of aluminum plate. Heats from the upper surface are used by the airflow to increase its thermal energy.

The reason to use an aluminum plate as the material to absorb heat from heating element is because the aluminum has a high thermal conductivity, so that heat can be quickly distributed (conducted) along the aluminum plate. Therefore, a uniform distribution of heat is expected from the implementation of aluminum as heat absorber. The upper surface temperature is measured at the center of aluminum plate as indicator for the amount of input (heats) given to the airflow. The design of heating system used in the experiment is presented in Fig. 5.1 which shows the dimension and the arrangement of aluminum plate, heating element, and the isolator material.

5.2.2 Design of Collector

The collector in a lab-scale solar updraft power generator has the same job with the collector in a real outdoor prototype. Although the necessity to have a translucent material for the collector is not compulsory since the solar radiation has been replaced by heating element, a transparent thermoplastic material is used in the current experiment. The material is poly(methyl methacrylate) under the name of acrylic glass. The purpose to have a transparent cover/collector in this experiment is to allow visual inspection of the airflow inside the collector when flow visualization experiment is conducted.

The collector has been selected for two design which is labeled as collector type A and collector type B. The design of collector type B is selected to be presented in Fig. 5.2 which shows the dimension of the collector in (mm). Collector type A is obtained by simply turning backwards the collector type B as in Fig. 5.2. Therefore in this experiment, only one collector is manufactured but it can be utilized to obtain two different design of collector.

5.2.3 Design of Tower

The tower for the experiment is also made from translucent materials which is the same materials as the collector. Three different diameter of transparent tube was manufactured and used in the experiment. The diameter for each tube is 50 mm, 100 mm, and 150 mm. The smallest diameter is selected to be 50 mm in consideration of friction between the updraft flow and the solid walls of tube. Thus, a constant increment (50 mm) is selected for the other two diameters. The design of the tower is presented in Fig. 5.3

Not only the diameter is varied in the experiment but also the height of tower is investigated, so that three different heights of transparent tube were ordered for each diameter. The height of tower for each tube is 250 mm, 500 mm, and 750 mm. The experiment is conducted for 4 cases of tower height since the optimum point is not observed from these three height configurations. Thus the experiment cases were conducted for 250 mm, 500 mm, 750 mm, and 1500 mm of tower height. The 1500 mm of tower height is realized by combining all the transparent tubes into one tall tower.

5.2.4 Design of Guide Walls

Schematic drawing regarding design of guide walls can be found in Fig. 5.4. In this figure, dimension of the guide walls is displayed in (mm). Although the guide walls can be implemented for two types of collector, but in this experiment the guide is designed only for the collector type B. This is because from the experiment without guide walls. It was found that the collector type B produces a higher updraft velocity – for the same amount of heats given to the airflow – compare to the collector type A.

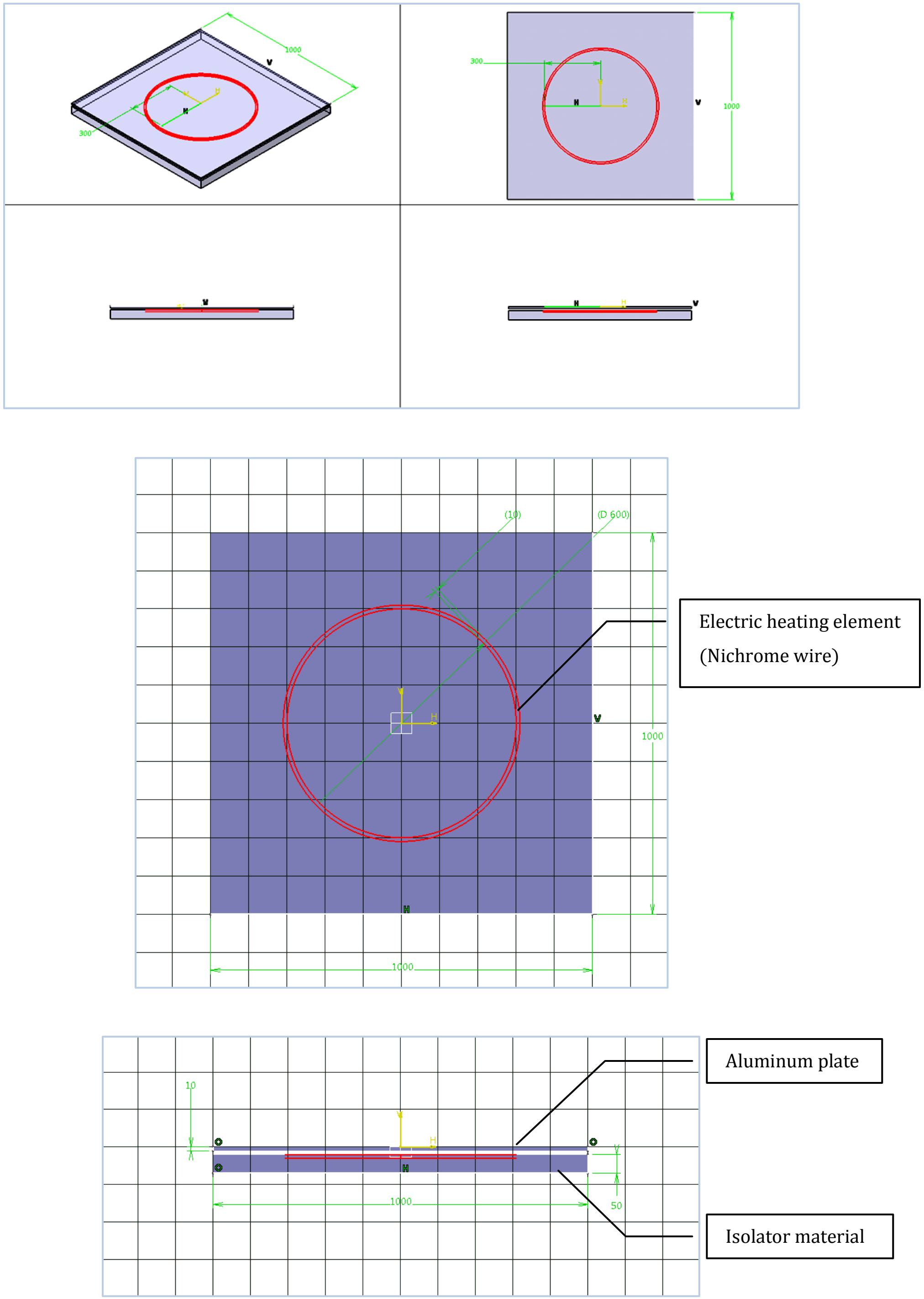

Fig. 5.1 Design of heating system.

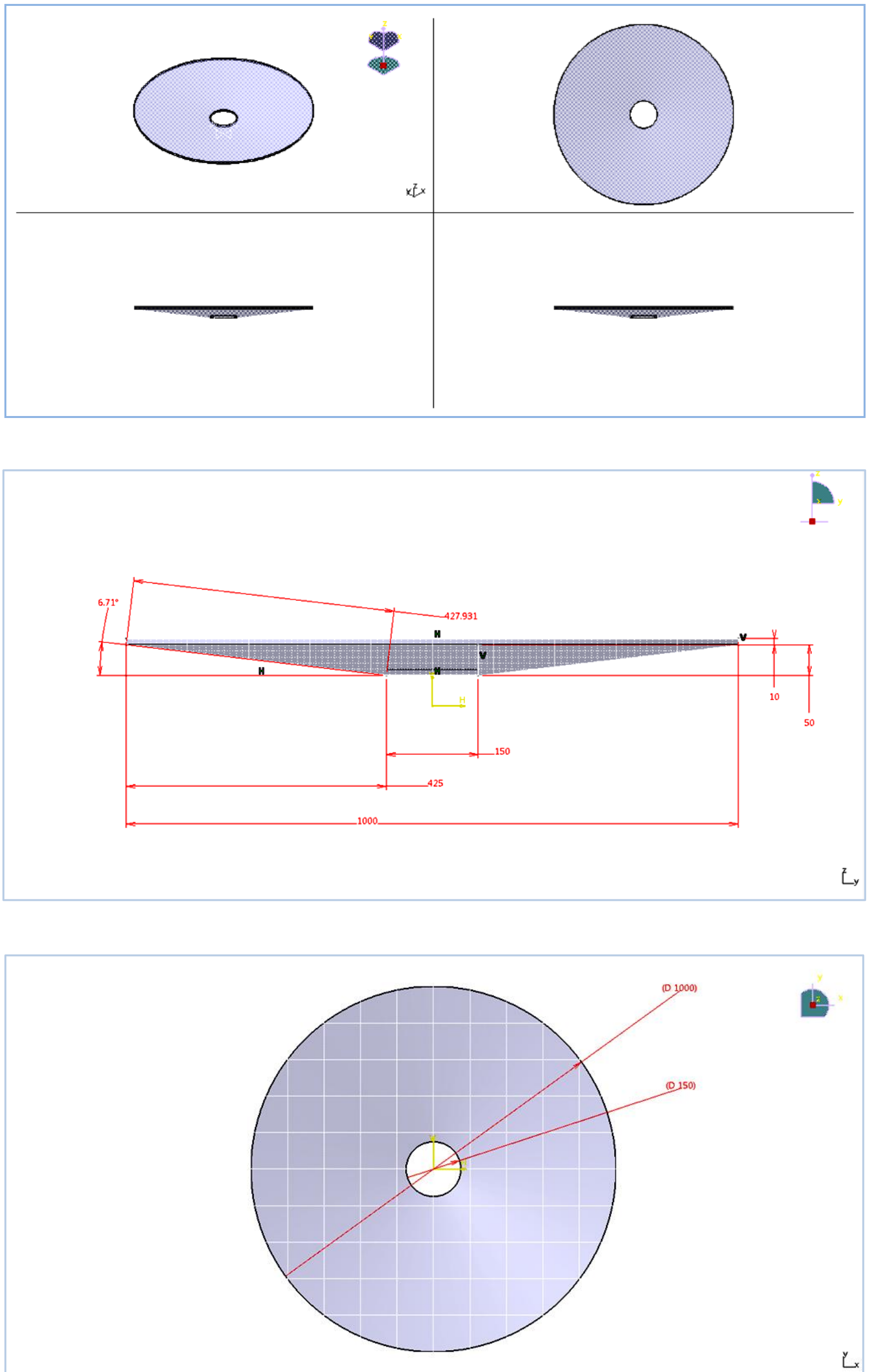

Fig. 5.2 Design of collector.

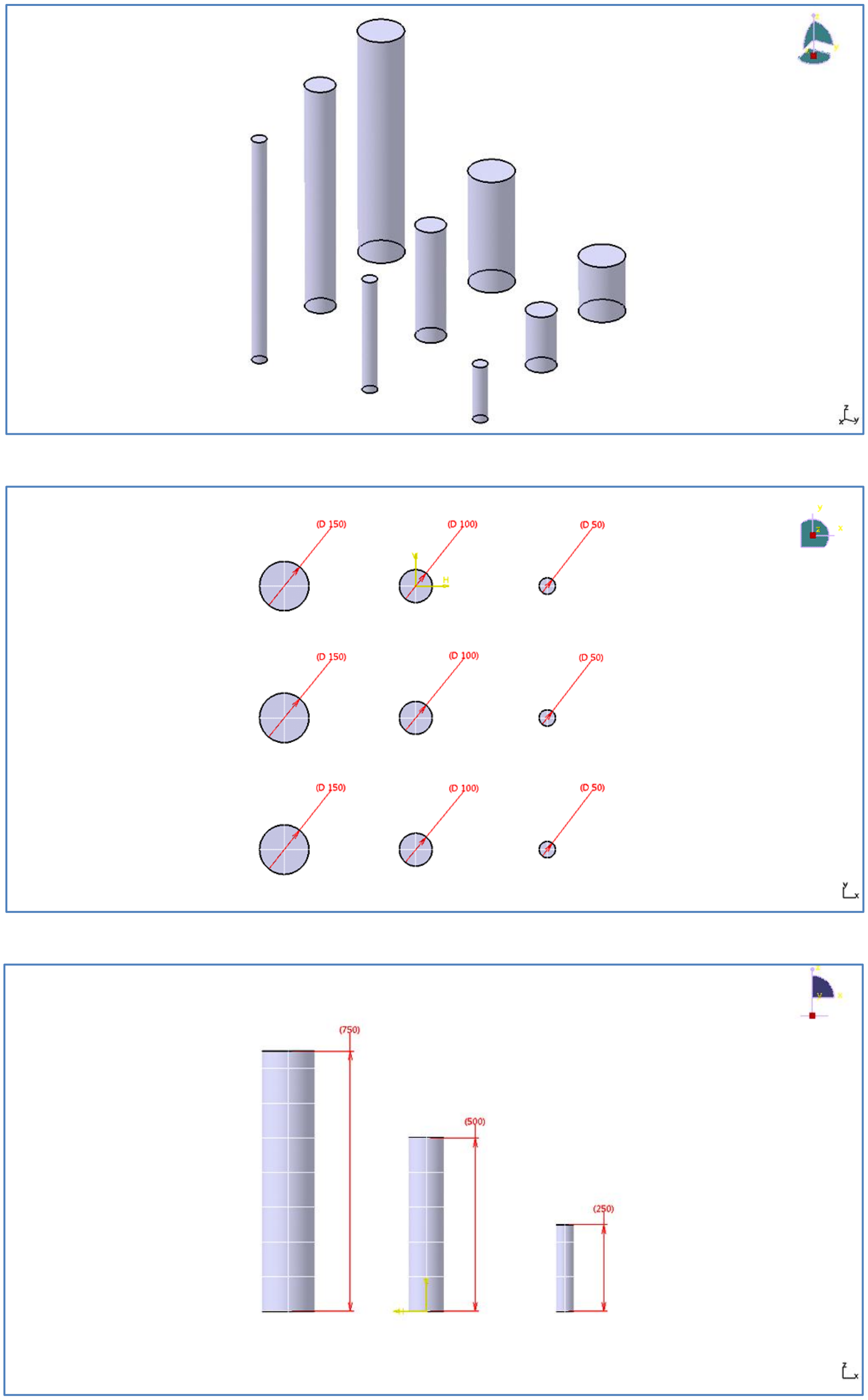

Fig. 5.3 Design of tower.

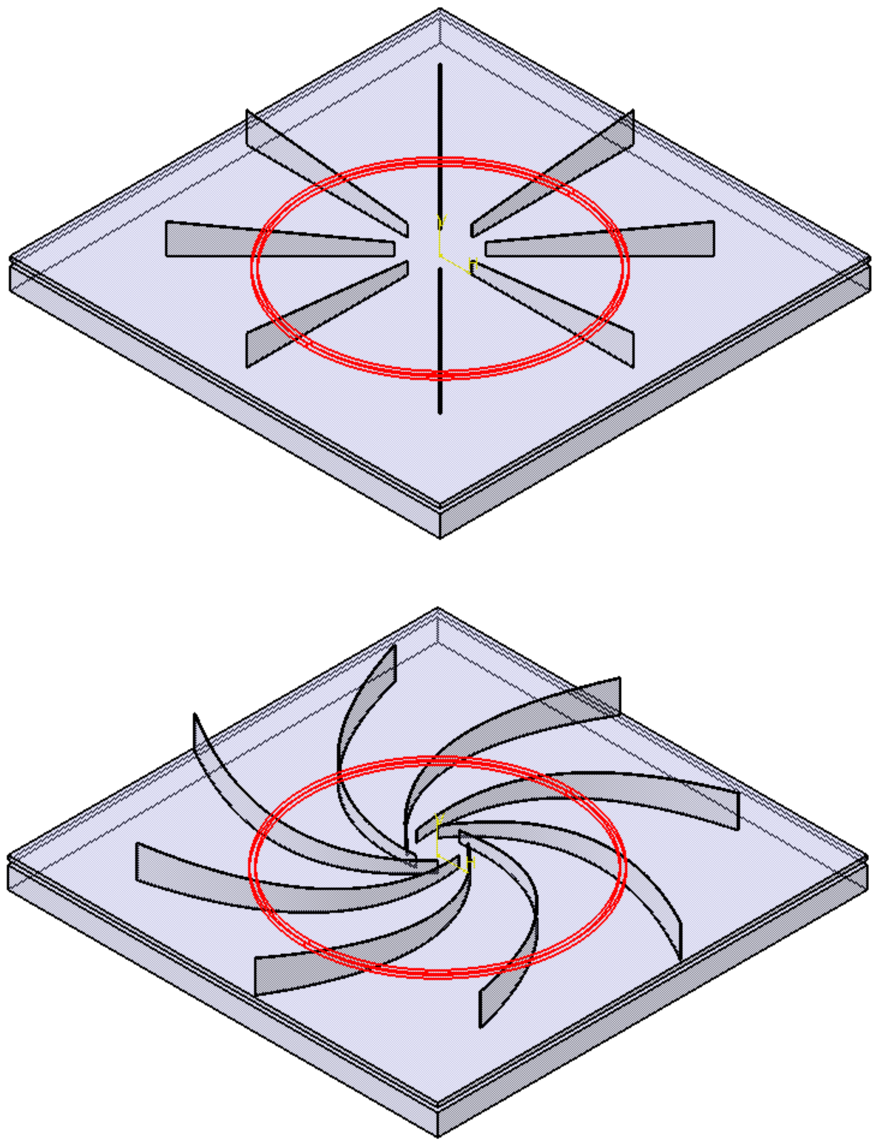

Fig. 5.4 Design of Guide Walls.

5.3 Experimental Setup

The collector, tower, and the heating system are combined to form a lab-scale solar updraft power generator. The arrangements of these parts with regards to the type of collector are presented in Fig. 5.5 and Fig. 5.6. In Fig. 5.5, experimental setup for collector type A is displayed. The location of each sensor is also showed. The first sensor is located at the center of aluminum plate to measure its surface temperature. The second sensor is placed at the turbine region where the velocity reaches its maximum value at this position. Although the placement of turbine can also be realized in circumferential manner at the center of collector, a single turbine (at the bottom of tower) configuration is chosen in this work to be investigated and discussed. The second sensor measures both temperature and velocity of the updraft flow simultaneously. The third sensor is installed at the top part of the tower to measure temperature and velocity of the exit updraft flow.

Fig. 5.6 shows experimental setup for collector type B. Description of each parts of lab-scale solar updraft power generator is presented in this figure. From this figure, component of a lab-scale solar updraft power generator can be listed as follows: tower/chimney, collector/cover, small fan, aluminum plate, isolator, and supporter structure. Sensor placement is similar with the setup for collector type A. There exist small height differences between the placement of 2nd sensor in the collector type A and collector type B relative from the aluminum plate surface. Nevertheless, the turbine will be placed right at the bottom of the tower so this height difference does not matter in the view of turbine placement.

The collector height is investigated for three different cases. The height of collector to be tested for collector type A is selected as follows: 25 mm, 50 mm, and 75 mm. This height is measured at the outer part of collector, so that the distance between the surface of aluminum plate and the outer part of collector will gives the selected height configuration. This distance can also be regarded as the airflow opening distance of a solar updraft power generator. For collector type B, the collector height configuration is selected as follows: 65 mm, 75 mm, and 100 mm. This height is also measured at the outer part of collector. Both collector designs have slope configuration, thus the height at the outer part of collector is different with the inner part of collector.

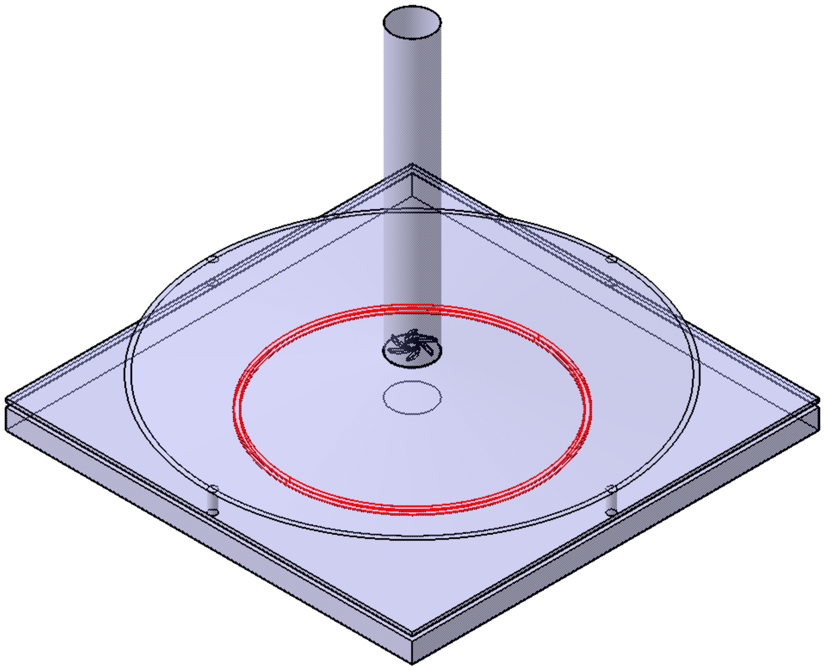

(a) Perspective view of collector type A setup

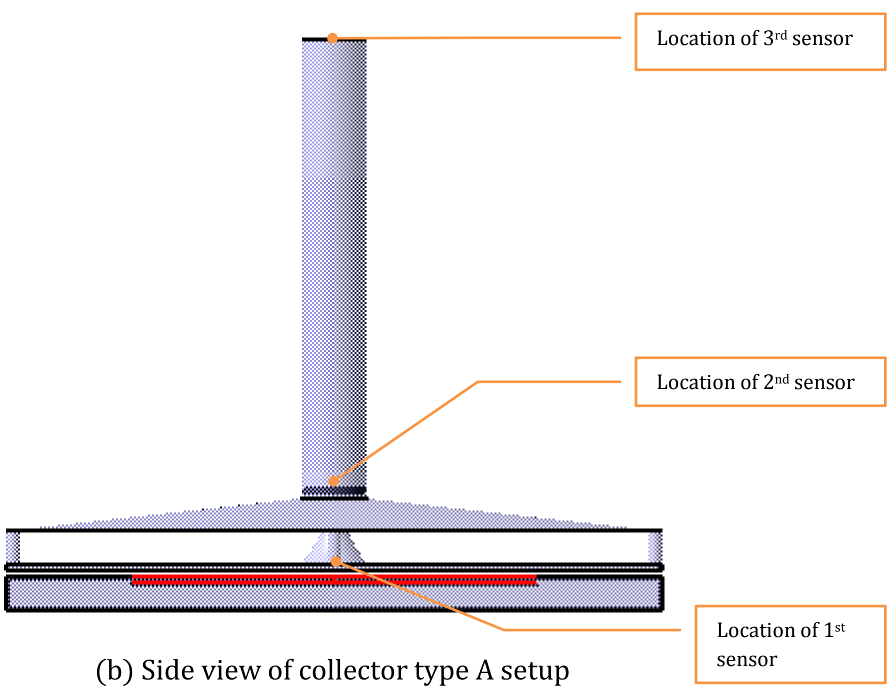

(b) Side view of collector type A setup

Fig. 5.5 Combination of collector type A, tower, and heating system forming a lab-scale solar updraft power generator.

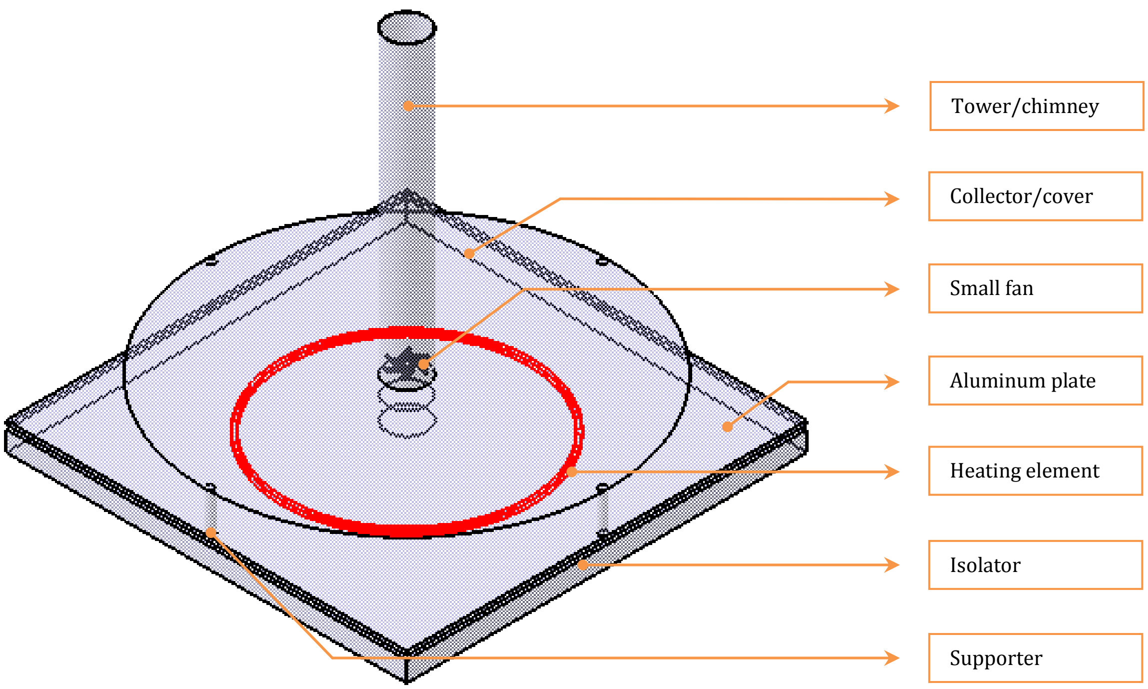

(a) Perspective view of collector type B setup

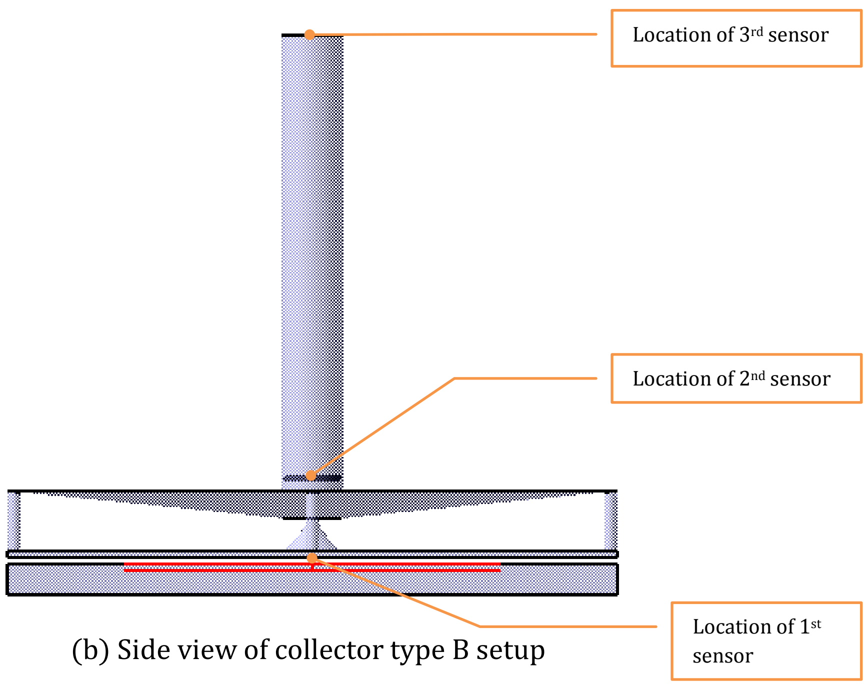

(b) Side view of collector type B setup

Fig. 5.6 Combination of collector type B, tower, and heating system forming a lab-scale solar updraft power generator.

5.4 Measurement Procedures

In this section, measurement procedures are discussed as shown in Table 5.1. At first, select one configuration of collector type, collector height, tower diameter and tower height. For example collector type A with collector height = 50 mm, tower diameter = 100 mm, and tower height = 750 mm. After that, assemble each part to form a solar updraft power generator system excluding the fan. Furthermore, prepare the sensors and installed them according to the setup shown in Fig. 5.5 or Fig. 5.6. The first sensor is a thermocouple placed at the center of aluminum plate to measure the surface temperature of aluminum plate. The second and the third sensors are fixed at the turbine region or right at the bottom and at the top part of the tower respectively. The updraft velocity as well as the updraft temperature was measured by the Kanomax-Anemomaster model 6036. The sensor consist of one probe connect to a build-in analog to digital converter unit and also equipped with LCD displays. Since the probe has its own directivity characteristics, thus the direction mark must be situated perpendicular to the airflow direction. Two independent thermo-anemometers were used to measure the temperature and velocity at the bottom and top part of the tower, so that the gathered data can be obtained simultaneously for one set of experiment.

After that, the thermo-anemometers must be set up according to the following conditions: sampling time for temperature is fixed for 5 [sec] since the temperature does not fluctuate much during the experiment, sampling time for velocity is set for 60 [sec] so that the average value of velocity during one minute is stored. Sampling number is set for 60 with measurement time fixed for 60 [min]. To collect the data, connect the thermo-anemometer sensor with the computer. The reading should give 60 point of temperature and velocity data at the end of measurement. Furthermore, turn on the electric heating element to start the heating process and immediately start measure the temperature and velocity for each sensor by pressing the “store “ button at the thermo-anemometer sensors. The velocity is automatically sampled for every 60 [sec] but the temperature must be sampled manually by pressing the “store” button in the thermo-anemometer sensors. In addition, temperature of aluminum plate is also manually sampled. Conduct the measurement for 60 [min] and after that save data digitally into computer. Repeat the same procedures for another configuration of lab-scale solar updraft power generator.

Table 5.1 Step by step of measurement procedures

Step 1	Select a collector type, tower diameter, and tower height and combines them to construct one configuration of a lab-scale solar updraft power generator.
Step 2	Setup a digital thermocouple at the center of aluminum plate to measure the temperature of plate and install two digital thermo-anemometers at the bottom and top part of the tower.
Step 3	Connect the thermo-anemometers with computer so that temperatures and velocities data can be stored digitally. After that set the sampling time for temperature into 5 [sec] and sampling time for velocity into 60 [sec]. Also, set measurement time for 60 [min] with 1 [min] data sampling.
Step 4	Turn on the electric heating element and immediately start the measurement. Velocity is automatically sampled by the sensor, but temperature must be manually sampled for every 1 [min] by pressing the "store" button in the sensor device. In addition, temperature of plate must also be manually recorded for every 1 [min].
Step 5	After 60 [min] of measurement, turn off the electric heating element. Save temperatures and velocities data from the thermo-anemometer sensors.
Step 6	Repeat the procedures for another configuration of lab-scale solar updraft power generator.

5.5 Measurement Results

The results of experiment are presented in this section. They are divided into two cases according to the type of collector: case 1: results from collector type A, and case 2: results from collector type B. Each experiment results are labeled according to the naming convention presented in Table 5.2. This naming convection is used to tag the data from experiment for both type of collector. The data consists of updraft temperature and updraft velocity at the bottom and top part of the tower. Temperature of aluminum plate is also recorded and it is regarded as the input for simulation works in Chapter 4 where a comparison study was made to validate the mathematical model.

Table 5.2 Naming convention used in the experiment

A-25E-75C-50-250	A	A refers to the type of collector
	25E	25 means height of collector in mm and E refers to Edge (location)
	75C	75 means height of collector in mm and C refers to Center (location)
	50	50 means diameter of tower in mm
	250	250 means height of tower in mm
B-75E-125C-100-1500	B	B refers to the type of collector
	75E	75 means height of collector in mm and E refers to Edge (location)
	125C	125 means height of collector in mm and C refers to Center (location)
	100	100 means diameter of tower in mm
	1500	1500 means height of tower in mm

5.5.1 Result of Collector Type A

Experiment results of collector type A are presented and discussed in this section. The results are divided into 9 measurement groups as seen in Fig. 5.7 to Fig. 5.15. Series of graphical results in Fig. 5.7 represents experiment results from the 1st measurement group of collector type A. Experiment was conducted for a fixed collector height of 25 mm on the edge and 75 mm on the center where the tower diameter is also fixed for 50 mm and the tower height is varied for 250 mm, 500 mm, 750 mm, and 1500 mm.

From this figure it is observed that the updraft velocity at the bottom of the tower hardly reach 1 m/s. All of the exit updraft velocity at the bottom of the tower – except for tower height 500 mm – shows a reducing trend with increasing of temperature while its updraft velocity at the bottom gives almost a constant increasing trend. It means that there is no more updraft flow reaches to the top of the tower. This condition might be caused by the friction between the airflow and the tower walls since the diameter of the tower is quite small, and it also might be due to the reverse flow at the top of the tower, in other words the cold air associated with high density fall inside the tower and the updraft flow is not strong enough to compensate this condition. Furthermore, the updraft temperature profile for all cases – except for tower height 250 mm – in Fig, 5.7 shows an increasing trend until one point it decrease with time. This condition is due to the heat source is turned off because the operating temperature for thermo-anemometers sensor is limited to 70 [^{0}C], thus before the airflow temperature reach this value the source of heat is cut off.

Fig. 5.8 shows the experiment results for the 2nd measurement group of collector type A. In this figure, the updraft velocity at the bottom and top of the tower shows a consistent trend with the updraft temperature. There is no decreasing trend is observed for updraft velocity in this group. Fig. 5.9 presents the experiment results for the 3rd measurement group of collector type A. From this figure, both the updraft velocity and temperature shows increasing trend in quadratic profile. The remaining measurement groups are showing the same repeating pattern as shown in the 1st to 3rd measurement groups, however they produces higher updraft velocity both at the bottom and top of the tower. It looks like that the velocity result from measurement group with 100 mm of tower diameter exhibits higher updraft velocity compare to the other tower diameter groups.

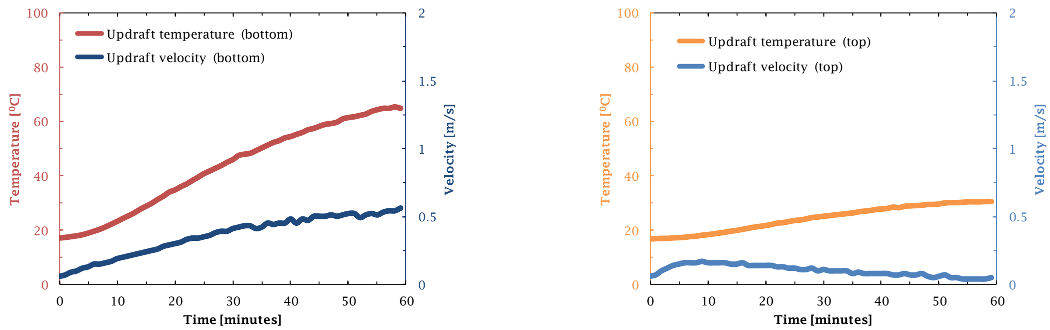

A-25E75C-50-250

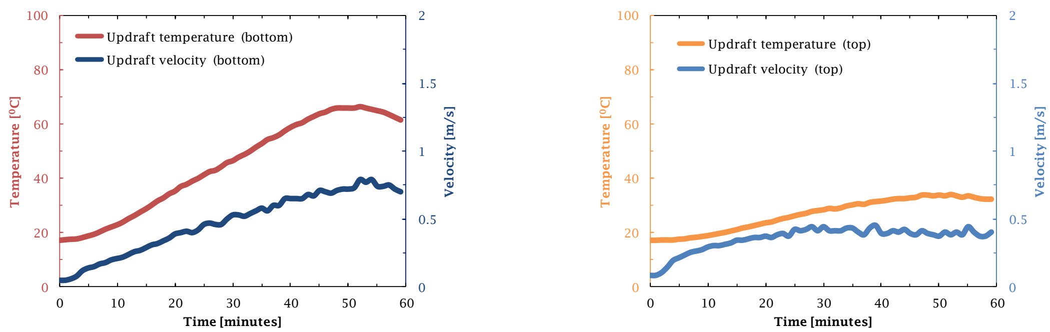

A-25E75C-50-500

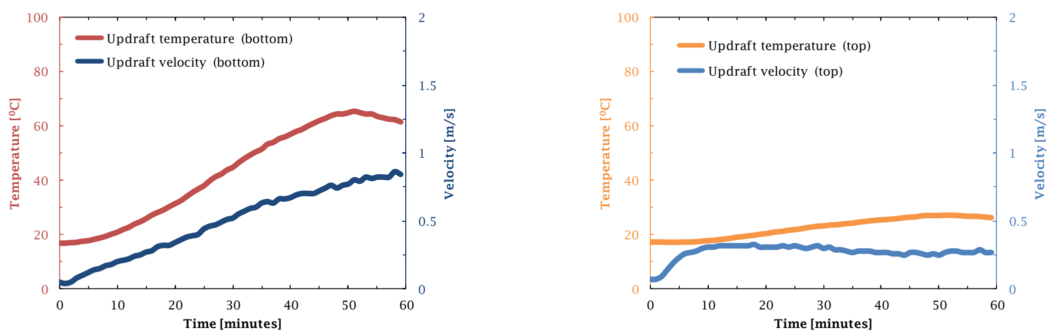

A-25E75C-50-750

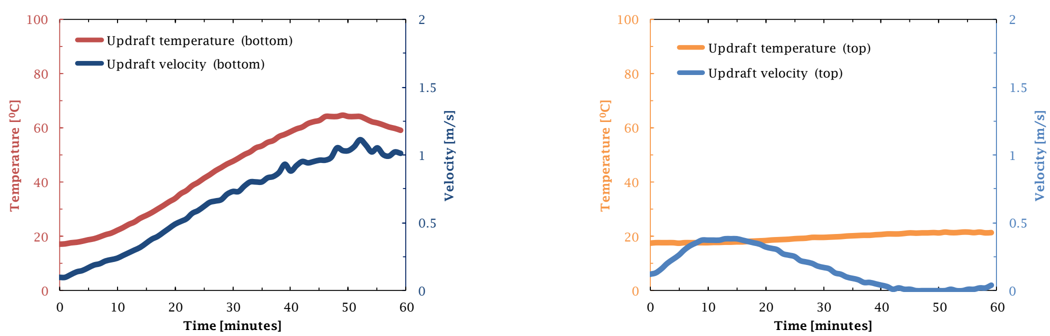

A-25E75C-50-1500

Fig. 5.7 Experimental results for the 1st measurement group of collector type A.

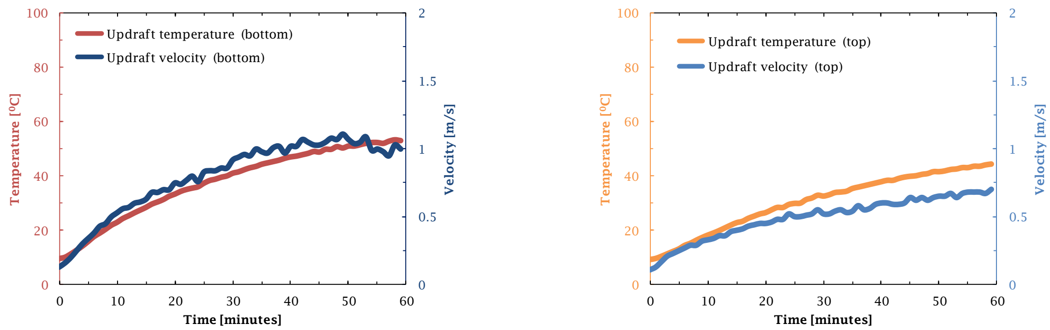

A-25E75C-100-250

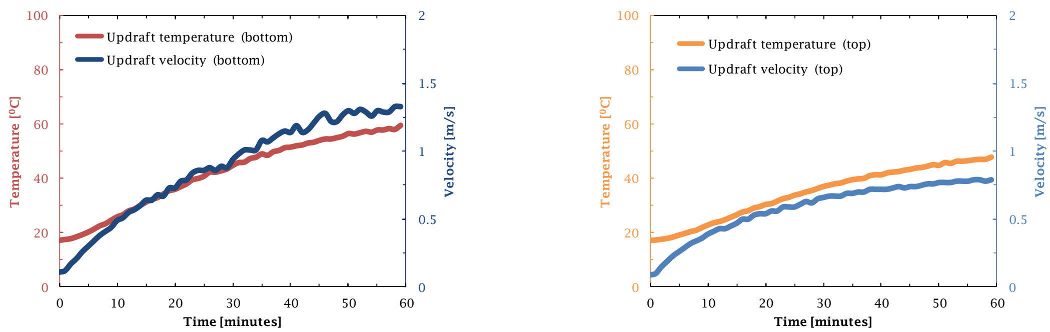

A-25E75C-100-500

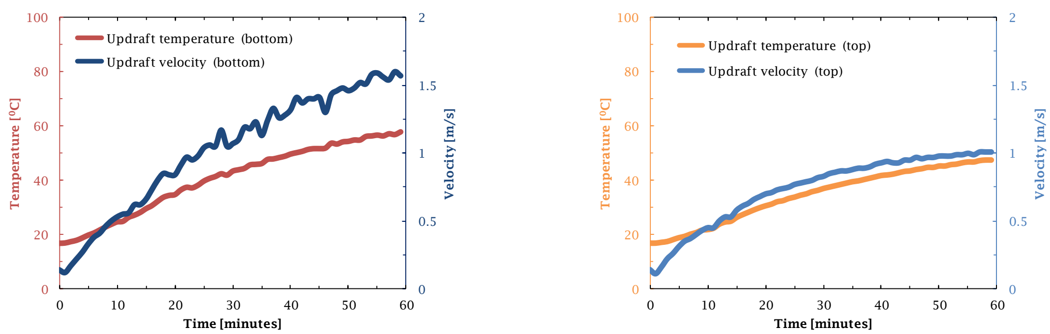

A-25E75C-100-750

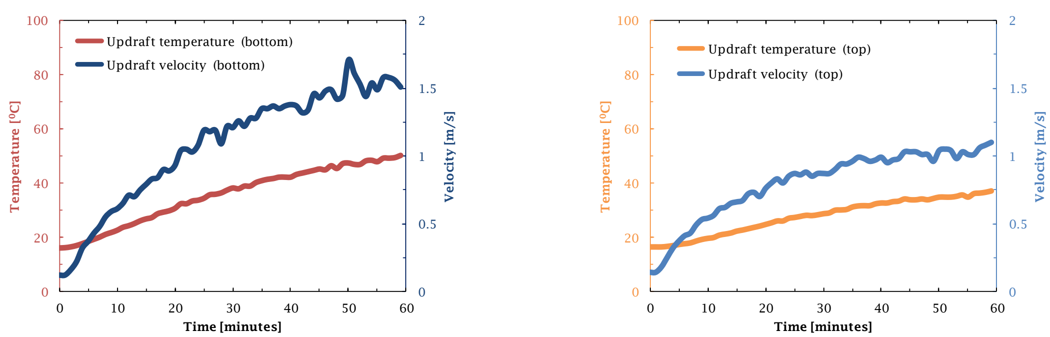

A-25E75C-100-1500

Fig. 5.8 Experimental results for the 2nd measurement group of collector type A.

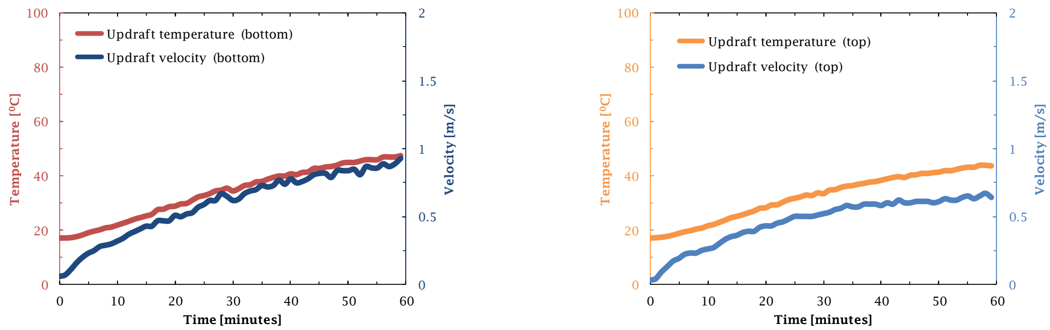

A-25E75C-150-250

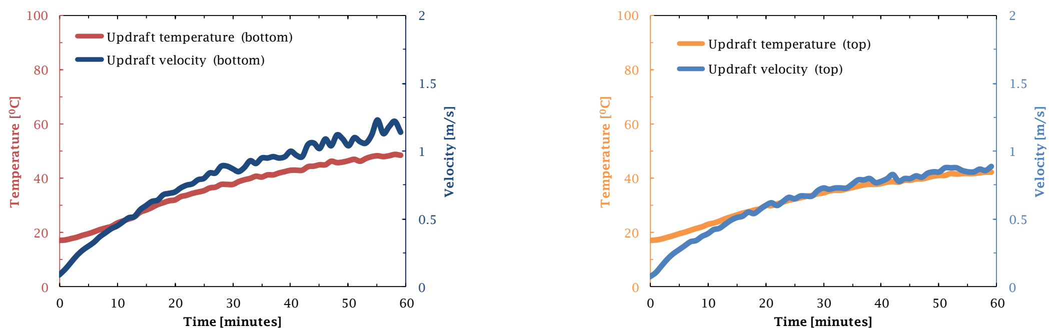

A-25E75C-150-500

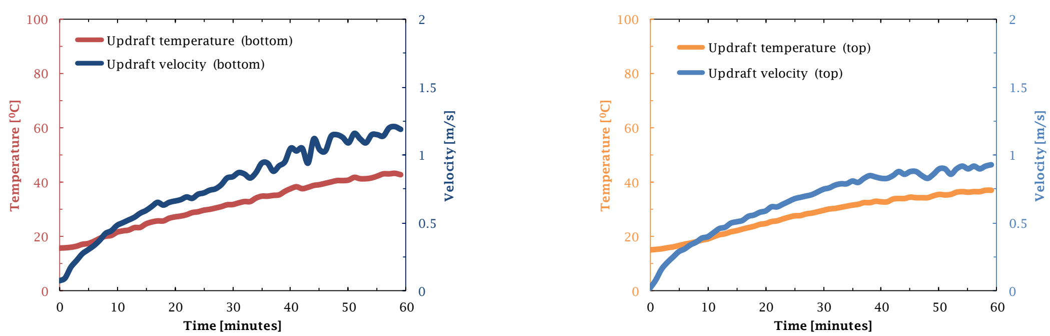

A-25E75C-150-750

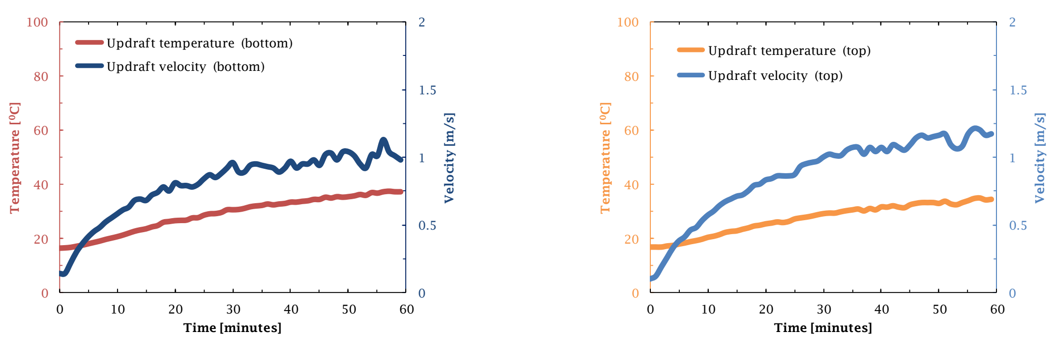

A-25E75C-150-1500

Fig. 5.9 Experimental results for the 3rd measurement group of collector type A.

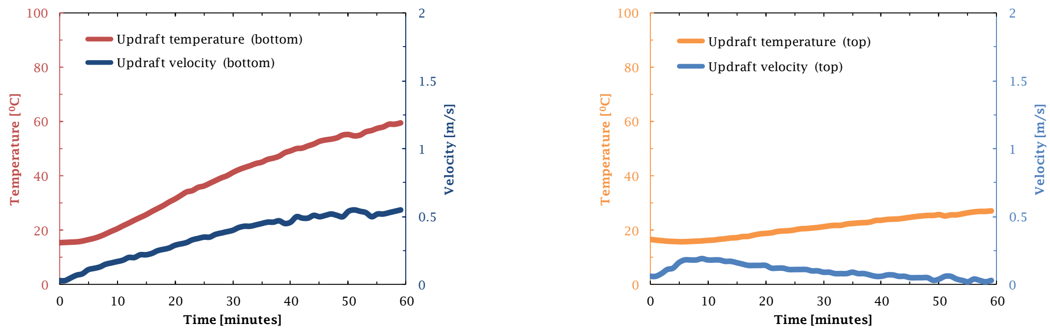

A-50E100C-50-250

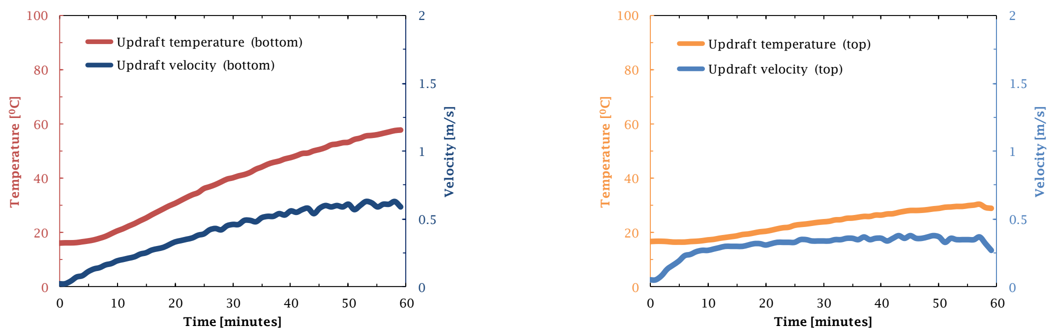

A-50E100C-50-500

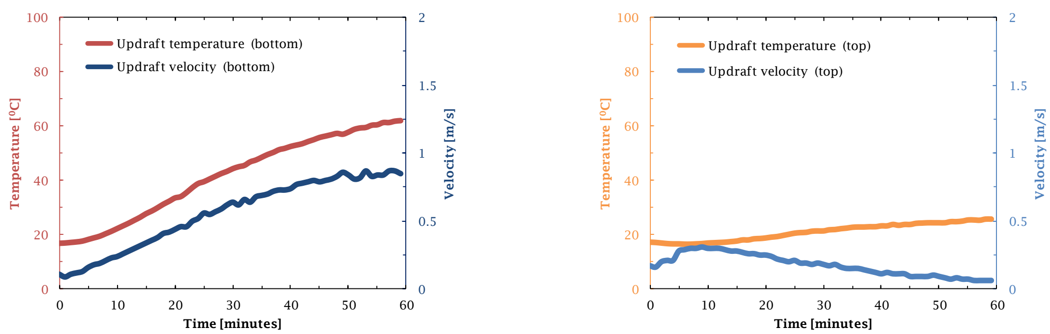

A-50E100C-50-750

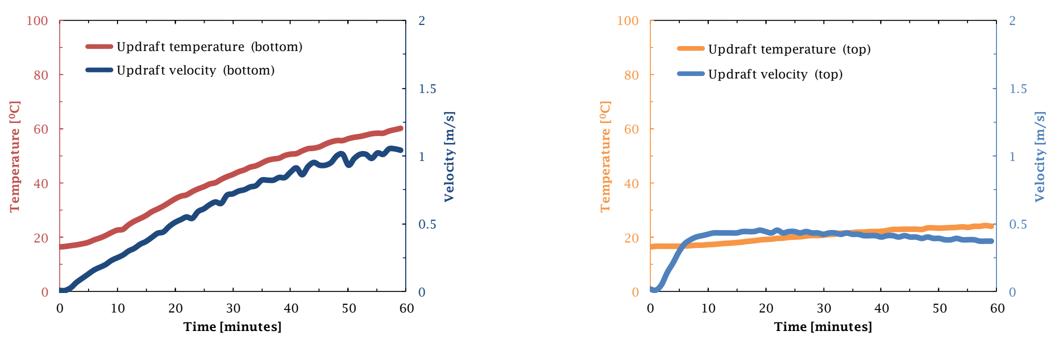

A-50E100C-50-1500

Fig. 5.10 Experimental results for the 4th measurement group of collector type A.

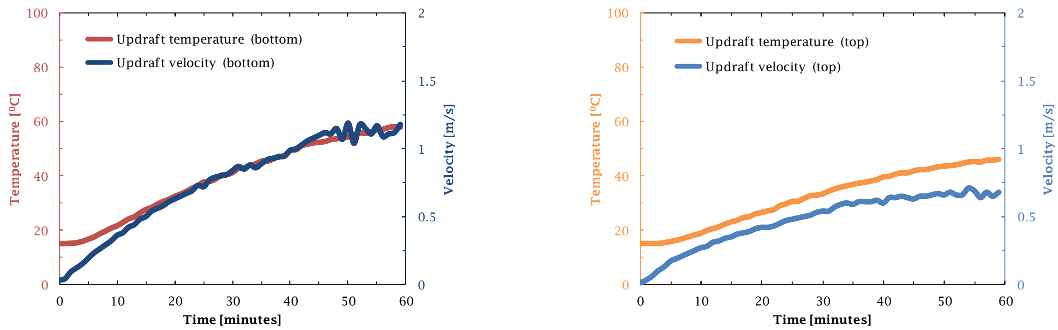

A-50E100C-100-250

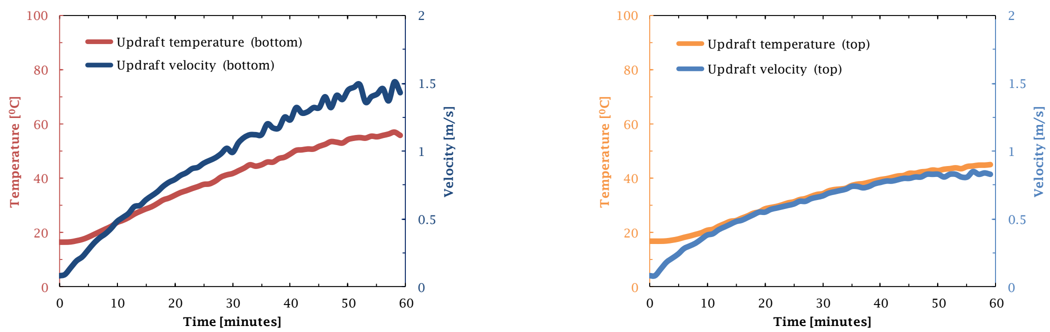

A-50E100C-100-500

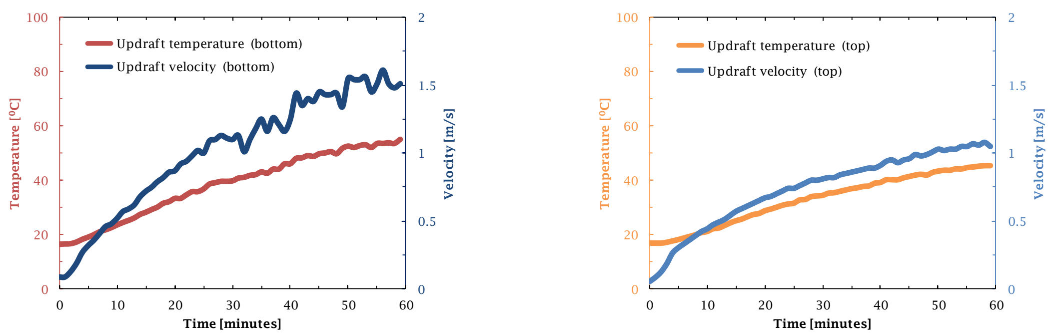

A-50E100C-100-750

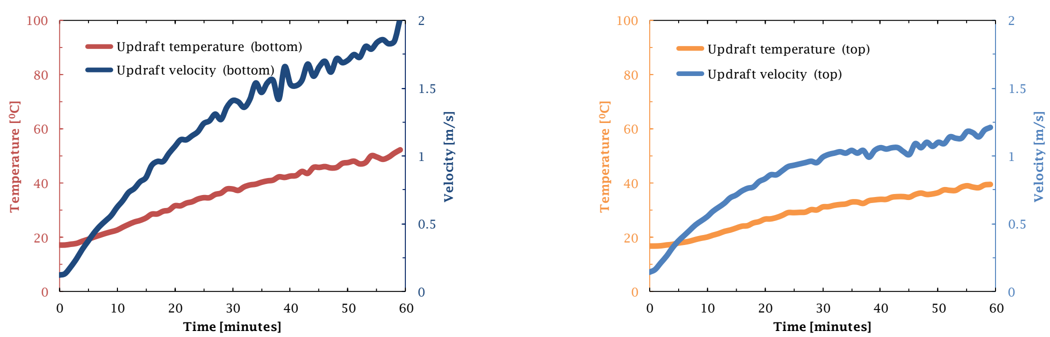

A-50E100C-100-1500

Fig. 5.11 Experimental results for the 5th measurement group of collector type A.

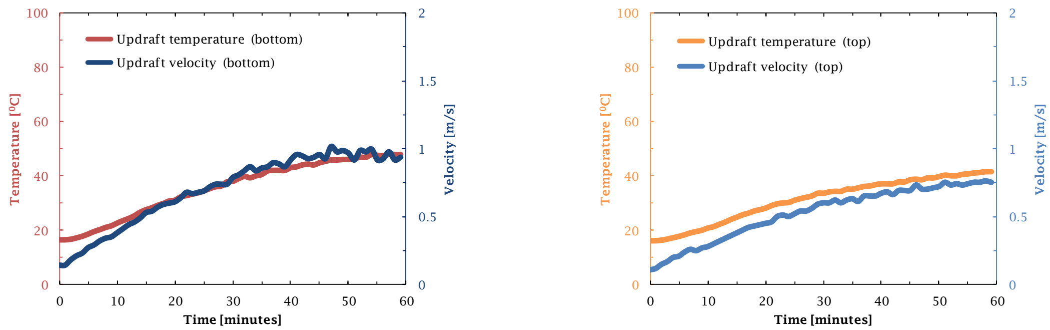

A-50E100C-150-250

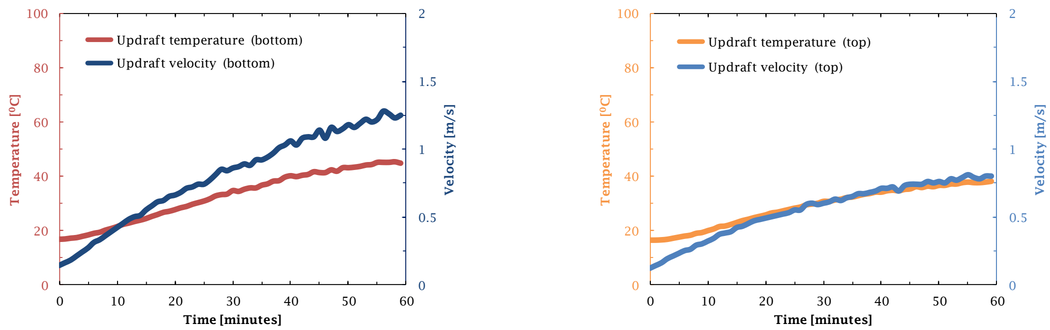

A-50E100C-150-500

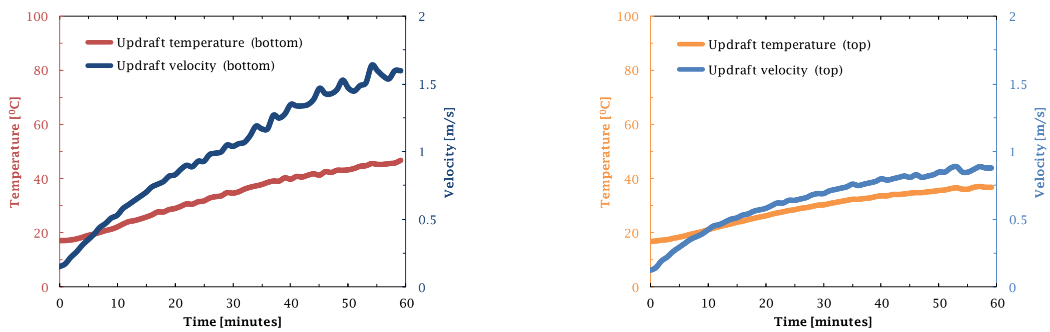

A-50E100C-150-750

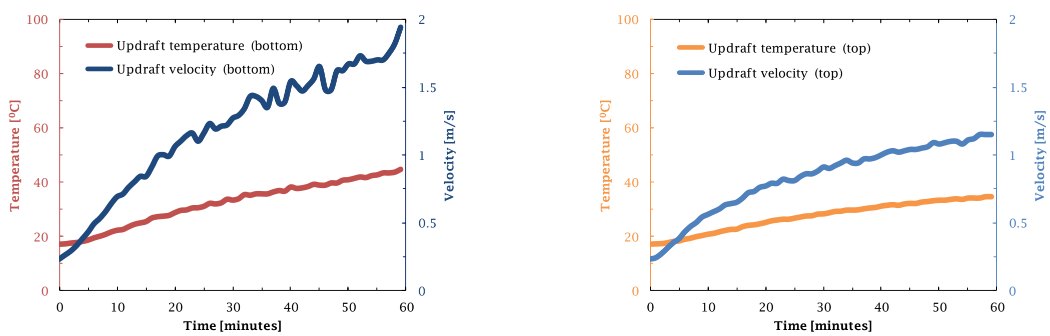

A-50E100C-150-1500

Fig. 5.12 Experimental results for the 6th measurement group of collector type A.

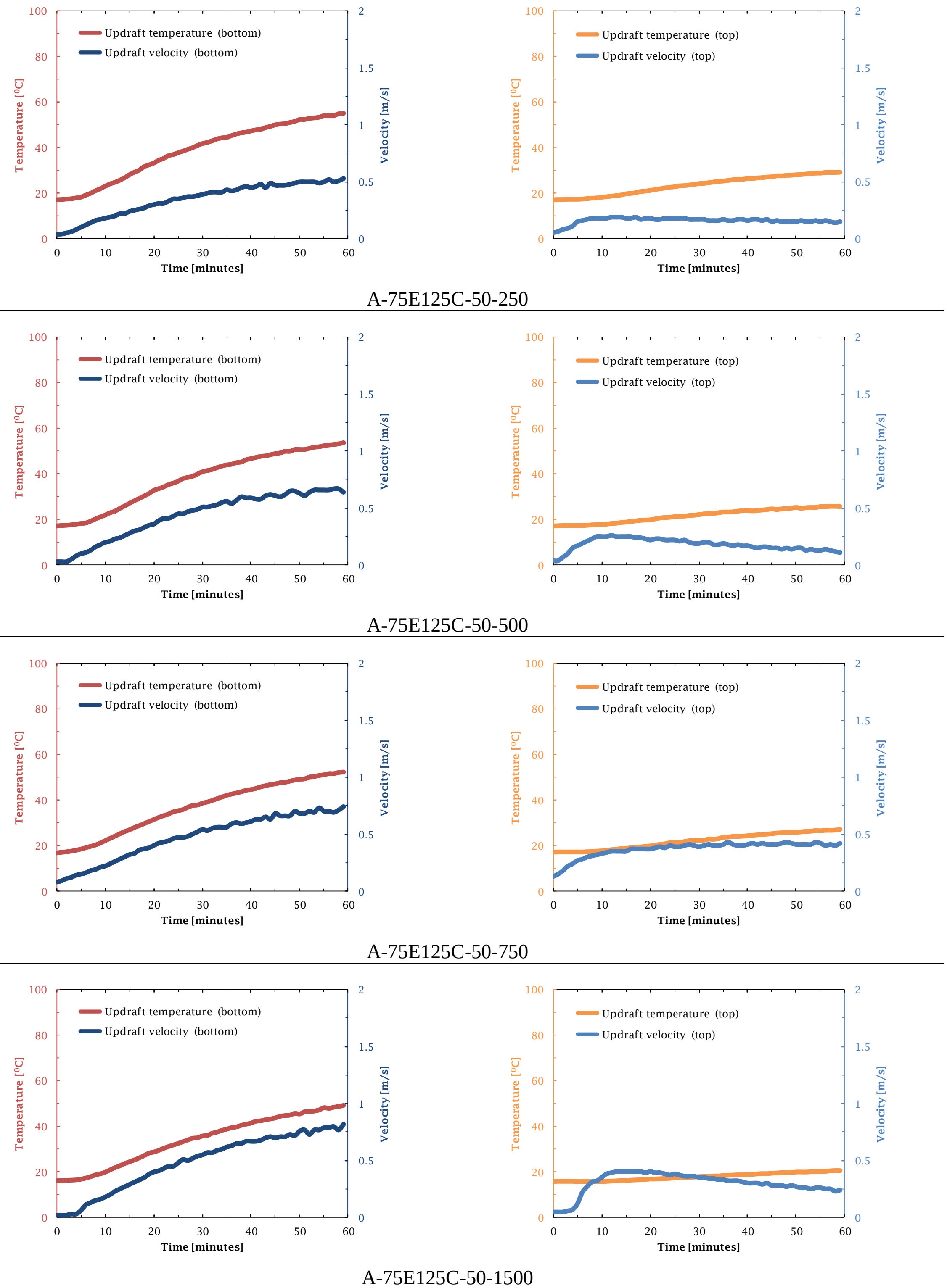

Fig. 5.13 Experimental results for the 7th measurement group of collector type A.

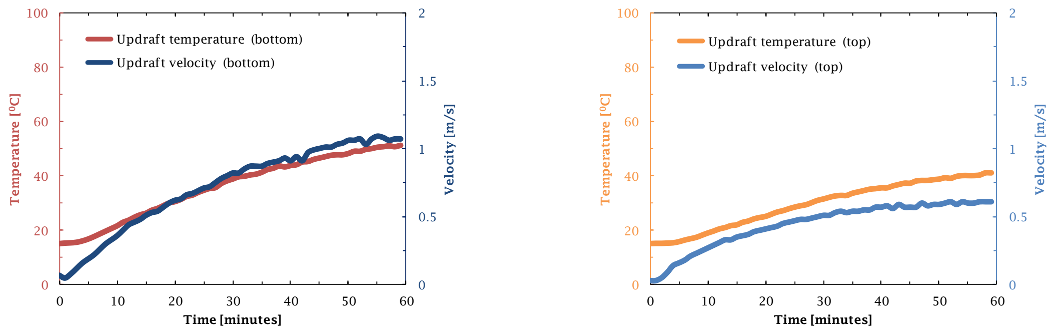

A-75E125C-100-250

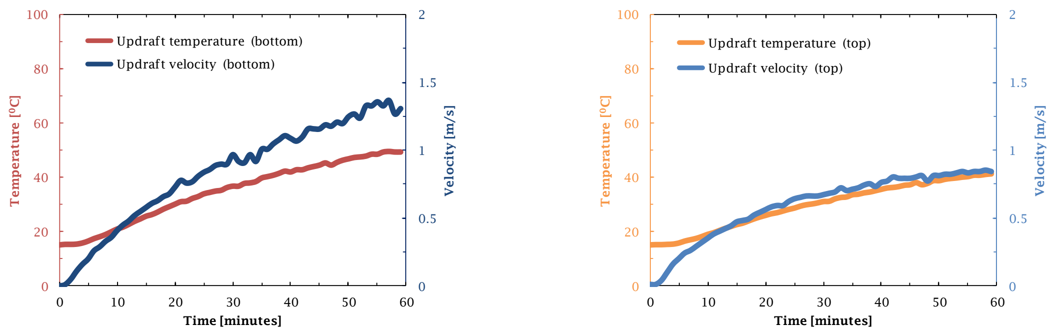

A-75E125C-100-500

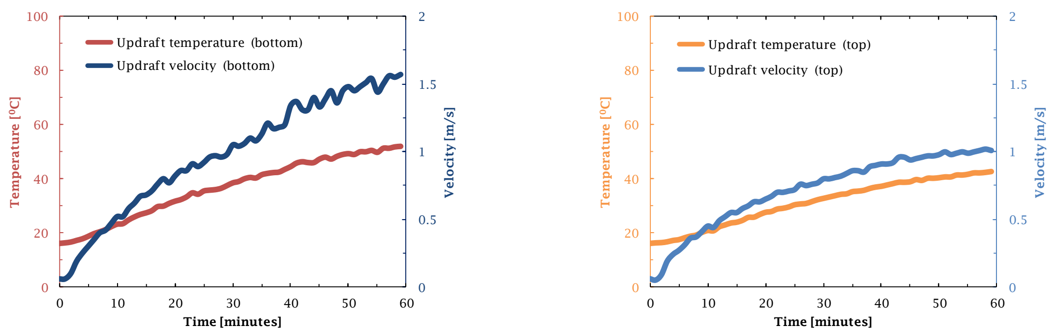

A-75E125C-100-750

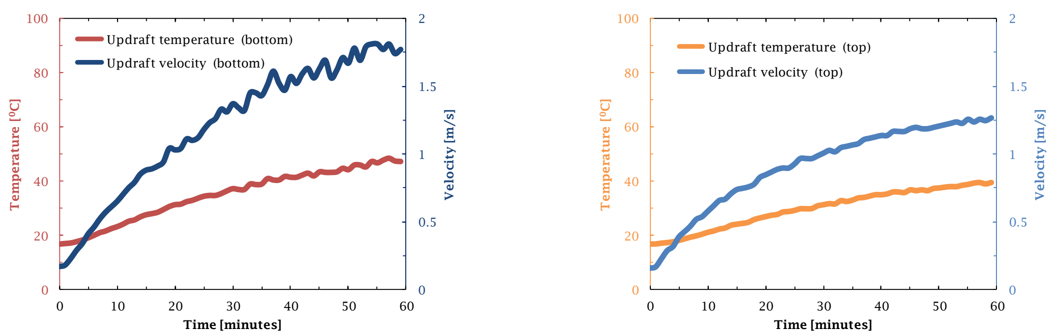

A-75E125C-100-1500

Fig. 5.14 Experimental results for the 8th measurement group of collector type A.

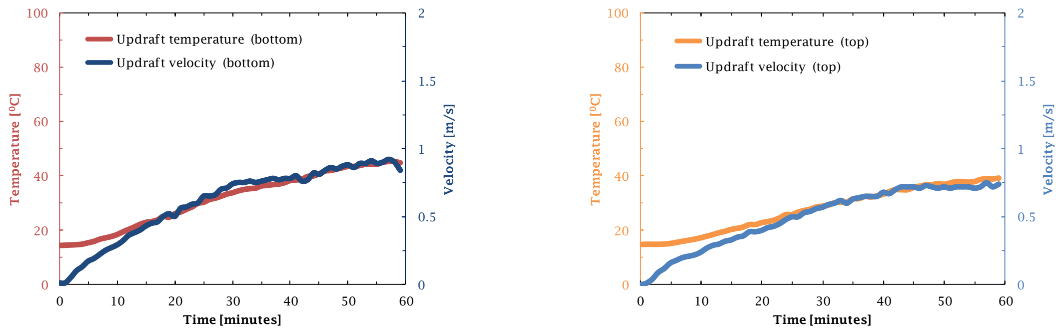

A-75E125C-150-250

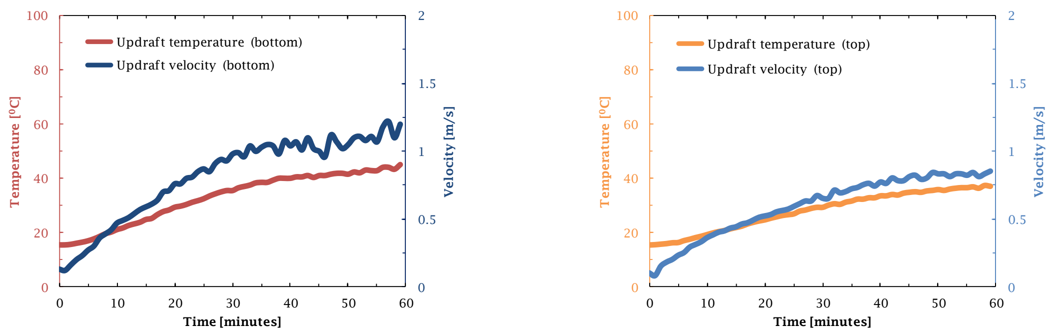

A-75E125C-150-500

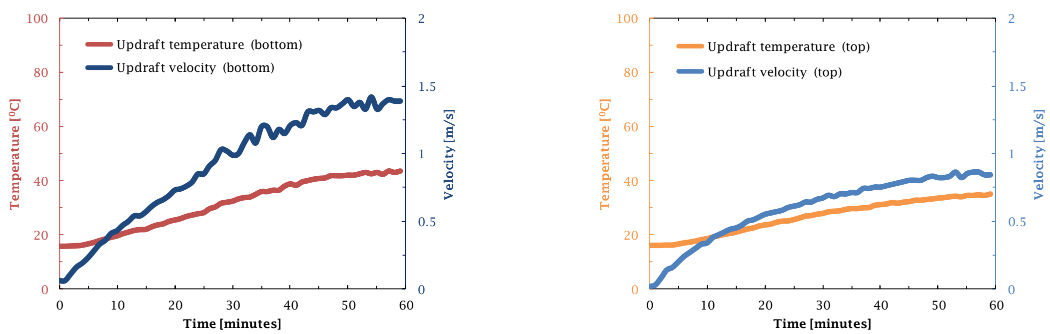

A-75E125C-150-750

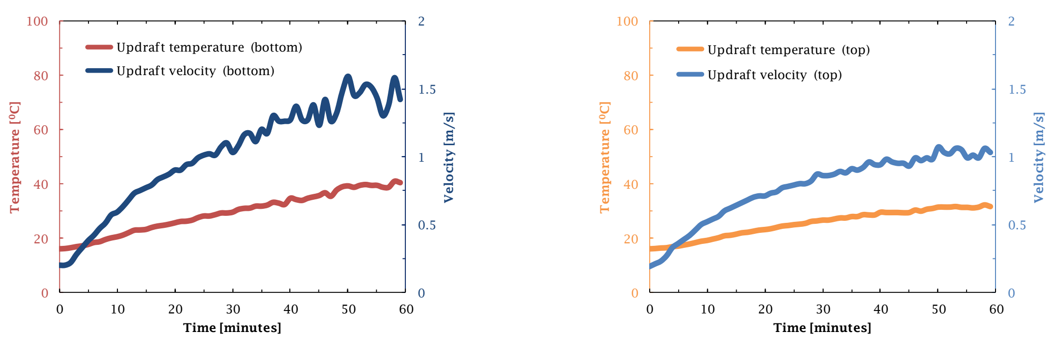

A-75E125C-150-1500

Fig. 5.15 Experimental results for the 9th measurement group of collector type A.

5.5.2 Result of Collector Type B

In this section, experiment results of collector type B are presented and discussed. Similar with previous discussion (collector type A), the results are also divided into 9 measurement groups as presented in Fig. 5.16 to Fig. 5.24. Results in Fig. 5.16 show the updraft temperature and velocity for the 1st measurement group of collector type B. Experiment was conducted with collector height of 65 mm on the edge and 15 mm on the center, the tower diameter is fixed for 50 mm and the tower height is varied for 250 mm, 500 mm, 750 mm, and 1500 mm.

From Fig. 5.16, updraft velocity at the bottom of tower shows increasing trend. However, all the updraft velocity at the top of tower exhibits a decreasing trend through time. The reason is similar with the discussion in the result of collector type A. In addition, this type of collector would also produce significant heat losses at the edge of collector. These heat losses will entrain the collector airflow and thus reducing the amount of updraft flow to the top of tower. A contrast situation is observed when the updraft velocity from the 1st measurement group is compared for both collector types.

Fig. 5.17 shows experiment results for the 2nd measurement group. Updraft velocity from this group shows an increasing trend in quadratic profile. However, this updraft velocity fluctuate considerably trough time compare to the result in collector type A. This situation is recognized due to the characteristic of collector type B where it has large airflow opening distance. Consequently the airflow is prone to losses its energy to the surrounding airflow. Moreover, a high temperature difference condition between the airflow at edge of collector and the surrounding ambient air results in convection current from collector to the ambient air. This convection current – although its effect can be considered small to the whole updraft process – will entrain the airflow inside the collector and makes the reading of velocity fluctuates as shown in Fig. 5.17, Fig. 5.18, and Fig. 5.20.

Similar trend as in the 2nd measurement group is also shown by the 3rd measurement group but it seems the updraft velocity is lower than the 2nd group; indicating that the 100 mm of tower diameter group produce a higher velocity compare to the other two tower diameter groups. The remaining groups seem to follow the pattern of the 1st, 2nd, and 3rd groups, but the updraft velocity is different for each measurement groups.

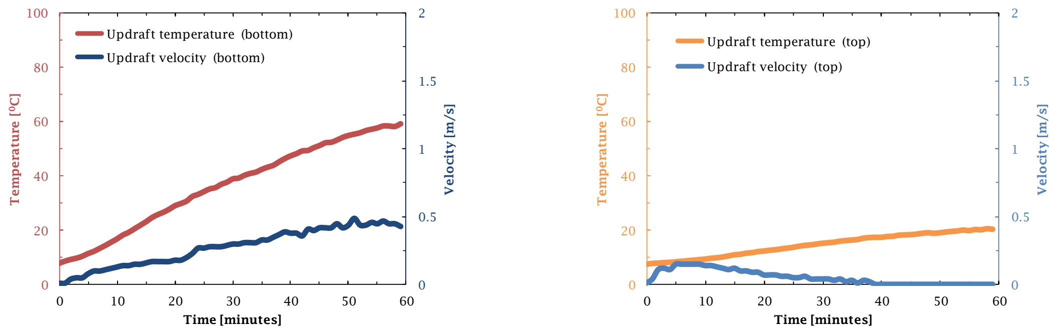

B-65E15C-50-250

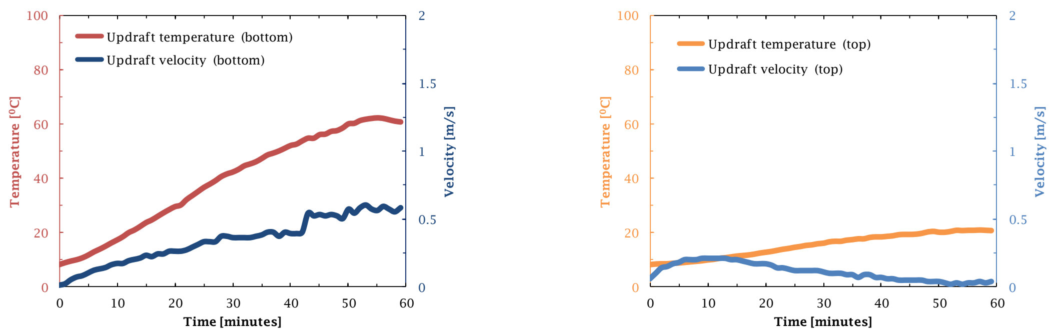

B-65E15C-50-500

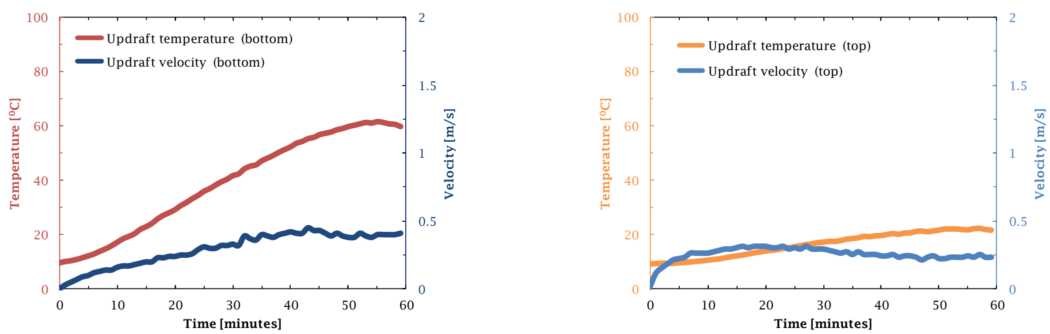

B-65E15C-50-750

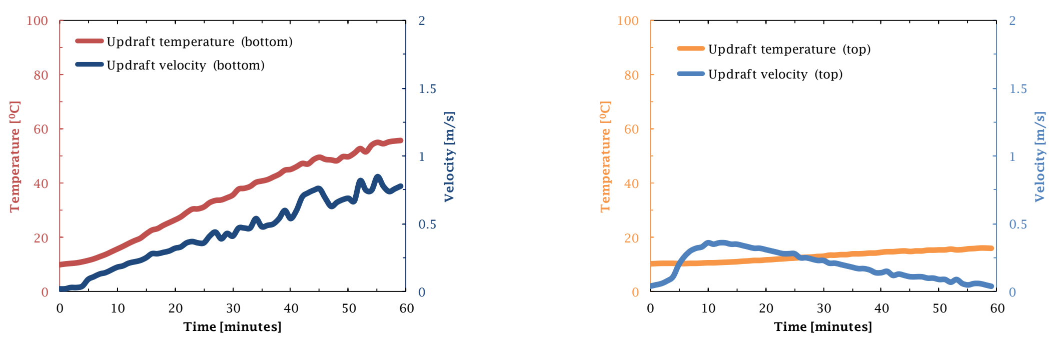

B-65E15C-50-1500

Fig. 5.16 Experimental results for the 1st measurement group of collector type B.

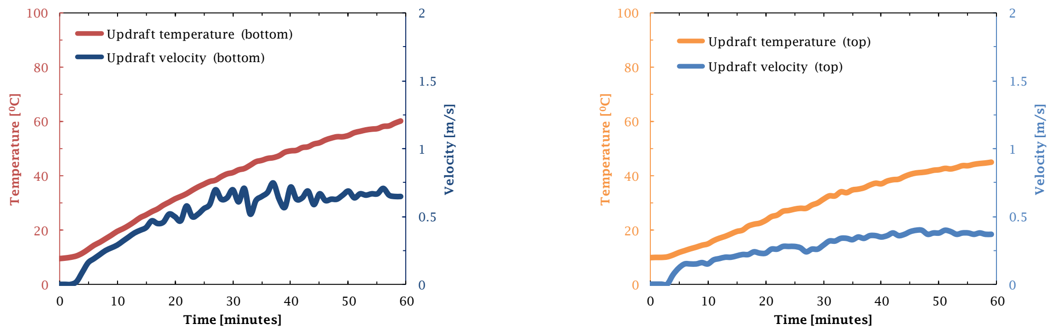

B-65E15C-100-250

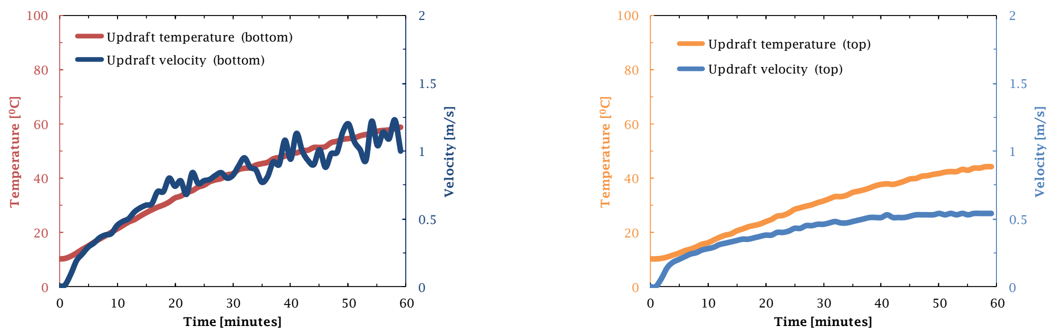

B-65E15C-100-500

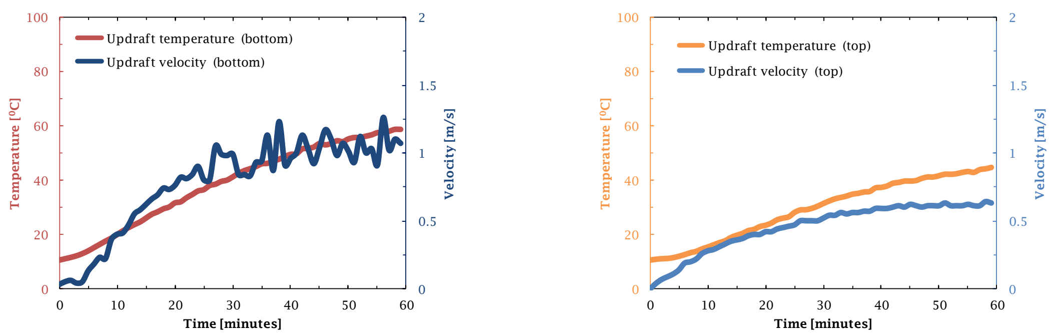

B-65E15C-100-750

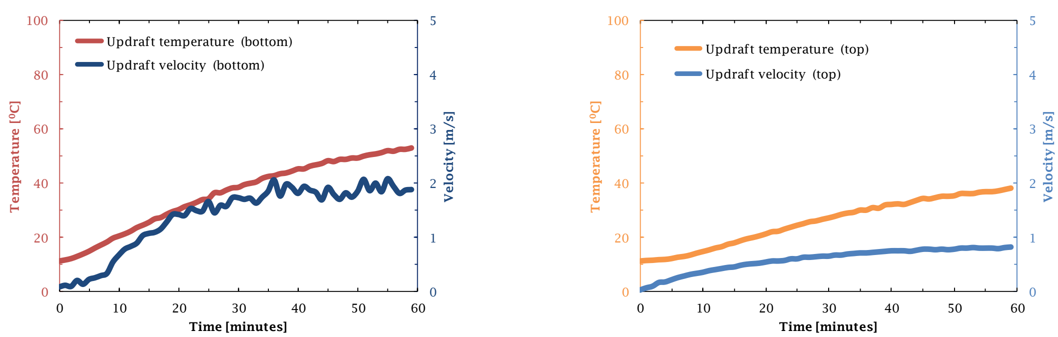

B-65E15C-100-1500

Fig. 5.17 Experimental results for the 2nd measurement group of collector type B.

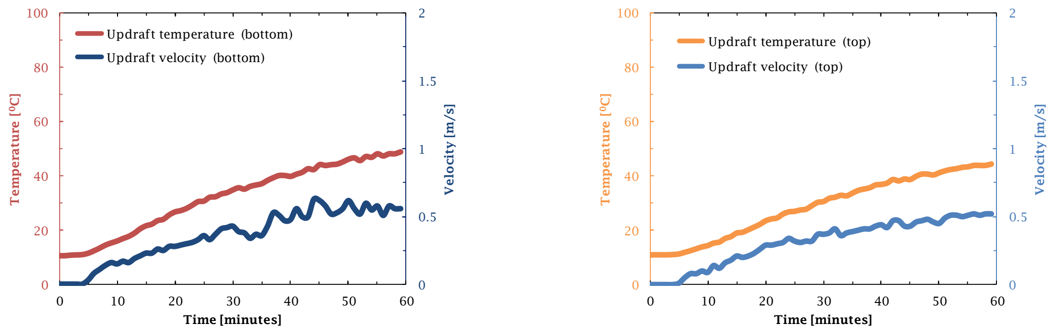

B-65E15C-150-250

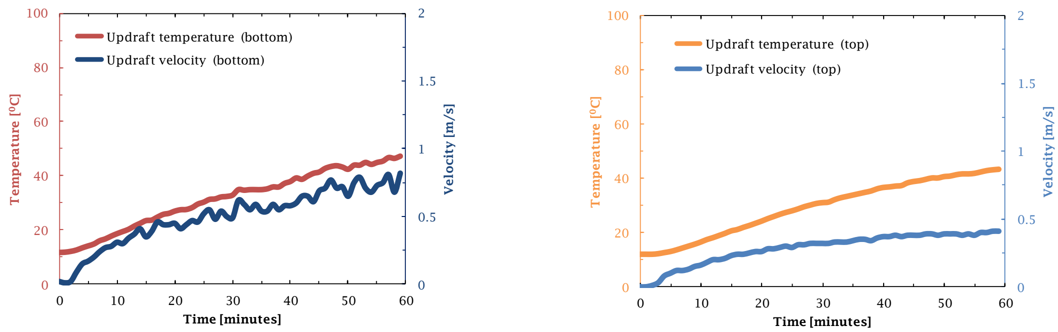

B-65E15C-150-500

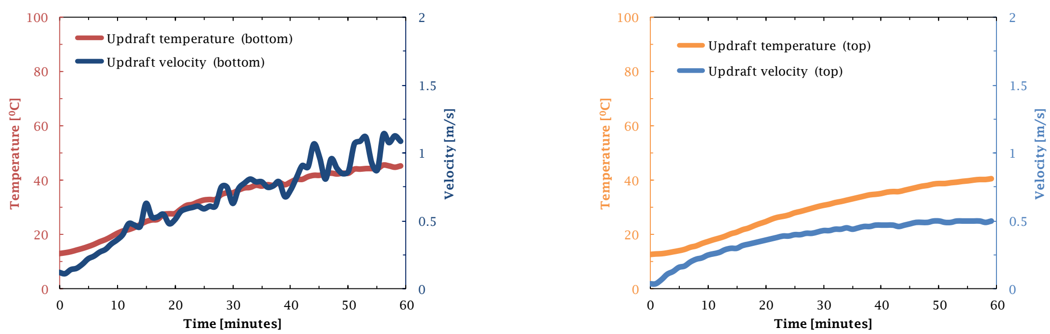

B-65E15C-150-750

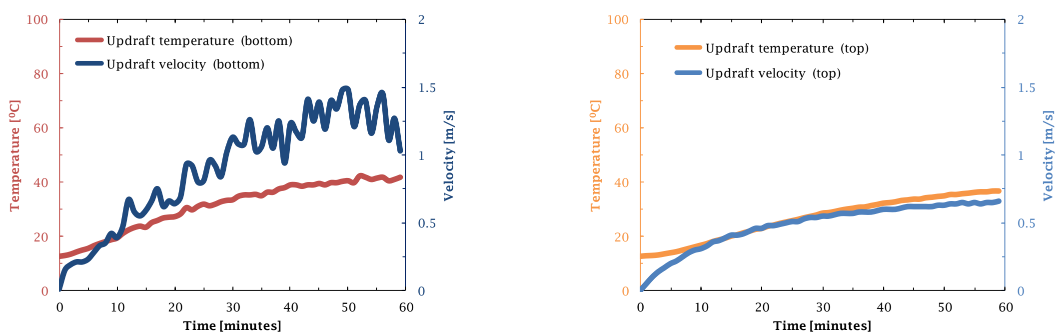

B-65E15C-150-1500

Fig. 5.18 Experimental results for the 3rd measurement group of collector type B.

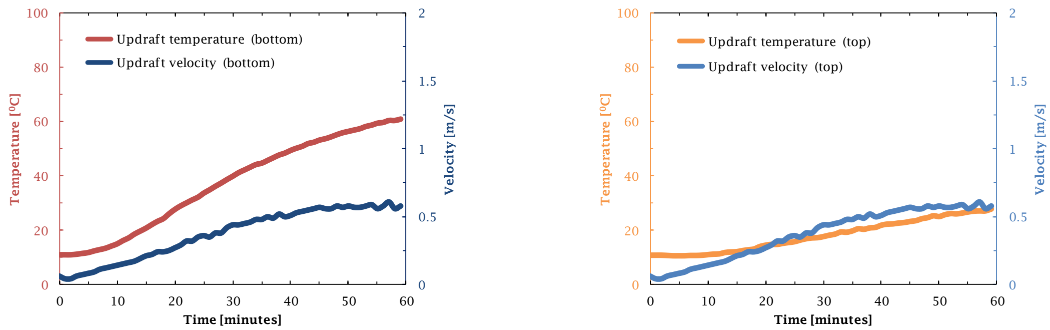

B-75E25C-50-250

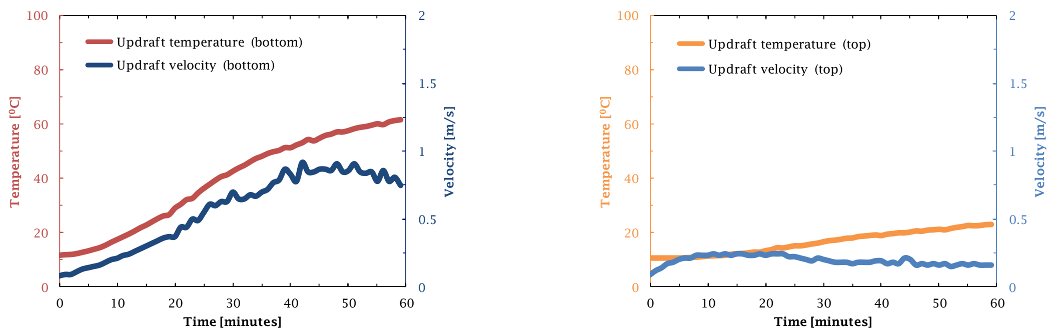

B-75E25C-50-500

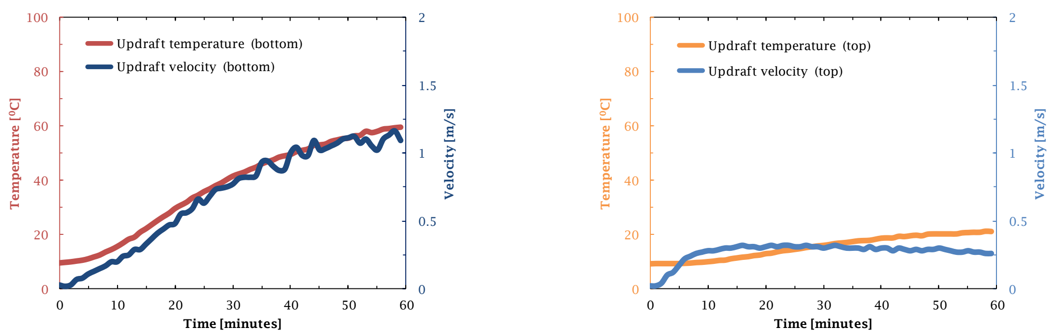

B-75E25C-50-750

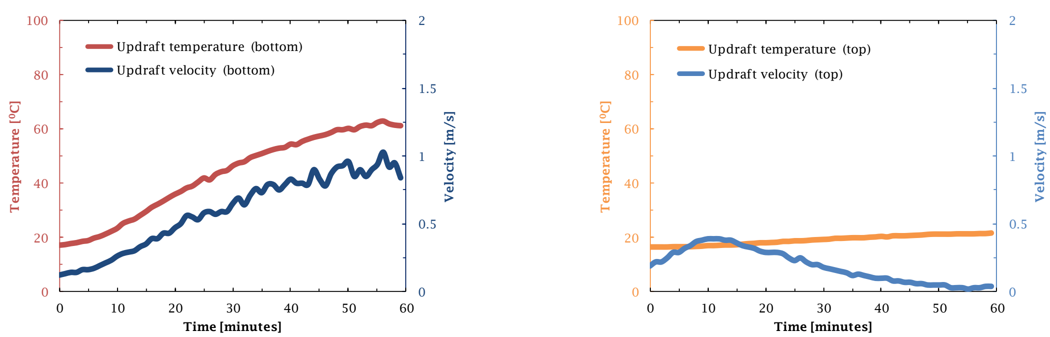

B-75E25C-50-1500

Fig. 5.19 Experimental results for the 4th measurement group of collector type B.

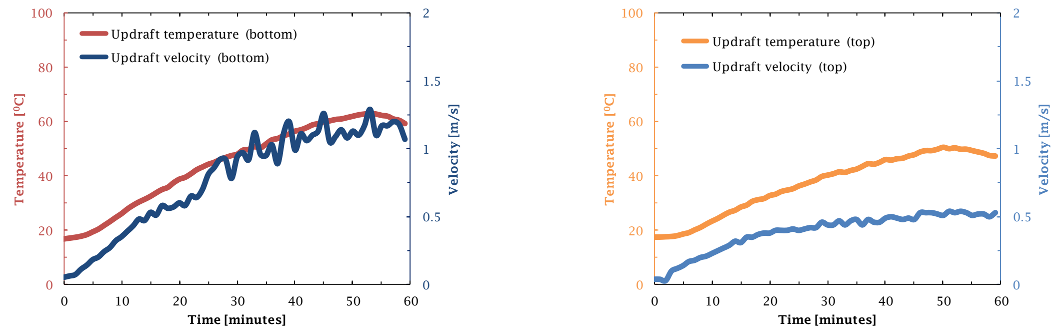

B-75E25C-100-250

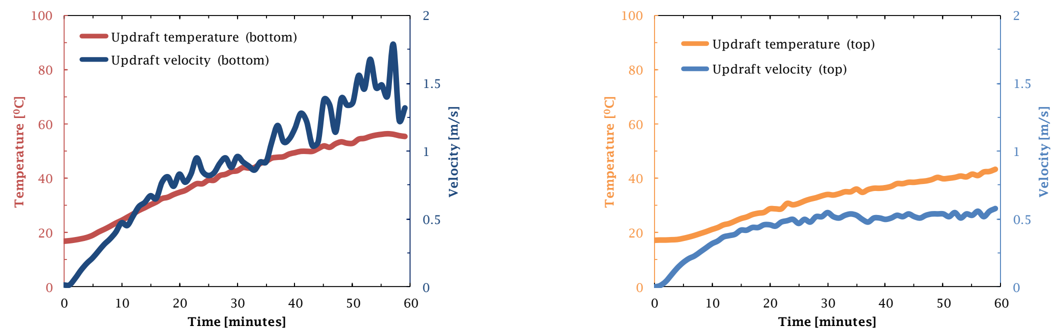

B-75E25C-100-500

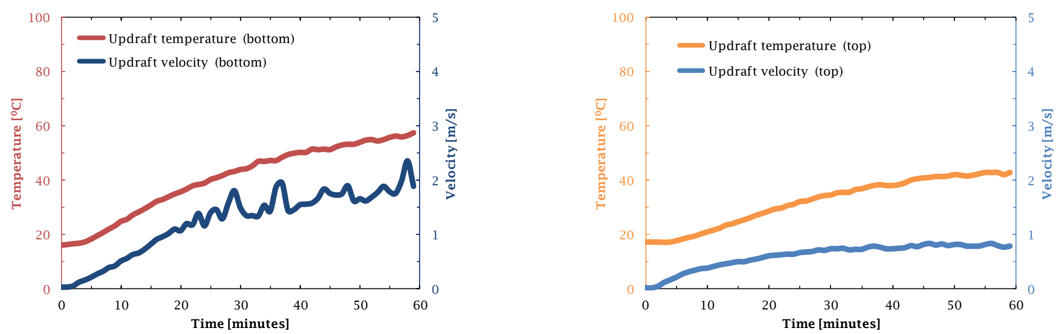

B-75E25C-100-750

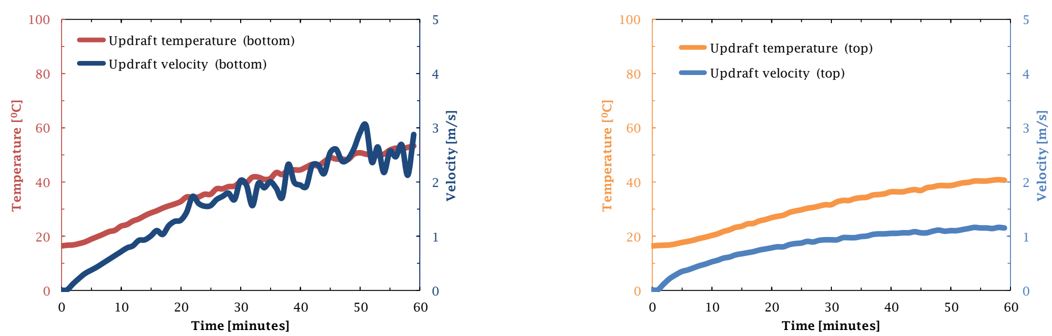

B-75E25C-100-1500

Fig. 5.20 Experimental results for the 5th measurement group of collector type B.

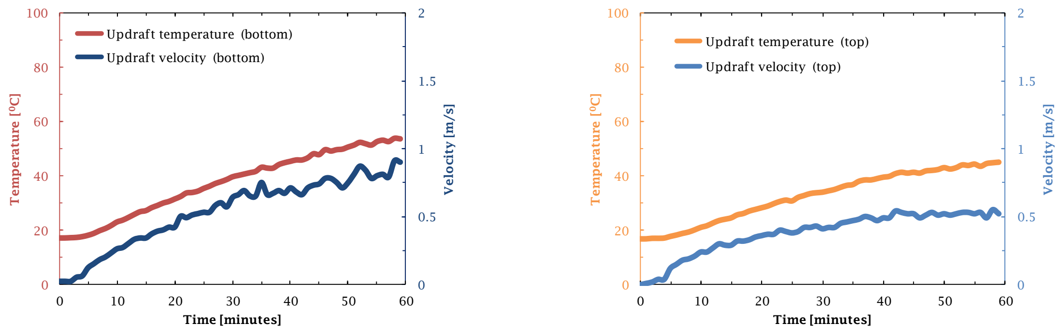

B-75E25C-150-250

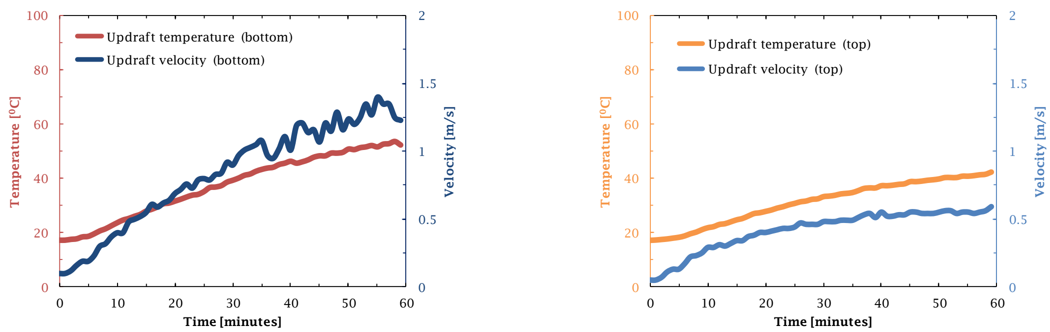

B-75E25C-150-500

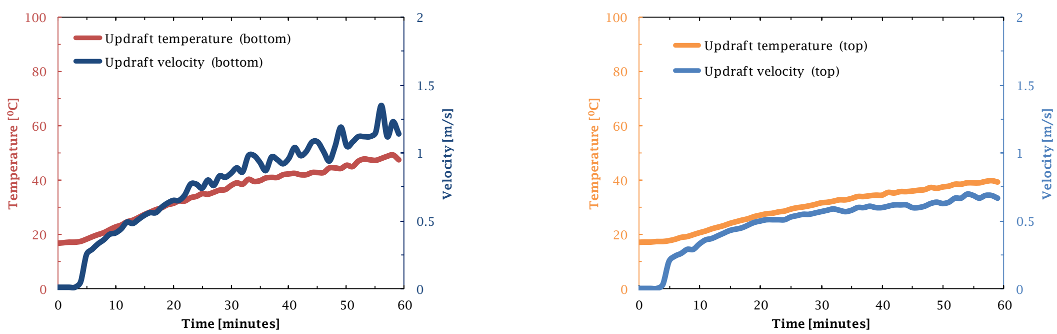

B-75E25C-150-750

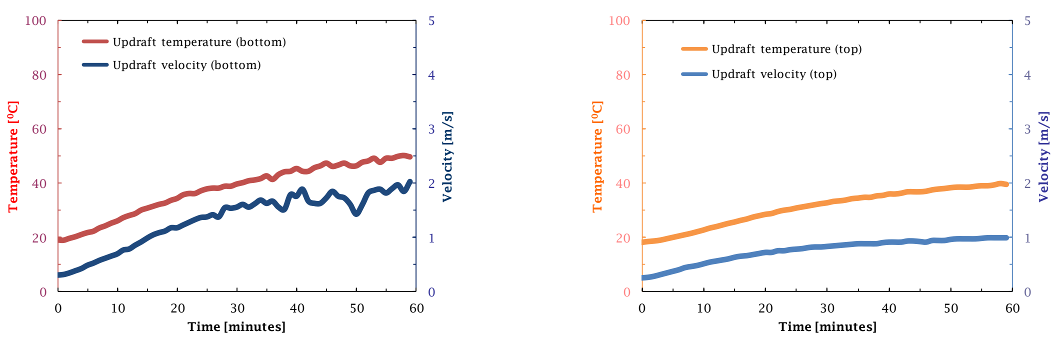

B-75E25C-150-1500

Fig. 5.21 Experimental results for the 6th measurement group of collector type B.

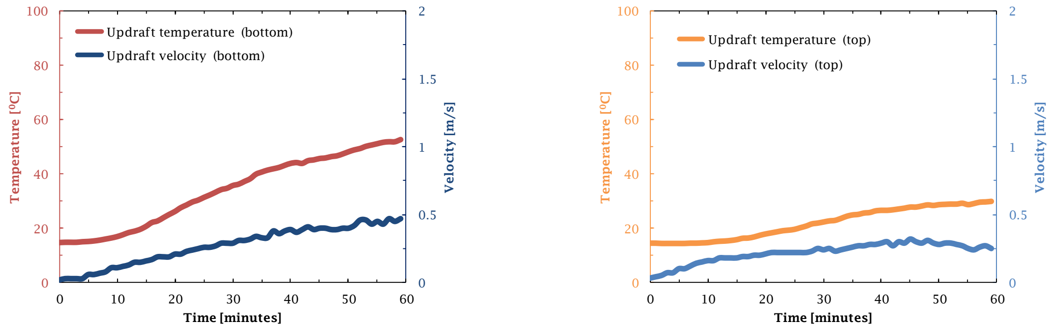

B-100E50C-50-250

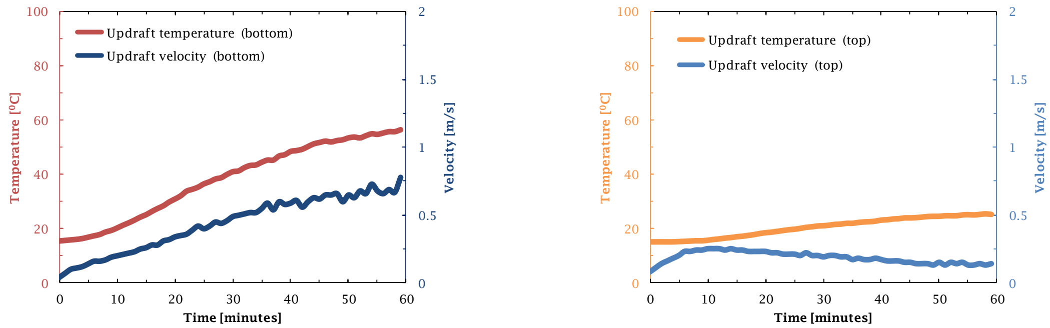

B-100E50C-50-500

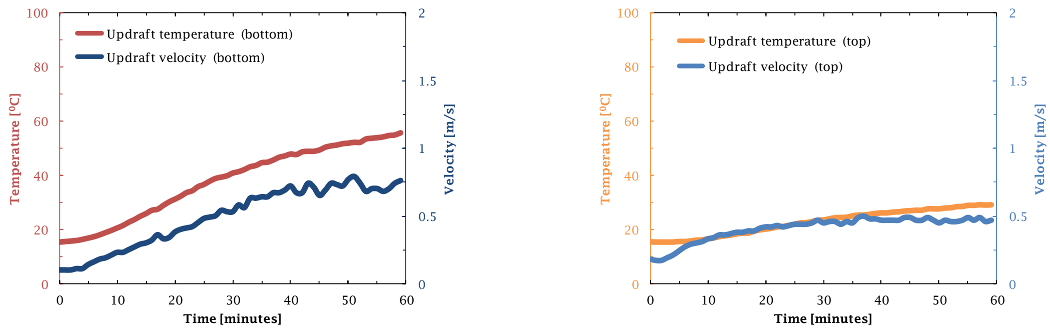

B-100E50C-50-750

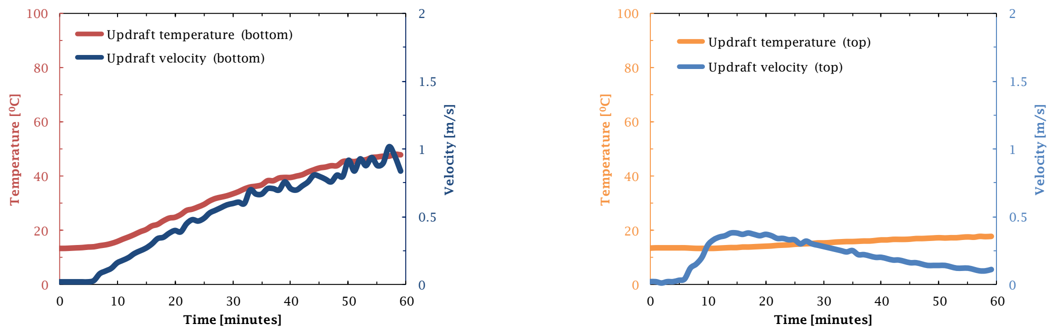

B-100E50C-50-1500

Fig. 5.22 Experimental results for the 7th measurement group of collector type B.

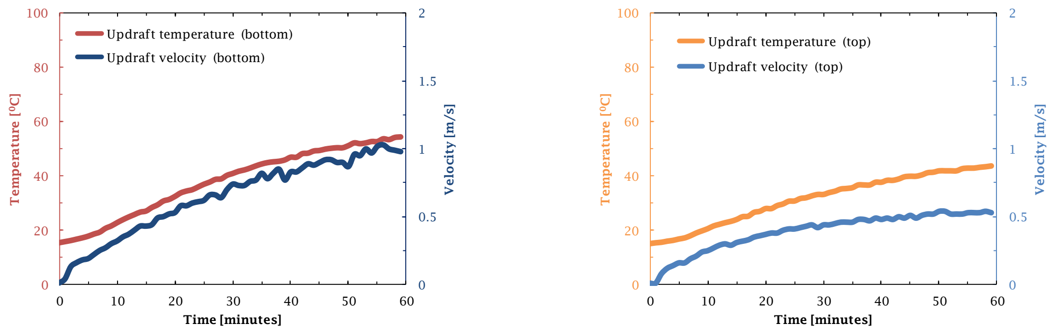

B-100E50C-100-250

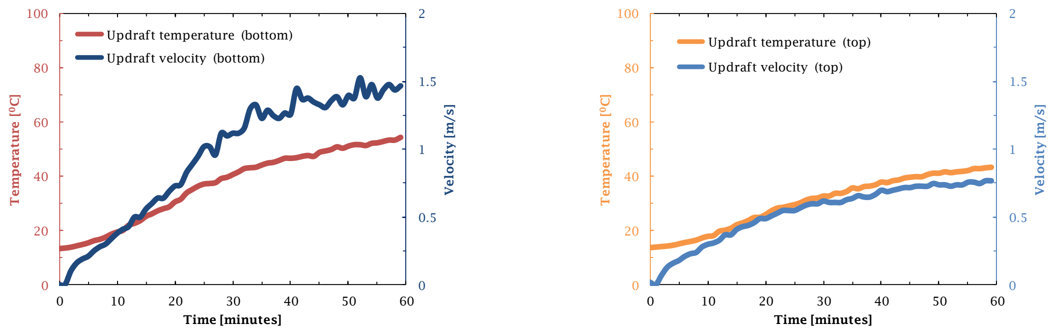

B-100E50C-100-500

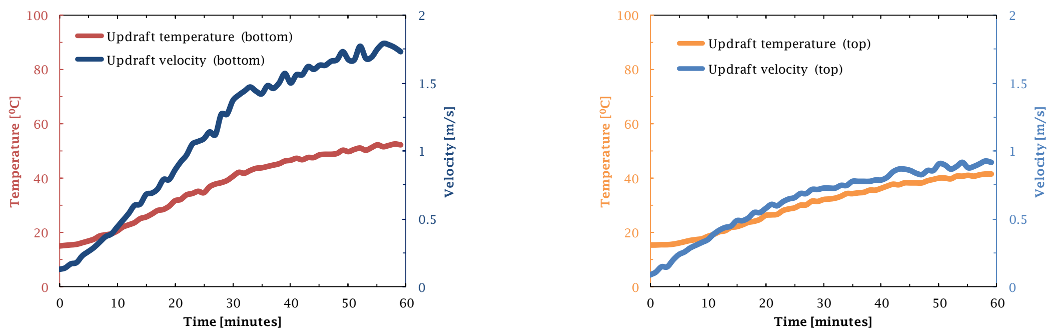

B-100E50C-100-750

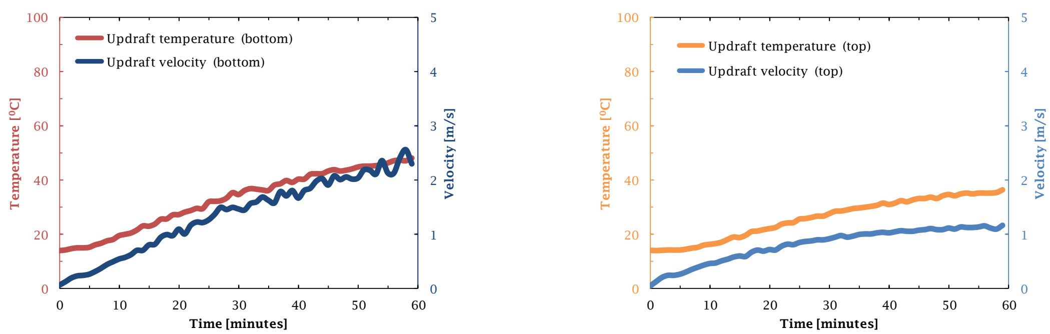

B-100E50C-100-1500

Fig. 5.23 Experimental results for the 8th measurement group of collector type B.

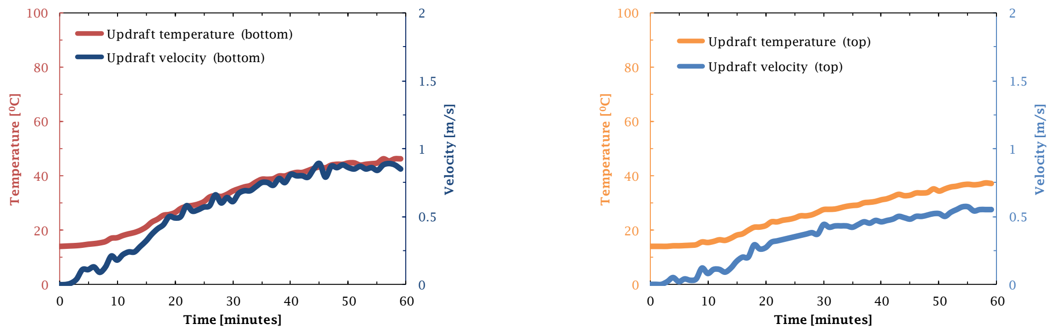

B-100E50C-150-250

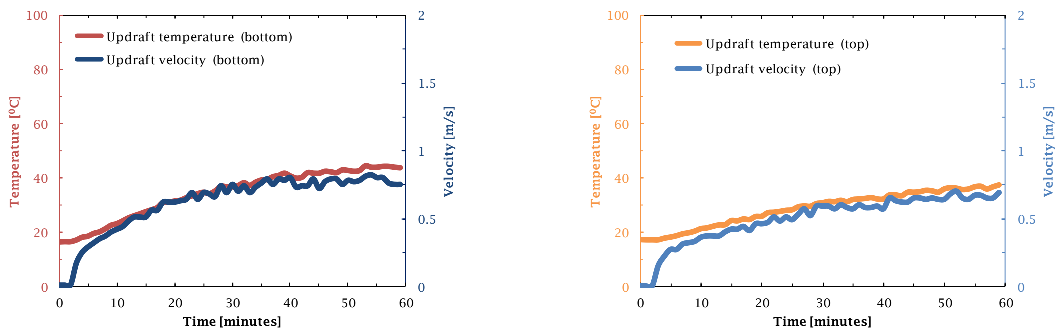

B-100E50C-150-500

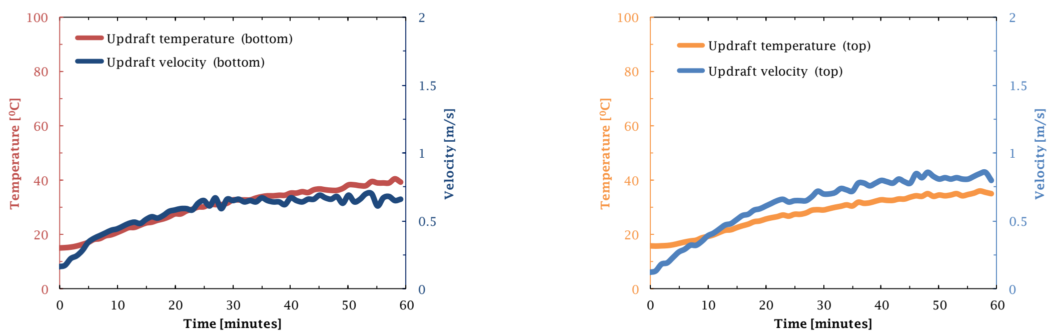

B-100E50C-150-750

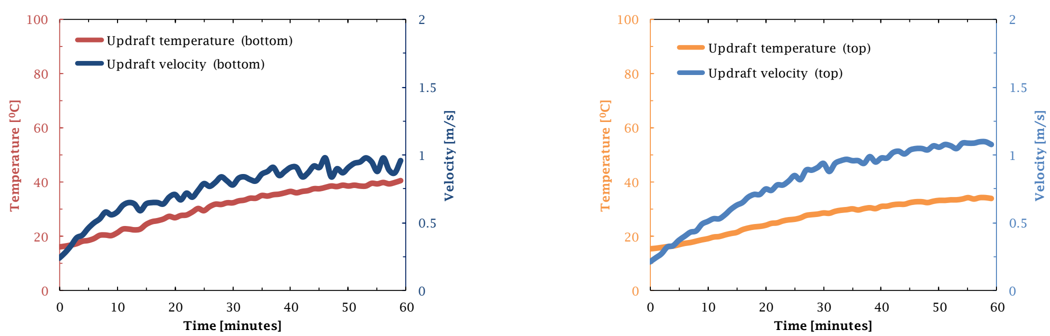

B-100E50C-150-1500

Fig. 5.24 Experimental results for the 9th measurement group of collector type B.

5.5.3 Inclusion of Guide Walls

One optimum configuration from experimental results of collector type A and B is selected to be further investigated by installing series of guide walls inside the collector. The idea of using guide walls is upon the effort to concentrate the axial and vortex flow for straight and curved guide walls configuration respectively. It is expected that the guide walls configuration able to improve the efficiency from those without the guide walls.

Updraft velocity for curved guide walls configuration is no longer in form of axial updraft flow inside the tower and radial flow inside the collector. The airflow will be in form of swirl flow rather than radial flow as in the conventional SUPG. This swirl flow is forced to produce due to flow guiding effects by the presence of guide walls. Inside the tower, the airflow exhibits a 3-D columnar updraft vortex. Such kind of flow is difficult to measure in term of its absolute velocity. Initially the absolute velocity from axial updraft flow in the case without guide walls would be compared with the absolute velocity from the 3-D columnar updraft vortex. However, it is impractical to measure the absolute velocity of such complex flow since the streamline pattern of this flow will also change with the temperature. Another alternative to measure the absolute velocity is proposed by installing a small fan at the bottom of tower. This small fan will rotate when exposed to the airflow either radial or vortex flow. Therefore, with this configuration a comparison study can be made for the case with and without guide walls.

Comparison was made by counting the time taken by the small fan to produce 1 complete rotation, and for this purpose the small fan was marked in order to track its rotation by using a high-speed camera placed on top of the tower. Results of counting the time taken by this fan for 1 rotation are presented in Fig. 5.25. This figure shows the implementation of 8 curved guide walls at the collector when small fan is placed at the center of collector or at the bottom of tower. Electric heating element was then turn on and the swirl flow gradually formed at the collector resulting in a gradual columnar updraft vortex inside the tower which in turn rotate the fan. This fan was situated in a simple hand-made bearing which perform well since the friction is much lower than the commercial bearing initially used in this fan. Experiment was carried out for the case without and with guide walls (8 and 4 curved guide walls) which will be analyzed in Chapter 6.

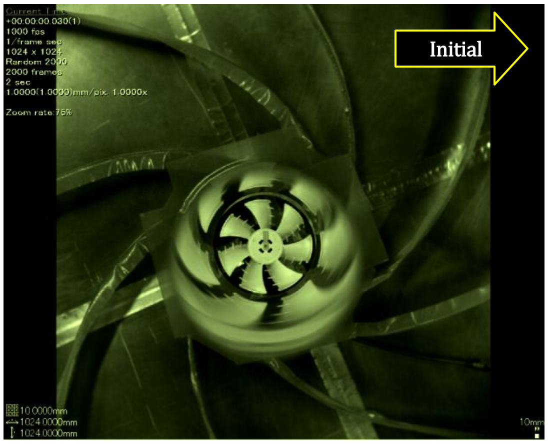

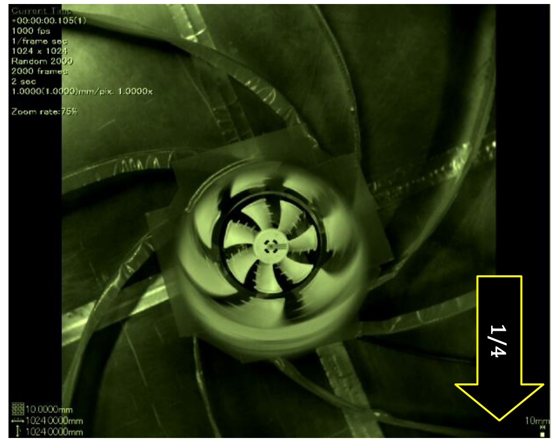

Position	Time [s]	rpm
Initial	0.030	
¼ rotation	0.105	200
½ rotation	0.181	197.37
¾ rotation	0.258	194.81
1 rotation	0.334	197.37

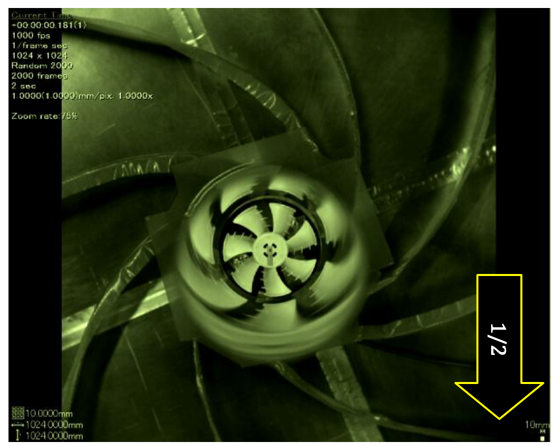

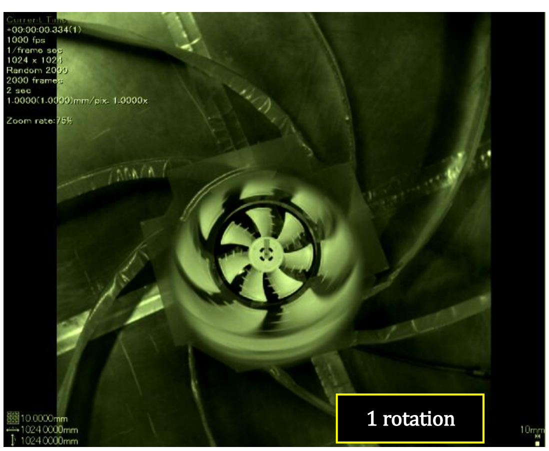

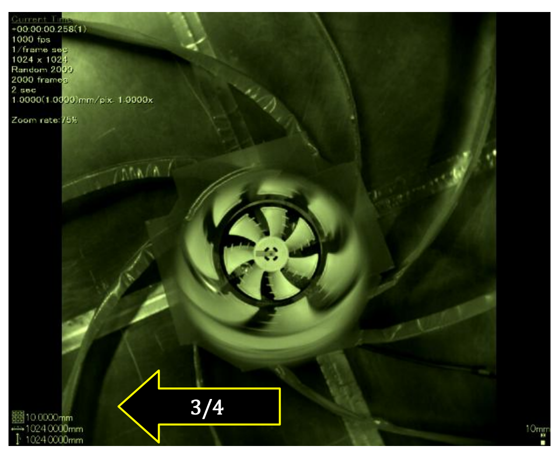

Fig. 5.25 Snapshot picture from high-speed camera showing a complete one rotation of small fan inside the tower.

5.5.4 Flow inside the Collector and Tower

In order to study about the formation of updraft flow – either axial updraft flow or columnar updraft vortex – at the collector and at the inside of tower, a further investigation is conducted. Flow visualization techniques are implemented in this case to study the flow pattern inside a lab-scale solar updraft power generator. To visualize the airflow, smoke tracer method is used in this experiment and to enhance the visualization the smoke is exposed to a laser sheet. The result of flow visualization at the collector is presented in Fig. 5.26 for collector type A and collector type B.

The source of smoke was provided at the edge of collector where it was initially placed inside a considerably large box in order to prevent the influence of artificial pressure from the smoke generator. From collector type A, concentrated smoke is observed at the edge of collector. Concentration of smoke at the edge of collector is recognized due to the area in this region is the smallest in collector type A. Soon after the smoke make an entrance in this small area, it quickly diffuse to the remaining inner area of collector and speed-up when it is about to reach the bottom of the tower. Concentrated smoke is associated with a high mass flux which is the product of air density and its velocity.

As for the result of flow visualization in collector type B, concentrated smoke is observed at the center of collector instead of at the edge of collector as observed in collector type A. It means that the collector type B has a high mass flux region at the center of collector when it is about to reach the tower. High mass flux is a desirable property in order to improve the efficiency through increasing the updraft velocity. Therefore, from this study it can be concluded that the collector type B is able to entrain more airflow – as indicates by the concentrated smoke in Fig. 5.26 – compare to the collector type A.

Fig. 5.27 shows another flow visualization result for the case with guide walls, in particular for the curved guide walls configuration. The columnar updraft vortex inside the tower is examined with purpose to investigate the formation mechanism of an updraft vortex and also to reveal the inner structure of an updraft vortex, although in this case is showing only in one plane. From this figure it can be seen that the smoke was concentrated near the walls or suppose adjacent to the boundary layer region. At the core of this updraft vortex, a low pressure region is also observed.

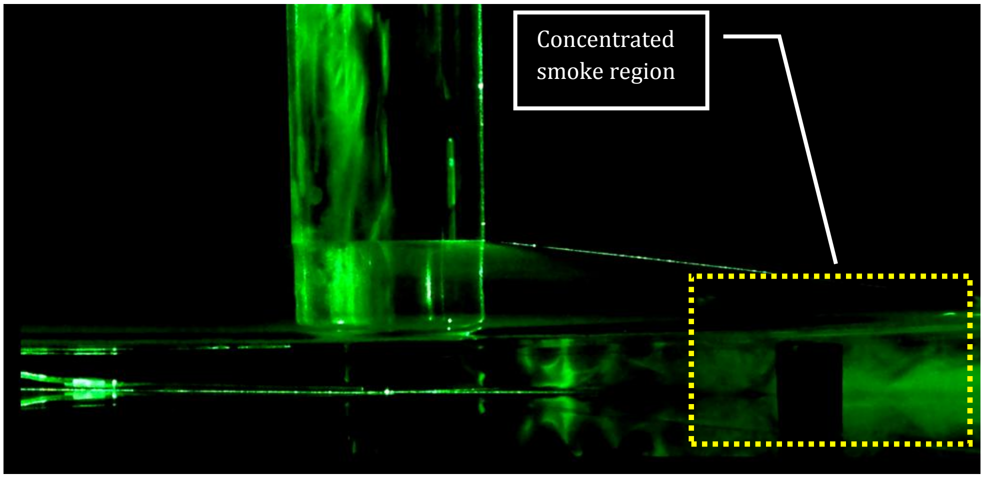

(a) Collector type A

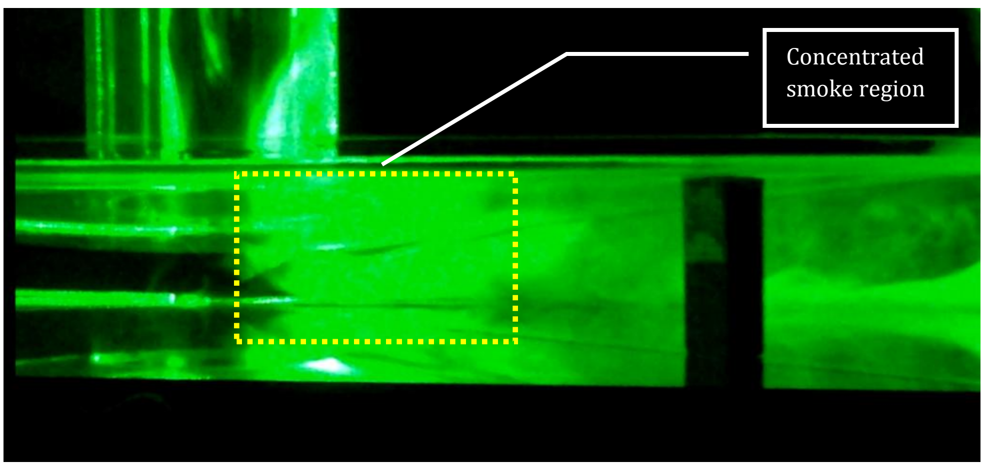

(b) Collector type B

Fig. 5.26 Snapshot picture of airflow visualization inside the collector for two types of collector.

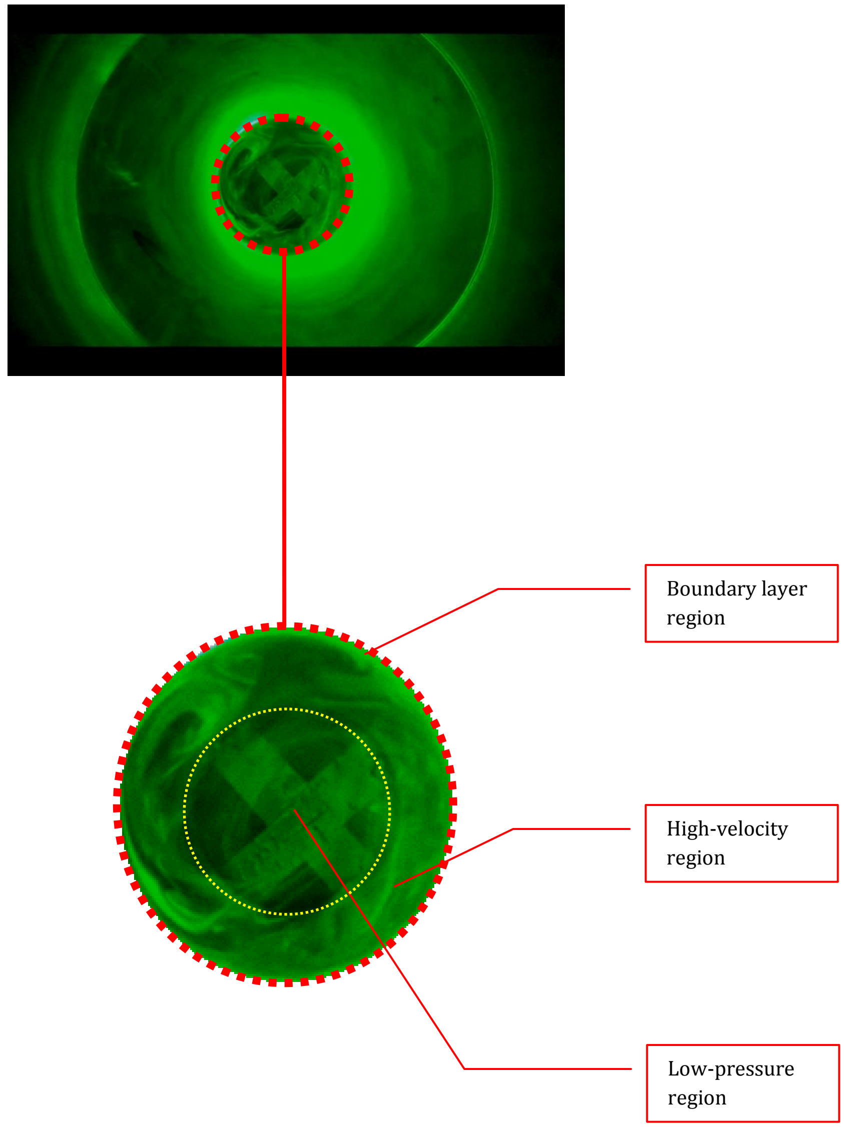

Fig. 5.27 Snapshot picture inside the tower showing the formation of a columnar updraft vortex.

5.6 Remarks

Experimental works on a lab-scale solar updraft power generator has been discussed in this chapter. Design of each component of a lab-scale SUPG has also been presented in the design of experiment section. The purpose of providing this section is to guide the manufacturing process of collector, tower, and also the heating system so that they satisfy the experimental requirement. One quantity of transparent collector was manufactured and utilized to obtain two types of collector namely collector type A and collector type B. 9 transparent tubes was manufactured to be used as the tower in a lab-scale SUPG system. 1 set of heating system has been built where 1 m × 1m of aluminum plate was purchased as heat absorber. All together these components are combined to form a lab-scale SUPG system.

Experimental setup and measurement procedures have also been elaborated in this chapter. Measurement procedures begin with selecting one configuration of lab-scale SUPG to be tested. After that, three independent sensors are prepared and set up for three locations of measurement. Measurement was conducted for 60 [min] for one case where sampling time was set for 60 [sec]. The collected data was then saved digitally into computer and the measurement can be repeated for the next case with the same procedures.

From experimental results, updraft temperature and updraft velocity at the bottom and top of the tower have been presented in the measurement result section. The results have been presented into two cases. The first case is the measurement result of collector type A. From this result, it was found that for certain diameter and collector height configuration, the updraft velocity could exhibit a higher value. The second case is the measurement result of collector type B. Similar conclusion as in collector type A is also obtained in this case; for certain combination of diameter and collector height, updraft velocity at the bottom of the tower could also exhibit a higher value compare to the other configuration. One optimum configuration from these two cases was used to study the effect of inclusion of guide walls. In this experiment, rotation of a small fan is traced by a high-speed camera and the time taken to produce 1 rotation was counted to analyze its performance. In addition, results from flow visualization experiment have also been presented.

Optimization Design Analysis Chapter 6

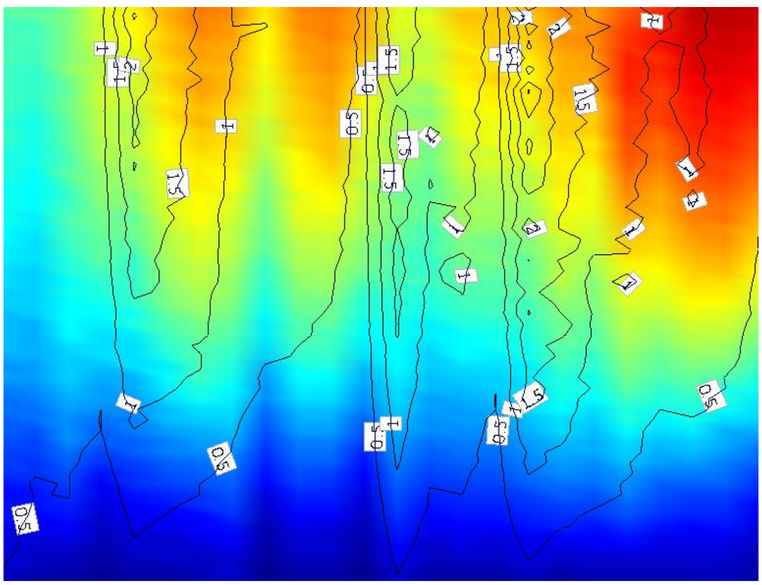

Chapter 6 provides the analysis concerning optimization of a lab-scale solar updraft power generator. Analysis is based on the experimental results in Chapter 5 and has the purpose to examine the influence of geometry to the updraft velocity and updraft temperature. The geometry being considered in the analysis is listed as follows: 1) collector height, 2) tower diameter, 3) tower height. Analysis is conducted for two types of collector (type A and type B). Evaluation is focused in finding one optimum configuration from combination of various collector height, tower diameter, and tower height. This optimum configuration is then used to study the effect of inclusion of guide walls (straight and curved configuration) to the updraft velocity and updraft temperature. The results showed that the addition of straight guide walls successfully attenuate the fluctuation of updraft velocity. Moreover, the addition of curved guide walls demonstrates a significant increase of updraft velocity which is favorable for power production or improving the total efficiency. In addition, similarity analysis is also conducted through Froude number calculation.

6.1 Introduction

Analysis concerning optimization of a lab-scale solar updraft power generator is discussed according to the experimental results in Chapter 5. Optimization is conducted with purpose to find one or more optimum design and configuration which will gives the highest updraft velocity at the bottom of the tower. To do so, the following framework has been proposed and discussed.

At first, the experiment is conducted by selecting at least three configurations of collector height, tower diameter, and tower height. The reason to choose three configurations is because the optimum point can only be obtained if there are at least three point data available, with assumption only one optimum point exist. Experiment is conducted by adjusting collector height, tower diameter, and tower height. Moreover, economical reason is also one of the considerations of choosing only three configurations. Of course the experiment can be conducted for more configurations. Hence, more items need to be purchased. It may not be economical if many material or item is purchased in order to seek an optimum design and configuration, thus the challenge in this works is to design an experiment where high chances of optimum configuration can be obtained by minimizing the total cost spend to purchase the materials.

After that, collector height, tower diameter, and tower height are combined to form a lab-scale solar updraft generator for two type of collector namely collector type A and collector type B. There are 3 configurations of collector height, 3 configurations of tower diameter, and 4 configurations of tower height. Therefore, 36 combinations can be obtained from this configuration for each type of collector. Experiment case of tower height is carried out for 4 configurations instead of 3 configurations because the optimum point cannot be observed during the experiment and this additional case or configuration is the tallest height that the available material could produces. Even with the tallest tower configuration, the optimum point still cannot be observed.

Furthermore, dimension of those three configurations i.e. collector height, tower diameter, and tower height must be designed carefully. The smallest tower diameter was chosen to be 50 mm in consideration of walls friction. If the tower diameter too small, thus the updraft velocity will be significantly reduces due to friction between the airflow and the tower walls, thus 50 mm is reasonable to be the smallest diameter in this case. The other two configurations are obtained by increasing the smallest diameter with interval increment 50 mm, resulting in 100 mm and 150 mm configurations. If the interval increment is set too small, the optimum point might be difficult to obtain. Thus, with assumption that only one optimum point exist, a bigger interval increment is a reasonable choice, it does not matter that the exact optimum point could be located or not, since the purpose of experiment is to clarify that whether there is optimum point exist or not in the selected configuration. The optimum configuration is associated with a high efficiency process, so by finding this optimum configuration the main aim of this research works (how to increase the total efficiency of a solar updraft power generator) can be answered straightforwardly.

As for collector height configuration, they are selected for three height configurations where the shortest one is 25 mm for collector type A and 65 mm for collector type B, both are measuring from the edge of collector. Increment interval for collector type A was selected as 25 mm so that the other two height configurations become 50 mm and 75 mm. A slightly different treatment for collector type B, collector height configuration initially was tested for 75 mm and 100 mm height configurations. From these two cases the updraft velocity from 75 mm case was higher than the 100 mm case. Thus, if the collector height is increased, the optimum point would not be attained. Reasonable choice was to lowered the collector height and 65 mm from the edge was selected because at the center, the collector height already reach 15 mm which means the distance of the collector wall with the plate surface is very short. Therefore 65 mm was selected instead of keeping the same interval decrement for this particular case.

As for the choice of tower height configuration, it was selected based on the purchased materials. Transparent tube for the tower was ordered for 3 different diameters i.e. 50 mm, 100 mm, and 150 mm, and all these three tubes had 1500 mm of total height. They were cut into three height configurations which are 250 mm, 500 mm, and 750 mm. By using these three height configurations, 3 cases were also obtained. However during the measurement, the optimum point had not been observed and additional case must be added, in other words the tower height must be increased. Thus, by combining all these three tubes, a 1500 mm of tower height can be realized.

6.2 Effect of Collector Height

In this section, the influence of collector height or the airflow opening distance to updraft velocity is discussed. The discussion is based on the experiment results in Chapter 5 where the updraft velocity is presented with respect to temperature difference between airflow at the center of collector and the ambient air. The reason of choosing the temperature difference as parameter in this discussion is because the experiment was conducted for different days where the ambient temperature was also different. Thus, in order to make a comparison study, the following framework is adopted: how much the updraft velocity (considered as the output) could be generated by one configuration of a lab-scale SUPG for a given of heat gain (considered as the input). This heat gain which is considered as the input to the system was obtained by taking the difference of airflow temperature at the center of collector with the ambient temperature. Noted that, the ambient air temperature is measured in the beginning of experiment and it has been assumed to hold a constant value throughout the measurement (1 hour measurement time). Therefore, comparison study can be conducted regardless the data was obtained from different days of measurement.

Effect of collector height for collector type A can be seen in Fig. 6.1 where it has been grouped into 12 graphs. Each graph represents one tower diameter configuration and one tower height configuration where the collector height for this setup is tested with three collector height configurations which are 25 mm, 50 mm and 75 mm. For example: one configuration of a lab-scale solar updraft power generator consists of 50 mm tower diameter, 250 mm tower height and three configurations of collector height (25 mm, 50 mm, and 75 mm). This set of measurement is grouped into one graph in Fig. 6.1 in order to discuss the influence of collector height to the updraft velocity at bottom of the tower.

It is observed that for all configurations in Fig. 6.1, increasing the collector height does not give appreciable effects to the updraft velocity except for the last two cases which are: 1) tower diameter 150 mm, tower height 750 mm, and 2) tower diameter 150 mm, tower height 1500 mm. In this two results, the updraft velocity for collector height 25 mm seems give a lower value compare to the other two collector heights (50 mm and 70 mm). Perhaps it is due to lack of airflow opening distance which results in low input of mass flow rate.

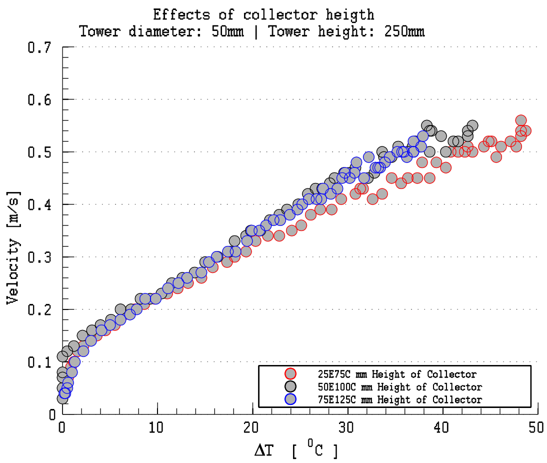
Effects of collector heigth
Tower diameter: 50mm | Tower height: 250mm
Velocity [m/s]
ΔT [°C]
25E75C mm Height of Collector
50E100C mm Height of Collector
75E125C mm Height of Collector

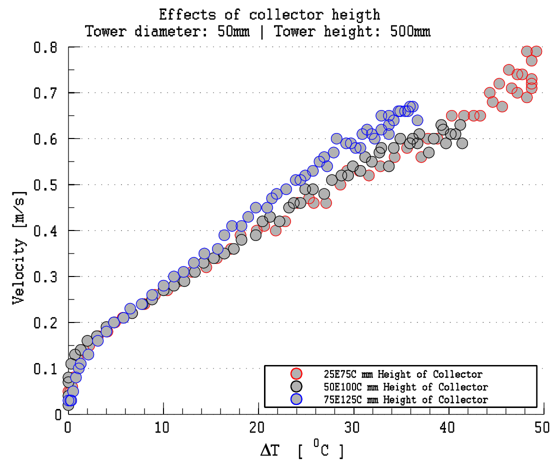
Effects of collector heigth
Tower diameter: 50mm | Tower height: 500mm
Velocity [m/s]
ΔT [°C]
25E75C mm Height of Collector
50E100C mm Height of Collector
75E125C mm Height of Collector

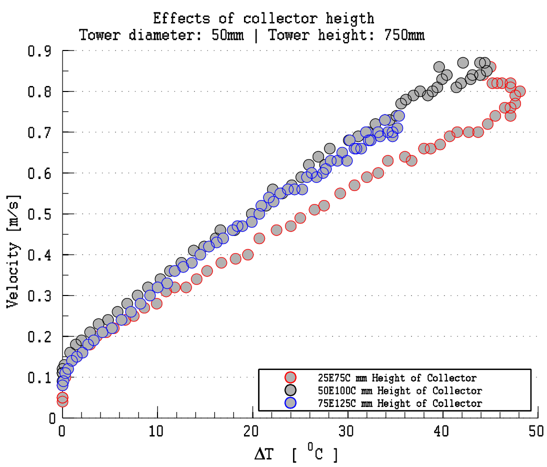
Effects of collector heigth
Tower diameter: 50mm | Tower height: 750mm
Velocity [m/s]
ΔT [°C]
25E75C mm Height of Collector
50E100C mm Height of Collector
75E125C mm Height of Collector

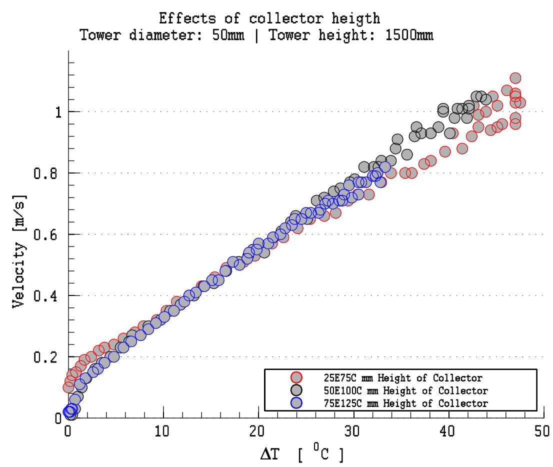
Effects of collector heigth
Tower diameter: 50mm | Tower height: 1500mm
Velocity [m/s]
ΔT [°C]
25E75C mm Height of Collector
50E100C mm Height of Collector
75E125C mm Height of Collector

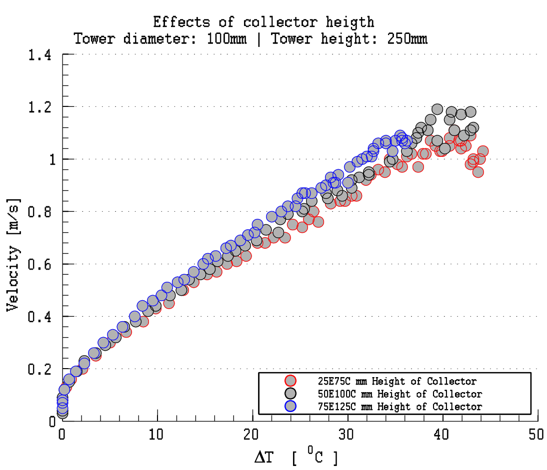
Effects of collector heigth
Tower diameter: 100mm | Tower height: 250mm
Velocity [m/s]
ΔT [°C]
25E75C mm Height of Collector
50E100C mm Height of Collector
75E125C mm Height of Collector

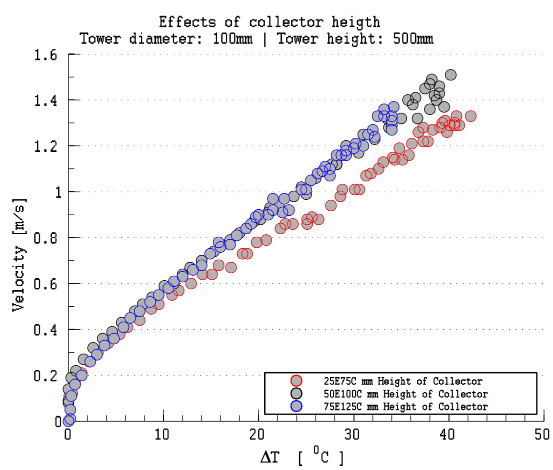
Effects of collector heigth
Tower diameter: 100mm | Tower height: 500mm
Velocity [m/s]
ΔT [°C]
25E75C mm Height of Collector
50E100C mm Height of Collector
75E125C mm Height of Collector

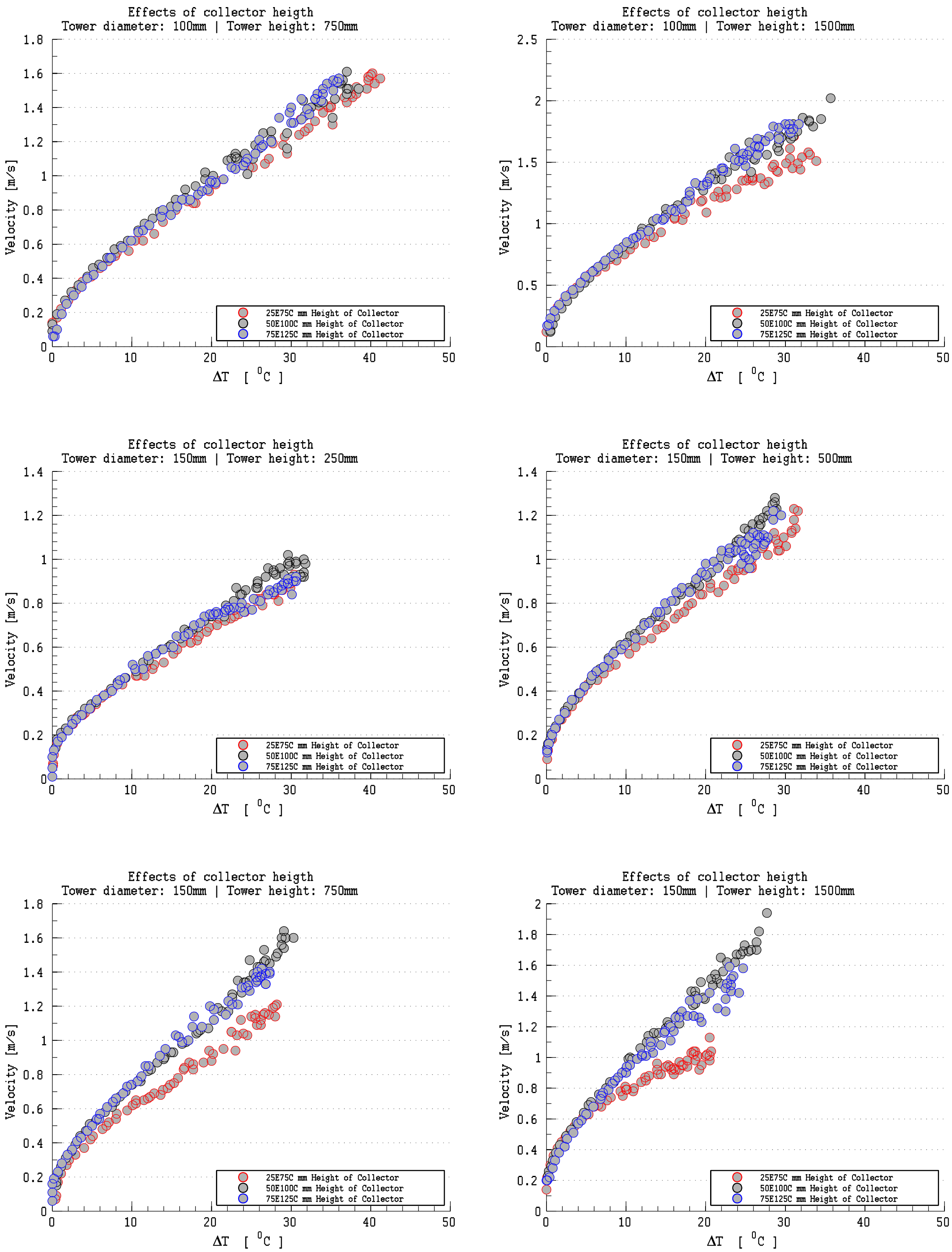

Fig. 6.1 Effects of collector height to the updraft velocity in collector type A.

Fig. 6.2 shows the influence of collector height to the updraft velocity in collector type B. Discussion is also made by grouping the experiment results into 12 graphs (summarized in Fig. 6.2). Each graph showing the result of updraft velocity against temperature difference for three collector height configurations. Collector height configurations in this case (collector type B) was set for 65 mm, 75 mm, and 100mm.

The first 4 graphs are assigned for the following configurations: tower diameter 50 mm and tower height 250 mm, 500 mm, 750 mm, and 1500 mm. These configurations are for collector height 65 mm and their updraft velocity is the smallest following by collector height 100 mm, and 75 mm as the best configuration. It seems that collector height 75 mm exhibits higher updraft velocity and can be regarded as the optimum height configuration in this case (collector type B). This is because collector height 100 mm, although generate the same amount of updraft velocity with those in 75 mm (except for the case tower diameter 50 mm, tower height 1500), but for 60 [min] of measurement time, collector height 75 mm was able to gain more heat which results in longer data of updraft velocity. Noted that the measurement time for all these configurations were carried out for 60 [min], it means collector height 100 mm was fail to utilize or to gain more heat to be converted into updraft velocity which is indicated by the shorter data in Fig. 6.2.

The next 4 graphs are for: tower diameter 100 mm, tower height 250 mm, 500 mm, 750 mm, and 1500 mm. They showed that the updraft velocity for collector height 65 mm is the smallest among the other two collector heights configurations. It is also observed that the updraft velocity for collector height 75 mm and 100 mm is similar in term of its profile but collector height 75 mm produces longer updraft velocity data which indicates that this configuration was able to gain more heat to be converted into updraft velocity. A remarkable result is shown by the configuration of collector height 75 mm, tower diameter 100 mm, and tower height 1500 m where maximum updraft velocity reach about 3 m/s although the profile exhibits a fluctuation throughout the temperature difference.

The last 4 figures are for: tower diameter 150 mm, tower height 250 mm, 500 mm, 750 mm, and 1500 mm. They demonstrates a similar pattern with those previous configuration, except for collector height 100 mm, tower diameter 150 mm, and tower heights 750 mm and 1500 mm. These two cases show a decreasing trend of updraft velocity with regards to temperature difference due to excessive of heat losses.

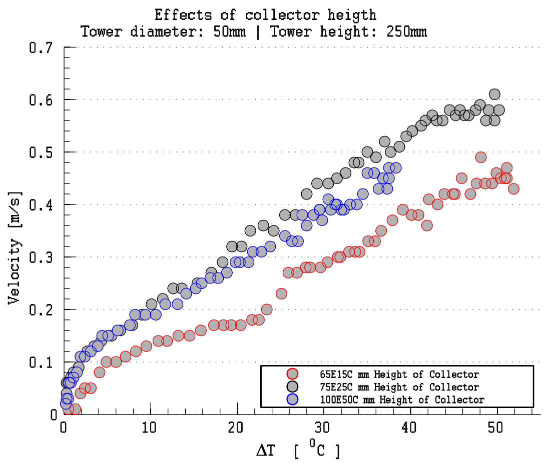
Effects of collector heigth
Tower diameter: 50mm | Tower height: 250mm
Velocity [m/s]
ΔT [0C]
65E15C mm Height of Collector
75E25C mm Height of Collector
100E50C mm Height of Collector

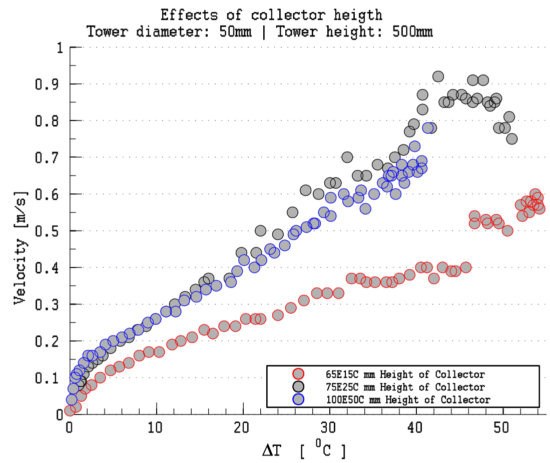
Effects of collector heigth
Tower diameter: 50mm | Tower height: 500mm
Velocity [m/s]
ΔT [0C]
65E15C mm Height of Collector
75E25C mm Height of Collector
100E50C mm Height of Collector

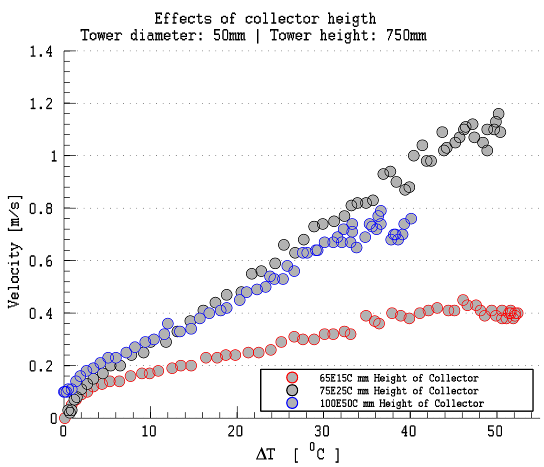
Effects of collector heigth
Tower diameter: 50mm | Tower height: 750mm
Velocity [m/s]
ΔT [0C]
65E15C mm Height of Collector
75E25C mm Height of Collector
100E50C mm Height of Collector

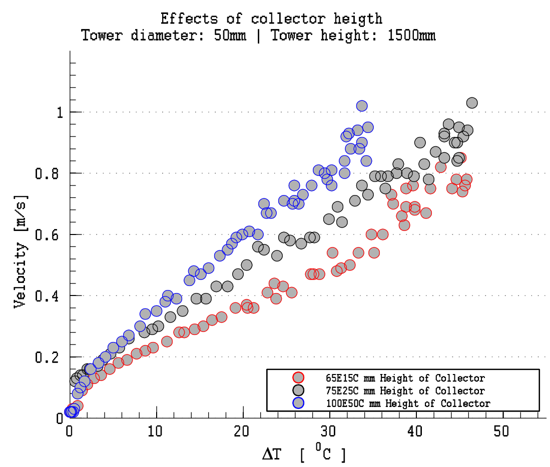
Effects of collector heigth
Tower diameter: 50mm | Tower height: 1500mm
Velocity [m/s]
ΔT [0C]
65E15C mm Height of Collector
75E25C mm Height of Collector
100E50C mm Height of Collector

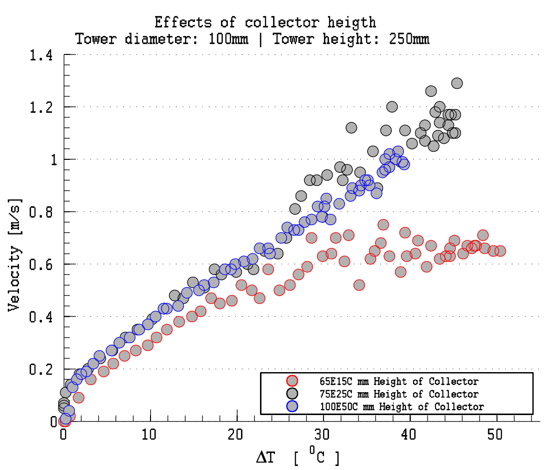
Effects of collector heigth
Tower diameter: 100mm | Tower height: 250mm
Velocity [m/s]
ΔT [0C]
65E15C mm Height of Collector
75E25C mm Height of Collector
100E50C mm Height of Collector

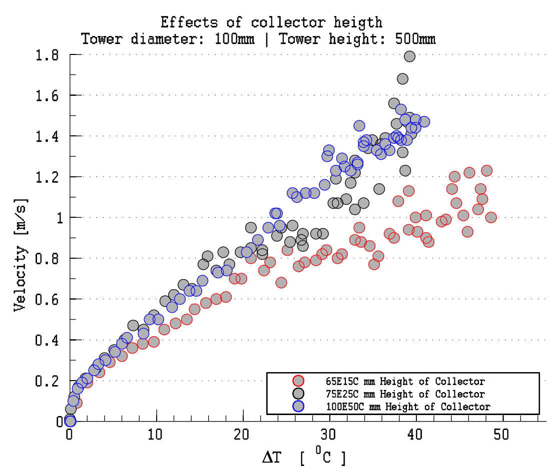
Effects of collector heigth
Tower diameter: 100mm | Tower height: 500mm
Velocity [m/s]
ΔT [0C]
65E15C mm Height of Collector
75E25C mm Height of Collector
100E50C mm Height of Collector

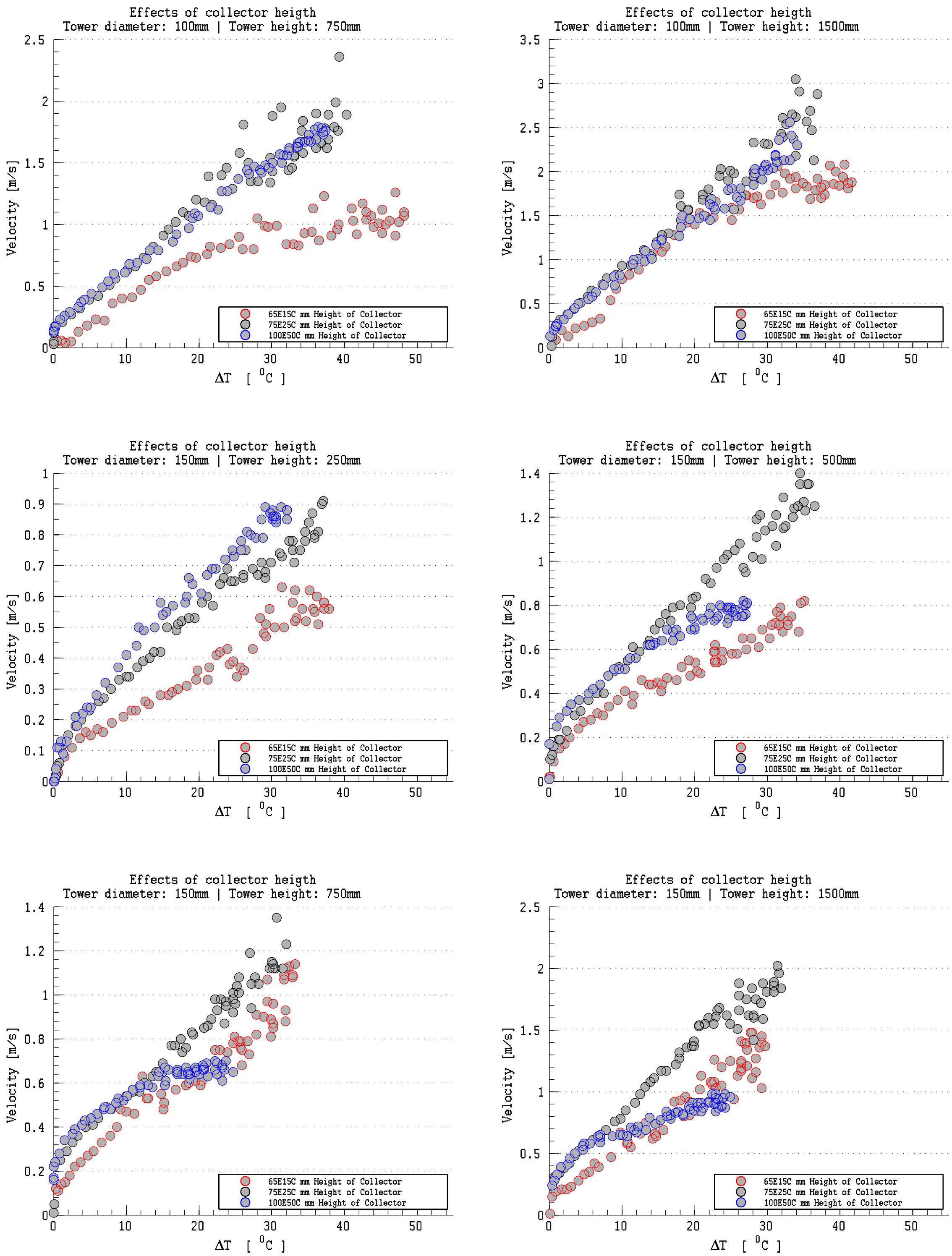

Fig. 6.2 Effects of collector height to the updraft velocity in collector type B.

6.3 Effect of Tower Diameter

Influence of tower diameter to updraft velocity at the bottom of tower is discussed in this section. The discussion is also based on the experiment results in Chapter 5 and they are presented in Fig. 6.3 where each graph represent one configuration of collector height, one configuration of tower height, and three configurations of tower diameters.

The first 4 figures are for: collector height 25 mm, tower height 250 mm, 500 mm, 750 mm, and 1500 mm. They showed an almost identical profile of updraft velocity between the 100 mm and 150 mm tower diameters configurations. However, updraft velocity data for the case of 100 mm tower diameter, exhibits a longer data than the case of 150 mm tower diameter. Thus, the case of 100 mm tower diameter was able to gain more heat to be converted into updraft velocity than the case of 150 mm of tower diameter since the amount of heat was given approximately similar for 60 [min]. The case of 50 mm tower diameter generates the least amount of updraft velocity among other two tower diameter configurations. Although this configuration was able to produce a longer updraft velocity data (even longer than the case of 100 mm tower diameter) but the magnitude of updraft velocity exhibits a lower value than the other two tower diameter configurations. Thus, the case of 50 mm tower diameter is excellent in gaining the heat given to the system but the small tower diameter prevent this configuration to produce a high magnitude of updraft velocity. Therefore, the case of 100 mm tower diameter can be regarded as optimum tower diameter configuration.

The next 4 figures are for: collector height 50 mm, tower height 250 mm, 500 mm, 750 mm, and 1500 mm. They showed similar pattern with the previous configurations, except for two cases: 50 mm of collector height, 750 mm and 1500 mm of tower height, and 150 of tower diameter configurations. These two configurations demonstrate a slightly bigger value of updraft velocity while maintaining approximately similar profile. However, the case of 100 mm tower diameter still produces a longer updraft velocity data which means that this configuration is excellent in gaining the heat given to the system. The last 4 figures are for: collector height 75 mm, tower height 250 mm, 500 mm, 750 mm, and 1500 mm, They also demonstrates similar pattern with the two previous configurations, so that it can be concluded that the case of 100 mm tower diameter is the optimum diameter.

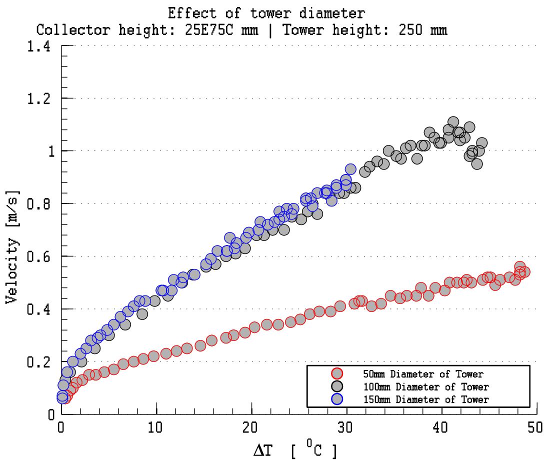
Effect of tower diameter
Collector height: 25E75C mm | Tower height: 250 mm
Velocity [m/s]
ΔT [°C]
50mm Diameter of Tower
100mm Diameter of Tower
150mm Diameter of Tower

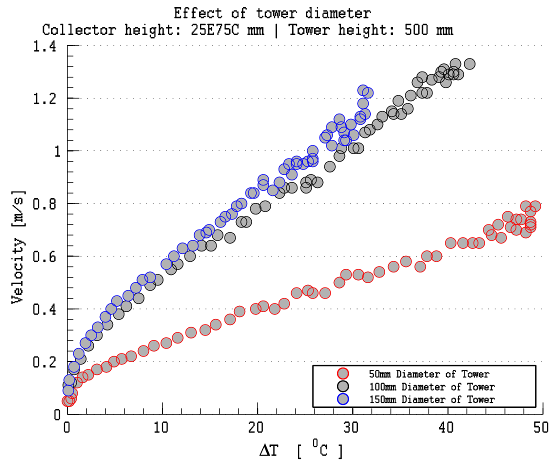
Effect of tower diameter
Collector height: 25E75C mm | Tower height: 500 mm
Velocity [m/s]
ΔT [°C]
50mm Diameter of Tower
100mm Diameter of Tower
150mm Diameter of Tower

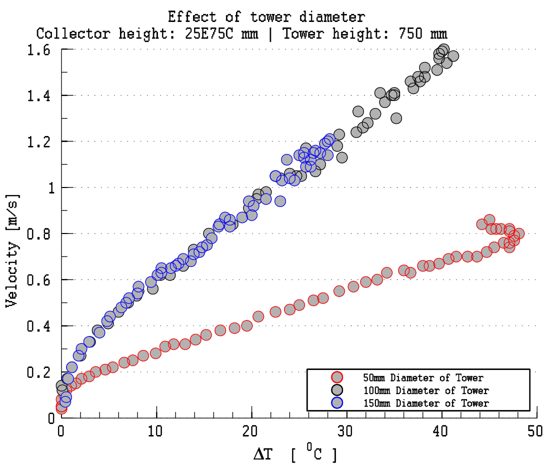
Effect of tower diameter
Collector height: 25E75C mm | Tower height: 750 mm
Velocity [m/s]
ΔT [°C]
50mm Diameter of Tower
100mm Diameter of Tower
150mm Diameter of Tower

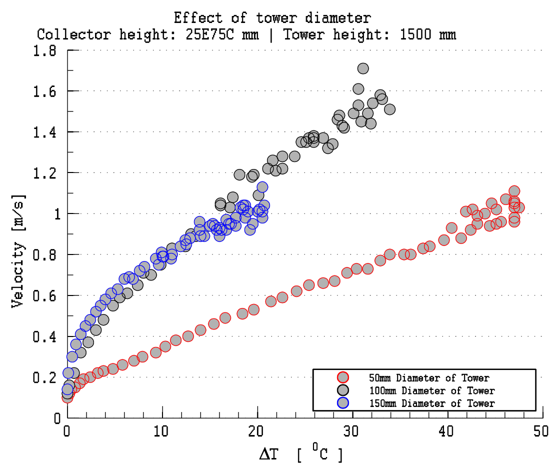
Effect of tower diameter
Collector height: 25E75C mm | Tower height: 1500 mm
Velocity [m/s]
ΔT [°C]
50mm Diameter of Tower
100mm Diameter of Tower
150mm Diameter of Tower

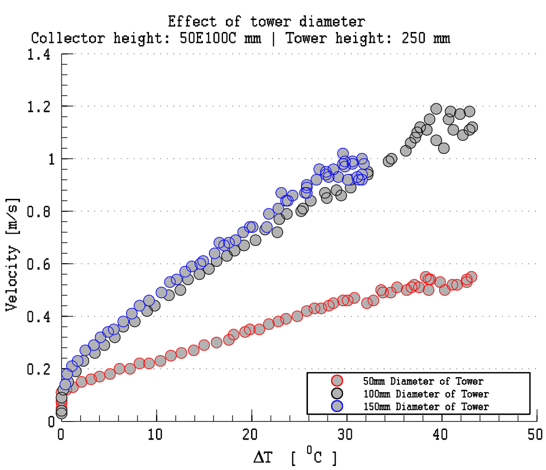
Effect of tower diameter
Collector height: 50E100C mm | Tower height: 250 mm
Velocity [m/s]
ΔT [°C]
50mm Diameter of Tower
100mm Diameter of Tower
150mm Diameter of Tower

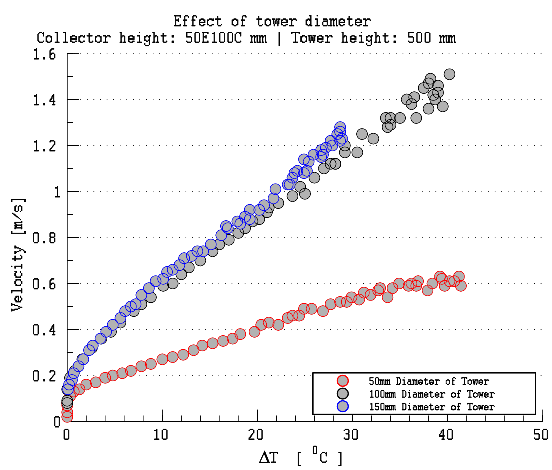
Effect of tower diameter
Collector height: 50E100C mm | Tower height: 500 mm
Velocity [m/s]
ΔT [°C]
50mm Diameter of Tower
100mm Diameter of Tower
150mm Diameter of Tower

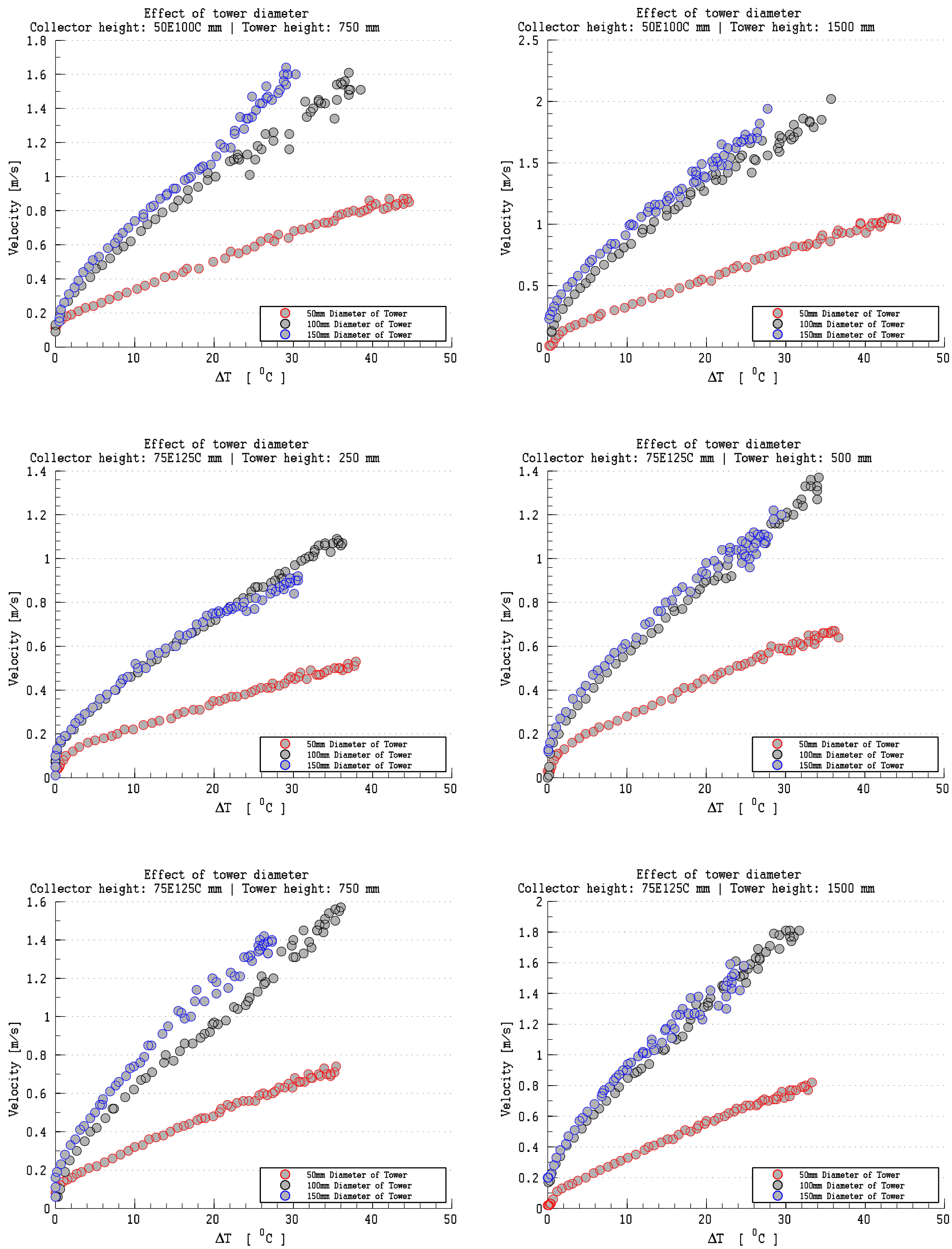

Fig. 6.3 Effects of tower diameter to the updraft velocity in collector type A.

Fig. 6.4 shows the influence of tower diameter to the updraft velocity at the bottom of tower in collector type B. In this analysis the experiment results for collector type B has been grouped into 12 graphs. Each graph shows the updraft velocity as function of temperature difference for one configuration of collector height, one configuration of tower height, and three configurations of tower diameters.

The first 4 figures are for: collector height 65 mm, tower height 250 mm, 500 mm, 750 mm, and 1500 mm. They clearly showed that the case of 50 mm tower diameter produces the least amount of updraft velocity compare to the other two tower diameter configurations. The case of 100 mm tower diameter shows slightly higher updraft velocity than the case of 150 mm tower diameter. Moreover, it also generates longer updraft velocity data due to the ability to gain more heat given to the system. In contrast with the result in collector type A, the updraft velocity profile in collector type B exhibits a fluctuation throughout the temperature difference.

The next 4 figures are for : collector height 75 mm, tower height 250 mm, 500 mm, 750 mm, and 1500 mm. They demonstrate that the case of 100 mm tower diameter generates the highest magnitude of updraft velocity compare to the other two tower diameter configurations. The case of 100 mm tower diameter has attained approximately 3 m/s of maximum updraft velocity. Its collector height is 75 mm and tower height 1500 mm. The case of 50 mm tower diameter shows the lowest magnitude of updraft velocity. This is can be explained as follows: in order to entrain the collector airflow into updraft velocity inside the tower, the tower diameter holds an important role since the entrainment effects is related to how much mass flow rate could be inserted into the tower. The bigger the tower – thus it is expected that – the more mass flow rate that can be inserted into the tower. Thus, having a small diameter of tower is not beneficial in producing higher updraft velocity or mass flow rate. However, too big tower diameter is also not helpful in producing higher updraft velocity since this mass flow rate is governed by the buoyancy force which is depends on the temperature of airflow. If the temperature of airflow is not high enough due to heat distribution over large volume of air inside the tower, thus the buoyancy force will also produces a lower mass flow rate. This condition is best describe by the last two graphs in Fig. 6.4 for the case 100 mm of collector height, 750 mm and 1500 mm of tower height configurations.

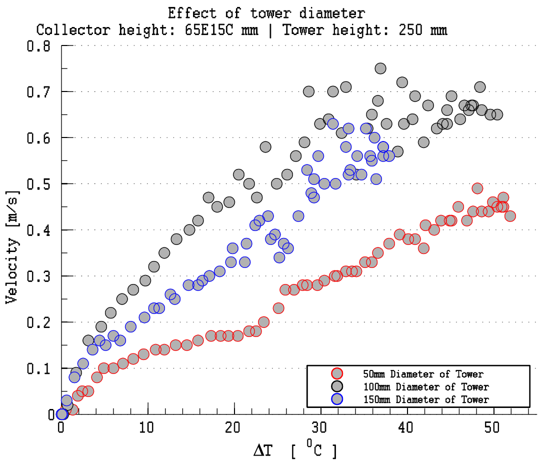
Effect of tower diameter
Collector height: 65E15C mm | Tower height: 250 mm
Velocity [m/s]
ΔT [°C]
50mm Diameter of Tower
100mm Diameter of Tower
150mm Diameter of Tower

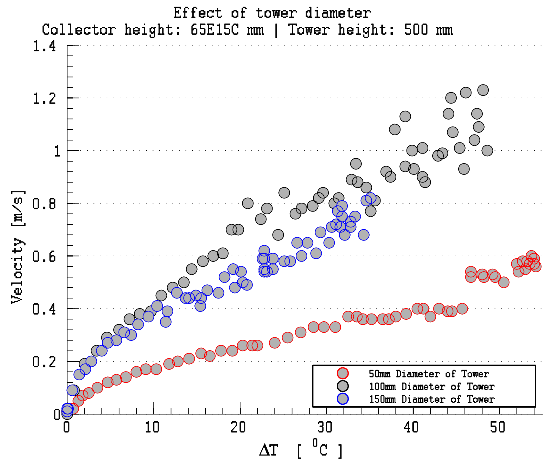
Effect of tower diameter
Collector height: 65E15C mm | Tower height: 500 mm
Velocity [m/s]
ΔT [°C]
50mm Diameter of Tower
100mm Diameter of Tower
150mm Diameter of Tower

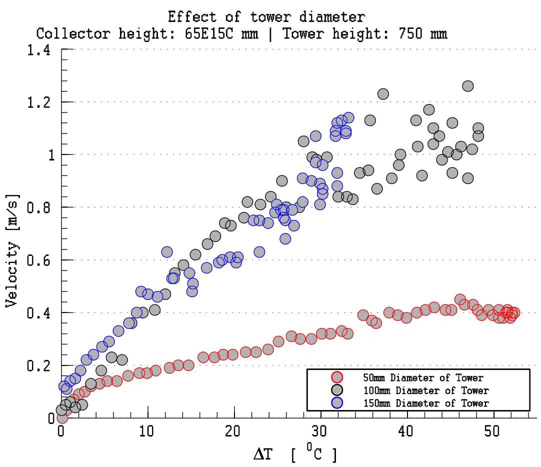
Effect of tower diameter
Collector height: 65E15C mm | Tower height: 750 mm
Velocity [m/s]
ΔT [°C]
50mm Diameter of Tower
100mm Diameter of Tower
150mm Diameter of Tower

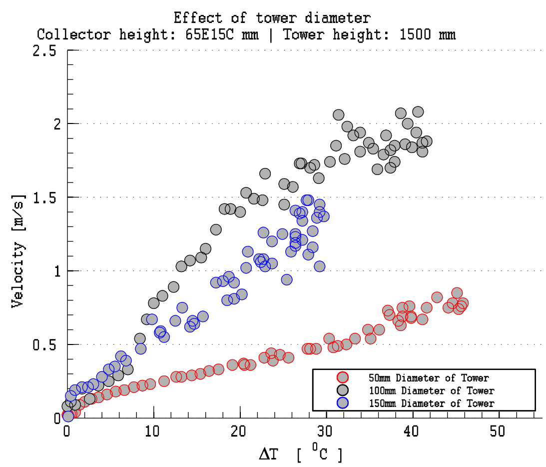
Effect of tower diameter
Collector height: 65E15C mm | Tower height: 1500 mm
Velocity [m/s]
ΔT [°C]
50mm Diameter of Tower
100mm Diameter of Tower
150mm Diameter of Tower

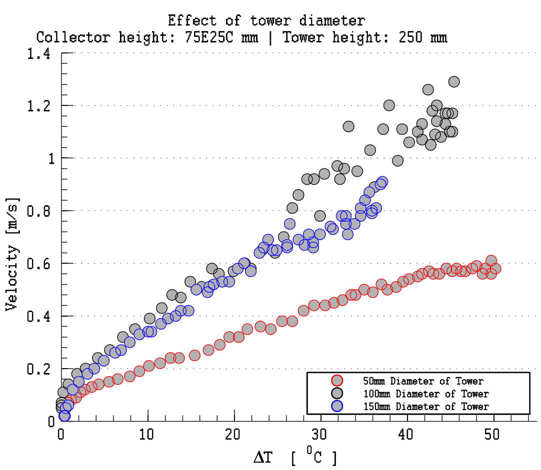
Effect of tower diameter
Collector height: 75E25C mm | Tower height: 250 mm
Velocity [m/s]
ΔT [°C]
50mm Diameter of Tower
100mm Diameter of Tower
150mm Diameter of Tower

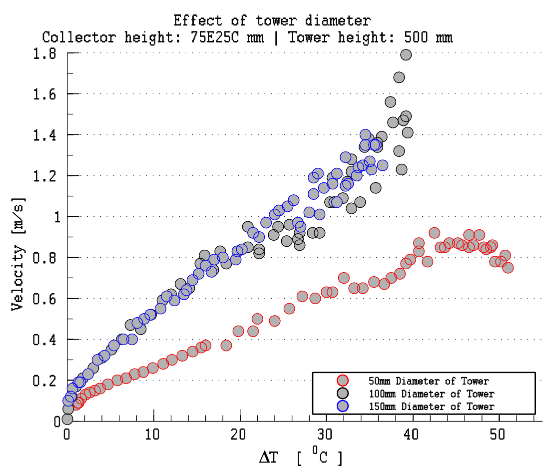
Effect of tower diameter
Collector height: 75E25C mm | Tower height: 500 mm
Velocity [m/s]
ΔT [°C]
50mm Diameter of Tower
100mm Diameter of Tower
150mm Diameter of Tower

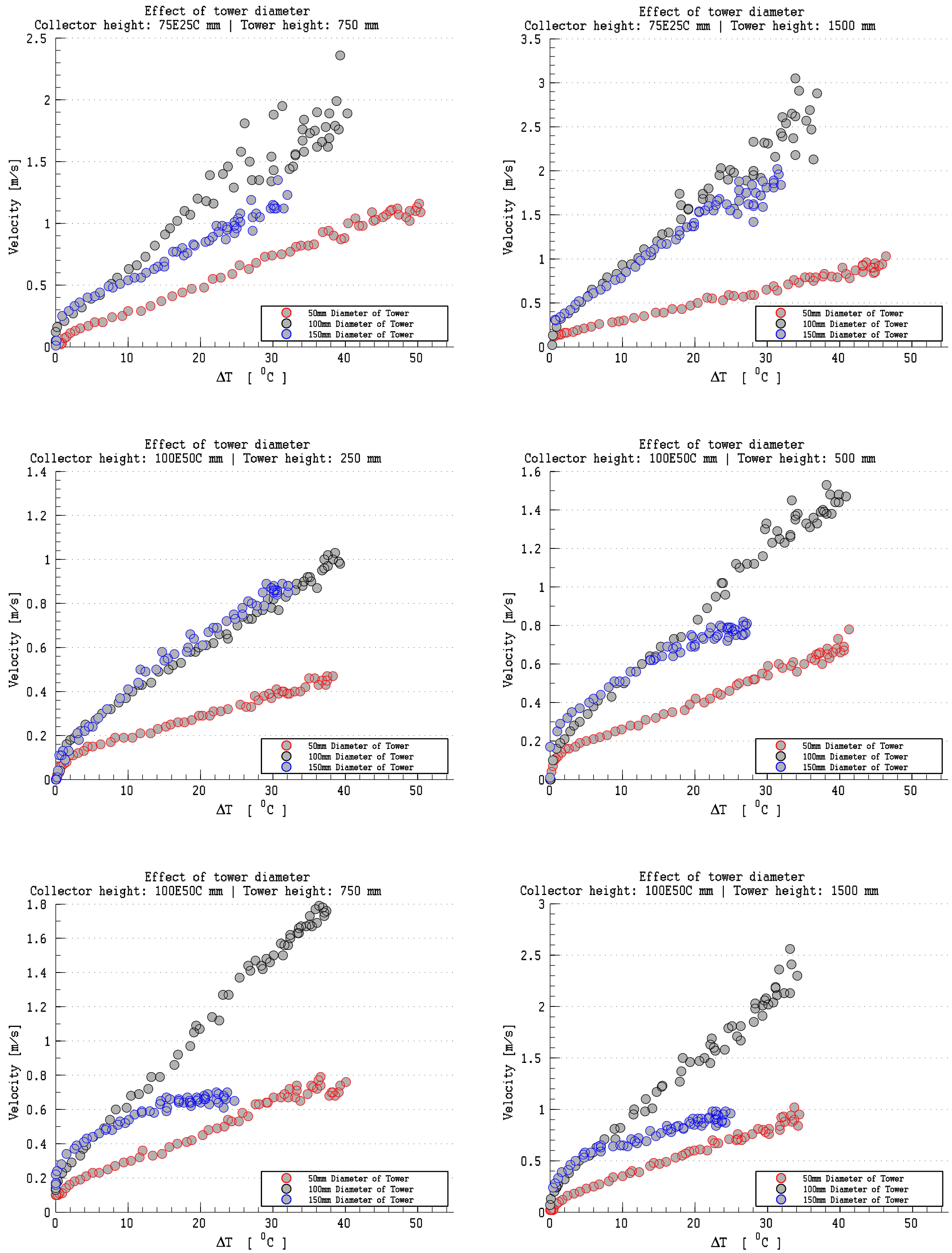

Fig. 6.4 Effects of tower diameter to the updraft velocity in collector type B.

6.4 Effect of Tower Height

A more clear result is obtained in analyzing the effect of tower height to updraft velocity of a lab-scale solar updraft power generator. Discussion is made based on the experimental results presented in Fig. 6.5 and Fig. 6.6 for collector type A and collector type B respectively. According to these two figures, the longer the tower, the higher the updraft velocity. However, an optimum point cannot be observed in this case even after 4 configurations of tower height. The tallest tower that could be realized in this experiment is 1500 mm. Thus, the experiment data shows consistent results with those from theoretical prediction through numerical simulation as presented in Chapter 4.

In the result of collector type A, the influence of tower height is presented in Fig. 6.5. Experimental result has been grouped according to the tower height. Each graphs represents one configuration of collector height, one configuration of tower diameter, and four configurations of tower heights. The first three figures are for: collector height 25 mm, tower diameter 50 mm, 100 mm, and 150 mm. They showed that the case of 250 mm tower height has the least magnitude of updraft velocity and it followed by 500 mm, 750 mm, while the case of 1500 mm tower height configurations produces the highest magnitude of updraft velocity. The remaining figures are for collector height 50 mm with 50mm, 100 mm, 150 mm of tower diameters configurations and collector height 75 mm with 50 mm, 100 mm, and 150 mm of tower diameters configurations.

The same situation is also observed in collector type B where the highest updraft velocity is also produced by the highest tower and vice versa. The results of 100 mm tower diameter for every collector height configurations and tower height variations seems fluctuate throughout the temperature difference. Moreover, these configurations are recognized gaining more heat given to the systems and subsequently these configurations produce higher updraft velocity compare to the other cases. Thus, it can be concluded that the case of 100 mm tower diameter in collector type B is the optimum diameter. Therefore, the answer to the research question posses in Chapter 1 (does a solar updraft power generator have optimum configuration) can be answered. There is an optimum configuration not only for diameter but also for collector height. Moreover, collector type B seems produces higher updraft velocity than collector type A.

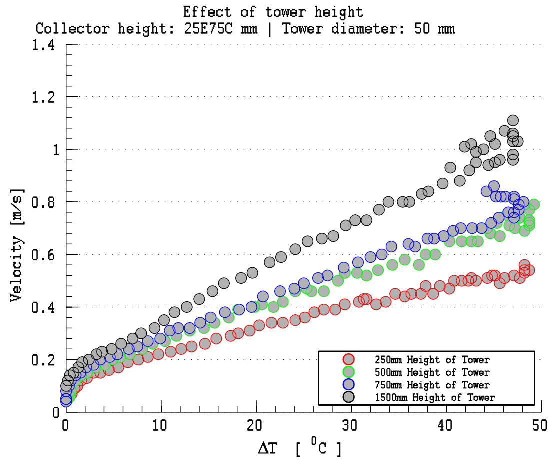
Effect of tower height
Collector height: 25E75C mm | Tower diameter: 50 mm
Velocity [m/s]
ΔT [0C]
250mm Height of Tower
500mm Height of Tower
750mm Height of Tower
1500mm Height of Tower

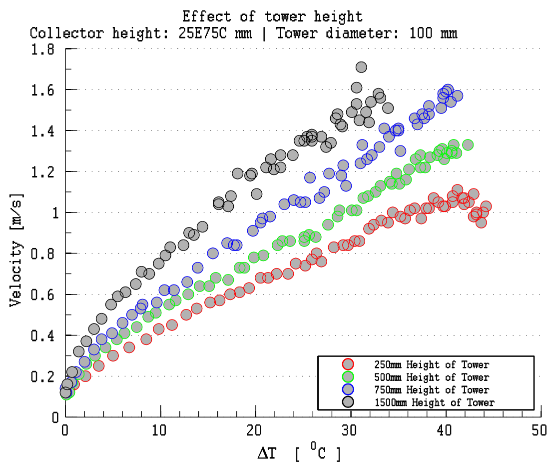
Effect of tower height
Collector height: 25E75C mm | Tower diameter: 100 mm
Velocity [m/s]
ΔT [0C]
250mm Height of Tower
500mm Height of Tower
750mm Height of Tower
1500mm Height of Tower

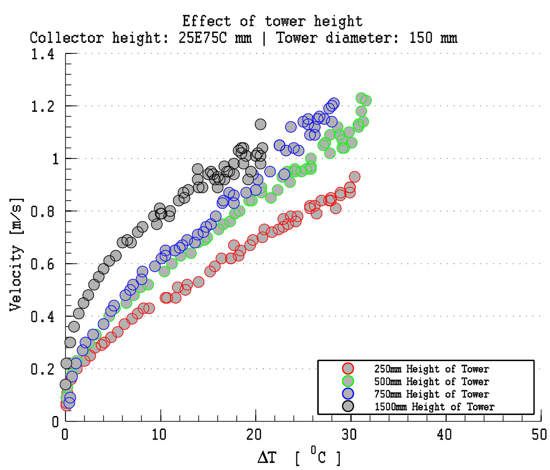
Effect of tower height
Collector height: 25E75C mm | Tower diameter: 150 mm
Velocity [m/s]
ΔT [0C]
250mm Height of Tower
500mm Height of Tower
750mm Height of Tower
1500mm Height of Tower

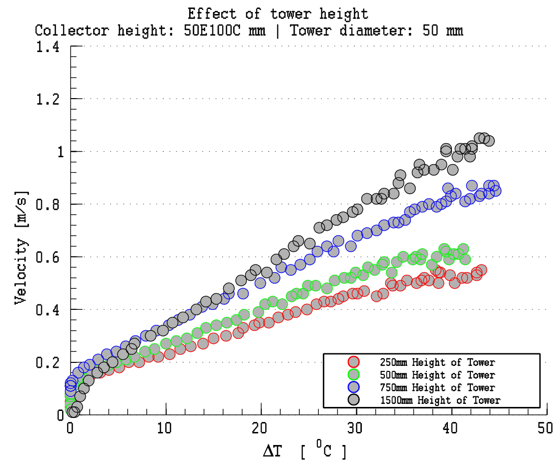
Effect of tower height
Collector height: 50E100C mm | Tower diameter: 50 mm
Velocity [m/s]
ΔT [⁰C]
250mm Height of Tower
500mm Height of Tower
750mm Height of Tower
1500mm Height of Tower

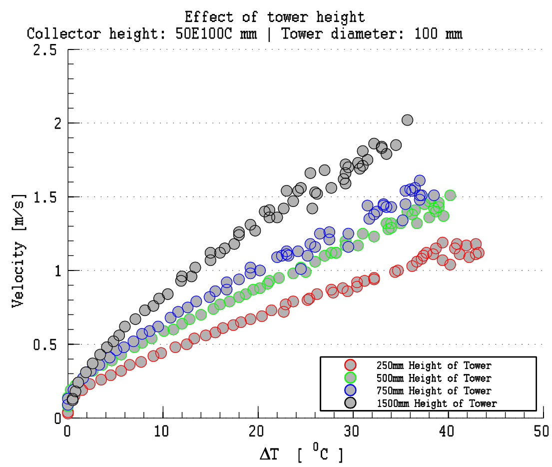
Effect of tower height
Collector height: 50E100C mm | Tower diameter: 100 mm
Velocity [m/s]
ΔT [⁰C]
250mm Height of Tower
500mm Height of Tower
750mm Height of Tower
1500mm Height of Tower

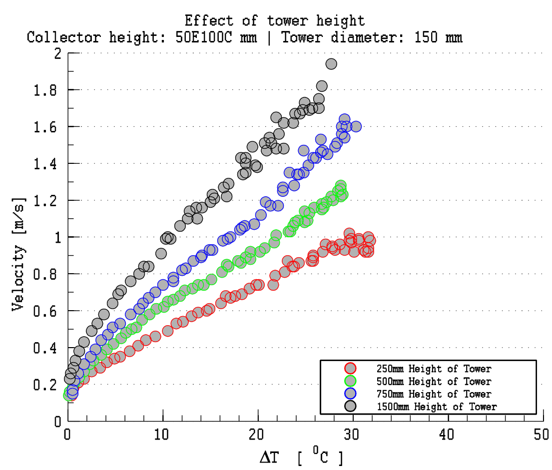
Effect of tower height
Collector height: 50E100C mm | Tower diameter: 150 mm
Velocity [m/s]
ΔT [⁰C]
250mm Height of Tower
500mm Height of Tower
750mm Height of Tower
1500mm Height of Tower

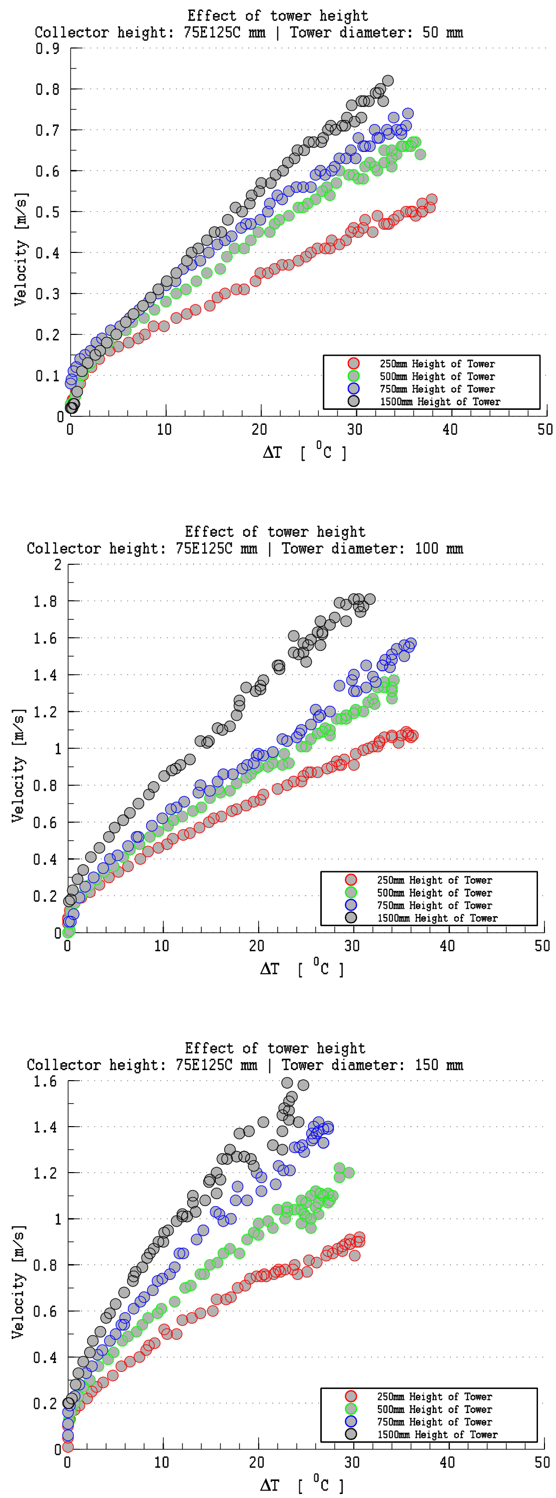

Fig. 6.5 Effects of tower height to the updraft velocity in collector type A.

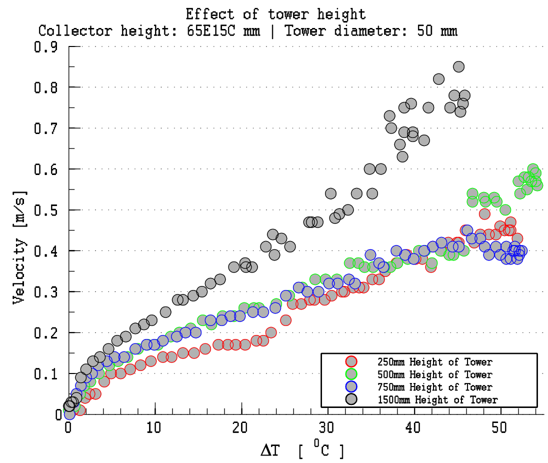
Effect of tower height
Collector height: 65E15C mm | Tower diameter: 50 mm
Velocity [m/s]
ΔT [°C]
250mm Height of Tower
500mm Height of Tower
750mm Height of Tower
1500mm Height of Tower

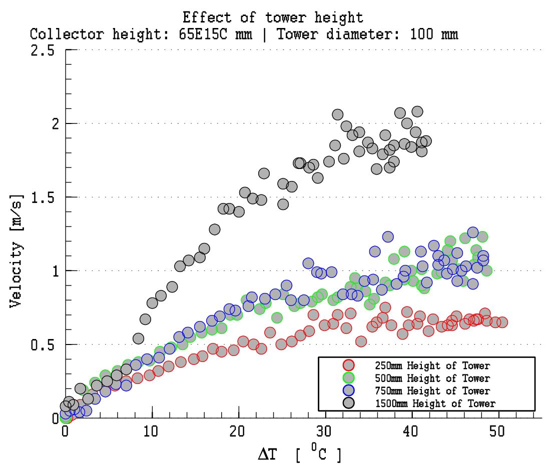
Effect of tower height
Collector height: 65E15C mm | Tower diameter: 100 mm
Velocity [m/s]
ΔT [°C]
250mm Height of Tower
500mm Height of Tower
750mm Height of Tower
1500mm Height of Tower

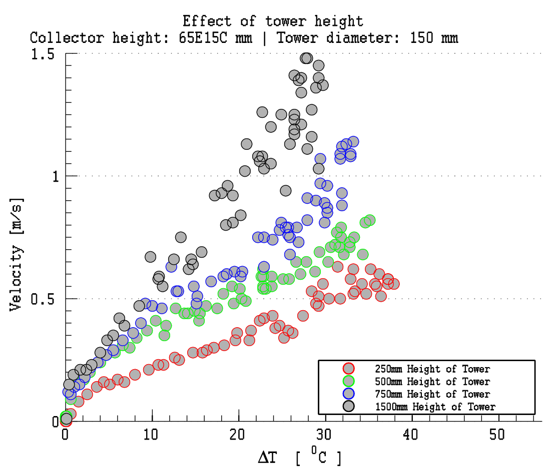
Effect of tower height
Collector height: 65E15C mm | Tower diameter: 150 mm
Velocity [m/s]
ΔT [°C]
250mm Height of Tower
500mm Height of Tower
750mm Height of Tower
1500mm Height of Tower

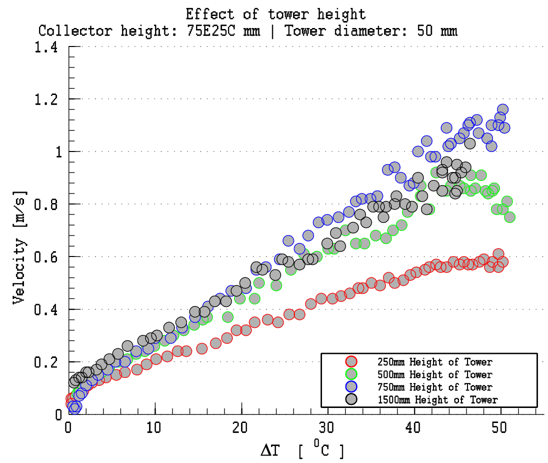
Effect of tower height
Collector height: 75E25C mm | Tower diameter: 50 mm
Velocity [m/s]
ΔT [0C]
250mm Height of Tower
500mm Height of Tower
750mm Height of Tower
1500mm Height of Tower

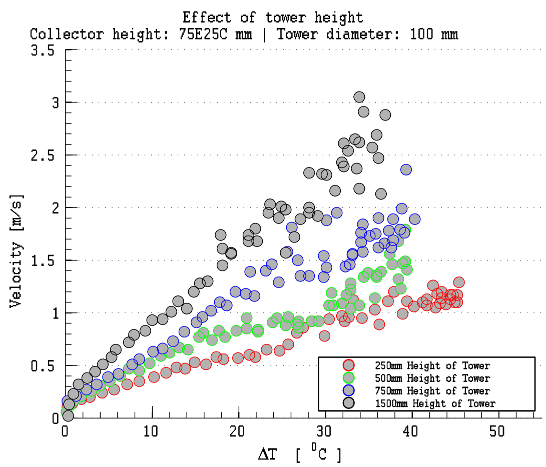
Effect of tower height
Collector height: 75E25C mm | Tower diameter: 100 mm
Velocity [m/s]
ΔT [0C]
250mm Height of Tower
500mm Height of Tower
750mm Height of Tower
1500mm Height of Tower

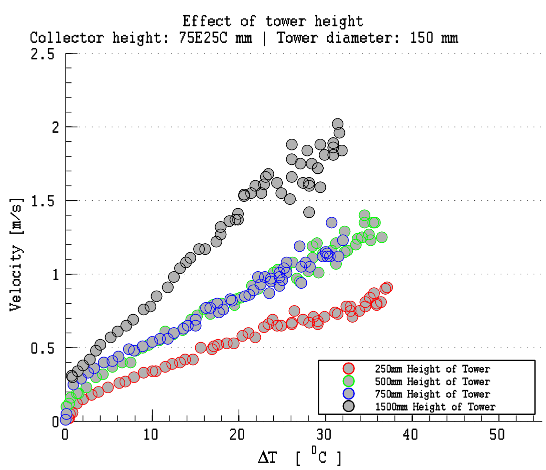
Effect of tower height
Collector height: 75E25C mm | Tower diameter: 150 mm
Velocity [m/s]
ΔT [0C]
250mm Height of Tower
500mm Height of Tower
750mm Height of Tower
1500mm Height of Tower

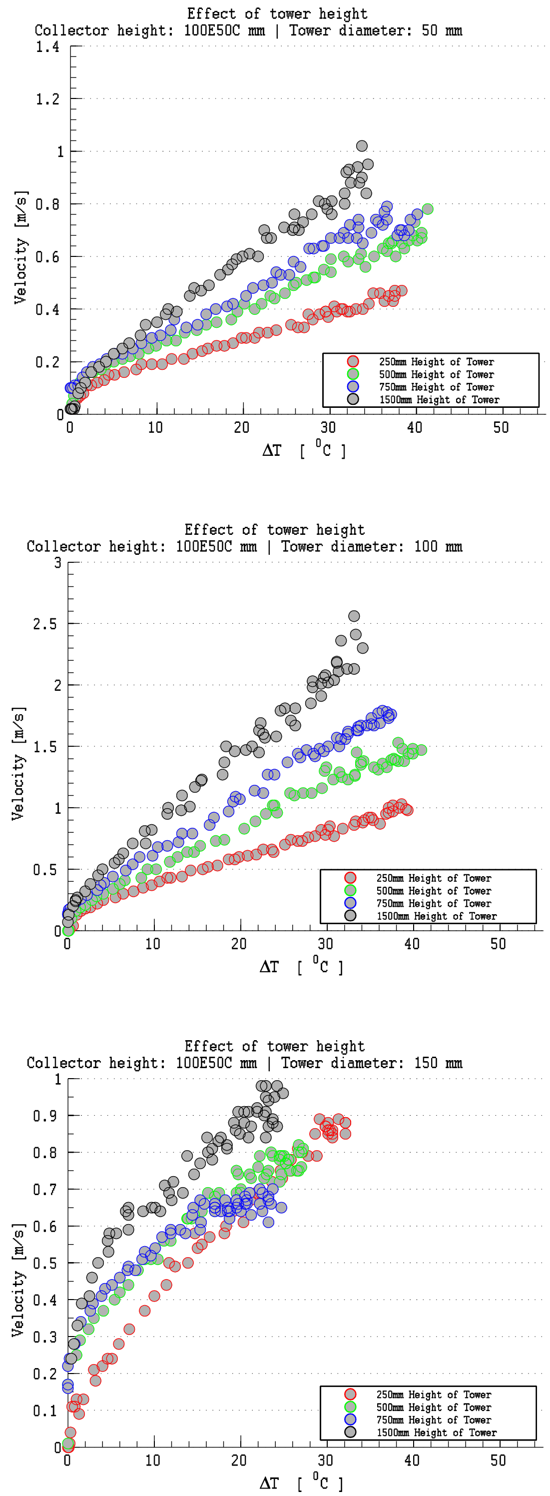

Fig. 6.6 Effects of tower height to the updraft velocity in collector type B.

6.5 Optimum Design and Configuration

Analysis considering the influence of geometry to the updraft velocity of a lab-scale solar updraft power generator has the purpose to find an optimum design and configuration. In this section the optimum design and configuration is defined not based on the updraft velocity or the mass flow rate but based on the mechanical power that could be produced from one particular configuration. The mechanical power is generated from a wind turbine placed at the bottom of the tower. The equation to calculate the amount of mechanical power has been derived in Chapter 3 (mathematical model for wind turbine). Thus, this equation is used in this section where the mass flow rate in the power equation of wind turbine was obtained from experiment results. Moreover, a temporal-spatial chart which shows the evolution of updraft temperature and updraft velocity in one diagram is proposed as can be seen in Fig. 6.7 for collector type A (top) and collector type B (bottom) respectively. The results are plotted for each experiment cases which are labeled as Case No. and its conversion to the naming convention in experiment cases is shown in Table 6.1.

Fig. 6.7 provides the information regarding the best design and configuration in term of utilizing thermal energy given to the system (indicated by the temperature difference) to be converted into kinetic energy (indicated by the updraft velocity). The results are divided into three groups separated by white dashed line. One group represents the same collector height with various tower diameters and tower heights. The red color in this chart indicates a high temperature region. For example case number A1 – A4 and B1 – B4. These cases exhibit a high temperature region but the updraft velocity remains low. Hence, this configuration is considered as the worst combination. The best combinations are observed for the case number A-20, A-24, B-20, and B-24 because these cases successfully utilize the heat given to the system to be converted into high updraft velocity.

Fig. 6.8 shows the updraft velocity (top) and the mass flow rate (bottom) for each experiment cases and it is presented in a 2 dimensional diagram where the data actually represent 3 dimensions. The maximum updraft velocity for collector type A is realized by experiment case A-20 and for collector type B is realized by experiment case B-20. The maximum mass flow rate for collector type A is realized by case A-24 and for collector type B is observed for case B-24.

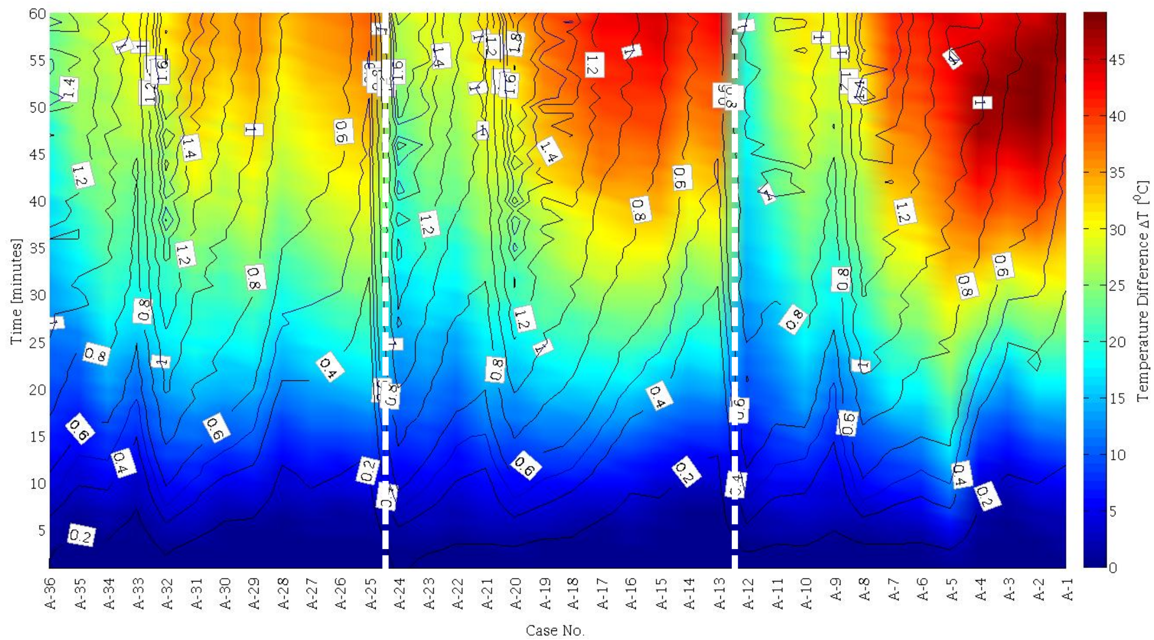

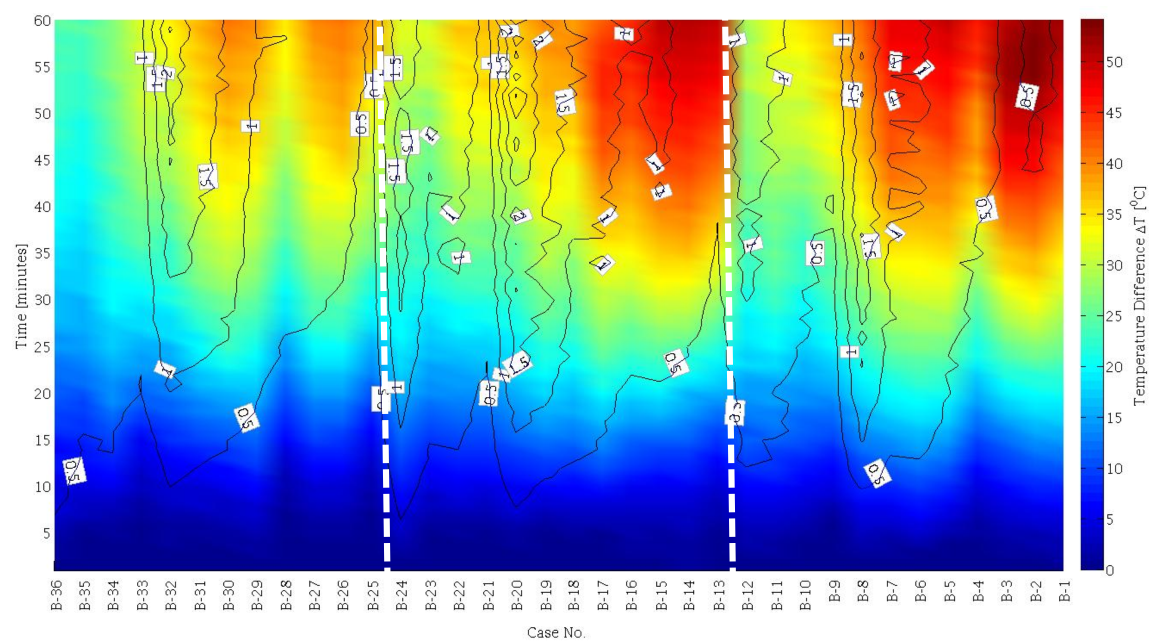

Fig. 6.7 Temporal-spatial chart showing the evolution of updraft temperature and velocity for each experiment case of collector type A (top) and B (bottom).

Table 6.1 Conversion of case number with the naming convention in experiment

Case No.	Naming convention for collector type A	Case No.	Naming convention for collector type B
A-1	A-25E-75C-50-250	B-1	B-65E-15C-50-250
A-2	A-25E-75C-50-500	B-2	B-65E-15C-50-500
A-3	A-25E-75C-50-750	B-3	B-65E-15C-50-750
A-4	A-25E-75C-50-1500	B-4	B-65E-15C-50-1500
A-5	A-25E-75C-100-250	B-5	B-65E-15C-100-250
A-6	A-25E-75C-100-500	B-6	B-65E-15C-100-500
A-7	A-25E-75C-100-750	B-7	B-65E-15C-100-750
A-8	A-25E-75C-100-1500	B-8	B-65E-15C-100-1500
A-9	A-25E-75C-150-250	B-9	B-65E-15C-150-250
A-10	A-25E-75C-150-500	B-10	B-65E-15C-150-500
A-11	A-25E-75C-150-750	B-11	B-65E-15C-150-750
A-12	A-25E-75C-150-1500	B-12	B-65E-15C-150-1500
A-13	A-50E-100C-50-250	B-13	B-75E-25C-50-250
A-14	A-50E-100C-50-500	B-14	B-75E-25C-50-500
A-15	A-50E-100C-50-750	B-15	B-75E-25C-50-750
A-16	A-50E-100C-50-1500	B-16	B-75E-25C-50-1500
A-17	A-50E-100C-100-250	B-17	B-75E-25C-100-250
A-18	A-50E-100C-100-500	B-18	B-75E-25C-100-500
A-19	A-50E-100C-100-750	B-19	B-75E-25C-100-750
A-20	A-50E-100C-100-1500	B-20	B-75E-25C-100-1500
A-21	A-50E-100C-150-250	B-21	B-75E-25C-150-250
A-22	A-50E-100C-150-500	B-22	B-75E-25C-150-500
A-23	A-50E-100C-150-750	B-23	B-75E-25C-150-750
A-24	A-50E-100C-150-1500	B-24	B-75E-25C-150-1500
A-25	A-75E-125C-50-250	B-25	B-100E-50C-50-250
A-26	A-75E-125C-50-500	B-26	B-100E-50C-50-500
A-27	A-75E-125C-50-750	B-27	B-100E-50C-50-750
A-28	A-75E-125C-50-1500	B-28	B-100E-50C-50-1500
A-29	A-75E-125C-100-250	B-29	B-100E-50C-100-250
A-30	A-75E-125C-100-500	B-30	B-100E-50C-100-500
A-31	A-75E-125C-100-750	B-31	B-100E-50C-100-750
A-32	A-75E-125C-100-1500	B-32	B-100E-50C-100-1500
A-33	A-75E-125C-150-250	B-33	B-100E-50C-150-250
A-34	A-75E-125C-150-500	B-34	B-100E-50C-150-500
A-35	A-75E-125C-150-750	B-35	B-100E-50C-150-750
A-36	A-75E-125C-150-1500	B-36	B-100E-50C-150-1500

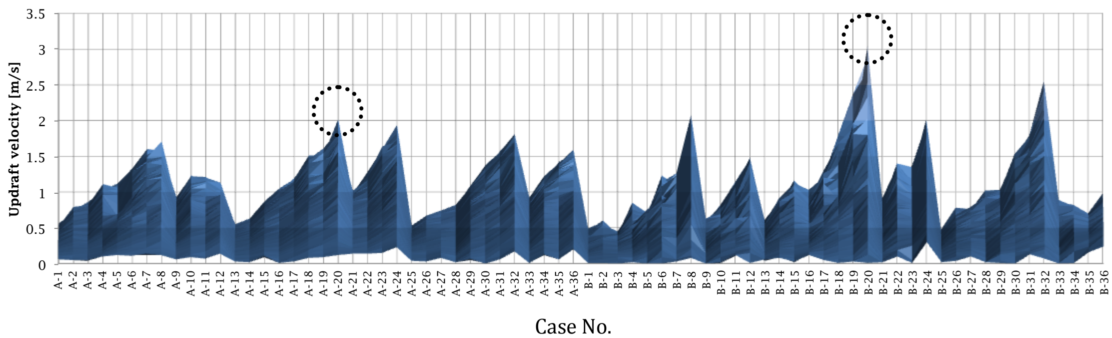

Maximum updraft velocity for type A A-50E100C-100-1500	Maximum updraft velocity for type B B-75E25C-100-1500

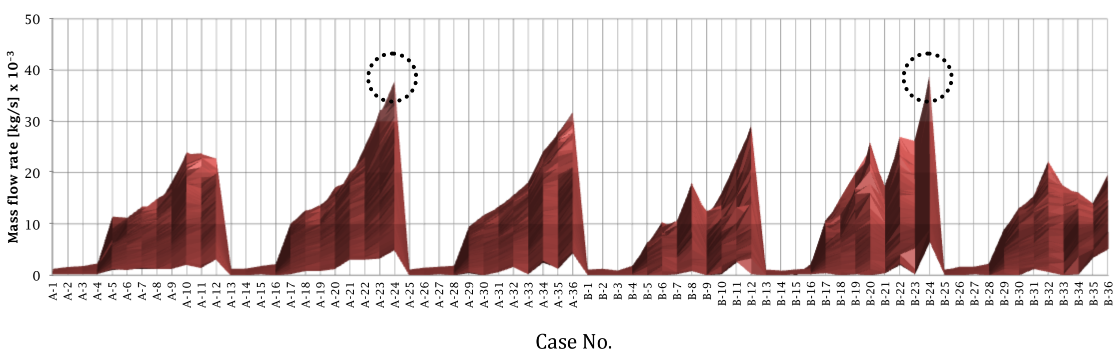

Maximum mass flow rate for type A A-50E100C-150-1500	Maximum mass flow rate for type B B-75E25C-150-1500

Fig. 6.8 Maximum updraft velocity (top) and mass flow rate (bottom) for each experiment cases of collector type A and type B.

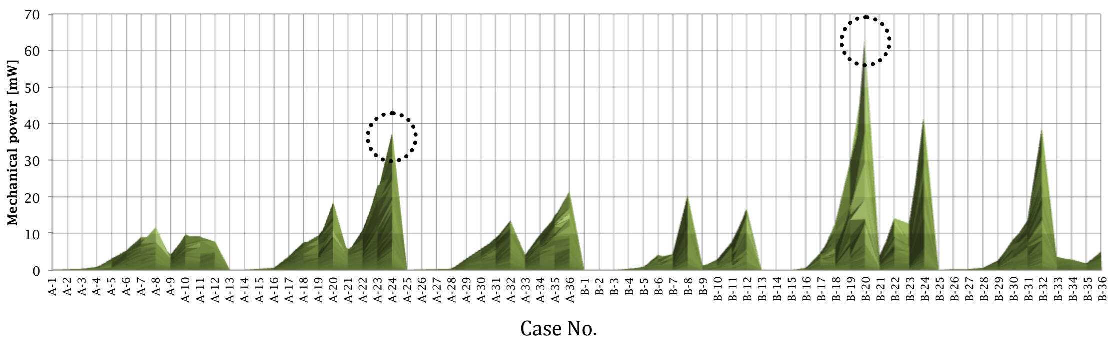

Maximum mechanical power for type A	Maximum mechanical power for type B
A-50E100C-150-1500	B-75E25C-100-1500

Fig. 6.9 Maximum mechanical power for each experiment cases of collector type A and type B.

From Fig. 6.9 it is observed that the case number A-24 exhibits the highest magnitude of mechanical power among the other configurations in collector type A. Case number A-24 is for experiment case A-50E-100C-150-1500 where tower diameter is not 100 mm. From previous analysis, the case of 100 mm tower diameter produces the highest updraft velocity, but when it is converted to mechanical power, 150 mm of tower diameter configuration is bigger since it is also produces high mass flow rate. So the product of turbine area and updraft velocity is the factor who determines the amount of mechanical power. As for the collector type B, case number B-25 produce the highest magnitude of mechanical power. This case number is for experiment case B-75E25C-100-1500. If both collector types are compared in order to select one optimum design and configurations, thus the case B-75E25C-100-1500 is regarded as the optimum design and configuration. This optimum design will be used to study the effects of addition of guide walls.

6.5.1 Effect of Guide Walls

As discussed in the previous section that the collector type B was able to generates higher updraft velocity than collector type A, but the result seems highly fluctuates. This condition is not favorable for power production since the updraft velocity will be extracted by wind turbine. Uniform oncoming flow is desirable to provide smooth power production. Thus, in attempt to provide a more uniform updraft velocity, series of straight guide walls was installed at the collector and tested for its feasibility. The experiment was conducted for two configurations which are 4 and 8 guide walls forming a straight profile towards the center of collector.

Analysis carried out in the previous section recognized that the fluctuation of updraft velocity comes from the excessive heat losses at the edge of collector, since the airflow opening distance exposing quite large volume of hot air to the surrounding ambient. The temperature difference between ambient air and collector airflow is getting high through time and that is the reason why the highly fluctuation occur at the high temperature difference. This large temperature difference inducing a convective flows from the edge of collector to the surrounding ambient while it is supposed to flow to the center of collector. The buoyancy and inertia forces which responsible to entrain the collector airflow to the center of collector and inside the tower is competing with the convective current due to heat losses at the edge of collector and this competing process is realized in fluctuation of updraft velocity.

Therefore, to minimize the convective current at the edge of collector, a strategy to concentrate the collector airflow is proposed by installing series of guide walls. The hypothesis is: by concentrating the collector airflow through implementation of guide walls will enhance the inertia and buoyancy forces so that the entrainment effect towards the center of collector is higher than it is at the edge of that collector. The result is expected to have a smooth profile or even higher updraft velocity. This hypothesis is confirmed by experimental results in Fig. 6.10 which shows the updraft velocity versus time (the color representing temperature difference). Comparing Fig. 6.10 (a) for the case without guide walls and Fig. 6.10 (b) and (c) for the case with 4 and 8 guide walls, demonstrates that the straight guide walls has an important role in smoothing the profile of updraft velocity.

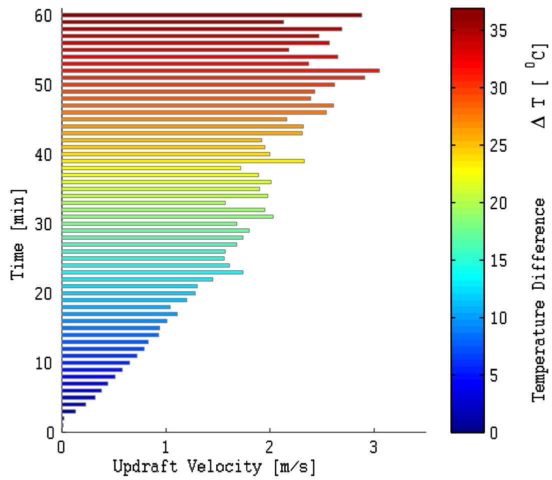

(a) Without guide walls configuration

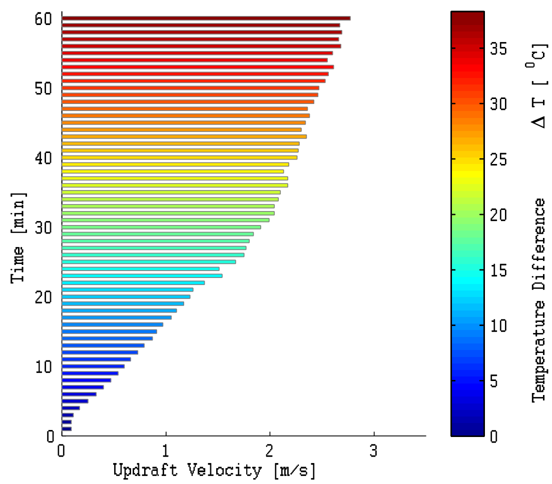

(b) 4 straight guide walls configuration

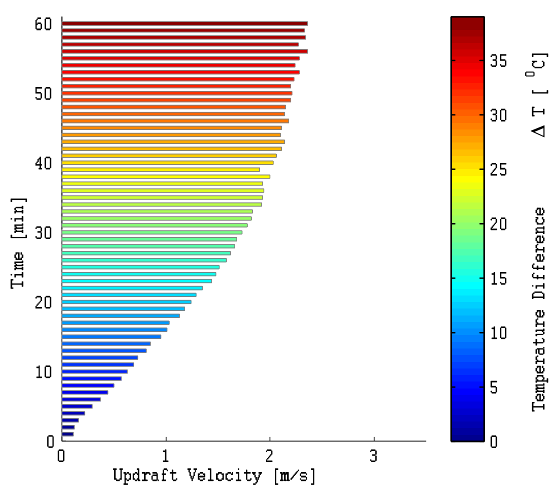

(c) 8 straight guide walls configuration

Fig. 6.10 Effects of straight guide walls to the updraft velocity in optimum configuration.

From the result of implementation of straight guide walls, a smooth updraft velocity profile can be obtained. Therefore, the previous hypothesis can be confirmed. However, only the smoothing process has been confirmed but the higher magnitude of updraft velocity cannot be obtained from these straight guide walls configurations. Since the objective is to increase the total efficiency through an optimum design which will gives high magnitude of updraft velocity, thus another attempt to increase this velocity is proposed. In pursuance of increasing the updraft velocity at the bottom of tower, instead of straight guide wall, a curve-like form of guide walls is proposed and tested. To gain knowledge about the feasibility of the curved guide walls, series of experiment was conducted.

The experiment is attempted to compare the magnitude of updraft velocity for without guide walls configuration (optimum configuration) and those with curved guide walls configuration. Updraft velocity for without guide walls can be easily measured since the resulting flow inside the tower is in form of axial updraft flow and the thermo-anemometer sensors can be placed perpendicular to the axial updraft flow. However, in the curved guide walls configuration, the resulting flow inside the tower exhibits a fully 3 dimensional flow which in form of a columnar updraft vortex. Seeking and tracking the magnitude of this velocity is considered not practical since it direction is also changes with the temperature. Thus, an alternative method to measure the magnitude of the updraft flow for both cases is proposed by placing a small fan at the bottom of the tower. This fan will rotate due to the oncoming updraft either in form of axial flow or a columnar updraft vortex flow.

The rotation of this small fan was tracked by a high-speed camera which has capability of taking the picture up to 1000 frame per second. So the small fan was marked on its surface and the time taken for this marked to finish one rotation is followed and recorded. The results are presented in Table 6.2 and Fig. 6.11. Experiment was conducted for three configurations i.e. without guide walls, 4 curved guide walls, and 8 curved guide walls. Rotations of small fan for each case are recorded for three different plate temperatures (50 ^{0}C, 60 ^{0}C, and 70 ^{0}C). The plate temperature was chosen in this case because the airflow temperature sensor would disturb the airflow and affect the fan rotation, but the thermocouple used to measure the plate temperature will not disturb the airflow during the measurement. It was found that the case with 8 curved guide walls exhibits a higher fan rotation at high temperature.

Table 6.2 Results of counting the fan rotation

Case	Temperature [C]	RPM		
		Min	Max	Mean
	50	111	132	119
GW0	60	141	160	151
	70	169	199	184
	50	135	153	145
GW4	60	183	199	190
	70	206	221	214
	50	113	152	134
GW8	60	174	205	194
	70	224	242	232

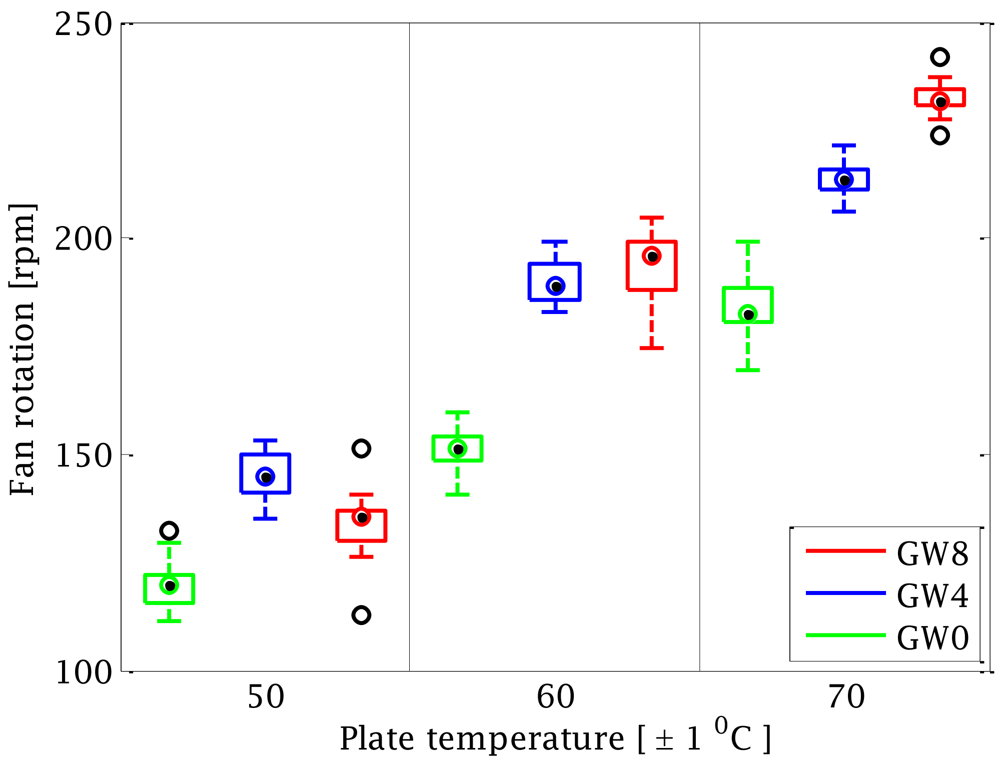

Fig. 6.11 Graphical results of counting the fan rotation.

6.5.2 Froude Number Analysis

The main purpose of experimental work is to find an optimum design and configuration. However, it is also desirable to compare the performance of the optimum design with the Manzanares SUPG. For example, how much the updraft velocity or the mechanical power could be increased or decreased by implementing the optimum design and configuration to the Manzanares SUPG. Because experimentation on a full-size model like the Manzanares prototype is often very expensive, thus a scale model that is smaller than the full-size are particular interest in design. Such model has been realized through a lab-scale SUPG. However, the flat collector configuration in the Manzanares SUPG was not tested in the current work. Rather than testing the flat collector configuration, numerical simulations for this particular configuration have been conducted to replace the result from experiment.

Results from the lab-scale SUPG must have principles link with the full-scale Manzanares SUPG. This relation is usually achieved through similarity analysis. If the dimensionless parameters are the same for the lab-scale SUPG as well as for the Manzanares SUPG, the flow and transport regimes are the same and the dimensionless results are also the same. There are several types of similarity such as geometric similarity, kinematic similarity, dynamic similarity, and thermal similarity. However, it may not possible to satisfy all the parameters for complete similarity. Moreover, each problem has its own specific requirement. Thus, it is useful to determine the dominant parameters in the problem and establish similitude [85].

In the current work, the geometric similarity is not satisfied since the geometry of lab-scale SUPG has been designed with purpose to find the optimum design by adjusting each geometrical parameter instead of testing the geometry scale down of the Manzanares SUPG. Although the geometry of lab-scale SUPG is not similar with the Manzanares SUPG, the similarity analysis can be conducted through dynamic similarity by recognizing the dominant parameters in the SUPG system. Two forces are dominant and act as the driving force in the SUPG system. They are inertia and buoyancy forces. These two forces can be combined into one dimensional parameter which is Froude number; representing the ratio of inertia and buoyancy forces. Thus by calculating the Froude number between the lab-scale SUPG and the Manzanares SUPG, a comparison analysis can be studied.

By comparing the Froude number of lab-scale SUPG with the Manzanares SUPG, increasing or decreasing of updraft velocity can be accessed. This is also directly related to the improvement of the total efficiency of SUPG system. Comparative study through similarity analysis via Froude number (Fr) is then proposed. The Froude number from the Manzanares SUPG is calculated for $\Delta T = 20\,K$ and for the same amount of temperature difference, the Froude number from the lab-scale SUPG is also computed from numerical simulation with flat collector configuration. The same Froude number means a similar flow in the solar tower of two different sizes and their corresponding buoyant flows regardless the shape of the solar collector. Mathematically Froude number is expressed as:

$$Fr(\Delta T) = \frac{{u_z}^2(\Delta T)}{g h_{tow}} \frac{\rho_a(\Delta T)}{\rho_{a_\infty} - \rho_a(\Delta T)} \tag{6.1}$$

The updraft velocity of Manzanares SUPG at $\Delta T = 20\,K$ is around 15 m/s with height of tower almost reaches 200 m. Therefore, the Froude number is obtained as

$$Fr(20)|_{Manzanares} = 1.73$$

For the same amount of temperature difference, the Froude number of optimum configuration obtained from the experiment on a lab-scale SUPG is

$$Fr(20)|_{Experiment} = 2.50$$

Table 6.3 Improvement calculation through Froude number analysis

	Manzanares (Full scale)	Optimum Configuration (Experiment)	Improvement
ΔT	20	20	
Fr(ΔT)	1.73	2.5	
Updraft Velocity	15 m/s	17.7 m/s	18 %
Mechanical Power	47.26 kW	77.65 kW	64 %
Tower Height	200 m	144 m	28 %

Froude number from the current experiment is higher than the Manzanares SUPG for the same amount of input indicated by the same condition of temperature difference. Hence, if the optimum configuration obtained from the current experiment is scaled up to the size of Manzanares SUPG, the updraft velocity is expected to be increased along with its mechanical power. How much the improvement of updraft velocity and mechanical power or even how much the tower could be reduced for the same amount of Froude number can be computed and the results are presented in Table 6.3. However, how to make sure that the Froude number does not change if the geometry is scaled up or scaled down, series of numerical simulation to compute the Froude number for Manzanares SUPG case is conducted. The result shows that there is a slight change in logarithmic trend of Froude number from full scale (1:1) configuration as shown in Fig. 6.9.

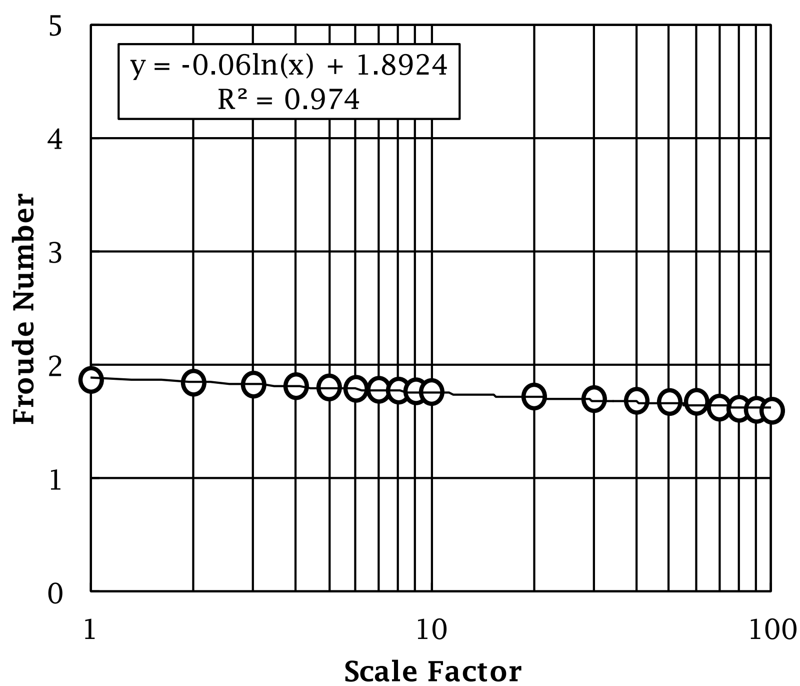

Fig. 6.12 Simulated Froude number of Manzanares SUPG for several geometry scales down showing that a slight changes when the geometry becomes smaller.

Table 6.4 Scale factor for calculation of Froude number in Fig. 6.12

Scale	Scale Factor	Fr	Scale	Scale Factor	Fr
1:1	1	1.87	1:10	10	1.76
1:2	2	1.84	1:20	20	1.72
1:3	3	1.83	1:30	30	1.70
1:4	4	1.81	1:40	40	1.68
1:5	5	1.80	1:50	50	1.67
1:6	6	1.79	1:60	60	1.67
1:7	7	1.78	1:70	70	1.62
1:8	8	1.77	1:80	80	1.61
1:9	9	1.77	1:90	90	1.60
1:10	10	1.76	1:100	100	1.60

Despite a slight change in Froude number when the geometry is scaled down, the comparative study can still be conducted because the expected Froude number from small scale SUPG should not deviate much from the full scale SUPG. Moreover, Froude number from optimum configuration obtained in this work has been able to produce a higher Froude number compare to the Manzanares SUPG, and if this configuration is scaled up thus the Froude number is expected not deviate much from its small scale model as shown by numerical simulation in Fig. 6.12. The scale factors corresponding to the geometry scale down of Manzanares SUPG in Fig. 6.12 are presented in Table 6.4. Froude numbers for several geometry scales down of Manzanares SUPG in Fig. 6.12 are simulated by using solar radiation as the input and the associated Froude numbers are presented for the maximum updraft velocity condition for all cases.

6.6 Remarks

Analysis regarding the optimum design and configuration of a lab-scale solar updraft power generator has been presented in this chapter. Discussion has been made through scrutinization of the geometrical influence to the updraft velocity. Furthermore the mechanical power is selected as parameter for selecting an optimum configuration. According to these study and analysis several conclusion can be listed as follows:

- The influence of collector height to the updraft velocity in collector type A does not shows an appreciable effects.
- The influence of collector height to the updraft velocity in collector type B shows that the case of 75 mm collector height had been able to gain more heat given to the system and utilize the heat to produces higher updraft velocity.
- The optimum tower diameter for both collector types is 100 mm. This selection is based on the heat gained by the associated tower diameter configuration and also the capability to produce higher updraft velocity.
- The longer the tower, the higher the updraft velocity will be, although there is no limit was observed in the current experiment.
- The optimum design and configuration has been obtained for experiment case B-75E50C-100-1500.
- The straight guide walls configuration implemented to the optimum configuration was able to attenuate the fluctuation of updraft velocity without significant changes in its magnitude.
- The curved guide walls configuration implemented to the optimum configuration – in particular for 8 curved guide walls configuration – has better performance compare to without guide walls configuration.

Finally the last concluding remark comes from Froude number analysis. If the optimum design and configuration obtained from the current experiment is implemented to the Manzanares SUPG case, thus an improvement in term of updraft velocity and mechanical power can be obtained which are around 18 % and 64 % respectively.

Power Potential Study

Chapter 7

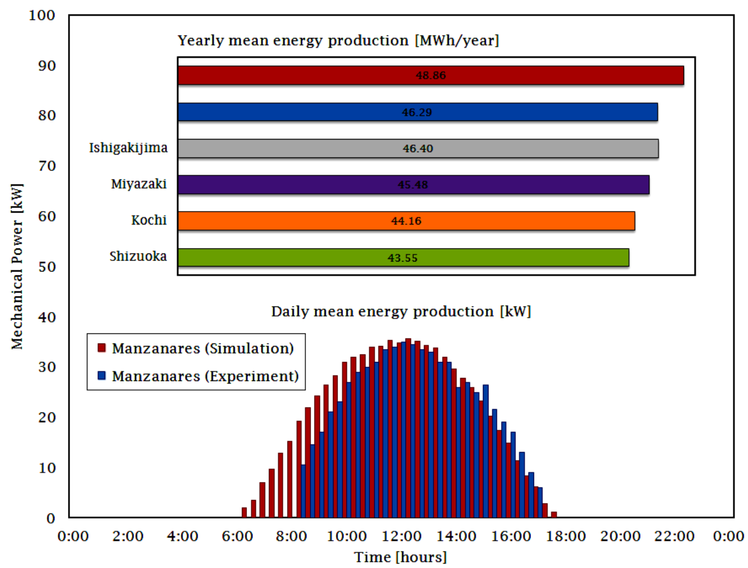

Chapter 7 provides the assessment concerning power potential of a solar updraft power generator through theoretical analysis and numerical simulation from Chapter 3 and Chapter 4. Validated model of solar updraft power generator developed in Chapter 3 and simulated in Chapter 4 is used in this chapter to estimate the amount of power generated for selected region in Japan and Indonesia. Therefore, real meteorological data such as solar radiation data and ambient air temperature data are implemented in the computer program so that the assessment regarding the power potential can be conducted. The results are presented in this chapter for 4 selected regions in Japan and 7 selected regions in Indonesia. Assessment to the power potential in Japan showed that the annual power production does not have significant difference with those in Spain, for the same geometry of the Manzanares SUPG. In contrast, in Indonesia the power production exhibits a larger energy production due stronger solar radiation in certain locations.

7.1 Introduction

Implementation of the developed mathematical model in Chapter 3 and numerical simulation in Chapter 4 is presented in this chapter. The implementation is in form of estimation of power potential of a solar updraft power generator for several regions in Japan and Indonesia with the same geometry as the Manzanares SUPG. So it can be interpreted as: how much the amount of power that could be produced if the same prototype of SUPG in Manzanares is built in Japan and Indonesia. Therefore, this chapter is devoted to assess that power by using real meteorological data in Japan and Indonesia.

The meteorological data used in this calculation are the mean global solar radiation either monthly or daily, and also mean ambient air temperature. These data are then fed to the computer program as input to predict the amount of power that could be produced for certain location depending on the meteorological data, especially solar radiation. Solar radiation has direct impact to the power production as calculated in Chapter 4. Thus, it is important to obtain a reliable source of solar radiation data.

Estimation of amount of mechanical power in Japan is carried out for 4 selected cities where the solar radiation is stronger than other locations. The monthly mean power production is estimated and it has been recognized that the southern part of Japan produce a favorable condition for power production since it has strongest solar radiation than the other 3 cities. Thus, the daily mean power production in this region is calculated for further investigation and analysis. The purpose of this investigation is to access the feasibility of a reduced scale solar updraft power generator as in Manzanares Spain. A 1:20 scale model is proposed and the amount of power is then estimated through numerical simulation by using mean daily solar radiation data as well as with mean daily ambient air temperature data at selected locations in the southern part of Japan.

Estimation of the power production in Indonesia is carried out for 7 selected locations where the solar radiation is also stronger than other locations. Each of this location represents one city in Major Island in Indonesia. For example: Pekanbaru for Sumatera Island, Semarang for Java Island, Kupang for Nusa Tenggara region, Pontianak for Kalimantan Island, Makassar for Sulawesi Island, Ambon for Maluku Island and Jayapura for Papua Island.

7.2 Power Potential of SUPG in Japan

The following chapter discusses the power potential of a solar updraft power generator for selected locations in Japan. Four cities were selected for theoretical calculation of monthly mean energy, namely, Shizuoka, Miyazaki, Kochi, and Ishigakijima, where solar radiation is stronger than other locations in Japan. These four cities are located in different regions of Japan; Honshu Island for Shizuoka, Kyushu Island for Miyazaki, Shikoku Island for Kochi, and Okinawa region for Ishigakijima. Locations of each area are marked in the solar radiation map (Fig. 7.1) provided by NEDO (New Energy and Industrial Technology Development Organization) [81].

The monthly mean meteorological data, necessary for calculation of theoretical energy output are provided by the Japan meteorological agency (JMA) [82] and atmospheric science data center NASA [83]. The solar radiation data, together with the monthly mean temperature are accessed through the JMA and NASA websites. These meteorological data serve as input for computation of theoretical energy output. Procedure to calculate the theoretical energy output is similar with those described in Chapter 4.

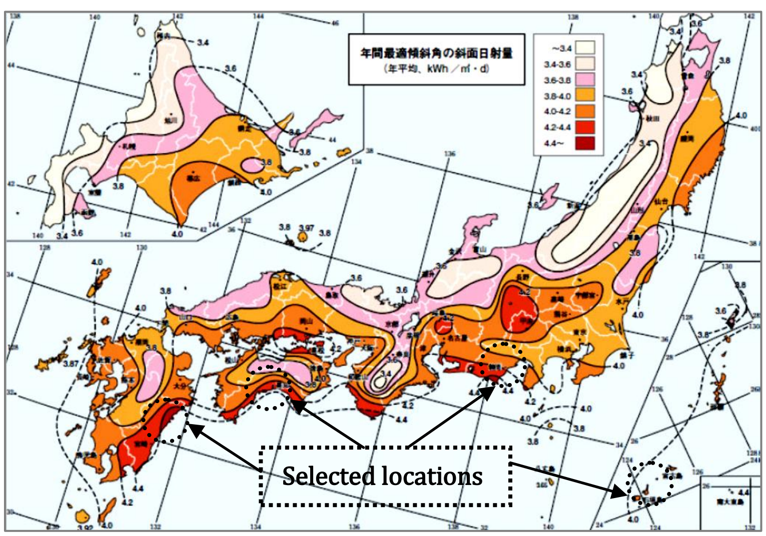

Fig. 7.1. Solar radiation map of Japan showing the selected locations for calculation of monthly mean energy production.

7.2.1 Monthly Mean Power Potential

Meteorological data are presented in Table 7.1 showing the monthly mean global solar radiation, and in Table 7.2 the monthly mean ambient air temperature is presented. From Table 7.1, the highest monthly mean global solar radiation in Shizuoka city appears in May, as for Miyazaki city it appears in July. For Kochi city, it is observed for two months: May and June while the Ishigakijima city appears in July. Also, Ishigakijima city is recognized to have the highest monthly mean global solar radiation among the other 3 cities.

Furthermore, the highest ambient air temperature for Shizuoka city is appears in August while the highest solar radiation appears in May. As for the remaining cities: Miyazaki, Kochi, and Ishigakijima, the highest ambient air temperature is also appears in July with the magnitude is around 29 [^{0}C].

Table 7.1 Monthly mean global solar radiation data for selected locations in Japan

Months	Monthly Mean Global Solar Radiation [MJ/m^2]			
	Shizuoka	Miyazaki	Kochi	Ishigakijima
January	10.9	11.5	10.9	10.1
February	11.9	12.1	12.3	13
March	15.9	15.2	15.3	14.8
April	18.6	19.3	19.7	12.4
May	20.5	20.6	20.4	17.9
June	15.3	12	13.8	22.1
July	17.6	21.7	20.4	24.3
August	19.2	20.8	19.6	20.4
September	17.2	16.5	15.4	19.8
October	10.9	12.3	11.9	14.4
November	10.7	11.6	10.5	10.9
December	9.7	10.1	9.8	6.3

Table 7.2 Monthly mean ambient air temperature data for selected locations in Japan

Months	Monthly Mean Ambient Air Temperature [^{0}C]			
	Shizuoka	Miyazaki	Kochi	Ishigakijima
January	5.7	6.8	5.8	18.7
February	7.3	9.4	7.8	21.2
March	13.3	13.8	12.7	22
April	15.4	15.6	14.8	22.3
May	19.2	20.3	19.9	26
June	22.6	23.2	23.2	29.2
July	26.4	29	28.1	29.5
August	28.4	29.3	29	29.7
September	25.4	24.9	24.9	28.5
October	21.1	20.6	20.7	25.7
November	13.1	13.5	12.9	22.6
December	8.2	8.1	7.4	18.7

Fig. 7.2 and Fig. 7.3 present the calculated mean energy output for 4 cities in Japan. Result of the Manzanares prototype, provided by Schlaich et al. [23] was used for comparison. Since the original meteorological data for Manzanares results was not available in the literature, thus we use meteorological data from the atmospheric science data center NASA for simulation. Simulation result produces 6% deviation from the experiment in term of yearly mean energy production. Despite different pattern of monthly mean energy production, the 4 cities in Japan have relatively small difference in term of yearly mean energy production.

Also, in Fig. 7.2 and Fig. 7.3 the monthly mean energy production at the Okinawa region shows different pattern with the other three locations. Despite the different pattern of monthly mean energy, the yearly mean energy production will not have a significant difference with those in Spain. This is the essential information from the analysis concerning power potential in Japan.

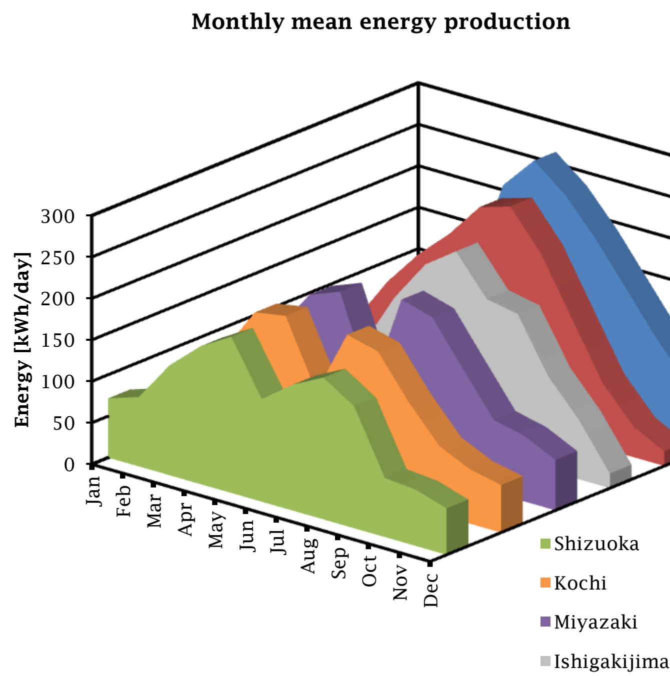

Fig. 7.2 Calculated monthly mean energy production in Japan.

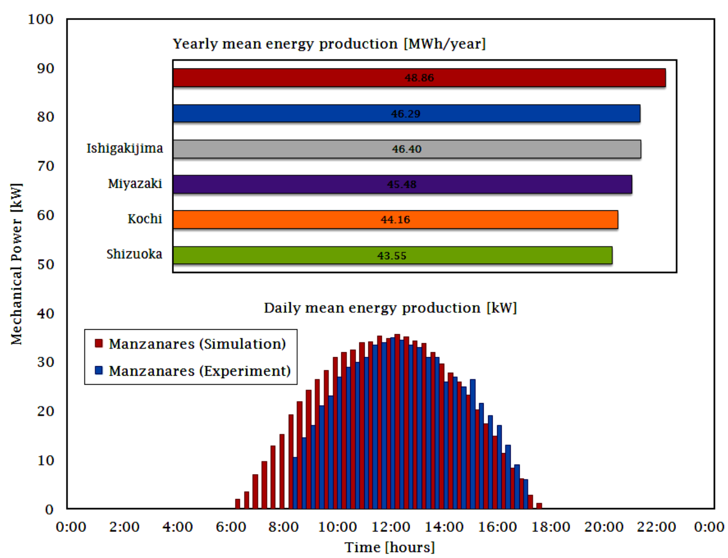

Fig. 7.3 Calculated yearly mean energy production In Japan and comparison of daily mechanical power between simulation and experiment.

7.2.2 Daily Mean Power Potential

The southern part of Japan is recognized to have a relative stronger solar radiation than the northern part. It has been demonstrated in the previous analysis regarding the monthly mean power potential in Japan. Thus, in this section the daily performance of a scale model SUPG is accessed via numerical simulation. The simulations were carried out for 1:20 scale model of Manzanares SUPG with dimension as follows:

Collector radius: 6.1 m

Collector Height: 0.1 m

Tower radius: 0.5 m

Tower height: 10 m

Results were computed for three consecutive days (Aug 2nd – Aug 4th, 2014) in selected locations at Okinawa prefecture i.e. Oku, Nago, and Naha as shown in Fig. 7.4.

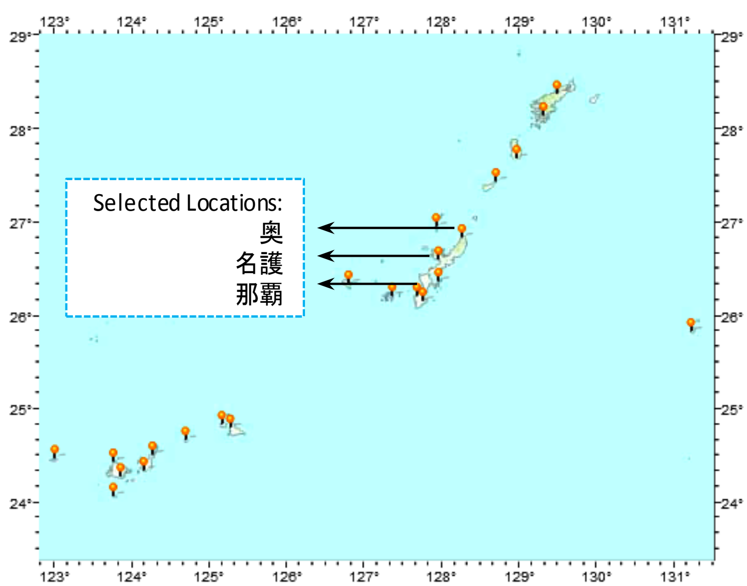

Fig. 7.4 A map of southern part of Japan showing three selected locations for daily power assessment of a 1:20 scale model Manzanares SUPG.

Fig. 7.5 presents the calculated mechanical power, updraft velocity as well as the updraft temperature. The results are presented as follows:

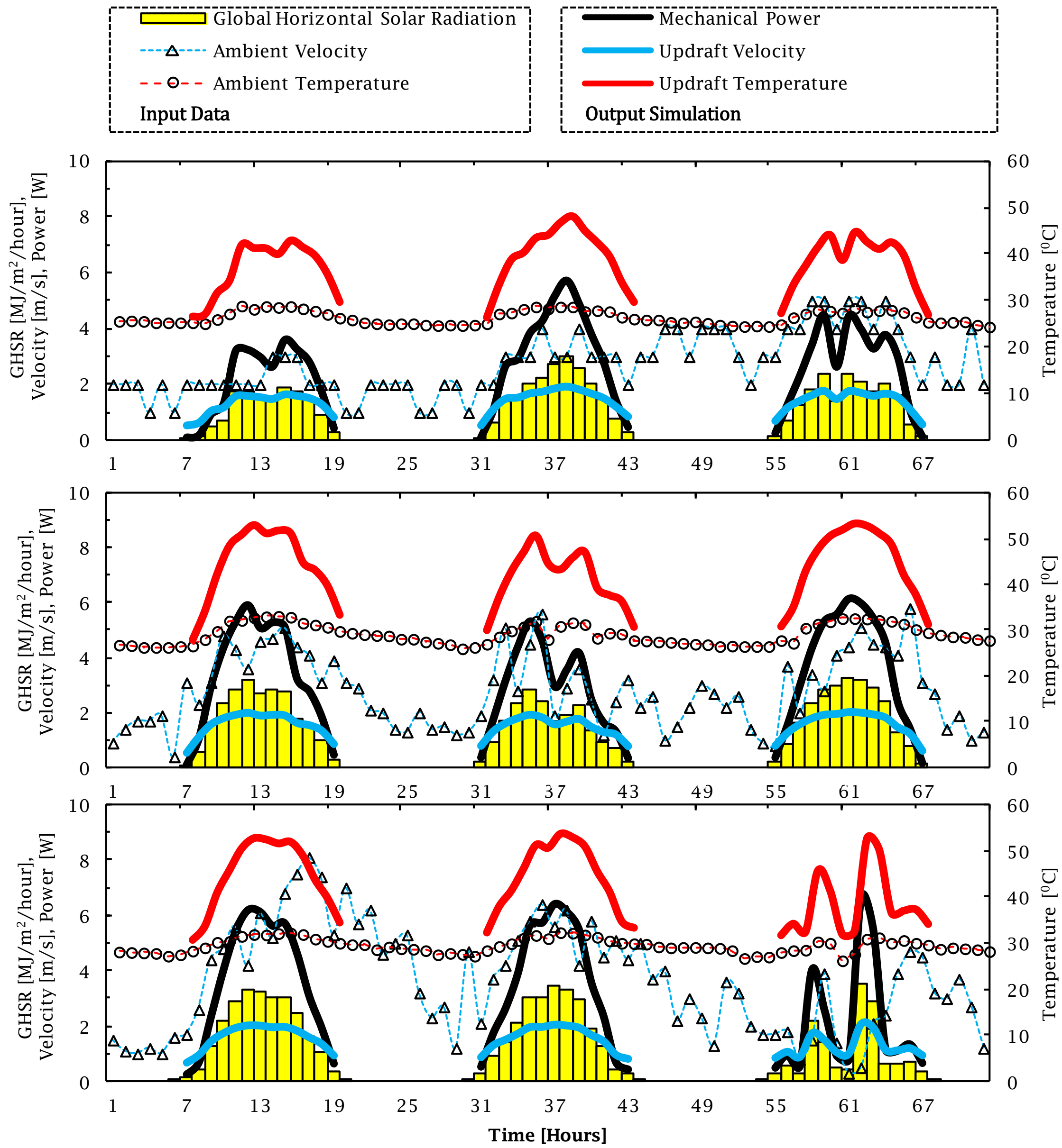

Fig. 7.5 Calculated daily mean mechanical power, updraft velocity, and updraft temperature for a 1:20 scale model Manzanares SUPG.

7.3 Power Potential of SUPG in Indonesia

In this section, the power potential of a solar updraft power generator for selected locations in Indonesia is accessed. It is recognized that solar radiation in Indonesia is much stronger than those in Japan and even from those in Spain as highlighted in the regional opportunity section in Chapter 1. Thus, it is interesting to know how much the power could be generated if a solar updraft power generator with the size of the Manzanares SUPG is built in Indonesia.

Therefore, 7 locations has been selected which are Pekanbaru in Sumatera Island, Semarang in Java Island, Kupang in Nusa Tenggara Regions, Pontianak in Kalimantan Island, Ambon in Maluku Island, and Jayapura in Papua Island. The locations of each city in the solar radiation map of Indonesia from SolarGIS database – which is provided by SolarGIS © 2013 GeoModel Solar [84] – can be seen in Fig. 7.6 as follow:

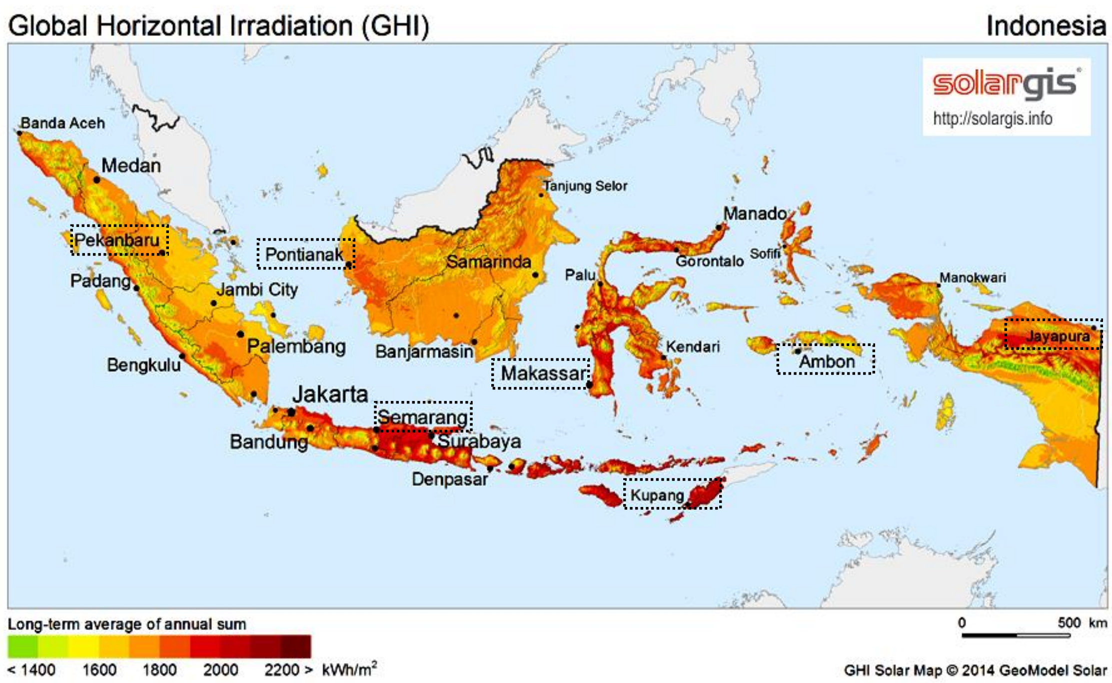

Fig. 7.6 Solar radiation map of Indonesia showing the selected locations for calculation of monthly mean energy production.

7.3.1 Monthly Mean Power Potential

Monthly mean power potential in Indonesia was calculated according to the meteorological data in Table 7.3 and Table 7.4. The first table shows the monthly mean global solar radiation for different months at 7 cities in major islands in Indonesia. The highest solar radiation for Pekanbaru is appears in March, and for Semarang it is appears in August. Kupang city has the strongest solar radiation in September while Pontianak and Makassar cities in July and August respectively. Ambon and Jayapura cities have the strongest solar radiation also in October and September respectively. The maximum record for ambient air temperature in Pekanbaru is appears in June while its highest solar radiation is in March. Semarang and Kupang cities have the highest ambient air temperature in October and November respectively. As for Pontianak and Makassar cities it is in July and May respectively. Ambon and Jayapura cities have the highest ambient air temperature in December and March respectively.

Table 7.3 Monthly mean global solar radiation data for selected locations in Indonesia

Months	Monthly mean global solar radiation [kWh/m^2/day]						
	Pekanbaru	Semarang	Kupang	Pontianak	Makassar	Ambon	Jayapura
January	5.41	4.85	5.56	5.17	5.3	5.52	4.95
February	5.85	5.04	5.96	5.17	5.47	5.57	5
March	6.06	5.14	6.37	5.11	5.74	5.49	4.9
April	5.54	5.15	5.78	5.08	5.99	5.37	4.9
May	4.87	5.21	5.96	5.03	5.96	5.17	4.8
June	5.02	5.59	5.88	4.98	5.92	5.16	4.76
July	5.21	6.1	6.7	5.31	6.41	5.3	4.89
August	5.15	6.64	7.16	5.3	6.74	6	4.99
September	4.75	6.21	7.54	5.2	6.65	6.02	5
October	4.39	5.05	7.41	4.99	5.51	6.25	4.93
November	3.99	4.9	6.68	4.85	4.92	6.2	4.87
December	4.63	5.15	4.6	5.27	5.36	6.04	4.57

Table 7.4 Monthly mean ambient air temperature data for selected locations in Indonesia

Months	Monthly Mean Ambient Air Temperature [^{0}C]						
	Pekanbaru	Semarang	Kupang	Pontianak	Makassar	Ambon	Jayapura
January	26.56	26.64	27.50	26.72	27.33	27.57	27.84
February	27.86	27.32	26.61	27.38	27.76	27.47	28.36
March	27.76	28.05	27.47	27.75	28.15	27.87	28.88
April	28.89	28.74	28.24	27.88	28.36	27.65	28.29
May	28.70	29.44	28.30	28.22	29.03	27.53	28.59
June	29.73	29.21	27.35	28.49	28.44	26.54	28.47
July	28.29	28.55	26.80	28.63	27.86	26.16	28.15
August	27.88	28.55	26.77	27.67	27.46	25.46	28.20
September	27.93	29.34	26.11	28.17	27.64	25.93	27.82
October	28.34	30.06	28.10	27.96	28.58	26.53	28.74
November	27.95	29.40	29.08	27.66	28.99	27.71	28.59
December	27.55	28.19	28.34	27.69	27.86	28.31	28.40

These meteorological data is then fed to the computer program developed in Chapter 4 to simulate the amount of power that could be produced by a solar updraft power generator with the same size as the Manzanares SUPG. Noted that the Manzanares SUPG in Spain was able to generate maximum monthly mean power around: 278 kWh/day [19].

The result of calculated monthly mean energy for selected locations in Indonesia is presented in Fig. 7.7. From this figure, it is observed that the monthly mean energy produced in Pekanbaru has the highest record in March. The fact that the solar radiation is also has the strongest record in this month, it produce a consistent results; the solar radiation has a direct effect to the power production. Furthermore, it is observed that the other cities have also produced the highest monthly mean energy in the same month of the strongest solar radiation which are August for Semarang, September for Kupang, August for Pontianak and Makassar, October for Ambon, and September for Jayapura. Thus, as expected, the monthly mean energy follow the monthly profile of solar radiation.

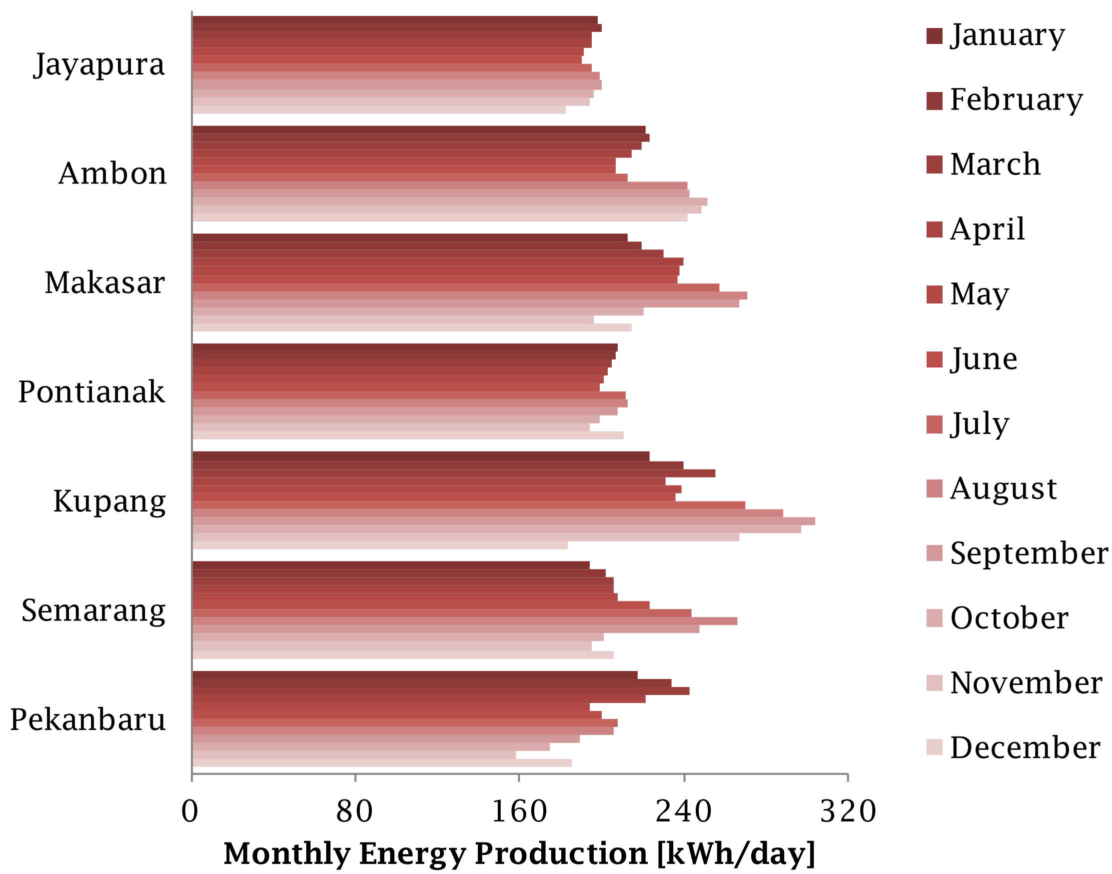

Fig 7.7 Calculated monthly mean energy production for 7 selected cities in major islands in Indonesia.

Furthermore, Pekanbaru city has the maximum monthly mean energy around 243 kWh/day in March and minimum around 159 kWh/day in November. The average is around 203 kWh/day for 1 year. Semarang city has the maximum monthly mean energy around 266 kWh/day in August and minimum around 195 kWh/day in January. As for Kupang city it exhibits a 304 kWh/day maximum monthly mean energy in September and 183 kWh/day of minimum monthly mean energy in December. Pontianak city has the maximum around 212 kWh/day in August and minimum around 194 kWh/day in November. Makassar city has maximum monthly mean energy around 271 kWh/day in

August and minimum around 197 kWh/day in November. The last two cities which are Ambon and Jayapura have the maximum energy around 252 kWh/day and 200 kWh/day in October and September respectively and minimum around 207 kWh/day and 182 kWh/day in June and December respectively. These data can be summarized by including the result from the Manzanares experiment as a comparison and it is presented in Table 7.5.

Table 7.5 Monthly mean energy production in Indonesia and Manzanares

City	Monthly mean energy [kWh/day]		
	Minimum	Maximum	Average
Pekanbaru	158.74	242.96	202.72
Semarang	194.51	265.73	216.44
Kupang	183.45	304.11	252.79
Pontianak	193.97	212.25	204.90
Makassar	196.09	270.64	233.44
Ambon	207.05	251.57	227.82
Jayapura	182.20	199.98	194.81
Manzanares	10	278	126.83

7.4 Remarks

Assessment of power potential for selected locations in Japan and Indonesia have been conducted and discussed in this chapter. Power production has been calculated from the validated model in Chapter 3 and 4 with the geometry same as the Manzanares SUPG. Based on the results in this study, the following conclusion can be made: 1) for power potential assessment in Japan: despite the different pattern of monthly mean energy, the yearly mean energy production will not have a significant difference with those in Spain. 2) for power potential assessment in Indonesia: The selected cities in Indonesia shows a higher monthly mean energy production compared to those in Spain. In particular a site like Kupang would produce more than 2 times the energy of the Manzanares SUPG in Spain.

Conclusions and Future Work Chapter 8

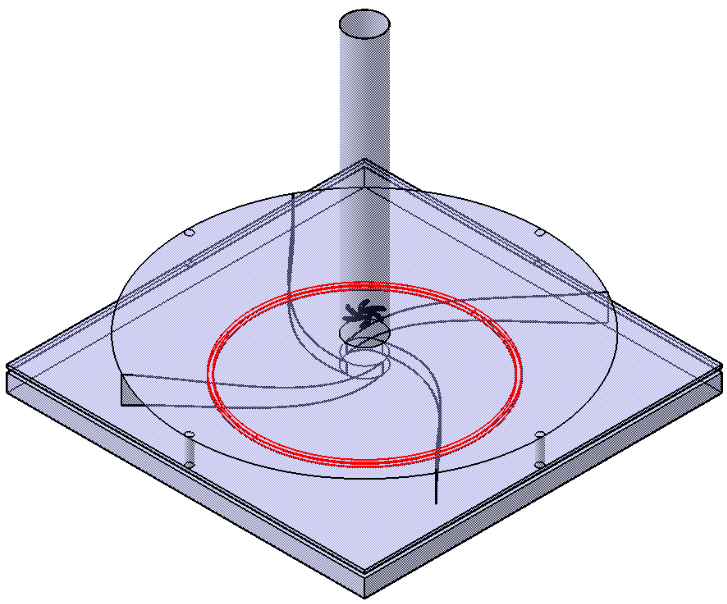

Chapter 8 is the last chapter in this dissertation. Series summary is listed in this chapter along with several suggestions concerning the future work. This dissertation begin with the research background emphasizing the global energy potential where solar radiation is promising as one of the future renewable energy resource and the solar updraft power generator is one of renewable energy facilities which offers an attractive concept in utilizing solar radiation. After that, mathematical model of a solar updraft power generator based on the Manzanares SUPG has been developed and solved in Chapter 3 and Chapter 4. The developed model and the developed computer program have been carried out based on the review works in Chapter 2. Further investigation on a lab-scale SUPG in Chapter 5 and Chapter 6 reveals that the optimum configuration can be obtained by considering the tower diameter and collector height design. Hence, the total efficiency of SUPG can be increased since optimum process is associated with an efficient process. In addition, implementation of SUPG has also been presented in Chapter 7.

8.1 Conclusions

Analysis on the global energy potential in Chapter 1 has pointed out that solar radiation is the biggest energy resource for both finite and renewable energy resources. Taking advantage of this condition, allow the solar updraft power generator as one of renewable energy facilities to join the existing commercial solar thermal power generator such as concentrating solar power and photovoltaic in utilizing solar radiation for power production. The solar updraft power generator offers attractive concepts in producing electrical energy: using solar radiation to increase the temperature of collector airflow, so it is less dense than the ambient air at the top of the tower, inducing buoyancy force in form of updraft flow which simultaneously entrains the collector airflow. Thus, this power generator can be regarded as a device to generate a consistent and controllable artificial wind. This concept is also offers an alternative to the existing commercial wind turbine where the oncoming wind necessary to rotate a giant turbine are often intermittent. Solar radiation as the source of heat in SUPG is also intermittent resource, but the absorbed heats during day can be stored to be used during night time.

Considering the previous compelling offers, a theoretical analysis is carried out to develop a mathematical model of a solar updraft power generator. This model is used not only to gain knowledge on the physical mechanism of energy conversion in SUPG, but also as prediction tools, for example to access the performance of SUPG in selected regions considering real meteorological data. Therefore, the development of mathematical model of SUPG is discussed and has been presented in Chapter 3. From this study, a thermal network model of a single collector in SUPG system is proposed to derive the heat balance equations. Furthermore, the simplified governing equation of fluid dynamics – where the following assumption has been enforced from the review work results in Chapter 2: steady 1D-axisymmetric flow, inviscid, Boussinesq fluid, and ideal gas fluid – are used to obtain the collector airflow equation, the tower airflow equation, and the turbine airflow equation. All of these equations are combined to form an integrated model of SUPG. The result is a set of nonlinear equation describing the transformation of solar radiation into heat-flux of collector airflow. This nonlinear set of equation is to be solved in Chapter 4 through numerical techniques.

In order to solve the nonlinear set of SUPG equation, iterative scheme is applied rather than solving all the governing equation simultaneously through computational fluid dynamics (CFD) procedure. The choice of a solver to be developed in this dissertation is also based on the review work in Chapter 2. Most of the earlier works implement the CFD procedure – either by commercial software or by in-house solver – to solve the governing equations of SUPG. However, the current work aims to develop a traceable, simple but accurate mathematical model along with its solvers, so that a reliable model can be obtained. Considering these constraint, it seems that description of nonlinear radiation problem in most CFD solvers is difficult to trace, for example transformation of solar radiation into thermal energy in form of heat-flux of collector airflow. Thus, the tractability of CFD radiation model motivate the current work to develop a solver based on the iterative scheme, which has been able to compute the amount of heat-flux contained in airflow as a result of energy conversion from solar radiation. Such solver has been discussed and presented in Chapter 4.

The performance of Manzanares SUPG and lab-scale SUPG have been accessed numerically. Both results have also been validated by comparing the result from numerical simulation with the experimental data where a good agreement has been obtained. Also, from the result of simulation it has been recognized that the optimum configuration of a SUPG cannot be obtained from geometrical point of view since the electrical energy produced by SUPG is in proportion to the size of collector and the tower. This statement is consistent with the other researcher results and thus the current opinion is that there is no optimum configuration of SUPG from geometrical point of view.

To clarify whether the optimum configuration can be observed in a SUPG system, series of experiment on a lab-scale SUPG was conducted and the results have been presented in Chapter 5. The experiment was carried out for two types of collector namely collector type A (which has the design divergent to the center) and collector type B (which has the design convergent to the center). For each type of collector, tower diameter, tower height, and collector height, were varied to form in total 72 combinations or experiment cases. From experimental optimization study, it has been noticed that the optimum configuration is indeed achievable considering the tower diameter, collector height, and collector design.

These three parameters must be carefully selected in order to guarantee a strong updraft flow will always be formed. Also, the longer the tower, the higher the updraft flow will be.

Further analysis in Chapter 6 showed that collector type B has been able to produce a higher updraft velocity compare to collector type A. Hence, an optimum design and configuration has been obtained for experiment case labeled as B-75E25C-100-1500. However the updraft velocity for this optimum configuration was highly fluctuated over time and temperature difference (between airflow and the ambient air). Therefore, although the highest updraft velocity has been achieved in the optimum configuration, but the highly fluctuate profile is not favorable for power production. It is desirable to have a smooth oncoming flow to the turbine so that the power produced by the turbine is also results in smooth profile. It has been recognized from the study in Chapter 6 that the fluctuation comes from the excessive heat losses at the edge of collector since the airflow opening distance exposing quite large volume of hot air to the surrounding ambient.

To overcome this issue, a hypothesis was made: concentrating the collector airflow through implementation of guide walls will enhance the inertia and buoyancy forces so that the entrainment effect towards the center of collector is higher than to the edge of collector and a smooth profile with higher magnitude of updraft velocity will be obtained. To test the feasibility of this solution, series of experiment was conducted for 3 three cases: without guide walls configuration, 4 straight guide walls configuration, and 8 straight guide walls configuration. The results showed that the straight guide walls were able to produce smoother profile of updraft velocity, but the higher magnitude was not observed. Thus only one part of the hypothesis has been confirmed.

Nevertheless, a higher updraft velocity is desirable since the objective of this work is to increase the total efficiency through an optimum design which will gives high magnitude of updraft velocity. Thus another hypothesis was made: rotating updraft flow will enhance the inertia and buoyancy forces so that the entrainment effect towards the center of collector is higher than the axial updraft flow. The rotating updraft flow was then realized by implementing series of curved guide walls in attempt to imitate a logarithm spiral design. In order to test the feasibility of this curved guide walls design, three set experiments were conducted and compared: without guide walls configuration, 4 curved guide walls configuration, and 8 curved guide walls configuration. Since the rotating updraft flow exhibits a fully 3 dimensional flow, thus it was considered not practical to track the movement of this columnar updraft vortices in attempt to measure its absolute velocity.

Instead of seeking and tracking the direction of this columnar updraft vortex inside the tower, an alternative measurement method was proposed and applied. A small fan was placed at the bottom of the tower and it will rotate due to the oncoming updraft flow either in form of axial updraft flow or vortex updraft flow. The rotations of this small fan were tracked by a high-speed camera – capable to produce image up to 1000 frame per second – so that the time taken to finish one rotation can be obtained and then converted into revolutions per minute (RPM). Experiment results exposed that the case of 8 curved guide walls exhibits a higher RPM in high temperature condition compare to the other two cases. It demonstrates that this configuration has the potential to increase the total efficiency of a solar updraft power generator.

As a closing discussion, Chapter 7 provides the implementation of a solar updraft power generator through the assessment of its power potential in selected locations. Two countries have been selected as case studies which are Japan and Indonesia. Calculated daily, monthly, and yearly mean energy production of a SUPG with the same size as the Manzanares SUPG have been presented for selected location in Japan. It was found that the yearly mean energy production in Japan will not have a significant difference with those in Spain despite the different pattern of monthly mean energy. Also, the monthly mean energy production in all selected city in Indonesia exhibit a higher value compare to those in Spain, in particular for a site like Kupang, would generate twice the energy than an identical one in areas such as Manzanares, Spain. The power production is sufficient for the needs of the isolated area in Indonesia and has the potential to feed the main electrical grid.

8.2 Suggestions for Future Work

Theoretical analysis along with experimental optimization process have been conducted in the current work as a part of bigger research project which aims to increase the total efficiency of a solar updraft power generator. It is undoubtedly that the effort to increase the total efficiency not only limited to geometry optimization as had been presented in this dissertation but also includes other alternative and innovative method such as designing thermal storage system for heat utilization at night, finding the best design and the best placement of wind turbine for maximum energy extraction, investigating the possibility of a hybrid power production concept by incorporating translucent photovoltaic as the solar collector and many other innovative methods. Further development can be almost ever ongoing; it is sometimes only limited by the cost of production. In the current work the analysis was focused to the geometry optimization because in the future work, an attempt to produces a strong updraft vortex which simultaneously sustain itself will be investigated. Therefore, the most essential requirement to produce a strong updraft vortex is having a strong axial updraft flow in the first place. Hence, the current work focused on finding the optimum design and configuration which always guarantee a strong axial updraft flow will be formed.

The larger project will be based on the following frameworks: 1) Concentrating the wind energy (axial updraft flow and updraft vortex flow) and 2) Concentrating the solar energy. The attempts to concentrate the wind energy, in particular for updraft vortex flow will be divided into two innovative concepts namely passive method and active method. In the passive method series of curved guide walls will be used to concentrate the vortex flow and this method had been partly investigated in the current work. The active method will involve a rotating impeller installed either at the bottom or the top of the tower in order to organize the updraft flow into a strong updraft vortex which of course requires far less energy to rotate the impeller. The placement of wind turbine will be investigated for circumferential arrangement surrounding the inner, middle or outer part of collector. In the effort to concentrate the solar energy, a thermal storage in form of guide walls will be proposed. This method can be realized by installing a series of parabolic solar thermal collector on top of the guide walls so that the other part of collector will still able to receive solar radiation. The mirror is arranged so the energy from sunlight is concentrated on the tube, which is heated to a high temperature. The tube which contains a working fluid is directly assembled and connected to the guide walls inside the collector, and the heat is immediately transferred to the airflow via convection process. The parabolic solar thermal collector is a well developed technology and the process has been proved to be economical with relative high thermal efficiency. Nevertheless, the door is kept open to the other concentrating method such as heliostats.

In the current work, there is several items need improvement and can be included in the list of future research as follows:

- In Chapter 3, the mathematical model was derived by employing several assumptions such as steady state condition, 1-dimensional axisymmetric flow, inviscid flow, Boussinesq fluid's, and ideal gas assumptions. The future research can be extended to develop a more complete model by incorporating the thermal inertia effects due to heat storage in the ground, thus the steady state assumption should not be included in the modeling process. Such model will be able to calculate the performance of a SUPG for 24 hours with inclusion of thermal inertia effects.
- In Chapter 4, computer program was developed by applying iterative scheme and solving the matrix equation numerically for steady state condition. The computer program can be modified to suit the unsteady condition due to incorporating the thermal inertia effects. Moreover, the developed computer program for lab-scale SUPG was used an average height of collector. Future research can be focused on developing the algorithm to incorporating the collector slope so that an accurate analysis can be attained.
- In Chapter 5, experiment was conducted for a lab-scale SUPG in laboratory room. An experiment on a small-scale SUPG for outdoor testing by using real solar radiation and exposing to the outdoor ambient air temperature can be conducted as a future work. Moreover, the current work used two types of collector. It can be extended for another type collector which is flat collector and compare the results with the other two collectors.
- In Chapter 6, the method to measure the magnitude velocity of a columnar updraft vortex can be improved. The small fan implemented in the current work was

situated inside a hand-made bearing system, thus the fan rotation may not gives a consistent result due inconsistency of the hand-made bearing system. Another measurement method should be carried out and compare with the current result in order to ensure its consistency and accuracy.

As final statement, research work presented in this dissertation can be summarized in Fig. 8.1 where an optimum design and configuration for experiment case B-75E25C-100-1500 with addition of 8 curved guide walls is displayed and will be used as proposed outdoor testing prototype for the future work.

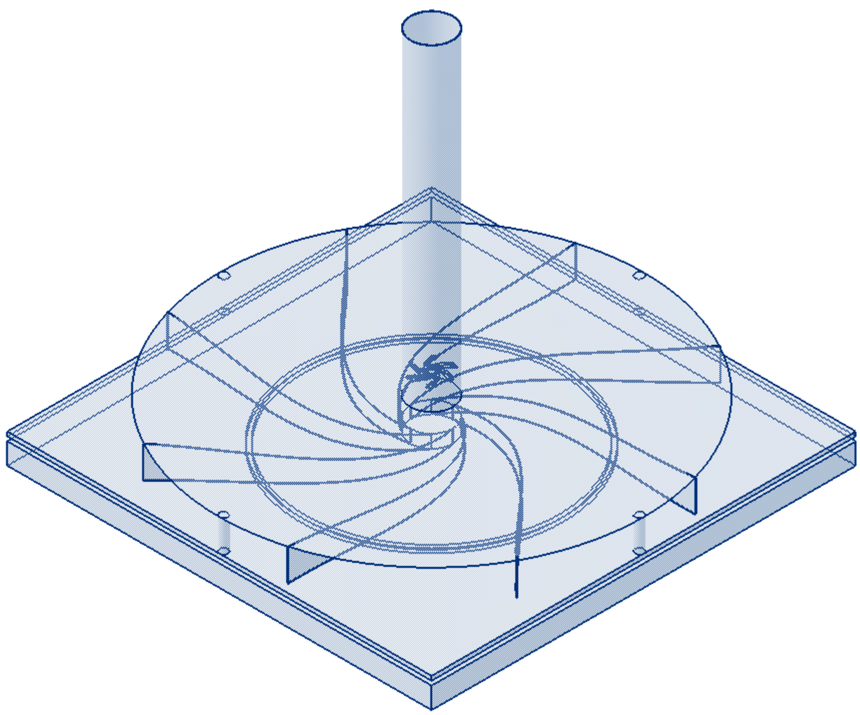

Fig. 8.1 Schematic drawing of optimum design and configuration of solar updraft power generator from the current works to be proposed as outdoor testing prototype.

References

[1] Haaf, W., Friedrich, K., Mayr, G., Schlaich, J., Solar Chimneys Part I: Principle & Construction of the Pilot Plant in Manzanares, *Int. J. Solar Energy*, Vol. 2, pp. 3-20, 1983.

[2] Haaf, W., Friedrich, K., Mayr, G., Schlaich, J., Solar Chimneys Part II: Preliminary Test Results from the Manzanares Pilot Plant, *Int. J. Solar Energy*, Vol. 2, pp. 141-161, 1984.

[3] http://solar-updraft-tower.com

[4] http://hyperion energy.com.au

[5] http://enviromission.com.au

[6] http://vortexengine.ca

[7] http://fmrl.gatech.edu/drupal/projects/solarvortex

[8] Perez R., Perez M., A Fundamental Look at Energy Reserves for the Planet, IEA SHC, Solar Update, 2009.

[9] http://eia.gov

[10] David J.C. McKay, *Sustainable Energy – Without the Hot Air*, 2009. Available in http://withouthotair.com

[11] M. Rumbayan, A. Abudureyimu, K. Nagasaka, “Mapping of solar energy potential in Indonesia using artificial neural network and geographical information system”, Renewable and Sustainable Energy Reviews, Vol. 16, 1437-1449, 2012.

[12] J. A. Duffie, W. A. Beckman, *Solar Engineering of Thermal Processes*, John Wiley & Sons, Inc: New Jersey, 2013.

[13] N. Pasumarthi, S. A. Sherif, “Experimental and theoretical performance of a demonstration solar chimney model – Part I: Mathematical model development”, International Journal of Energy Research, 22, 277-288, 1998.

[14] N. Pasumarthi, S. A. Sherif, “Experimental and theoretical performance of a demonstration solar chimney model – Part II: Experimental and theoretical results and economical analysis”, International Journal of Energy Research, 22, 443-461, 1998.

[15] M.M. Padki, S.A. Sherif, “On a simple analytical model for solar chimneys”, International Journal of Energy Research, 23, 345-349, 1999.

[16] A.J. Gannon, T.W. von Backstrom, “Solar chimney cycle analysis with system loss and solar collector performance”, Journal of Solar Energy Engineering, 122, 133-137, 2000.

[17] R.A. Hedderwick, *“Performance evaluation of a solar chimney power plant”,* Master Thesis, University of Stellenbosch, South Africa, 2000.

[18] T.W. von Backstrom, A.J. Gannon, “Compressible flow through solar power plant chimneys”, Journal of Solar Energy Engineering, 122, 138-145, 2000.

[19] J. Shclaich, R. Bergermann, W. Schiel, G. Weinrebe, “Design of commercial solar tower systems – Utilization of solar induced convective flows for power generation”, Proceedings of ISEC, Hawaii, 2003.

[20] M.A. dos S. Bernardes, A. Voß, G. Weinrebe, “Thermal and technical analyses of solar chimneys”, Solar Energy, 75, 511-524, 2003.

[21] J.P. Pretorius, *“Solar tower power plant performance characteristics”*, Master Thesis, University Stellenbosch, South Africa, 2004.

[22] H. Pastohr, O. Kornadt, K. Gurlebeck, “Numerical and analytical calculations of the temperature and flow field in the upwind power plant”, International Journal of Energy Research, 28, 495-510, 2004.

[23] J. Schlaich, R. Bergermann, W. Schiel, G. Weinrebe, “Design of commercial solar updraft tower systems – Utilization of solar induced convective flows for power generation”, Journal of Solar Energy Engineering, 127, 117-124, 2005.

[24] T. Ming, W. Liu, G. Xu, “Analytical and numerical investigation of the solar chimney power plant systems”, International Journal of Energy Research, 30, 861-873, 2006.

[25] T.W. von Backstrom, T.P. Fluri, “Maximum fluid power condition in solar chimney power plants – An analytical approach”, Solar Energy, 80, 1417-1423, 2006.

[26] A. Koonsrisuk, T. Chitsomboon, “Dynamic similarity in solar chimney modeling”, Solar Energy, 81, 1439-1446, 2007.

[27] X. Zhou, J. Yang, B. Xiao, G. Hou, “Experimental study of temperature field in a solar chimney power setup”, Applied Thermal Engineering, 27, 2044-2050, 2007.

[28] X. Zhou, J. Yang, B. Xiao, G. Hou, “Simulation of a pilot solar chimney thermal power generating equipment”, Renewable Energy, 32, 1637-1644, 2007.

[29] T.P. Fluri, T.W. von Backstrom, “Comparison of modeling approaches and layouts for solar chimney turbines”, Solar Energy, 82, 239-246, 2008.

[30] T.P. Fluri, T.W. von Backstrom, “Performance analysis of the power conversion unit of a solar chimney power plant”, Solar Energy, 82, 999-1008, 2008.

[31] A. Koonsrisuk, T. Chitsomboon, “A single dimensioneless variable for solar chimney power plant modeling”, Solar Energy, 83, 2136-2143, 2009.

[32] A. Koonsrisuk, T. Chitsomboon, “Accuracy of theoretical models in the predicition of solar chimney performance”, Solar Energy, 83, 1764-1771, 2009.

[33] A. Koonsrisuk, T. Chitsomboon, “Partial geometric similarity for solar chimney power plant modeling”, Solar Energy, 83, 1611-1618, 2009.

[34] C.B. Maia, A.G. Ferreira, R.M. Valle, M.F.B. Cortez, “Theretical evaluation of the influence of geometric parameters and materials on the behavior of the airflow in a solar chimney”, Computers & Fluids, 38, 625-636, 2009.

[35] M.A. dos S. Bernardes, T.W. von Backstrom, D.G. Kroger, “Analysis of some available heat transfer coefficients applicable to solar chimney power plant collectors”, Solar Energy, 83, 264-275, 2009.

[36] X. Zhou, J. Yang, B. Xiao, G. Hou, F. Xing, “Analysis of chimney height for solar chimney power plant”, Applied Thermal Engineering, 29, 178-185, 2009.

[37] A. Koonsrisuk, S. Lorente, A. Bejan, “Constructal solar chimney configuration”, International Journal of Heat and Mass Transfer, 53, 327-333, 2010.

[38] S. Nizetic, B. Klarin, “A simplified analytical approach for evaluation of the optimal ratio of pressure drop across the turbine in solar chimney power plants”, Applied Energy, 87, 587-591, 2010.

[39] A. Koonsrisuk, “Mathematical modeling of sloped solar chimney power plants”, Energy, 47, 582-589, 2012.

[40] A. Koonsrisuk, “Mathematical modeling of solar chimney power plants:, Energy, 51, 314-322, 2013.

[41] E. Gholamalizadeh, S.H. Mansouri, “A comprehensive approach to deisgn and improve a solar chimney power plant: A special case – Kerman project”, Applied Energy, 102, 975-982, 2013.

[42] M.O. Hamdan, “Analysis of solar chimney power plant utilizing chimney discrete model”, Renewable Energy, 56, 50-54, 2013.

[43] T. Ming, F. Meng, W. Liu, Y. Pan, R.K. de Richter, “Analysis of output power smoothing method of the solar chimney power generating system”, International Journal of Energy Research, 37, 1657-1668, 2013.

[44] X. Zhou, Y. Xu, S. Yuan, R. Chen, B. Song, “Pressure and power potential of sloped-collector solar updarft tower power plant”, International Journal of Heat and Mass Transfer, 75, 450-461, 2014.

[45] M.A. dos S. Bernardes, R.M. Valle, M.F.B. Cortez, “Numerical analysis of natural laminar convection in a radial solar heater”, International Journal of Thermal Science, 38, 42-50, 1999.

[46] T. Ming, W. Liu, G. Xu, Y. Xiong, X. Guan, Y. Pan, "Numerical simulation of the solar chimney power plant systems coupled with turbine", Renewable Energy, 33, 897-905, 2008.

[47] X. Zhou, Y. Yang, R.M. Ochieng, X. Li, B. Xiao, "Numerical investigation of a plume from a power generating solar chimney in an atmospheric cross flow", Atmospheric Research, 91, 26-35, 2009.

[48] T. Chergui, S. Larbi, A. Bouhdjar, "Thermo-hydrodynamic aspect analysis of flows in solar chimney power plants – A case study", Renewable and Sustainable Energy Reviews, 14, 1410-1418, 2010.

[49] R. Sangi, M. Amidpour, B. Hosseinizadeh, "Modeling and numerical simulation of solar chimney power plants", Solar Energy, 85, 829-838, 2011.

[50] T. Ming, R.K. de Richter, F. Meng, Y. Pan, W. Liu, "Chimney shape numerical study for solar chimney power generating systems", International Journal of Energy Research, 37, 310-322, 2013.

[51] T. Ming, X. Wang, R.K. de Richter, W. Liu, T. Wu, Y. Pan, "Numerical analysis on the influence of ambient crosswind on the performance of solar updraft power plant systems", Renewable and Sustainable Energy Reviews", 16, 5567-5583, 2012.

[52] F. Cao, H. Li, L. Zhao, T. Bao, L. Guo, "Design and simulation of the solar chimney power plants with TRNSYS", Solar Energy, 98, 23-33, 2013.

[53] H.F. Fasel, F. Meng, E. Shams, A. Gross, "CFD analysis for solar chimney power plants", Solar Energy, 98, 12-22, 2013.

[54] P. Guo, J. Li, Y. Wang, Y.Liu, "Numerical analysis of the optimal turbine pressure drop ratio in a solar chimney power plant", Solar Energy, 98, 42-48, 2013.

[55] T. Ming, J. Gui, R.K. de Richter, Y. Pan, G. Xu, "Numerical analysis on the solar updraft power plant system with a blockage", Solar Energy, 98, 58-69, 2013.

[56] W.B. Kratzig, "An integrated computer model of a solar updarft power plant", Advances in Engineering Software", 62-63, 33-38, 2013.

[57] W.B. Kratzig, “Physics, computer simulation and optimization of thermo-fluidmechanical processes of solar updarft power plants”, Solar Energy, 98, 2-11, 2013.

[58] E. Gholamalizadeh, M.H. Kim, “Three-dimensional CFD analysis for simulating the greenhouse effect in solar chimney power plants using a two-band radiation model”, Renewable Energy, 63, 498-506, 2014.

[59] H. Xu, F. Karimi, M. Yang, “Numerical investigation of thermal characteristics in a solar chimney projects”, Journal of Solar Energy Engineering, 136, 011008-011008-7, 2013.

[60] P. Guo, J. Li, Y. Wang, “Numerical simulation of solar chimney power plant with radiation model”, Renewable Energy, 62, 24-30, 2014.

[61] S.K. Patel, D. Prasad, M.R. Ahmed, “Computational studies on the effect of geometries parameters on the performance of a solar chimney power plant”, Energy conversion and Management, 77, 424-431, 2014.

[62] X, Zhou, Y. Xu, “Solar updraft tower power generation”, Solar Energy, 2014, doi: 10.1016/j.solener.2014.06.029

[63] X. Zhou, F. Wang, R.M. Ochieng, “A review of solar chimney power technology”, Renewable and Sustainable Energy Reviews, 14, 2315-2338, 2010.

[64] C. Ketlogetswe, J.K. Fiszdon, O.O. Seabe, “Solar chimney power generation project – The case for Botswana”, Renewable and Sustainable Energy Reviews, 12, 2005-2012, 2008. (Retraction published October 2012, “Retraction notice to Solar chimney power generation project – The case for Botswana”, Renewable and Sustainable Energy Reviews, 16, 6488, 2012.

[65] M. Najmi, A. Nazari, H. Mansouri, G. Zahedi, “Feasibility study and optimization of a typical solar chimney power plant”, Heat Mass Transfer, 48, 475-485, 2012.

[66] A.G. Ferreira, C.B. Maia, M.F.B. Cortez, R.M. Valle, “Technical feasibility assessment of a solar chimney for food drying”, Solar Energy, 82, 198-205, 2008.

[67] http://ren-energy.it

[68] M.W. Simpson, A.J. Pearlstein, A. Glezer, "Electric power generation using buoyancy-induced vortices", ICREPQ 13, Spain, March 2013.

[69] M. Zhang, X. Luo, T. Li, L. Zhang, X. Meng, K. Kase, S. Wada, C.W. Yu, Z. Gu, "From dust devil to sustainable swirling wind energy", Nature Scientific Reports, 5, 8322, 2015.

[70] J.D. Anderson, *Computational Fluid Dynamics – The Basics with Application*, McGraw-Hill, 1995.

[71] J.D. Anderson, *Fundamentals of Aerodynamics 5th Edition*, McGraw-Hill, 2007.

[72] Y.A. Cengel, J.M. Cimbala, R.H. Turner, *Fundamentals of Thermal-Fluid Sciences 4th Edition,* McGraw-Hill, 2012.

[73] G. Nellis, S. Klein, *Heat Transfer*, Cambridge University Press, 2009.

[74] P. Jamieson, *Innovation in Wind Turbine Design*, John Wiley & Sons, 2011.

[75] P. Jamieson, "Generalized limits for energy extraction in a linear constant velocity flow field", Wind Energy, 11, 445-457, 2008.

[76] W.C. Swinbank, "Long-wave radiation from clear skies". Quarterly Journal of the Royal Meteorological Society, 89 (381), 1963.

[77] T. L. Bergman, A. S. Lavine, F. P. Incropera, D. P. Dewitt, *Fundamentals of Heat and Mass Transfer 7th Edition,* John Wiley & Sons, 2011.

[78] S. Chapra, *Applied Numerical Methods with MATLAB for Engineers and Scientists*, McGraw-Hill: New York, [2005].

[79] S. Chapra, R. P. Canale, *Numerical methods for Engineers*, McGraw-Hill, 2010.

[80] T. Burton, N. Jenkins, D. Sharpe, E. Bossanyi, *Wind Energy Handbook 2nd Edition,* John Wiley & Sons, 2011.

[81] NEDO, Guidelines for PV Power Generation Field Test Project (Design, Construction and System), 2010.

[82] Tables of Monthly Climate Statistics, Retrieved from http://www.data.jma.go.jp, [Accessed 1/10/2014].

[83] NASA – SSE Release 6.0 Data Set, Retrieved from http://eosweb.larc.nasa.gov, [Accessed 14/1/2015].

[84] http://solargis.info [Accessed 14/6/2015].

[85] Y. Jaluria, *Design and Optimization of Thermal Systems 2nd Edition*, CRC Press, 2008.

Appendix A *Derivation of Governing Equations*

Principle of Conservation of Mass

The concept of mass flow can be described as follows. Consider a given area A arbitrarily oriented in a flow field. It is assumed that area is small enough in order to satisfy uniform velocity V distribution across A. If the fluid element with velocity V pass through area A, in time dt they have travelled a distance Vdt and have swept the shaded volume as shown in Fig. A1. The swept out volume is equal to the base area A multiply by the height of the cylinder $V_n dt$. V_n is the normal velocity component with respect to area A [71].

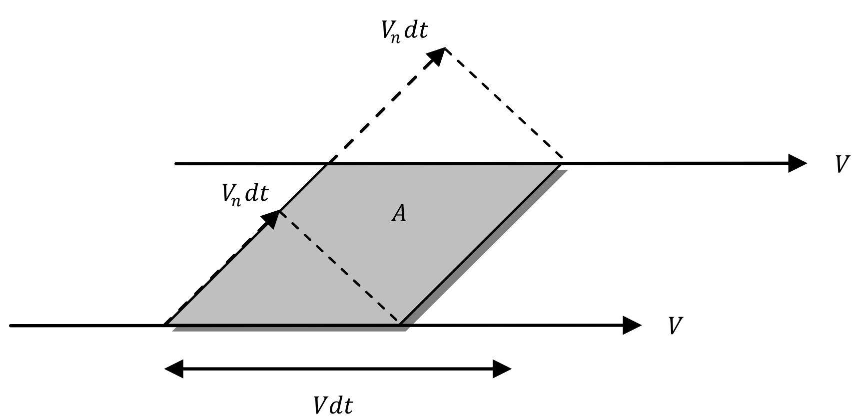

Fig. A1: Fluid element passes through area A in a flow field.

Therefore the mass of air which occupy the shaded volume can be deduced mathematically from the definition of air volume. Furthermore, the concept of mass flow rate can also be written as

$$Volume = \frac{m}{\rho} = A(V_n dt) \rightarrow m = \rho A(V_n dt)$$

$$\frac{d}{dt}(m) = \frac{d}{dt}\big(\rho A(V_n dt)\big) \rightarrow Mass\ flow\ rate = \dot{m} = \rho A V_n$$

Another important concept is the amount of mass flow rate $\dot{m}$ per unit area A. This is defined as mass flux and it can be obtained as

$$Mass\ flux = \frac{\dot{m}}{A} = \rho V_n$$

Hence it can be defined that the mass flux across an area with its velocity normal to that area is product of its density and velocity. The next process is to apply the mass conservation principle to a finite control volume fixed in space. The law of physic regarding conservation of mass stated that

Mass can be neither created nor destroyed

Its physical meaning is the net mass flow into the control volume through surface $\vec{S}$ must be equal to the time rate increase of mass inside control volume $\mathcal{V}$. Mathematical expression of an elemental net mass of fluid into the control volume through elemental surface $d\vec{S}$ can be deduced from the concept of mass flow rate as shown in Fig. A2 below

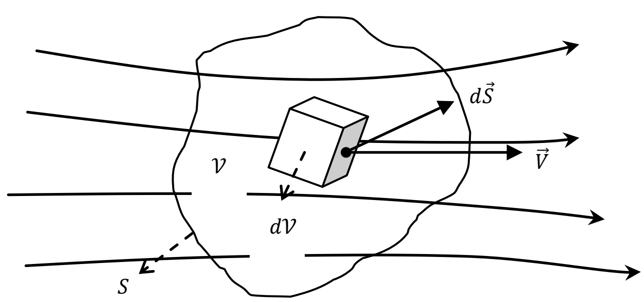

Fig. A2: A Finite control volume fixed in space.

From Fig. A2 the following sign convention is defined. If the velocity of fluid $\vec{V}$ leaving an elemental surface $d\vec{S}$, thus it is define as positive, and negative if the velocity of fluid $\vec{V}$ entering an elemental surface $d\vec{S}$. Therefore the mathematical expression of the net mass flow into the control volume through an elemental surface and its summation over surface $\vec{S}$ as surface integral can be written as

$$Elemental\ mass\ flow = \rho V_n d\vec{S} = \rho\left(-\vec{V}\right) \cdot d\vec{S}$$

$$Summation\ of\ elemental\ mass\ flow = -\oiint_{S} \rho\vec{V} \cdot d\vec{S}$$

Next evaluation is to express the time rate increase of mass inside control volume $\mathcal{V}$ into a mathematical equation. The mass occupy the elemental volume $d\mathcal{V}$ is product of its density ρ and elemental volume $d\mathcal{V}$. Its summation over volume $\mathcal{V}$ is expressed as volume integral. Hence

$$Elemental\ of\ mass\ inside\ control\ volume = \rho\, d\mathcal{V}$$

$$Summation\ of\ mass\ inside\ control\ volume = \oiiint_{\mathcal{V}} \rho\, d\mathcal{V}$$

From physical interpretation of mass conservation law which is the net mass flow into the control volume through a surface must be equal to the time of increase of mass inside that control volume, we can obtain the following equation, such that

$$-\oiint_{S} \rho\vec{V} \cdot d\vec{S} = \frac{\partial}{\partial t}\oiiint_{\mathcal{V}} \rho\, d\mathcal{V}$$

$$\oiiint_{\mathcal{V}} \frac{\partial\rho}{\partial t} d\mathcal{V} + \oiint_{S} \rho\vec{V} \cdot d\vec{S} = 0$$

The above equation is known as continuity equation and latter it will be used to derive the velocity equation inside the solar collector of a SUPG system. The continuity equation is in integral form. It can also be transformed into differential form by applying the Divergence or Gauss's theorem into the continuity equation. The theorem states that the outward flux of a velocity vector through a closed surface is equal to the volume integral of the divergence over the region inside the surface. The result is

$$\oiint_{S} \rho\vec{V}\cdot d\vec{S} = \oiiint_{\mathcal{V}} \left(\nabla\cdot\rho\vec{V}\right) d\mathcal{V}$$

Substitute the result from implementation of the Gauss's theorem, thus the continuity equation becomes

$$\oiiint_{\mathcal{V}} \frac{\partial\rho}{\partial t} d\mathcal{V} + \oiiint_{\mathcal{V}} \left(\nabla\cdot\rho\vec{V}\right) d\mathcal{V} = 0$$

Since the control volume is fixed in space, the derivative can be rearranged under the integral sign.

$$\oiiint_{\mathcal{V}} \left(\frac{\partial\rho}{\partial t} + \nabla\cdot\rho\vec{V}\right) d\mathcal{V} = 0$$

The equation must hold for any control volume, thus the integrand must be equal to zero and leads to differential or conservative form of continuity equation.

$$\frac{\partial}{\partial t}\rho + \left(\nabla\cdot\rho\vec{V}\right) = 0$$

Expanding the divergence term in the continuity equation, leads to an alternative form of continuity equation.

$$\left(\nabla\cdot\rho\vec{V}\right) = \vec{V}\cdot\nabla\rho + \rho\nabla\cdot\vec{V}$$

Substitute this relation gives

$$\frac{\partial}{\partial t}\rho + \vec{V}\cdot\nabla\rho + \rho\nabla\cdot\vec{V} = 0$$

From definition of total or material derivatives, continuity equation can be rewritten in form of its convective form. The material derivative D/Dt is defined as summation between local derivative $\partial/\partial t$ and convective derivative $\vec{V}\cdot\nabla$, and for $\vec{V} = u\cdot\vec{s} = u_1\hat{e}_1 + u_2\hat{e}_2 + u_3\hat{e}_3$, continuity equation becomes

$$\rho\left(\frac{\partial}{\partial t}+\vec{V}\cdot\nabla+\nabla\cdot\vec{V}\right)=0$$

$$\rho\left(\frac{\partial}{\partial t}+\{u_1\hat{e}_1+u_2\hat{e}_2+u_3\hat{e}_3\}\cdot\left\{\frac{\partial}{\partial s_1}\hat{e}_1+\frac{\partial}{\partial s_2}\hat{e}_2+\frac{\partial}{\partial s_3}\hat{e}_3\right\}+\nabla\cdot\vec{V}\right)=0$$

$$\rho\left(\frac{\partial}{\partial t}+\frac{\partial}{\partial s_1}u_1+\frac{\partial}{\partial s_2}u_2+\frac{\partial}{\partial s_3}u_3+\nabla\cdot\vec{V}\right)=\rho\left(\frac{D}{Dt}+\nabla\cdot\vec{V}\right)=0$$

$$\frac{D\rho}{Dt}+\rho\nabla\cdot\vec{V}=0$$

Finally, the mathematical forms of continuity equation in their integral form, partial differential form, and total differential form respectively can be summarized as follows

$$\oiiint_{\mathcal{V}}\frac{\partial\rho}{\partial t}d\mathcal{V}+\oiint_{S}\rho\vec{V}\cdot d\vec{S}=0\rightarrow Integral\ form$$

$$\frac{\partial}{\partial t}\rho+\left(\nabla\cdot\rho\vec{V}\right)=0\rightarrow Partial\ differential\ form$$

$$\frac{D\rho}{Dt}+\rho\nabla\cdot\vec{V}=0\rightarrow Total\ differential\ form$$

Principle of Conservation of Momentum

Physical principle of momentum equation implies that the force equal to the time rate of change of momentum. The second law of motion derived by Sir Isaac Newton gives an example of application of the principle of conservation of momentum. It is written as

$$Force\ equal\ to\ the\ time\ rate\ of\ change\ of\ momentum \rightarrow F = ma = \frac{d}{dt}\left(m\vec{V}\right)$$

where F is the force exerted on a body of mass m with acceleration a, $\vec{V}$ is the velocity vector of a body in motion.

It can be deduced that the general form of Newton's second law of motion can be represented by force equal to the time rate of change of momentum. Obtaining the expression of both force and momentum is the objective in this section. To do so, all the possible force acting on the fluid as it flows through a fixed control volume have to be listed in the first place. The body forces and surface forces are given in [71] as: 1) Body forces; any forces that act throughout the volume of a body (for example, gravity and electromagnetic forces). 2) Surface forces; any forces that act across an internal or external surface element in a material body (for example, pressure and shear stress).

Next evaluation is to express the body and surface forces into mathematical equation. If $\vec{F}_{body}$ is denoted as the total body forces exerted on the fluid per unit mass in the elemental control volume $d\mathcal{V}$ as in Fig. A2, thus the summation of the body force over the volume $\mathcal{V}$ can be written as

$$Elemental\ body\ forces\ inside\ control\ volume = \rho\vec{F}_{body}\, d\mathcal{V}$$

$$Summation\ of\ elemental\ \ body\ forces\ inside\ control\ volume = \oiiint_{\mathcal{V}} \rho\vec{F}_{body}\, d\mathcal{V}$$

As for the surface forces, if p is denoted as the total surface forces due to pressure acting on the elemental surface $d\vec{S}$ as in Fig. A2, thus the summation of the surface force over the area $d\vec{S}$ cab be expressed as

$$Elemental\ surface\ forces\ inside\ control\ volume = -p\ d\vec{S}$$

$$Summation\ of\ elemental\ surface\ forces\ inside\ control\ volume = -\oiint_S p\ d\vec{S}$$

Noted that the pressure acting inward to the surface $d\vec{S}$. The sign convention states that if any flux acting inward to the surface or volume thus it is denoted as negative sign and positive sign if acting outward to the surface.

Since the fluid have resistive force when subjected to some forces, or in other words the fluid is viscous thus the shear and normal viscous stresses are also exert a surface force. If $\vec{F}_{viscous}$ is denoted as the total viscous force exerted on the control surface, therefore the summation of the total force acting on a fluid as it flow through a control volume yields

$$\vec{F} = \oiiint_{\mathcal{V}} \rho \vec{F}_{body}\, d\mathcal{V} - \oiint_S p\ d\vec{S} + \vec{F}_{viscous}$$

Mathematical expression of the forces acting on a fluid as it flows through a control volume has been obtained. Next evaluation is to derive the mathematical expression for time rate of change of momentum of the fluid as it flows through a control volume. The concept of momentum flow rate is defined as the total time rate of change of momentum equal to the net flow of momentum out of control volume across surface $\vec{S}$ plus the time rate change of momentum due to unsteady fluctuations of flow properties inside control volume.

Mathematical expression of the net flow of momentum out of control volume across surface $\vec{S}$ can be obtain via the mass flow across the elemental surface $d\vec{S}$ multiply by its velocity $\vec{V}$. Therefore, the rate of momentum and its summation over a control volume can be expressed as

$$Elemental\ rate\ of\ momentum\ = \left(\rho\vec{V}\cdot d\vec{S}\right)\vec{V}$$

$$Summation\ of\ elemental\ rate\ of\ momentum = \oiint_S \left(\rho\vec{V}\cdot d\vec{S}\right)\vec{V}$$

Summation of elemental rate of momentum over the whole surface is combination of outflow of momentum and inflow of momentum. The integral representing the net outflow of momentum, thus if the integral has a positive value it means there is more momentum flowing out of the control volume. Conversely, if there is more momentum flowing into the control volume, the integral has a negative value.

As for the mathematical expression of the time rate change of momentum due to unsteady fluctuations of flow properties inside control volume, it can be obtained from the product of its momentum and elemental volume d$\mathcal{V}$. As shown before, momentum is expressed as fluid density ρ times its velocity $\vec{V}$ for elemental point of view. Summation of the elemental momentum contained in a control volume is defined as

$$Elemental\ of\ momentum\ inside\ control\ volume = (\rho\, d\mathcal{V})\vec{V}$$

$$Summation\ of\ momentum\ inside\ control\ volume = \oiiint_{\mathcal{V}} \rho\vec{V}\, d\mathcal{V}$$

Since the time rate of change of momentum of the fluid as it flow through a fixed control volume is defined as the sum of net flow of momentum out of control volume across surface $\vec{S}$ and time rate of change of momentum due to unsteady fluctuations of flow properties inside a control volume $\mathcal{V}$, thus the equation for momentum conservation is written by

$$\frac{d}{dt}(m\vec{V}) = \oiint_{S} (\rho\vec{V}\cdot d\vec{S})\vec{V} + \frac{\partial}{\partial t}\oiiint_{\mathcal{V}} \rho\vec{V}\, d\mathcal{V}$$

Substitute the expression of forces acting on a fluid and the time rate change of momentum as it flows through a control volume gives

$$\frac{d}{dt}(m\vec{V}) = \vec{F}$$

$$\oiint_{S} (\rho\vec{V}\cdot d\vec{S})\vec{V} + \frac{\partial}{\partial t}\oiiint_{\mathcal{V}} \rho\vec{V}\, d\mathcal{V} = \oiiint_{\mathcal{V}} \rho\vec{F}_{body}\, d\mathcal{V} - \oiint_{S} p\, d\vec{S} + \vec{F}_{viscous}$$

Momentum equation in integral form has been obtained. In order to derive its differential form, once again Gauss's theorem is applied. The velocity vector in the left hand side of momentum equation is written as $\vec{V} = u_1\hat{e}_1 + u_2\hat{e}_2 + u_3\hat{e}_3$, Hence it gives

1st Component

$$\oiint_S (\rho\vec{V}\cdot d\vec{S})u_1 = \oiint_S (\rho u_1\vec{V})\cdot d\vec{S} = \oiiint_V \nabla\cdot(\rho u_1\vec{V})\, d\mathcal{V}$$

2nd Component

$$\oiint_S (\rho\vec{V}\cdot d\vec{S})u_2 = \oiint_S (\rho u_2\vec{V})\cdot d\vec{S} = \oiiint_V \nabla\cdot(\rho u_2\vec{V})\, d\mathcal{V}$$

3rd Component

$$\oiint_S (\rho\vec{V}\cdot d\vec{S})u_3 = \oiint_S (\rho u_3\vec{V})\cdot d\vec{S} = \oiiint_V \nabla\cdot(\rho u_3\vec{V})\, d\mathcal{V}$$

Velocity vector in momentum equation can be written in Cartesian or cylindrical coordinate system instead of $\vec{V} = u_1\hat{e}_1 + u_2\hat{e}_2 + u_3\hat{e}_3$. However, a general unit vector $\vec{s} = \hat{e}_1, \hat{e}_2, \hat{e}_3$ is used in the current work to describe the spatial component of the momentum equation.

The pressure force in form of surface integral in the momentum equation can also be converted into integral volume with virtue of Gauss's theorem. The result is

$$\oiint_S p\, d\vec{S} = \oiiint_{\mathcal{V}} \nabla p\, d\mathcal{V}$$

The body force and the viscous forces in the momentum equation can be elaborated for each spatial component as

$$\vec{F}_{body} = (f_1)_{body}\hat{e}_1 + (f_1)_{body}\hat{e}_2 + (f_1)_{body}\hat{e}_3$$

$$\vec{F}_{viscous} = (f_1)_{viscous}\hat{e}_1 + (f_2)_{viscous}\hat{e}_2 + (f_2)_{viscous}\hat{e}_3$$

$$\nabla p = \left(\frac{\partial}{\partial s_1}\hat{e}_1 + \frac{\partial}{\partial s_2}\hat{e}_2 + \frac{\partial}{\partial s_3}\hat{e}_3\right)\cdot p = \frac{\partial p}{\partial s_1}\hat{e}_1 + \frac{\partial p}{\partial s_2}\hat{e}_2 + \frac{\partial p}{\partial s_3}\hat{e}_3$$

Therefore, the momentum equation for 1st component is then

$$\oiiint_{\mathcal{V}} \nabla \cdot \left(\rho u_1 \vec{V}\right) d\mathcal{V} + \oiiint_{\mathcal{V}} \frac{\partial \rho}{\partial t} u_1 \, d\mathcal{V} = \oiiint_{\mathcal{V}} \rho (f_1)_{body} \, d\mathcal{V} - \oiiint_{\mathcal{V}} \frac{\partial p}{\partial s_1} d\mathcal{V} + (f_1)_{viscous}$$

$$\oiiint_{\mathcal{V}} \nabla \cdot \left(\rho u_1 \vec{V}\right) d\mathcal{V} + \oiiint_{\mathcal{V}} \frac{\partial \rho}{\partial t} u_1 \, d\mathcal{V} + \oiiint_{\mathcal{V}} \frac{\partial p}{\partial s_1} d\mathcal{V}$$

$$- \oiiint_{\mathcal{V}} \rho (f_1)_{body} \, d\mathcal{V} - (f_1)_{viscous} = 0$$

$$\oiiint_{\mathcal{V}} \left(\nabla \cdot \left(\rho u_1 \vec{V}\right) + \frac{\partial \rho}{\partial t} u_1 + \frac{\partial p}{\partial s_1} - \rho (f_1)_{body} - (f_1)_{viscous} \right) d\mathcal{V} = 0$$

for 2nd component

$$\oiiint_{\mathcal{V}} \nabla \cdot \left(\rho u_2 \vec{V}\right) d\mathcal{V} + \oiiint_{\mathcal{V}} \frac{\partial \rho}{\partial t} u_2 \, d\mathcal{V} = \oiiint_{\mathcal{V}} \rho (f_2)_{body} \, d\mathcal{V} - \oiiint_{\mathcal{V}} \frac{\partial p}{\partial s_2} d\mathcal{V} + (f_2)_{viscous}$$

$$\oiiint_{\mathcal{V}} \nabla \cdot \left(\rho u_2 \vec{V}\right) d\mathcal{V} + \oiiint_{\mathcal{V}} \frac{\partial \rho}{\partial t} u_2 \, d\mathcal{V} + \oiiint_{\mathcal{V}} \frac{\partial p}{\partial s_2} d\mathcal{V}$$

$$- \oiiint_{\mathcal{V}} \rho (f_2)_{body} \, d\mathcal{V} - (f_2)_{viscous} = 0$$

$$\oiiint_{\mathcal{V}} \left(\nabla \cdot \left(\rho u_2 \vec{V}\right) + \frac{\partial \rho}{\partial t} u_2 + \frac{\partial p}{\partial s_2} - \rho (f_2)_{body} - (f_2)_{viscous} \right) d\mathcal{V} = 0$$

and for 3rd component

$$\oiiint_{\mathcal{V}} \nabla \cdot \left(\rho u_3 \vec{V}\right) d\mathcal{V} + \oiiint_{\mathcal{V}} \frac{\partial \rho}{\partial t} u_3 \, d\mathcal{V} = \oiiint_{\mathcal{V}} \rho (f_3)_{body} \, d\mathcal{V} - \oiiint_{\mathcal{V}} \frac{\partial p}{\partial s_3} d\mathcal{V} + (f_3)_{viscous}$$

$$\oiiint_{\mathcal{V}} \nabla \cdot \left(\rho u_3 \vec{V}\right) d\mathcal{V} + \oiiint_{\mathcal{V}} \frac{\partial \rho}{\partial t} u_3 \, d\mathcal{V} + \oiiint_{\mathcal{V}} \frac{\partial p}{\partial s_3} d\mathcal{V}$$

$$-\oiiint_{\mathcal{V}} \rho (f_3)_{body}\, d\mathcal{V} - (f_3)_{viscous} = 0$$

$$\oiiint_{\mathcal{V}} \left(\nabla \cdot \left(\rho u_3 \vec{V}\right) + \frac{\partial \rho}{\partial t} u_3 + \frac{\partial p}{\partial s_3} - \rho (f_3)_{body} - (f_3)_{viscous} \right) d\mathcal{V} = 0$$

The same reason as in continuity equation, since the equation must hold for any control volume, thus the integrand must be equal to zero and it yields

$$\nabla \cdot \left(\rho u_1 \vec{V}\right) + \frac{\partial \rho}{\partial t} u_1 = -\frac{\partial p}{\partial s_1} + \rho (f_1)_{body} + (f_1)_{viscous}$$

$$\nabla \cdot \left(\rho u_2 \vec{V}\right) + \frac{\partial \rho}{\partial t} u_2 = -\frac{\partial p}{\partial s_2} + \rho (f_2)_{body} + (f_2)_{viscous}$$

$$\nabla \cdot \left(\rho u_3 \vec{V}\right) + \frac{\partial \rho}{\partial t} u_3 = -\frac{\partial p}{\partial s_3} + \rho (f_3)_{body} + (f_3)_{viscous}$$

Expanding the time derivative terms in the momentum equation and divergence term by using vector identity for $i = 1 \dots 3$, leads to

$$\frac{\partial (\rho u_i)}{\partial t} = \rho \frac{\partial u_i}{\partial t} + u_i \frac{\partial \rho}{\partial t}$$

$$\left(\nabla \cdot \rho u_i \vec{V}\right) \equiv \nabla \cdot \left[u_i \left(\rho \vec{V}\right)\right] = u_i \nabla \cdot \left(\rho \vec{V}\right) + \left(\rho \vec{V}\right) \cdot \nabla u_i$$

Then substitute these relations, gives

$$\rho \frac{\partial u_1}{\partial t} + u_1 \left[\frac{\partial \rho}{\partial t} + \nabla \cdot \left(\rho \vec{V}\right)\right] + \left(\rho \vec{V}\right) \cdot \nabla u_1 = -\frac{\partial p}{\partial s_1} + \rho (f_1)_{body} + (f_1)_{viscous}$$

$$\rho \frac{\partial u_2}{\partial t} + u_2 \left[\frac{\partial \rho}{\partial t} + \nabla \cdot \left(\rho \vec{V}\right)\right] + \left(\rho \vec{V}\right) \cdot \nabla u_2 = -\frac{\partial p}{\partial s_2} + \rho (f_2)_{body} + (f_2)_{viscous}$$

$$\rho \frac{\partial u_3}{\partial t} + u_3 \left[\frac{\partial \rho}{\partial t} + \nabla \cdot \left(\rho \vec{V}\right)\right] + \left(\rho \vec{V}\right) \cdot \nabla u_3 = -\frac{\partial p}{\partial s_3} + \rho (f_3)_{body} + (f_3)_{viscous}$$

Analysis of continuity equation require that

$$\frac{\partial}{\partial t} \rho + \left(\nabla \cdot \rho \vec{V}\right) = 0$$

Therefore, the momentum equation reduces to

$$\rho\left(\frac{\partial u_1}{\partial t}+\vec{V}\cdot\nabla u_1\right)=-\frac{\partial p}{\partial s_1}+\rho(f_1)_{body}+(f_1)_{viscous}$$

$$\rho\left(\frac{\partial u_2}{\partial t}+\vec{V}\cdot\nabla u_2\right)=-\frac{\partial p}{\partial s_2}+\rho(f_2)_{body}+(f_2)_{viscous}$$

$$\rho\left(\frac{\partial u_3}{\partial t}+\vec{V}\cdot\nabla u_3\right)=-\frac{\partial p}{\partial s_3}+\rho(f_3)_{body}+(f_3)_{viscous}$$

From definition of material derivative of a scalar field $u_i(\vec{s},t), i=1\ldots3$

$$\frac{D}{Dt}=\frac{\partial u_i}{\partial t}+\vec{V}\cdot\nabla u_i$$

Thus, the momentum equation can be written as

$$\rho\frac{Du_1}{Dt}=-\frac{\partial p}{\partial s_1}+\rho(f_1)_{body}+(f_1)_{viscous}$$

$$\rho\frac{Du_2}{Dt}=-\frac{\partial p}{\partial s_2}+\rho(f_2)_{body}+(f_2)_{viscous}$$

$$\rho\frac{Du_3}{Dt}=-\frac{\partial p}{\partial s_3}+\rho(f_3)_{body}+(f_3)_{viscous}$$

Three set of momentum equation for 1st, 2nd, and 3rd components of spatial coordinate have been obtained and the continuity equation has also been derived. Currently there are three unknown parameters which are pressure p (1 variable), density ρ (1 variable) and velocity vector $\vec{V}$ (3 variables). In particular, there are total 5 unknown variables. The number of governing equation are three from momentum equation, and one from continuity equation, so the total equations are four with five unknown variables. In order to solve the equation simultaneously, one more equation which is needed which comes from the principle conservation of energy.

Principle of Conservation of Energy

Study regarding the energy conservation of fluid is always involving the science of thermodynamics. This is because the physical principle of conservation of energy in fluid is generally stated in first laws of thermodynamics. Physical principle of the energy conservation can be written as

Energy can be neither created nor destroyed; it can only change in form.

Despite the first law of thermodynamics may comes in many equivalent forms, it can be written in a single form equation as below

$$de = \delta q + \delta w$$

where dE is the change of total energy inside a control volume per unit mass, δq is the incremental of heat be added to the system from surroundings per unit mass, δw is the work done on the system by the surroundings per unit mass.

The rate change of energy of fluid as it flows through control volume can be expressed as summation between rate of heat added to fluid inside control volume from surroundings and rate of work done on fluid inside control volume. Thus,

$$\frac{d}{dt}(de) = \frac{d}{dt}(\delta q) + \frac{d}{dt}(\delta w) \rightarrow \; d\dot{e} = \delta\dot{q} + \delta\dot{w}$$

Next evaluation is to express the rate of heat transferred to or from the fluid and it can be represented as volumetric heating. For example, fluid inside a control volume is heated due to absorption of radiation originating outside the system or the local emission of radiation by the fluid itself. From Fig. A2, the mass contained within an elemental volume has been expressed as $\rho d\mathcal{V}$. Hence, the rate of heat addition to this volumetric mass is $\dot{q}(\rho d\mathcal{V})$. Summation over the complete control volume is then written as

$$Elemental\ rate\ of\ volumetric\ heating = \dot{q}(\rho d\mathcal{V})$$

$$Summation\ of\ elemental\ rate\ of\ volumetric\ heating = \oiiint_{\mathcal{V}} \dot{q}\rho \, d\mathcal{V}$$

As explained in the previous section that the fluid have resistive force, thus it is considered as viscous fluid, then heat can be transferred into the control volume by mean of thermal conduction and mass diffusion across the control surface. If $\dot{Q}_{viscous}$ is denoted as the rate of heat addition to the control volume due to viscous effects, therefore, the total rate of heat addition is

$$\delta\dot{q} = \oiiint_{\mathcal{V}} \dot{q}\rho \, d\mathcal{V} + \dot{q}_{viscous}$$

As for the rate of work done on fluid inside control volume, it can be expressed by examining the definition of work. Since work is force multiply by velocity, and from the analysis of momentum equation, forces are comes from body force and surface force, thus the rate of work done on the fluid inside the control volume can be analyzed as follows. Surface forces is comes from pressure and viscous effects. The pressure force expression on an elemental area $d\vec{S}$ has been derived in momentum balance section. In order to obtain the rate of work done on fluid inside control volume due to pressure force p, multiply this elemental surface pressure with velocity vector $\vec{V}$. Therefore, summation over the complete control volume is

Elemental work done on fluid inside control volume due to pressure force

$$= \left(-p \, d\vec{S}\right) \cdot \vec{V}$$

Summation of elemental work done on fluid inside control volume due to pressure force

$$= -\oiint_{S} \left(p \, d\vec{S}\right) \cdot \vec{V}$$

If the rate of work done on the fluid due to shear stress per unit mass on the control surface is denoted as $\dot{w}_{viscous}$, thus the total contribution from surface pressure to rate of work done on the fluid inside control volume is simply summation of these two parameters.

Next evaluation is to express contribution of body forces in the work done on the fluid. From previous section, the total body forces exerted on the fluid per unit mass is denoted as

$\vec{F}_{body}$, thus the work done is represented by volumetric body force multiply by velocity vector $\vec{V}$, it gives

Elemental work done on fluid per unit mass inside control volume due to body force

$$= \left(\rho \vec{F}_{body}\, d\mathcal{V}\right) \cdot \vec{V}$$

Summation of elemental work done on fluid per unit mass inside control volume due to body force

$$= \oiiint_{\mathcal{V}} \left(\rho \vec{F}_{body}\, d\mathcal{V}\right) \cdot \vec{V}$$

Expression of work done on fluid inside a control volume due to both surface and body forces has been obtained. However, these two forces are coming from the fluid. If there is work done on fluid which coming from external sources, thus it must be added into the energy equation. Example of external work is when a turbine placed inside the control volume and it rotate the fluid inside, then the rate of work per unit mass delivered by the turbine is defined as $\dot{w}_{external}$. Therefore, total rate of work done on fluid per unit mass inside a control volume can be written as

$$\delta \dot{w} = -\oiint_{S} \left(p\vec{V}\right) \cdot d\vec{S} + \oiiint_{\mathcal{V}} \rho\left(\vec{F}_{body} \cdot \vec{V}\right) d\mathcal{V} + \dot{w}_{viscous} + \dot{w}_{external}$$

One more component of the first law of thermodynamics needs to be formulated when applied to the fluid case. It is the rate of change of total energy inside a control volume per unit mass $d\dot{e}$. The total energy inside a control volume consists of internal energy, kinetic energy, and potential energy. However, the potential energy is implicitly stated in the body force expression, Therefore the rate of total energy inside a control volume per unit mass is written by

$$e = u + ke$$

$$\frac{\partial}{\partial t}(e) = \frac{\partial}{\partial t}(u) + \frac{\partial}{\partial t}\left(\frac{\vec{V}^2}{2}\right)$$

$$\dot{e} = \frac{\partial}{\partial t}\left(u + \frac{\vec{V}^2}{2}\right)$$

where u is the elemental internal energy per unit mass, ke is the elemental kinetic energy per unit mass.

During derivation of momentum equation, the time rate change of momentum is defined as the sum of net flow of momentum out of control volume across surface $\vec{S}$ and time rate of change of momentum due to unsteady fluctuations of flow properties inside a control volume $\mathcal{V}$. Therefore, similar concept is applied to the rate change of total energy inside a control volume. It can be expressed as the sum of net rate of flow of total energy across control surface $\vec{S}$ and the time rate of change of total energy inside control volume $\mathcal{V}$ due to transient fluctuations of the flow-field variables. It yields to the following definitions

Elemental net rate of total energy across control surface

$$= (\rho\vec{V} \cdot d\vec{S})e = (\rho\vec{V} \cdot d\vec{S})\left(u + \frac{\vec{V}^2}{2}\right)$$

Summation of elemental net rate of total energy across control surface

$$= \oiint_S (\rho\vec{V} \cdot d\vec{S})\left(u + \frac{\vec{V}^2}{2}\right)$$

Elemental time rate of change of total energy inside control volume

$$= (\rho\, d\mathcal{V})\dot{e} = (\rho\, d\mathcal{V})\frac{\partial}{\partial t}\left(u + \frac{\vec{V}^2}{2}\right)$$

Summation of elemental time rate of change of total energy inside control volume

$$= \oiiint_{\mathcal{V}} \rho \frac{\partial}{\partial t}\left(u + \frac{\vec{V}^2}{2}\right) d\mathcal{V}$$

Physical principle regarding conservation of energy stated that heat added to the fluid plus the rate of work done on the fluid is equal to the rate of change of total energy of the fluid as it flows through the control volume. This statement is an alternative way to say that energy is conserved. Now this physical principle can be expressed into a mathematical equation by combining the expression of heat added to the fluid via body or volumetric heating and due to viscous effects, work done on the fluid through body forces, surface forces, and viscous forces, and finally the rate change of total energy inside our control volume. The result is

$$\frac{\partial}{\partial t}\oiiint_{\mathcal{V}} \rho\left(u+\frac{\vec{V}^2}{2}\right)d\mathcal{V} + \oiint_{S}\left(\rho\vec{V}\cdot d\vec{S}\right)\left(u+\frac{\vec{V}^2}{2}\right) =$$

$$\oiiint_{\mathcal{V}} \dot{q}\rho\, d\mathcal{V} + \dot{q}_{viscous} - \oiint_{S}\left(p\vec{V}\right)\cdot d\vec{S} + \oiiint_{\mathcal{V}} \rho\left(\vec{F}_{body}\cdot\vec{V}\right)d\mathcal{V} +$$

$$\dot{w}_{viscous} + \dot{w}_{external}$$

Noted that, Example of work done from external sources is when a turbine placed inside our control volume then it rotates the fluid i.e. do work to fluid, thus $\dot{w}_{external}$ must be considered in the energy equation. If there is no turbine placed inside the control volume or no work coming from external source, then $\dot{w}_{external}$ can be neglected.

Differential form of our energy equation can also be obtained by following the same process during derivation of continuity and momentum equation. Altering the Gauss's theorem in order to convert surface integral to volume integral yields,

$$\oiint_{S}\left(\rho\vec{V}\cdot d\vec{S}\right)\left(u+\frac{\vec{V}^2}{2}\right) = \oiint_{S}\rho\left(u+\frac{\vec{V}^2}{2}\right)\vec{V}\, d\vec{S}$$

$$\oiint_{S}\rho\left(u+\frac{\vec{V}^2}{2}\right)\vec{V}\, d\vec{S} = \oiiint_{\mathcal{V}} \nabla\cdot\left[\rho\left(u+\frac{\vec{V}^2}{2}\right)\vec{V}\right]d\mathcal{V}$$

Conversion of surface integral into volume integral in the expression of pressure force result in

$$\oiint_{S}\left(p\vec{V}\right)\cdot d\vec{S} = \oiiint_{\mathcal{V}} \nabla\cdot\left(p\vec{V}\right)d\mathcal{V}$$

Substitute into energy equation yields

$$\frac{\partial}{\partial t}\oiiint_{\mathcal{V}} \rho\left(u+\frac{\vec{V}^2}{2}\right)d\mathcal{V} + \oiiint_{\mathcal{V}} \nabla\cdot\left[\rho\left(u+\frac{\vec{V}^2}{2}\right)\vec{V}\right]d\mathcal{V} =$$

$$\oiiint_{\mathcal{V}} \dot{q}\rho\, d\mathcal{V} + \dot{q}_{viscous} - \oiiint_{\mathcal{V}} \nabla\cdot\left(p\vec{V}\right)d\mathcal{V} + \oiiint_{\mathcal{V}} \rho\left(\vec{F}_{body}\cdot\vec{V}\right)d\mathcal{V} +$$

$$\dot{w}_{viscous} + \dot{w}_{external}$$

$$\oiiint_{\mathcal{V}} \frac{\partial}{\partial t}\left[\rho\left(u+\frac{\vec{V}^2}{2}\right)\right] + \nabla\cdot\left[\rho\left(u+\frac{\vec{V}^2}{2}\right)\vec{V}\right]d\mathcal{V} =$$

$$\oiiint_{\mathcal{V}} \left(\dot{q}\rho + \dot{q}_{viscous} - \nabla\cdot\left(p\vec{V}\right) + \rho\left(\vec{F}_{body}\cdot\vec{V}\right) + \dot{w}_{viscous} + \dot{w}_{external}\right)d\mathcal{V}$$

$$\oiiint_{\mathcal{V}} \frac{\partial}{\partial t}\left[\rho\left(u+\frac{\vec{V}^2}{2}\right)\right] + \nabla\cdot\left[\rho\left(u+\frac{\vec{V}^2}{2}\right)\vec{V}\right] - \dot{q}\rho - \dot{q}_{viscous} + \nabla\cdot\left(p\vec{V}\right) - \rho\left(\vec{F}_{body}\cdot\vec{V}\right)$$

$$- \dot{w}_{viscous} - \dot{w}_{external}\, d\mathcal{V} = 0$$

Since the equation must hold for any control volume, thus the integrand must be equal to zero and it gives

$$\frac{\partial}{\partial t}\left[\rho\left(u+\frac{\vec{V}^2}{2}\right)\right] + \nabla\cdot\left[\rho\left(u+\frac{\vec{V}^2}{2}\right)\vec{V}\right] =$$

$$\rho\dot{q} + \dot{q}_{viscous} - \nabla\cdot\left(p\vec{V}\right) + \rho\left(\vec{F}_{body}\cdot\vec{V}\right) + \dot{w}_{viscous} + \dot{w}_{external}$$

This equation can be written into total differential form by following the same procedure as in momentum equation. Once again, expanding the left hand side terms in the energy equation

$$\frac{\partial\left[\rho\left(u+\frac{\vec{V}^2}{2}\right)\right]}{\partial t} = \rho\frac{\partial\left(u+\frac{\vec{V}^2}{2}\right)}{\partial t} + \left(u+\frac{\vec{V}^2}{2}\right)\frac{\partial\rho}{\partial t}$$

$$\nabla\cdot\left[\rho\left(u+\frac{\vec{V}^2}{2}\right)\vec{V}\right] \equiv \nabla\cdot\left[\left(u+\frac{\vec{V}^2}{2}\right)\left(\rho\vec{V}\right)\right] =$$

$$\left(u + \frac{\vec{V}^2}{2}\right) \nabla \cdot (\rho\vec{V}) + (\rho\vec{V}) \cdot \nabla \left(u + \frac{\vec{V}^2}{2}\right)$$

Substitute these relations into energy equation and rearrange, gives

$$\rho \frac{\partial \left(u + \frac{\vec{V}^2}{2}\right)}{\partial t} + \left(u + \frac{\vec{V}^2}{2}\right)\left[\frac{\partial \rho}{\partial t} + \nabla \cdot (\rho\vec{V})\right] + (\rho\vec{V}) \cdot \nabla \left(u + \frac{\vec{V}^2}{2}\right) =$$

$$\rho\dot{q} + \dot{q}_{viscous} - \nabla \cdot (p\vec{V}) + \rho(\vec{F}_{body} \cdot \vec{V}) + \dot{w}_{viscous} + \dot{w}_{external}$$

Continuity equation state that

$$\frac{\partial}{\partial t}\rho + (\nabla \cdot \rho\vec{V}) = 0$$

Hence, the energy equation reduces to

$$\rho \frac{\partial \left(u + \frac{\vec{V}^2}{2}\right)}{\partial t} + (\rho\vec{V}) \cdot \nabla \left(u + \frac{\vec{V}^2}{2}\right) =$$

$$\rho\dot{q} + \dot{q}_{viscous} - \nabla \cdot (p\vec{V}) + \rho(\vec{F}_{body} \cdot \vec{V}) + \dot{w}_{viscous} + \dot{w}_{external}$$

From definition of material derivative of a scalar field

$$\frac{D}{Dt}\left(u + \frac{\vec{V}^2}{2}\right) = \frac{\partial}{\partial t}\left(u + \frac{\vec{V}^2}{2}\right) + \vec{V} \cdot \nabla \left(u + \frac{\vec{V}^2}{2}\right)$$

Thus, the energy equation can be written as

$$\rho \frac{D}{Dt}\left(u + \frac{\vec{V}^2}{2}\right) = \rho\dot{q} + \dot{q}_{viscous} - \nabla \cdot (p\vec{V}) + \rho(\vec{F}_{body} \cdot \vec{V}) +$$

$$\dot{w}_{viscous} + \dot{w}_{external}$$

Analysis of continuity and momentum equation result in 5 unknown variables with 4 equations. Now the equation has been added from the analysis of energy equation in order to solve all the unknown variables simultaneously. However, in energy equation, it also introduced one more unknown variable which is internal energy u. This condition leads to 6 unknown variables with 5 equations. Therefore one more equation is needed in order to solve the unknown variables simultaneously. This addition equation is obtained from the state equation. There are several model of state equations which able to describe the behavior of our fluid. In the current work, the ideal gas equation of state is implemented. Therefore, the next evaluation is about the equation of state.

Equation of state

Any equation that relates the pressure, temperature, and specific volume of a substance is called an equation of state [72]. Despite there are several equations of state has been established, the ideal gas equation of state for substances in the gas phase has been chosen in the current work. Discussion of state equation is presented based on the history of ideal gas thermometer in the Boyles's experiment.

Robert Boyle was conducted an experiment in 1662 with help of his assistant's Robert Hooke. He then discovered which now known as Boyle's law that the limit of the quantity pressure times the volume (in this work it is expressed as specific volume v) as we let pressure go to zero is constant, independent of the gas. This constant is function of the temperature thus it can be denoted as $f(T)$. Boyle's experiment was become foundation of determining the ideal gas thermometer.

From Boyle's law

$$\lim_{p \to 0}(pv) = constant = f(T)$$

Therefore a good reference in the making of temperature scale can be obtained since Boyle's law can be applied into any gas and it is only function of the temperature. For a substance i.e. gas, and have property $\lim_{p \to 0}(pv)$, a boiling point of water $\left(100\ {}^{0}C\right)$ and freezing point of water $\left(0\ {}^{0}C\right)$ as reference can be chosen. Hence, an interpolation scale in order to define how to go to one reference point to the other with $f(T)$ as property can be made. Since there are many ways to interpolate the reference point to the other, thus historically, it was chosen as linear interpolation and that turns out gives an important definition of absolute zero scale of temperature. It means that the value of the property $f(T)$ at the point of temperature reach absolute zero is also zero. Below the absolute zero the property p times v will be negative; however it is not possible, because negative pressure or volume does not make any sense. Therefore the absolute zero temperature is the lowest possible temperature that physically can make any sense. The value of absolute zero was defined in the Kelvin scale and in the Celcius scale was $-273.15\ {}^{0}C$. Since the boiling and freezing point of water as the reference is depend on the atmospheric pressure, thus, it is necessary to define the reference point that does not depends on the pressure. Those references are the absolute zero of temperature and a triplet point of water $f(T_{tp})$ where water exist in equilibrium of liquid, solid, and vapor phase. These two reference point are becomes a standard reference to define the temperature.

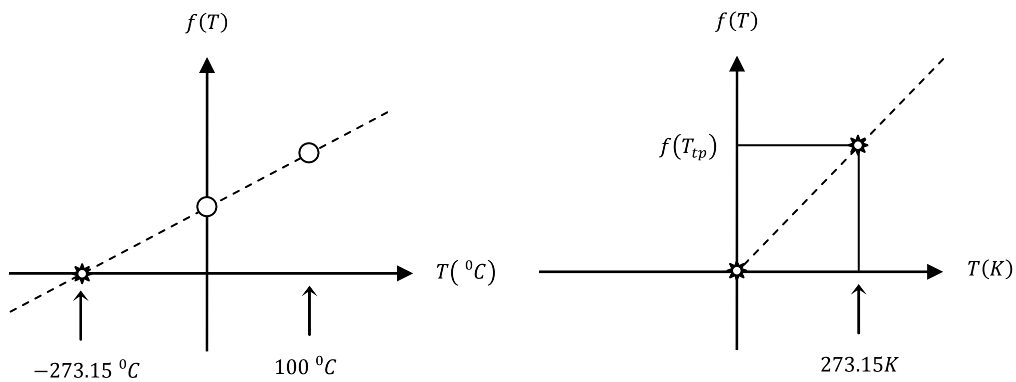

Fig. A3: Ideal gas thermometer scale.

Along with the ideal gas thermometer also comes out the ideal gas law. Because the slope of the linear interpolation during making the ideal gas thermometer as $f(T_{tp})$ can be utilized i.e. divided by 273.15. Therefore the linear equation can be written mathematically as follow

$$\frac{\Delta f(T)}{\Delta T} = \frac{f(T_{tp}) - 0}{273.15 - 0}$$

$$f(T) = \left(\frac{f(T_{tp})}{273.15}\right) T$$

Since $f(T)$ is defined as $f(T) = lim_{p\to 0}(pv)$, and defined the constant as R, gives

$$\lim_{p\to 0}(pv) = \left(\frac{f(T_{tp})}{273.15}\right) T = RT$$

The value of constant R is depends on type of gas but the relation is true for any gas, therefore the ideal gas law can be written as

$$p\mathcal{v} = RT$$

The ideal gas equation relates three states function together, the pressure, the volume and the temperature.

The energy balance equation is written as function of internal energy. Thus it is necessary to define this change of internal energy for the chosen equation of state which is the ideal gas model.

Internal Energy, Heat capacity, and Enthalpy of Ideal Gases

From first law of thermodynamics, the change of internal energy du inside a control volume $d\mathcal{V}$ is equal to the summation of heat added to the system δq, and work done to the system δw, all in per unit mass. It is also define that the total energy de contain in a system is summation of internal energy du and kinetic energy dke per unit mass. Define the internal energy as function of two states which are temperature and volume per unit mass, thus the partial change of our internal energy per unit mass can be expressed as

$$u(T, \mathscr{v}) \rightarrow du = \left(\frac{\partial u}{\partial T}\right)_{\mathscr{v}} dT + \left(\frac{\partial u}{\partial \mathscr{v}}\right)_{T} d\mathscr{v}$$

The equation simply says that differential of u is equal the partial differential of u with respect to T at constant $\mathscr{v}$, plus the partial differential of u with respect to $\mathscr{v}$ at constant T. The change of internal energy due to temperature at constant volume is turns out to be a heat capacity and for the second term will be analyzed to find out what this parameter is and how to define and relate them to the internal energy.

The heat capacity can be describes by using simple experiment as follows. Suppose we have a container gas with fixed volume and we do not let the gas escape then we heating this container with a candle. Second experiment is we also have a container full of gas and we also heating this container but now we put pressure to the container and we can say that pressure within the container do not change. The first experiment is representation of the change of internal energy due to heating process at constant volume, while the second experiment describes the heating process under constant pressure. Since heat capacity represents the heat storage capability of a material, thus mathematically

$$\delta q = c_{\mathscr{v}} dT$$

$$\delta q = c_p dT$$

Moreover, a great scientist James Prescott Joule conduct series of experiment that he suspect there must be a direct relationship between heat and work, and they are both forms of energy. Joule decide to conduct an experiment where the gas inside an isolated (adiabatic) container is rotates by a paddle wheel which represent work done to the system. What he found that the temperature increase at constant pressure condition. Thus relate these two parameters and the relationship between heat and work can be established.

Next evaluation is to express the second term in the differential expression of internal energy. Since this process is for constant volume condition, thus no work done on or by the system. Therefore in the first law of thermodynamics it can be obtained that

$$(du)_v = (\delta q)_v$$

Examine the differential expression of internal energy, for a constant volume process $dv = 0$, Thus, the relation between heat and the temperature through a proportional constant c_v can be written as

$$(du)_v = \left(\frac{\partial u}{\partial T}\right)_v dT + 0 = (\delta q)_v + 0$$

$$(\delta q)_v = c_v dT$$

Therefore now the heat capacity at constant volume can be measured. The internal energy now in form of

$$du = c_v dT + \left(\frac{\partial u}{\partial v}\right)_T dv$$

The second term is determined by the Joule free expansion experiment. This experiment was conducted for adiabatic condition, which allows no heat in or out. Inside the adiabatic container, there are two bulbs connected by a valve. First bulbs contain a gas with initial pressure and the other bulbs have vacuum pressure. By opening the valve thus the gas will flow to the vacuum until reach an equilibrium condition. This process was done with no heat and work involve. Thus $\delta w = \delta q = 0$ and it yields to

$$du = 0 = c_v dT_u + \left(\frac{\partial u}{\partial v}\right)_T dv_u$$

$$\left(\frac{\partial u}{\partial v}\right)_T = -c_v \frac{dT_u}{dv_u} = -c_v \left(\frac{dT}{dv}\right)_u$$

From Joule's experiment, he concludes that the change of temperature as he expands the gas is constant. In other words, the temperature did not increase measurably. This conclusion is true for ideal gas model, but incorrect for real gas. Hence, for constant $\left(\frac{\mathrm{dT}}{\mathrm{d}\mathcal{v}}\right)_{\mathrm{u}}$, we have the internal energy function of the temperature only. Furthermore

$$du = c_{\mathcal{v}} dT$$

$$\Delta u = \int c_{\mathcal{v}}\, dT$$

So, for ideal gas, the energy content is only dependent on the temperature. This relation also implies that our process is in constant volume process. However, the volume is not constant in this process in other words the pressure is constant in this process. Therefore it is necessary to find some sort equation of state that relates the heat going in or out of the system. From the first law of thermodynamics, equation for constant pressure process and reversible work is given as

$$du = \delta q + \delta w \rightarrow \int du = \int \delta q + \int \delta w$$

$$\Delta u = q + w = q_p - p\, \Delta \mathcal{v}$$

$$\Delta u + \Delta(p\mathcal{v}) = q_p$$

$$\Delta(u + p\mathcal{v}) = q_p$$

$$\Delta h = q_p \rightarrow dh = \delta q_p$$

where ΔH is known as enthalpy or Δh for specific enthalpy.

It can also be written in form of differential form, such that

$$h(p,T) \rightarrow dh = \left(\frac{\partial h}{\partial T}\right)_p dT + \left(\frac{\partial h}{\partial p}\right)_T dp$$

Next evaluation is to find what is the change of enthalpy due to temperature at constant pressure is. For reversible process with constant pressure $dh = \delta q_p$ and $dp = 0$, Thus

$$dh = \left(\frac{\partial h}{\partial T}\right)_p dT + 0 = \delta q_p$$

Relation of heat flow with temperature is

$$\delta q_p = c_p dT$$

So these two are equal to each other as well, which yields to

$$\left(\frac{\partial h}{\partial T}\right)_p = c_p$$

In order to define the second term in the differential expression of enthalpy, take a look at Joule-Thomson experiment. This experiment is an adiabatic experiment thus $\delta q = 0$, and the expression of work from this experiment is given by

$$w = -\Delta(pv)$$

$$\Delta u = \Delta q + \Delta w = 0 + -\Delta(pv)$$

$$\Delta u = -\Delta(pv)$$

Since $\Delta h = \Delta u + \Delta(pv)$, thus substitute the result of Joule-Thomson experiment yields

$$\Delta h = \Delta u + \Delta(pv)$$

$$\Delta h = -\Delta(pv) + \Delta(pv)$$

$$\Delta h = 0$$

Therefore, the process for constant enthalpy can be written as

$$dh = 0 = c_p dT + \left(\frac{\partial h}{\partial p}\right)_T dp$$

$$\left(\frac{\partial h}{\partial p}\right)_T = -c_p \left(\frac{dT}{dp}\right)_h = \mu_{JT}, \quad where\ \mu_{JT}\ is\ Joule - Thomson\ coefficient$$

Next evaluation is to relate the enthalpy for an ideal gas model. Notice that the internal energy is function of temperature only. Substitute the equation of state and the internal energy into enthalpy equation gives

$$h = u + pv$$

$$h = u + RT$$

So for an ideal gas, it only cares about temperature and it gives $\mu_{JT} = 0$. Previous work on the relation between internal energy, heat capacity, and enthalpy for ideal gas model can be summarized as follows

$$du = \frac{\partial u}{\partial T} = c_v dT$$

$$dh = \frac{\partial h}{\partial T} = c_p dT$$

Now the energy equation can be expressed for ideal gas model. Thus all the previous explanation concerning derivation of governing equations for fluid dynamics in differential form plus one equation of state can be summarized as follows:

Conservation of mass

$$\frac{\partial}{\partial t}\rho + \left(\nabla \cdot \rho\vec{V}\right) = 0$$

Conservation of momentum

$$\frac{\partial}{\partial t}\rho u_1 + \nabla \cdot \left(\rho u_1 \vec{V}\right) = -\frac{\partial p}{\partial s_1} + \rho (f_1)_{body} + (f_1)_{viscous}$$

$$\frac{\partial}{\partial t}\rho u_2 + \nabla \cdot \left(\rho u_2 \vec{V}\right) = -\frac{\partial p}{\partial s_2} + \rho (f_2)_{body} + (f_2)_{viscous}$$

$$\frac{\partial}{\partial t}\rho u_3 + \nabla \cdot \left(\rho u_3 \vec{V}\right) = -\frac{\partial p}{\partial s_3} + \rho (f_3)_{body} + (f_3)_{viscous}$$

Conservation of energy

$$\frac{\partial}{\partial t}\left[\rho\left(u + \frac{\vec{V}^2}{2}\right)\right] + \nabla \cdot \left[\rho\left(u + \frac{\vec{V}^2}{2}\right)\vec{V}\right] =$$

$$\rho\dot{q} + \dot{q}_{viscous} - \nabla \cdot \left(p\vec{V}\right) + \rho\left(\vec{F}_{body} \cdot \vec{V}\right) + \dot{w}_{viscous} + \dot{w}_{external}$$

State equation

$$p = \rho R T$$

The last four equations are used in the analysis of mathematical model of solar updraft power generator and presented in Table 3.1 in Chapter 3.

Pressure Equation

Recall the momentum equation and write for one spatial direction only which is radial direction, thus

$$\frac{\partial}{\partial t}\rho u_r + \nabla \cdot \left(\rho u_r \vec{V}\right) = -\frac{\partial p}{\partial r} + \rho (f_r)_{body} + (f_r)_{viscous}$$

The following assumptions are applied to the momentum equation

Steady state condition → $\partial/\partial t\,(\quad) = 0$

Inviscid flow → $(f_r)_{viscous} = 0$

Exclusion of body force → $(f_r)_{body} = 0$

Radial flow → circumferential and axial velocities $(u_\theta \; and \; u_z) = 0$

Implementing the above assumptions to the momentum equation and write in cylindrical coordinate yields

$$\left(\frac{\partial}{\partial r}\hat{e}_r + \frac{1}{r}\frac{\partial}{\partial \theta}\hat{e}_\theta + \frac{\partial}{\partial z}\hat{e}_z\right) \cdot (\rho u_r [u_r \hat{e}_r + u_\theta \hat{e}_\theta + u_z \hat{e}_z]) = -\frac{\partial p}{\partial r}$$

$$\rho u_r \frac{\partial u_r}{\partial r} = -\frac{\partial p}{\partial r}$$

This is a first-order nonlinear partial differential equation. The equation itself says that the total pressure for a steady inviscid flow must be constant along a streamline. Since the total pressure for a steady inviscid flow is summation between the static and dynamic pressure, thus it is essential to discuss these pressure as well in the next paragraph.

The concept of summation between static and dynamic pressure are constant along a streamline is always associated with the work done by Johann Bernoulli, Daniel Bernoulli, and Leonhard Euler in the early part of eighteenth century. This is because it was the first time people understood comprehensively the relation between pressure and velocity for a steady inviscid and in particular incompressible flow. From such concept, the inviscid momentum equation can be rearranged in order to form the summation of static pressure and dynamics pressure equal to total pressure and must be constant along a streamline. Such that

$$static\ pressure + dynamic\ pressure = total\ pressure$$

$$\frac{\partial p}{\partial r} + \rho u_r \frac{\partial u_r}{\partial r} = p_{total}$$

Next evaluation is to identify which part of the above equation is associated with static and dynamic pressure respectively. This is because it is desirable to solve for $\partial p/\partial r$, and a clear understanding which pressure this terms is associated must be established in the first place. It is obvious that $\partial p/\partial r$ is not a total pressure, and also not a dynamic pressure, since the dynamic pressure is usually associated with the velocity of the flowing fluid. Thus from first interpretation $\partial p/\partial r$ is a static pressure, and hence the momentum equation can be solved for static pressure along the solar collector. In order to gain a better understanding, take a look into the formal definition of static pressure given by Anderson [71] as a measure of the purely random motion of molecules in the gas; it is the pressure we feel when we ride along with the gas at the local flow velocity. Therefore, $\partial p/\partial r$ is the static pressure along solar collector. In order to solve for static pressure along solar collector, the partial derivatives term has to be converted into the total derivative form. By doing so, integrate them along the radius and multiplying both sides of the momentum equation with dr and it yields

$$-\frac{\partial p}{\partial r} dr = \rho u_r \frac{\partial u_r}{\partial r} dr$$

From definition of total derivative of a function

$$dp = \frac{\partial p(r)}{\partial r} dr, \qquad du_r = \frac{\partial u_r(r)}{\partial r} dr$$

Thus, the momentum equation becomes

$$-dp = \rho u_r (du_r)$$

The velocity in the momentum equation can also be written as

$$u_r du_r = \frac{1}{2} d({u_r}^2)$$

The above relationship must be valid if the pressure and velocity are function of radius only. Thus, by integrating both sides from r to r_{col} and substitute the expression of velocity in terms of mass flow rate, the result is

$$\int_{p(r)}^{p(r_{col})} dp = \frac{\rho}{2}\int_{u_r(r)}^{u_r(r_{col})} d({u_r}^2)$$

$$-[p(r_{col}) - p(r)] = \frac{\rho}{2}[{u_r}^2(r_{col}) - {u_r}^2(r)]$$

$$-\Delta p(r) = \frac{\rho}{2}\left[\frac{\dot{m}^2(r_{col})}{{\rho_a}^2(T_a){A_{col}}^2(r_c)} - \frac{\dot{m}^2(r)}{{\rho_a}^2(T_a){A_{col}}^2(r)}\right]$$

where r is the initial radial position, r_{col} is final radial position and it is equal to the total radius of solar collector.

According to the continuity equation, the mass flow rate must be constant everywhere. Moreover, the fluid's density has been considered as function of the fluid's temperature only. Therefore, the equation can be rearranged as

$$-\Delta p(r) = \frac{\rho}{2}\frac{\dot{m}^2}{\rho^2}\left[\frac{1}{{A_{col}}^2(r_{col})} - \frac{1}{{A_{col}}^2(r)}\right]$$

As mentioned earlier, the collector system can be viewed as two parallel large disks with fluid flowing in between, thus the area of collector can be calculated. Substitute the expression of collector area into the pressure equation gives

$$-\Delta p(r) = \frac{\dot{m}^2}{2\rho}\left[\frac{1}{(2\pi r_{col}h_{col})^2} - \frac{1}{(2\pi r h)^2}\right]$$

$$-\Delta p(r) = \frac{\dot{m}^2}{8\rho\pi^2{h_{col}}^2}\left[\frac{1}{{r_{col}}^2} - \frac{1}{r^2}\right]$$

The last equation is defined as the pressure equation and it is used for Eq. (3.13) in Chapter 3.

Temperature Equation

Recall the energy equation and write for one spatial direction only which is radial direction, thus

$$\frac{\partial}{\partial t}\left[\rho\left(u+\frac{\vec{V}^2}{2}\right)\right]+\nabla\cdot\left[\rho\left(u+\frac{\vec{V}^2}{2}\right)\vec{V}\right]=$$

$$\rho\dot{q}+\dot{q}_{viscous}-\nabla\cdot\left(p\vec{V}\right)+\rho\left(\vec{F}_{body}\cdot\vec{V}\right)+\dot{w}_{viscous}+\dot{w}_{external}$$

The following assumptions are applied to the energy equation

Steady state condition → $\partial/\partial t\ (\quad)=0$

Exclusion of viscous heating → $\dot{q}_{viscous}=0$

Exclusion of viscous work → $\dot{w}_{viscous}=0$

Exclusion of external work → $\dot{w}_{external}=0$

Exclusion of body force → $\vec{F}_{body}=0$

Radial flow → circumferential and axial velocities $(u_\theta \ and \ u_z)=0$

Implementing the above assumptions to the energy equation and rewrite for thermal energy equation in cylindrical coordinate yields

$$\rho u_r c_p\frac{\partial T}{\partial r}=\rho\dot{q}$$

Volumetric heating of a fluid element $\dot{q}$ is recognized due to 1) volumetric heating by absorption or emission of radiation and 2) volumetric heating due to temperature gradients which is thermal conduction. Therefore, the summation of volumetric heating is

$$\rho u_r\frac{\partial T}{\partial r}=\frac{\rho}{c_p}\left(\dot{q}^{cond}+\dot{q}^{rad}\right)$$

Next evaluation is to obtain the mathematical expression of these two volumetric heating processes. It is derived according to Fig. A4. This figure shows sketch of energy flux for a fixed control and moving infinitesimal fluid element.

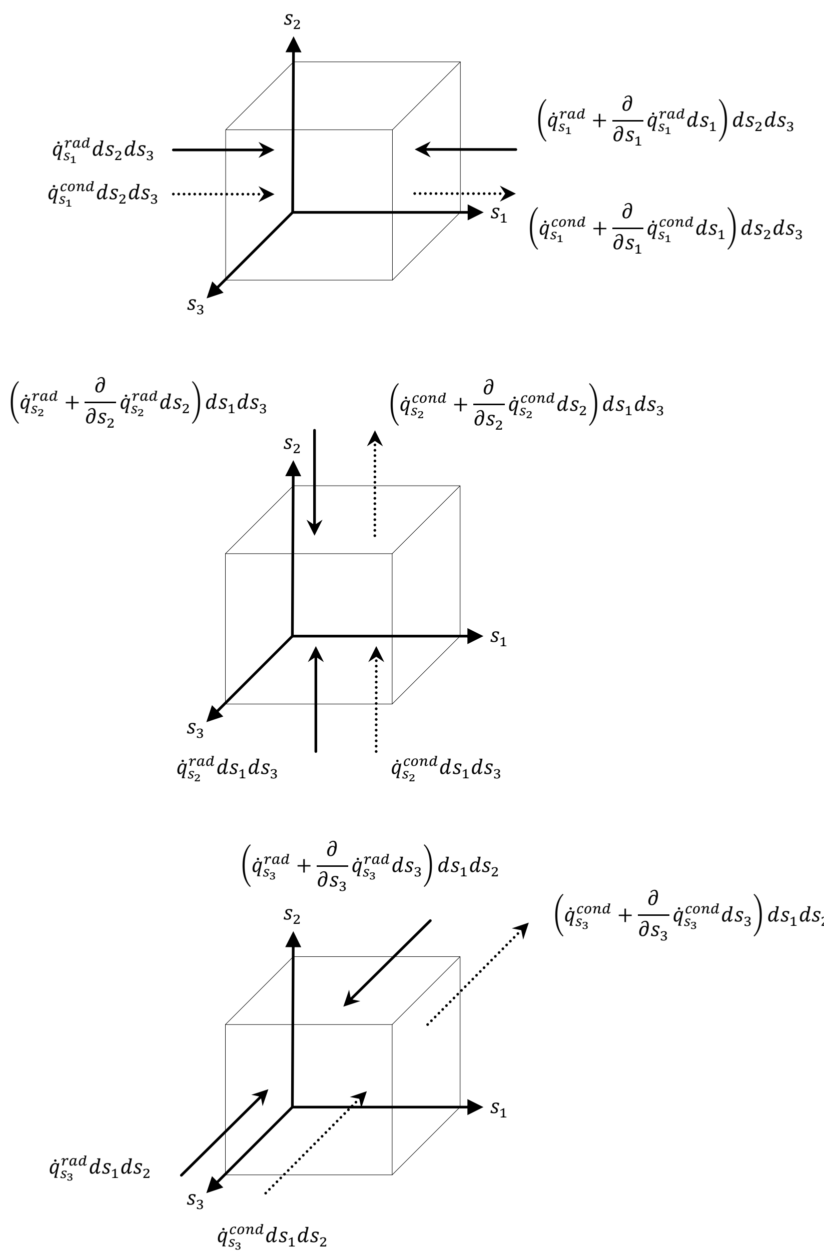

Fig. A4: Energy fluxes for conduction and radiation process associated with a fixed control and moving infinitesimal fluid element.

Recalling the first law of thermodynamic which govern the conservation of energy; Rate of change of energy inside fluid element equal to the summation of the net flux of heat into element and rate of work done due to pressure and stress forces on surface. Expression for rate of change of energy inside fluid element has been derived in terms of enthalpy, and for ideal gas model, it is proportional to the temperature and a constant which is the specific heat for constant pressure process. As for the rate of work done on element due to pressure and stress forces on surface, it is also has been derived in terms of shear stress. Now the evaluation has the purpose to obtain the expression for net flux of heat which is consist of conduction and convection process. Therefore, evaluation for s_1 component gives

$$\left[\dot{q}_{s_1}^{cond} - \left(\dot{q}_{s_1}^{cond} + \frac{\partial}{\partial s_1}\dot{q}_{s_1}^{cond} ds_1\right)\right] ds_2 ds_3 = 0$$

$$\left[\dot{q}_{s_1}^{rad} + \left(-\dot{q}_{s_1}^{rad} - \frac{\partial}{\partial s_1}\dot{q}_{s_1}^{rad} ds_1\right)\right] ds_2 ds_3 = 0$$

For s_2 component,

$$\left[\dot{q}_{s_2}^{cond} - \left(\dot{q}_{s_2}^{cond} + \frac{\partial}{\partial s_2}\dot{q}_{s_2}^{cond} ds_2\right)\right] ds_1 ds_3 = 0$$

$$\left[\dot{q}_{s_2}^{rad} + \left(-\dot{q}_{s_2}^{rad} - \frac{\partial}{\partial s_2}\dot{q}_{s_2}^{rad} ds_2\right)\right] ds_1 ds_3$$

and for s_3 component,

$$\left[\dot{q}_{s_3}^{cond} - \left(\dot{q}_{s_3}^{cond} + \frac{\partial}{\partial s_3}\dot{q}_{s_3}^{cond} ds_3\right)\right] ds_1 ds_2 = 0$$

$$\left[\dot{q}_{s_3}^{rad} - \left(-\dot{q}_{s_3}^{rad} - \frac{\partial}{\partial s_3}\dot{q}_{s_3}^{rad} ds_3\right)\right] ds_1 ds_2 = 0$$

Thus, the net flux of heat equation for conduction process are obtained as

$$\dot{q}_{s_1}^{cond} - \left(\dot{q}_{s_1}^{cond} + \frac{\partial}{\partial s_1}\dot{q}_{s_1}^{cond} ds_1\right) ds_2 ds_3 = -\frac{\partial}{\partial s_1}\dot{q}_{s_1}^{cond} ds_1 ds_2 ds_3$$

$$\dot{q}_{s_2}^{cond} - \left(\dot{q}_{s_2}^{cond} + \frac{\partial}{\partial s_2}\dot{q}_{s_2}^{cond} ds_2\right) ds_1 ds_3 = -\frac{\partial}{\partial s_2}\dot{q}_{s_2}^{cond} ds_1 ds_2 ds_3$$

$$\dot{q}_{s_3}^{cond} - \left(\dot{q}_{s_3}^{cond} + \frac{\partial}{\partial s_3}\dot{q}_{s_3}^{cond} ds_3\right) ds_1 ds_2 = -\frac{\partial}{\partial s_3}\dot{q}_{s_3}^{cond} ds_1 ds_2 ds_3$$

From energy equation regarding the summation of volumetric heating, the volumetric heating for conduction process can be written as

$$\dot{q}^{cond} = -\left(\frac{\partial}{\partial s_1}\dot{q}^{cond}_{s_1} + \frac{\partial}{\partial s_2}\dot{q}^{cond}_{s_2} + \frac{\partial}{\partial s_3}\dot{q}^{cond}_{s_3}\right) ds_1 ds_2 ds_3$$

The conduction heat rate is governed by Fourier's law, therefore the conduction heat rate analysis can be expressed as

$$\dot{q}^{cond}_{s_1} = -k\frac{\partial T}{\partial s_1}, \qquad \dot{q}^{cond}_{s_2} = -k\frac{\partial T}{\partial s_2}, \qquad \dot{q}^{cond}_{s_2} = -k\frac{\partial T}{\partial s_2}$$

Substitute these results into conduction volumetric heating equation. Hence

$$\dot{q}^{cond} = -\left(\frac{\partial}{\partial s_1}\left(-k\frac{\partial T}{\partial s_1}\right) + \frac{\partial}{\partial s_2}\left(-k\frac{\partial T}{\partial s_2}\right) + \frac{\partial}{\partial s_3}\left(-k\frac{\partial T}{\partial s_2}\right)\right) ds_1 ds_2 ds_3$$

$$\dot{q}^{cond} = k\left(\frac{\partial^2 T}{\partial {s_1}^2} + \frac{\partial^2 T}{\partial {s_2}^2} + \frac{\partial^2 T}{\partial {s_2}^2}\right) ds_1 ds_2 ds_3$$

The equation can be expressed as per unit mass, thus the following relation must be hold $\rho = 1/\mathcal{v}$, where $\mathcal{v}$ is volume per unit mass or specific volume. Furthermore,

$$\dot{q}^{cond} = k\left(\frac{\partial^2 T}{\partial {s_1}^2} + \frac{\partial^2 T}{\partial {s_2}^2} + \frac{\partial^2 T}{\partial {s_2}^2}\right) d\mathcal{v}$$

$$\dot{q}^{cond} = k\left(\frac{\partial^2 T}{\partial {s_1}^2} + \frac{\partial^2 T}{\partial {s_2}^2} + \frac{\partial^2 T}{\partial {s_2}^2}\right) \frac{1}{\rho}$$

Now the mathematical expression of volumetric heating due to thermal conduction has been obtained. The net heat flux for thermal radiation can be written as follow

$$\left[\dot{q}^{rad}_{s_1} + \left(-\dot{q}^{rad}_{s_1} - \frac{\partial}{\partial s_1}\dot{q}^{rad}_{s_1} ds_1\right)\right] ds_2 ds_3 = -\frac{\partial}{\partial s_1}\dot{q}^{rad}_{s_1} ds_1 ds_2 ds_3$$

$$\left[\dot{q}^{rad}_{s_2} + \left(-\dot{q}^{rad}_{s_2} - \frac{\partial}{\partial s_2}\dot{q}^{rad}_{s_2} ds_2\right)\right] ds_1 ds_3 = -\frac{\partial}{\partial s_2}\dot{q}^{rad}_{s_2} ds_1 ds_2 ds_3$$

$$\left[\dot{q}^{rad}_{s_3} - \left(-\dot{q}^{rad}_{s_3} - \frac{\partial}{\partial s_3}\dot{q}^{rad}_{s_3} ds_3\right)\right] ds_1 ds_2 = -\frac{\partial}{\partial s_3}\dot{q}^{rad}_{s_3} ds_1 ds_2 ds_3$$

Again, from energy equation regarding the summation of volumetric heating, the radiation volumetric heating equation can be expressed as

$$\dot{q}^{rad} = -\left(\frac{\partial}{\partial s_1}\dot{q}^{rad}_{s_1} + \frac{\partial}{\partial s_2}\dot{q}^{rad}_{s_2} + \frac{\partial}{\partial s_3}\dot{q}^{rad}_{s_3}\right) ds_1 ds_2 ds_3$$

The radiation volumetric heating equation can also be written as per unit mass. Substitute the relation $\rho = 1/\mathcal{v}$ gives

$$\rho\dot{q}^{rad} = -\left(\frac{\partial}{\partial s_1}\dot{q}^{rad}_{s_1} + \frac{\partial}{\partial s_2}\dot{q}^{rad}_{s_2} + \frac{\partial}{\partial s_3}\dot{q}^{rad}_{s_3}\right) d\mathcal{v}$$

$$\dot{q}^{rad} = -\left(\frac{\partial}{\partial s_1}\dot{q}^{rad}_{s_1} + \frac{\partial}{\partial s_2}\dot{q}^{rad}_{s_2} + \frac{\partial}{\partial s_3}\dot{q}^{rad}_{s_3}\right)\frac{1}{\rho}$$

The mathematical expression for heating of fluid element by thermal radiation now has been obtained. Rewriting these two equations regarding heating of fluid element by thermal conduction and radiation for cylindrical coordinate, yields

$$\dot{q}^{cond} = k\left(\frac{\partial^2 T}{\partial r^2} + \frac{1}{r}\frac{\partial^2 T}{\partial \theta^2} + \frac{\partial^2 T}{\partial z^2}\right)\frac{1}{\rho}$$

$$\dot{q}^{rad} = -\left(\frac{\partial}{\partial r}\dot{q}^{rad}_{r} + \frac{1}{r}\frac{\partial}{\partial \theta}\dot{q}^{rad}_{\theta} + \frac{\partial}{\partial z}\dot{q}^{rad}_{z}\right)\frac{1}{\rho}$$

Since energy analysis consider only in radial direction, thus substitute these results for radial direction only, the thermal energy equation now in form of

$$\rho u_r \frac{\partial T}{\partial r} = \frac{1}{c_p}\left[k\left(\frac{\partial^2 T}{\partial r^2}\right) - \left(\frac{\partial \dot{q}^{rad}_r}{\partial r}\right)\right]$$

In the current work, volumetric heating due to molecular conduction of fluid is excluded and only volumetric heating from solar radiation is included in the analysis. Thus the thermal energy equation reduces to

$$c_p \rho u_r \frac{\partial T}{\partial r} = -\frac{\partial \dot{q}^{rad}_r}{\partial r}$$

In order to integrate the equation, the partial derivative terms should be transformed into the total derivative form. This transformation could be done if T and $\dot{q}^{rad}_r$ are function of collector radius only. Thus, substitute the following relation in the thermal energy equation: $T = T_a$ and $\dot{q}^{rad}_r = \dot{q}$, it gives

$$dT_a = \frac{\partial T(r)}{\partial r} dr$$

$$d\dot{q} = \frac{\partial \dot{q}_r^{rad}(r)}{\partial r} dr$$

Several assumptions have been made that the temperature and volumetric heat rate of fluid are function of the collector radius only. Therefore, the above relation is valid. Furthermore, substitute these relations into the thermal energy equation and integrate along the solar collector for axisymmetric condition yields

$$dT_a c_p \rho u_r (2\pi r) dh = -d\dot{q}(2\pi r) dr$$

$$dT_a c_p \int_h^{h_{col}} \rho u_r (2\pi r) dh = -d\dot{q} \int_r^{r_{col}} (2\pi r) dr$$

$$[T_a(r_{col}) - T_a(r)]\dot{m}c_p = -d\dot{q}(\pi {r_{col}}^2 - \pi r^2)$$

The above relation suggests that only fluid's temperature and fluid's heat flux rate becomes the variable of collector radius. However, fluid's density and specific heat are function of fluid's temperature as well. It means that each collector radius position holds one particular value of density (which has been represented by the mass flow rate) and specific heat capacity. Note that the boundary condition has been substituted: fluid's temperature at the edge of collector equal to the ambient air temperature $T_a(r_c) = T_{a_\infty}$. Rearrange the previous equation to obtain the fluid temperature along the solar collector result in

$$\left[T_{a_\infty} - T_a(r)\right]\dot{m}c_p = -d\dot{q}(\pi {r_{col}}^2 - \pi r^2)$$

$$T_a(r) = T_{a_\infty} + \frac{d\dot{q}}{\dot{m}c_p}\pi({r_{col}}^2 - r^2)$$

The last equation is defined as the temperature equation and it is used for Eq. (3.16) in Chapter 3.

This temperature equation can be refined by elaborating the expression of heat flux as follow

$$d\dot{q}(r) = h_{c-a}^{conv}(T_c - T_a) - h_{a-g}^{conv}\left(T_a - T_g\right)$$

This equation states that for a given energy in form of heat to the fluid, it must be balanced every time by heat looses via convection to the surrounding which are cover and ground surfaces. This evaluation is carried out for one point in the flow field. For evaluation along the solar collector, the equation should be written as function of collector radius. Thus, substitute the change of heat flux rate in radial direction into the heat balance equation yields

$$dT_a c_p \rho u_r (2\pi r) dh = -\left[h_{c-a}^{conv}\left(T_c - T_a(r)\right) - h_{a-g}^{conv}\left(T_a(r) - T_g\right)\right](2\pi r) dr$$

Integrate the equation for axisymmetric condition gives

$$dT_a c_p \int_h^{h_{col}} \rho u_r (2\pi r) dh = -\left[h_{c-a}^{conv}\left(T_c - T_a(r)\right) - h_{a-g}^{conv}\left(T_a(r) - T_g\right)\right] \int_r^{r_{col}} (2\pi r) dr$$

$$dT_a \dot{m} c_p = -\left[h_{c-a}^{conv}\left(T_c - T_a(r)\right) - h_{a-g}^{conv}\left(T_a(r) - T_g\right)\right]\left(\pi {r_{col}}^2 - \pi r^2\right)$$

The cover and ground temperature is assumed to be constant along the collector radius. Furthermore, the convection heat transfer coefficients is also assumed constant along the radius, together with the specific heat constant $c_p(T_a)$. With these assumptions, the solution for temperature profile in radial direction can be obtained by substituting $T_a(r_c) = T_{a_\infty}$ as boundary condition and h^{conv} as convection heat transfer coefficient, it gives,

$$\left[T_{a_\infty} - T_a(r)\right]\dot{m} c_p = -\left[h^{conv}\left(T_c - T_a(r)\right) - h^{conv}\left(T_a(r) - T_g\right)\right]\left(\pi {r_{col}}^2 - \pi r^2\right)$$

$$\left[T_{a_\infty} - T_a(r)\right]\dot{m} c_p = -h^{conv}\left(T_c - 2T_a(r) + T_g\right)\left(\pi {r_{col}}^2 - \pi r^2\right)$$

$$-T_a(r) = -T_{a_\infty} + \frac{-h^{conv}\left(T_c - 2T_a(r) + T_g\right)\left(\pi {r_{col}}^2 - \pi r^2\right)}{\dot{m} c_p}$$

$$T_a(r) + \frac{h^{conv} 2T_a(r)\left(\pi {r_{col}}^2 - \pi r^2\right)}{\dot{m} c_p(T_a)} = T_{a_\infty} + \frac{h^{conv}\left(T_c + T_g\right)\left(\pi {r_{col}}^2 - \pi r^2\right)}{\dot{m} c_p}$$

$$T_a(r) = \frac{T_{a_\infty} + \dfrac{h^{conv}\left(T_c + T_g\right)\left(\pi {r_{col}}^2 - \pi r^2\right)}{\dot{m} c_p}}{\dfrac{2h^{conv}\left(\pi {r_{col}}^2 - \pi r^2\right)}{\dot{m} c_p(T_a)}}$$

Define the denominator part as

$$C = \left(1 + \frac{2h^{conv}\left(\pi {r_{col}}^2 - \pi r^2\right)}{\dot{m} c_p(T_a)}\right)^{-1}$$

Therefore the temperature equation becomes

$$T_a(r) = T_{a\infty} + \frac{h^{conv}\left(T_c + T_g\right)}{\dot{m}c_p}\left(\pi {r_{col}}^2 - \pi r^2\right)\mathcal{C}$$

The last equation is defined as the refined temperature equation and it is used for Eq. (3.18) in Chapter 3.

Updraft Velocity Equation

Recall the momentum equation and write for one spatial direction only which is axial direction, thus

$$\frac{\partial}{\partial t}\rho u_z + \nabla \cdot \left(\rho u_z \vec{V}\right) = -\frac{\partial p}{\partial z} + \rho (f_z)_{body} + (f_z)_{viscous}$$

The following assumptions are applied to the momentum equation at the solar tower

Steady state condition → $\partial/\partial t\,(\quad) = 0$

Inviscid flow → $(f_z)_{viscous} = 0$

Inclusion of body force (gravity force) → $(f_z)_{body} \neq 0$

Axial flow → radial and circumferential velocities $(u_r \; and \; u_\theta) = 0$

Implementing the above assumptions to the momentum equation yields

$$\rho u_z \frac{\partial u_z}{\partial z} = -\frac{\partial p}{\partial z} + \rho g$$

The boundary layer equation is implemented in the analysis of airflow inside the solar tower. The flow carrying heat from the collector is rises towards the tower due to its buoyancy forces. This fluid (inside the tower) is less dense than outside fluid (outside the tower), thus when these two flow mixed at the outlet of the tower, the equilibrium condition will be achieved and the pressure of this fluid will be the same with the atmospheric pressure.

Characteristic of laminar boundary layer for free convection problem is that the flow is dominantly driven by buoyancy forces. Recalling the momentum equation and rewritten for boundary layer case result in

$$\frac{\partial}{\partial z}\rho u_z u_z = -\frac{\partial p_a}{\partial z} + \rho_a g$$

The pressure term becomes the air pressure gradient outside the boundary layer region. The fluid velocity outside the boundary layer region is zero and eventually becomes equal to the fluid of hot air rises from the collector. Therefore, the boundary layer equation reduces to

$$\frac{\partial}{\partial z}\rho(0) = -\frac{\partial p_a}{\partial z} + \rho_a g \rightarrow \frac{\partial p_a}{\partial z} = \rho_a g$$

Substitute this result into momentum equation of the fluid inside the tower, it yields

$$\frac{\partial}{\partial z}\rho u_z u_z = -\rho_a g + \rho g$$

$$\frac{\partial}{\partial z}\rho u_z u_z = g(\rho - \rho_a)$$

The first term on the right hand side of the above equation is the buoyancy force per unit mass, and flow originates because the density ρ is a variable. Since the fluid is modeled as ideal gas, thus from the previous discussion, the ideal gas is only care about temperature; therefore the change of fluid density is only due to temperature in the equation of volumetric thermal expansion. The coefficient of volumetric thermal expansion is given as

$$\beta = -\frac{1}{\rho}\left(\frac{\partial \rho}{\partial T}\right)_p$$

The coefficient of volumetric thermal expansion is hold for constant pressure process which is also one of the assumptions during derivation of equation of states. The change of density to the temperature for ideal gas model can be written as

$$p = \rho RT \rightarrow \rho = \frac{p}{RT}$$

$$\frac{d}{dT}\rho = \frac{d}{dT}\left(\frac{p}{RT}\right) \rightarrow \frac{d\rho}{dT} = -\frac{p}{RT^2}$$

Substitute the relation from ideal gas model into coefficient of volumetric thermal expansion yields to the coefficient of volumetric thermal expansion for ideal gas as

$$\beta = -\frac{1}{\rho}\left(-\frac{p}{RT^2}\right) = \frac{1}{\rho}\left(\frac{\rho RT}{RT^2}\right) = \frac{1}{T}$$

Next evaluation is to relate the thermal expansion coefficient with momentum equation. Rearrange the thermal expansion coefficient yields

$$\beta = -\frac{1}{\rho}\left(\frac{\partial \rho}{\partial T}\right)_p \rightarrow \partial \rho = -\rho\beta\partial T$$

$$\rho_{a_\infty} - \rho_a = -\rho\beta\left(T_{a_\infty} - T_a\right)$$

The relation of density change due only to temperature is known as Boussinesq approximation. Substitute this relation into momentum equation, gives

$$\frac{\partial}{\partial z}\rho u_z u_z = g\left[-\rho\beta\left(T_{a_\infty} - T_a\right)\right]$$

$$u_z \frac{\partial u_z}{\partial z} = -g\beta\left(T_{a_\infty} - T_a\right)$$

The left hand side of momentum equation represents the change of momentum of fluid, while the right hand side represents the buoyancy force. The updraft velocity is denoted as u_z, g is gravity constant, β is thermal expansion coefficient, and T_{a_∞} and T_a is ambient temperature and working fluid temperature respectively.

In order to establish a discussion regarding natural convection phenomena inside the solar tower, the hot fluid at the base of solar tower has been modeled as the case of heating horizontal plate. The heated horizontal plate is treated as the source of heat which makes the natural convection phenomena occur inside the solar tower. Therefore, from the previous analysis of boundary layer equation an important relation in the absence of fluid motion can be obtained which is

$$\frac{\partial p_a}{\partial z} = \rho_a g$$

This equation implies that for aerostatic condition as shown in Fig. A6. The fluid's static pressure is balance with the gravity force. Since the model of fluid's density is function of temperature, then the pressure gradient (along line $A - B$) immediately adjacent to the heated plate will be different than the pressure gradient far from the heated plate (along line $C - D$). The pressure gradient away from the heated plate will hold the form

$$\left(\frac{\partial p}{\partial z}\right)_{C-D} = \rho_{T=T_{a_\infty}}(-g)$$

While the pressure gradient adjacent to the heated plate will be

$$\left(\frac{\partial p}{\partial z}\right)_{A-B} = \rho_{T=T_a}(-g)$$

Hence, a pressure difference will be induced between line $A - B$ and line $C - D$. Now the aerostatic pressure equation can be integrated in order to obtain a mathematical expression of pressure difference inside the solar tower. To do so, multiply both side of aerostatic pressure equation with dz yields

$$\frac{\partial p_a}{\partial z} dz = \rho_a g \, dz$$

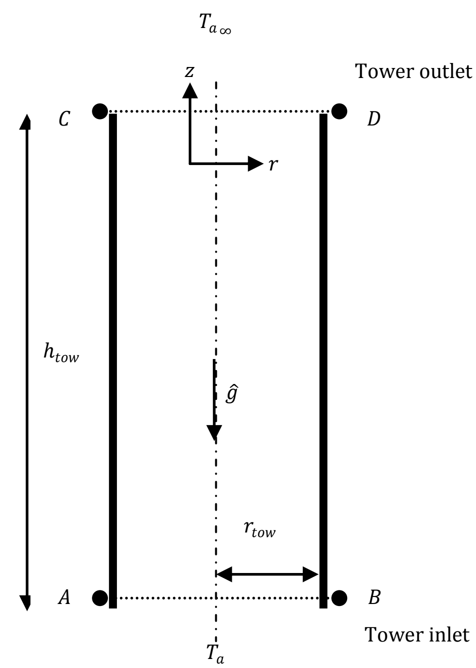

Fig. A5: Sketch for discussion of pressure difference at the inlet and outlet of solar tower.

From definition of total derivative

$$dp = \frac{\partial p(z)}{\partial z} dz, \text{valid for p function of } z \text{ only}$$

Substitute this relation into the aerostatic pressure equation and integrate along the length, thus

$$\int_{p_{AB}}^{p_{CD}} dp_a = \rho_a(T)[-g]\int_{h}^{h_{tow}} dz$$

$$p_{CD} - p_{AB} = [\rho_a(T_{a\infty}) - \rho_a(T_a)][-g]h_{tow}$$

$$-\Delta p = gh_{tow}[\rho_a(T_{a\infty}) - \rho_a(T_a)]$$

From this result, the pressure difference in radial direction will not exist. Instead, fluid will be pushed towards the plate where it is heated and rises against gravity. This pressure difference provides the driving force for fluid motion and allows the definition of a characteristic velocity for the natural convection problem u_{char}. The pressure difference will induce a consistent fluid momentum change, and for inviscid flow, the momentum equation can be written under Bernoulli principle. For a streamline in flow-field, the summation of static and dynamic pressure must be constant, thus writing the dynamic pressure as

$$p_{dynamic} = \frac{1}{2}\rho_a {u_{char}}^2$$

and the static pressure as the aerostatic equation

$$p_{aerostatic} = gh_{tow}[\rho_a(T_{a\infty}) - \rho_a(T_a)]$$

The total pressure equation can be obtained as

$$p_{dynamic} + p_{aerostatic} = constant \rightarrow p_{dynamic} = p_{aerostatic}$$

$$\frac{1}{2}\rho_a {u_{char}}^2 = gh_{tow}[\rho_a(T_{a\infty}) - \rho_a(T_a)]$$

From discussion regarding natural convection problems, the density is driven by a temperature difference. From definition of thermal expansion coefficient β in the previous section, it can be written that

$$\beta = -\frac{1}{\rho}\left(\frac{\partial\rho}{\partial T}\right)_p \rightarrow \partial\rho_a = -\rho_a\beta\partial T$$

Thus write the equation for

$$\partial\rho_a = \rho_a(T_{a\infty}) - \rho_a(T_a) \text{ and } \partial T = T_{a\infty} - T_a$$

The characteristic velocity becomes

$$u_{char}{}^2 = \frac{2gh_{tow}}{\rho_a}\left[-\rho_a\beta\left(T_{a\infty} - T_a\right)\right]$$

$$u_{char} = \sqrt{2gh_{tow}\beta\left(T_a - T_{a\infty}\right)}$$

Substitute $\beta = 1/T_{a\infty}$ gives

$$u_{char} = \sqrt{2gh_{tow}\frac{T_a - T_{a\infty}}{T_{a\infty}}}$$

Define the characteristic velocity u_{char} inside the solar tower for free convection process as the updraft velocity u_z (velocity at the bottom of the tower). Therefore, the updraft velocity equation inside the solar tower can be obtained as

$$u_z = \sqrt{2g\frac{T_a - T_{a\infty}}{T_{a\infty}}h_{tow}}$$

The last equation is defined as the updraft velocity equation and it is used for Eq. (3.22) in Chapter 3.

Appendix B *Experimental Apparatus*

Experiment was conducted by employing several equipments. In this section, arrangement of a lab-scale solar updraft power generator is presented in form of photo taking during the measurement for both type of collector. The sensors to measure the updraft temperature and velocity were also showed along with the flow visualization equipments in Fig. B.1 to Fig. B.4.

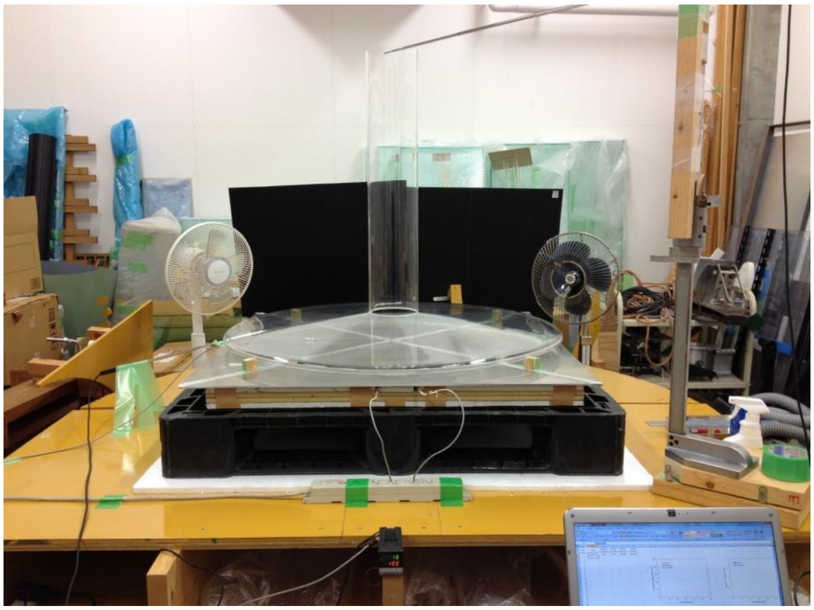

Fig. B.1 Setup of experiment for collector type A.

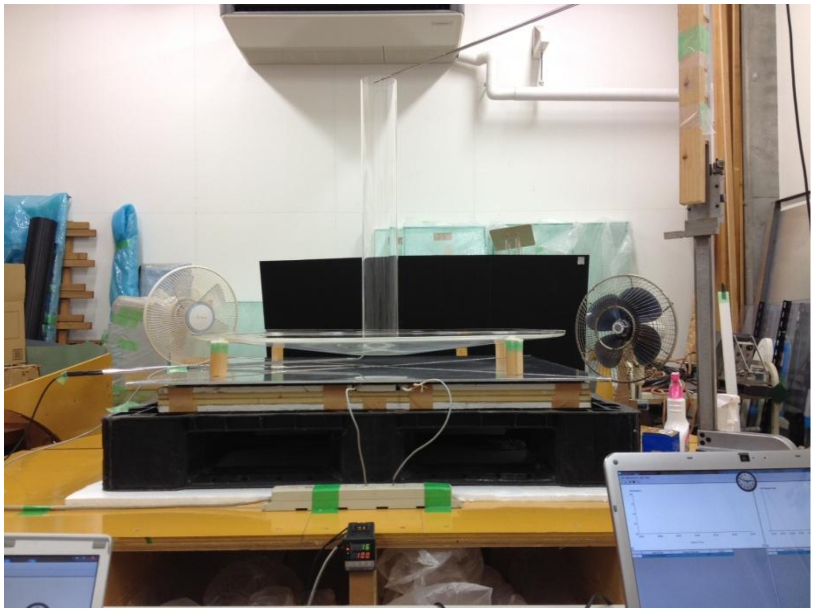

Fig. B.2 Setup of experiment for collector type B.

Fig. B.3 Equipments used in flow visualization experiment, showing a high-speed camera, laser generator and its controller.

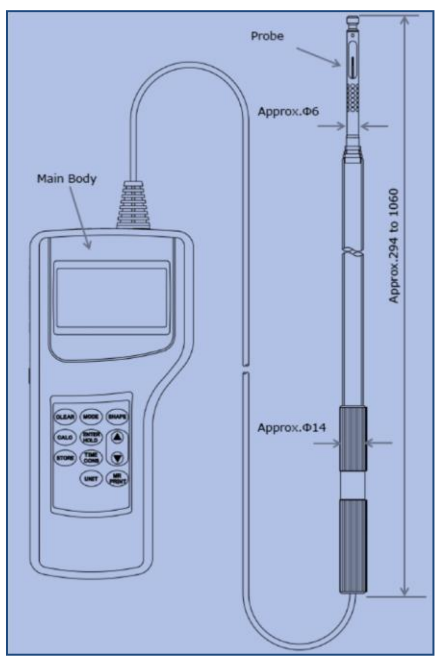

Fig. B.4 A thermo-anemometer sensor used in the experiment to measure the updraft temperature and updraft velocity.

Appendix C *Scientific Production*

Usage and performance assessment of solar-induced wind energy for power production in Indonesia. Solar updraft power generator (SUPG) is a renewable energy facility capable of harnessing the solar energy. The first large prototype of SUPG was built in 1980's in Manzanares, Spain to evaluate the projected performance of the facility and to serve as verification tools for future power simulator development. In this paper, the performance of a solar updraft power generator is assessed using the developed mathematical model. The model is validated by comparison with experimental data of Manzanares SUPG. The validated model is then used to calculate the amount of energy produced in seven selected locations in Indonesia. The selected cities in Indonesia exhibited a higher average monthly energy production compared to those in Manzanares. In particular a site like Kupang, would generate two times the energy of the Manzanares SUPG. The power production is sufficient for the needs of this isolated area in Indonesia and has the potential to solve the energy issue.

Hadyan Hafizh, Hiromichi Shirato, Daiki Yui, "Usage and performance assessment of solar-induced wind energy for power production in Indonesia", Accepted for presentation in the 1st International Conference on Science and Engineering (ICoSE), Pekanbaru, September 28-29, 2015.

Study on the efficiency of solar updraft power generator (in Japanese)

Daiki Yui, Hadyan Hafizh, Hiromichi Shirato, *Study on the efficiency of solar updraft power generator*, Annual Conference of Japanese Society of Civil Engineering (JSCE) – Kansai Branch, 30 May 2015.

Aerothermal simulation and power potential of a solar updraft power plant. In this paper we develop a theoretical model for calculating the steady inviscid flow subjected to solar radiation at the collector of a solar updraft power plant. The result was a set of nonlinear equation describing the transformation of the solar radiation into heat-flux of the collector airflow. Iterative scheme was employed in order to solve the equation for mass flow rate and temperatures, for which computer codes were developed. A comparison of simulation results with the Manzanares prototype experimental data was performed; demonstrating good agreement between the two. Computed power for selected locations in Japan was also demonstrated for potential application of a solar updraft power plant.

Hadyan Hafizh, Hiromichi Shirato, "Aerothermal Simulation and Power Potential of a Solar Updraft Power Plant", Journal of Structural Engineering, JSCE, Vol. 61A, 2015.

Heat transfer and fluid flow analysis of a solar updraft power plant: Development of numerical simulation and experimental investigation. We access the validity of the convective heat transfer correlations employed in the heat transfer analysis of a lab-scale solar updraft power plant. Assessments were conducted through scrutinization of Rayleigh, Reynolds, and Prandtl numbers, for which mathematical model and numerical simulation were developed. The results showed that those dimensionless numbers were in the valid range for all simulated cases, suggesting the selected heat transfer coefficients were applicable. Measurements of temperature and velocity of the airflow as part of a research to increase the total efficiency from geometrical point of view were used as a comparison. It showed that simulated results overestimates the experimental data.

Hadyan Hafizh, Daiki Yui, Hiromichi Shirato, "Heat Transfer and Fluid Flow Analysis of a Solar Updraft Power Plant: Development of Numerical Simulation and Experimental Investigation", The 2nd Open Seminar on Fluid Sciences, Katsura Campus, Kyoto, Japan, 10 March 2015.

Development of mathematical model of a solar updraft power plant. The solar updraft power plant is a device which produces energy by using solar radiation to allow the updraft flow entrained the working fluid and thus converting thermal energy into kinetic energy. A theoretical study was attempted to assess the performance characteristics of a solar updraft power plant. The mathematical model was developed for steady and inviscid flow condition which was part of the optimum design development. Results from the model were compared with the Manzanares prototype experimental data where fairly good quantitative agreement was obtained.

Hadyan Hafizh, Hiromichi Shirato, "Development of mathematical model of a solar updraft power plant", The 27th KKHCTNN Symposium in Civil Engineering, Shanghai, China, November 9-12, 2014.